

Evaluation and robotic simulation of the glenohumeral joint

Présentée le 7 février 2020

à la Faculté des sciences et techniques de l'ingénieur
Laboratoire de mesure et d'analyse des mouvements
Programme doctoral en génie électrique

pour l'obtention du grade de Docteur ès Sciences

par

Matteo MANCUSO

Acceptée sur proposition du jury

Dr J.-M. Vesin, président du jury
Prof. K. Aminian, directeur de thèse
Prof. C. Pichonnaz, rapporteur
Dr C. Charbonnier, rapporteuse
Prof. S. Micera, rapporteur

Acknowledgements

I would like to thank Professor Kamiar Aminian, for giving me the opportunity to work on this challenging project and be a member of his research team. I would especially like to express my gratefulness for the many hours spent reading and correcting all the documents that I had to produce (reports, thesis, papers) and for pushing me to work in directions that I would not have considered.

I would also like to express my gratitude to my “shoulder modeller” collaborators, Yasmine Boulanaache, Ehsan Sarshari and Alexandre Terrier for all of their help in understanding how the numerical simulations work and to develop a common interface to bridge our projects into a combined numerical-robotic simulation. Specially to Yasmine Boulanaache who provided precious help to mitigate sometimes very tense situation and who was always trying to help to the best of her capabilities. Alexandre Terrier also provided precious help in the initial phase of the SNSF project, specially for all the administrative work, for his help and contribution in writing a very successful funding request and for his general advices on the general design of the robotic shoulder simulator.

My gratitude goes to Pascal Morel, our very calm, yet with an incredibly curious and active mind, lab technician, who provided invaluable support in the conception, design and construction of the robotic simulator and whatever hardware-related question or problem.

I also thank all of my clinical partners, in particular to Professor Fabio Becce, MD., Professor Alain Farron, MD. Frédéric Vauclair, MD. Patrick Goetti, MD. Nicolas Gallusser, MD. for their help in understanding not only the mechanics of the shoulder but also the structure and functioning of a research clinic and all the processes that a patient has to undergo during his treatment. Special thanks to Fabio Becce and Patrick Goetti for always being the first ones to answer to my questions and to offer precious help whenever they could (for finding patients for my study and helping me to understand how to adapt the test to the patient’s needs, for performing last-minutes extra-measurements on the CT-scans to address my doubts about the GH angles and so many other little favors and tips all along the PhD). Special thanks also to Frédéric Vauclair, without whom, the problematic about the functional evaluation of the human shoulder would not appear in this thesis. He managed to motivate my curiosity and allowed the creation of the project Volfon by solving all the little problems (funding, need for patients, ethical committee permissions, etc) with great efficiency.

Many thanks to all of my LMAM colleagues, ex-colleagues, and friends, Christopher Moufawad El Achkar, Benedikt Fasel, Nan Wang, Mathieu Falbriard, Prithvi Chakravarty, Abolfazl Soltani, Fabien Massé, Arash Arami, Abdolmajid Yousefsani Seyed, Anisoara Ionescu, Martin Savary, Joaquin Cabeza De Pablo, Salil Apte, Mahdi Hamidi, Gaëlle Prigent, Lena Carcreff, Mina Arabbaniasad, Arash Atrsaiei, Yasaman Izadmehr, Hooman Dejnabadi, Francine Eglese, Danielle Alavarez and Alan Bourke for a relaxed and peaceful working atmosphere. Very particular thanks go to Nan for his precious help in orienting the *Volfon* project toward the use of VR technology and for teaching me the basics and philosophy of a Unity developer. I would like to express my gratitude to Christopher for always raising the spirits with his jokes, and even when he was overwhelmed with work, taking the time to provide some good advices. My gratitude goes also to Salil Apte for his wise and well-informed advices.

To all of my friends and advisors, who each gave his contribution to this project. I would like to thank in particular Paul-Arthur Dreyfus for his help in understanding how to control and particularly how not to control a robot, as well as for all of his salsa classes, advices and his involvement toward the dancing community. To Patrick Luca Sgrò for always being present, curious and eternally enthusiastic. For the long discussions on virtual reality applications and in particular on how to improve my VR tests. To Charles Hayoz for his friendship, for some very long and interesting discussion on the future of rehabilitation and for showing me how to solve the most horrible types of Unity bugs! Thank you to Galina Limorenko and Katarina Damjanovic for helping me clarifying my texts and bringing their spelling and grammar to a nearly flawless level. Thank you to Gwendoline Kok for her teaching and advices in statistical analysis. To Andrea Guerrieri for his teaching on communication protocols, and in particular on the CAN protocol.

But also to all of my friends that just helped to make these years more memorable. To my friends from the association Cubaliente that have been there to teach me how to dance and actually enjoy it. In particular Paul-Arthur Dreyfus, Patrick Sgrò, Katalina Landeata and Pattra Favrod that really allowed me to start dancing and pass the initial struggles. To Gianrocco Lazari, Igor Krawczuk, Laure Chomereau, Elahi Noore Shaik, Céline Mottet, Émilie Stegmüller, Cinzia Cinesi, Mervegul Kirci, Katherine Ramirez, Elena Cabello and so many others for all of the fantastic time we spent together. My gratitude to my fighter friends from the *UNIL’AHME* and the *École lémanique d’Art et d’Action* for teaching me the ways of the sword.

Last but not least, my warmest thank to my parents Francesco and Barbara Mancuso, to my brother Marco Mancuso and my family who always supported and encouraged me to the best of their abilities.

The work presented in this thesis was funded by grant CR32I2_162766 from the *Swiss National Science Foundation*, and *Lausanne Orthopedic Research Foundation*, who I thank for their support and thrust.

Lausanne, the 7th October 2019

Abstract

The shoulder is the joint with the largest range of motion in the human body. It is composed of three articulations, the glenohumeral articulation providing about two thirds of its mobility which is, also the most complex and fragile of the three. For this reason, it possesses a particularly complex stabilization mechanism involving a large number of different structures, making it particularly difficult to model, evaluate and treat. Since many structures are involved in the stabilization of this articulation, pathologies affecting any of these elements may compromise the whole stabilization mechanism. In that case, a good understanding of the mechanisms involved, combined with reliable evaluation tools are necessary to provide an effective treatment. At present, different modelling approaches tried to model the phenomenon of glenohumeral instability, but none was able to replicate the whole mechanism reliably. These limitations are particularly problematic during total shoulder replacement surgeries, where the inability to reproduce healthy glenohumeral motions is the main cause of implant failure. The development of a model able to predict the onset of GH instability based on the surgical planning, would greatly improve the general survivorship of the implants, and is one of the main goals of this thesis. Additionally, the clinical tools available for the evaluation of the functional outcome are limited. Clinical questionnaires, static apprehension and laxity scores and two-dimensional evaluations of the articular ranges being the instruments used in most situations. Although fast and simple, these instruments are either prone to biases based on patient's interpretation and psychological state or provide only a partial evaluation of the functional limitations. Considering that the main function of the upper limb (composed of the shoulder, arm, elbow and forearm) is to place and orient the hand in space, for the latter to perform a particular action; the reachable space defined as the total volume where the upper limb is able to place the hand, is a feature of great interest. In biomechanical research laboratories, measurements with standard motion capture system enables a more comprehensive and accurate evaluation of the whole upper limb, including the evaluation of its reachable space. Unfortunately, the use of such platforms is generally too complex, expensive and time-consuming for clinical examinations. To this end, the development of new tools able to bring some of the most interesting features recorded in biomechanical laboratories to the clinical context would offer promising new solutions for the functional evaluation of patients and represent the second goal of this thesis.

This thesis addresses these issues and proposes and evaluates two new instruments: a robotic platform for the evaluation of prosthetic instability of the shoulder complex, and an instrument for the functional evaluation of the upper limb and in particular of its reachable space. For both tools, a rigorous evaluation in the laboratory is proposed, followed by an evaluation of the first instrument by modelling patients, and for the second instrument, an evaluation of its reliability on patients recorded directly in a consultation room of the local hospital (CHUV).

In the first part, a five degrees of freedom robotic simulator is developed to reproduce the 3D net forces acting on the natural glenohumeral joint, as well as most of its range of motion. This robot is special because it utilizes real prostheses to form the glenohumeral joint, and doesn't offer any mechanism to prevent the joint's dislocations. All the elements of the robot are explained, from its mechanical conception all the way to its control. Its performance is then evaluated in several cases of increasing complexity. First using simple motions to evaluate its accuracy and dynamic behavior. Second to reproduce the instability assessment of a standardized robotic wear test for commercial prostheses. Third to reproduce the force patterns recorded *in vivo* by an instrumented prosthesis, both using a quasi-static and a dynamic approach. All these tests indicated that the robotic simulator is able to accurately and reliably reproduce the requested simulations.

Next, the robot is adapted to evaluate the potential onset of prosthetic instability in three patients planned for total shoulder replacement. The CT-scans and surgical planning from these patients are used to build a patient-specific musculoskeletal model with the planned prosthetic implant for each one of them. Data such as the physiological cross section of their muscles, their origin and insertion points and their bone morphologies are factored in this model, developed thanks to a partnership with the laboratory of biomechanical orthopedics (LBO - EPFL). The predicted glenohumeral forces and relative orientations of the prosthetic implant are then transmitted to the robotic simulator, which using an exact copy of the patient's prosthetic implant, reproduced three daily life motions with a potential to trigger instable behavior in the shoulder complex. While it was possible to simulate the data from the patients in the three different situations, the model indicated much more instability than the clinical results. The possible causes of this difference as well as the possibility to use this methodology for future research projects are reported.

In the second part, an instrument for the evaluation of the reachable space is developed using technologies designed to be used by the general public. This approach offers a cheaper, faster and simpler solution than the standard instruments available in motion capture laboratories, while providing comparable metrics. The proposed instrument is composed by a virtual reality setup, the HTC Vive, a modified backpack and two wrist-mounted sensors attached through regular watch-bands. After a short calibration, the backpack allows to monitor the 3D motions of the thorax, while the wrist-mounted sensors allow, thanks to a rigid-body model, to track the positions of the elbow and wrist in real-time. This information is then used to build an avatar of the patient's body, that he/she sees through the virtual reality headset. A set of simple tasks are then proposed to challenge the mobility of the patient's upper limbs, while distracting him/her from the clinical context of the examination, virtually leading him/her into a more natural environment. At the end of the set, a report of the patient's performance is automatically generated, and the main results are displayed on the examiner's screen, including an evaluation of the patient's reachable space, computed using a customized algorithm. The accuracy and reliability of this instrument are evaluated in the laboratory, achieving satisfactory results on a set of ten healthy young subjects performing a test retest protocol.

Next this instrument is evaluated on a population of older patients with different types of functional affections, directly in the consultation box of the local hospital. Early results indicated the test to be inappropriate for the population studied, mostly due to the onset of fatigue in the patients and of their potentially limited ability to turn the head as far as younger subjects would, preventing them to see some of the targets. An adapted version of the test is then proposed, including less exercises, and providing more guidance to the patients. It is evaluated in a test retest protocol on 16 new patients. All the patients managed to finish the test twice, for the test retest protocol. The repeatability of the reachable range and reachable space was excellent ($ICC = 0.94$; $ICC = 0.91$ respectively) and all the proposed scores were able to discriminate the pathologic upper limb from the healthy one. Additionally, the reachable space of the healthy upper limbs displayed similar values to those recorded using the longer version of the test.

This thesis proposes two original instruments for the evaluation and robotic simulation of the glenohumeral joint. It offers a tool for reproducing physiological forces and motions within the glenohumeral joint, opening new opportunities for the study of glenohumeral instability. At the same time, it also proposes a second instrument allowing to evaluate the functional impairment of a patient's upper limb in an objective and reliable way, extracting information that in the past required the deployment of unrealistic amounts of resources for a clinical examination.

Keywords

Clinical evaluation, functional evaluation, glenohumeral instability, motion capture, outcome evaluation, reachable space, shoulder biomechanics, surgery, total shoulder arthroplasty, upper limb evaluation, virtual reality, 3D kinematics, robotic simulations, musculoskeletal simulations

Résumé

L'épaule est l'articulation présentant la plus grande amplitude articulaire du corps humain. Elle est composée de trois articulations, l'articulation glénohumérale assurant environ les deux tiers de sa mobilité, est également la plus complexe et la plus fragile des trois. Pour cette raison, elle possède un mécanisme de stabilisation particulièrement complexe impliquant un grand nombre de structures différentes, la rendant particulièrement difficile à modéliser, évaluer et traiter. De nombreuses structures étant impliquées dans la stabilisation de cette articulation, les pathologies affectant l'un de ces éléments peuvent compromettre l'ensemble du mécanisme de stabilisation. Dans ce cas, une bonne compréhension des mécanismes impliqués ainsi que des outils d'évaluation fiables sont nécessaires pour fournir un traitement efficace. Actuellement, différentes approches de modélisation ont tenté de modéliser le phénomène de l'instabilité glénohumérale, mais aucune n'est en mesure de reproduire le mécanisme dans son ensemble, de façon fiable. Ces limitations sont particulièrement problématiques lors de chirurgies de remplacement total de l'épaule, où l'incapacité de reproduire des mouvements glénohuméraux sains est la principale cause d'échec de l'implant. Le développement d'un modèle capable de prédire sur base de la planification chirurgicale le risque de rencontrer des problèmes d'instabilité GH, améliorerait considérablement la survie générale des implants, et le développement de ce modèle constitue l'un des objectifs principaux de cette thèse. De plus, les outils cliniques disponibles pour évaluer l'état fonctionnel de cette articulation sont limités. Les questionnaires cliniques, les scores d'appréhension et de laxité statiques et les évaluations bidimensionnelles des amplitudes articulaires sont les instruments les plus utilisés. Bien qu'ils soient rapides et simples, ces instruments sont, soit sujets à des biais basés sur l'interprétation du patient et son état psychologique du moment, soit ne fournissent qu'une évaluation partielle des limitations fonctionnelles. Considérant que la fonction principale du membre supérieur (composé par l'épaule, le bras, le coude et l'avant-bras) est de placer et d'orienter la main dans l'espace afin que cette dernière puisse effectuer une action particulière ; l'espace atteignable est défini comme le volume total où le membre supérieur est capable de placer la main, et est une caractéristique particulièrement intéressante à analyser. Dans les laboratoires de recherche biomécanique, les mesures effectuées avec des systèmes standardisés de capture du mouvement permettent une évaluation plus complète et plus précise de l'ensemble du membre supérieur, y compris l'évaluation de son espace atteignable. Malheureusement, l'utilisation de telles plateformes est généralement complexe, coûteuse et chronophage pour des examens cliniques. De plus, ces systèmes peuvent impressionner le sujet expérimental et peuvent en le tendant, altérer sa mobilité naturelle. Pour palier à ces limitations, le développement de nouveaux outils utilisables dans un cadre clinique, mais capables de mesurer certaines des caractéristiques les plus intéressantes enregistrées par les systèmes de laboratoires offrirait de nouvelles perspectives pour l'évaluation fonctionnelle des patients. La mise en place d'un tel système représente le deuxième objectif de cette thèse.

Essentiellement, cette thèse propose et évalue deux nouveaux instruments: une plate-forme robotique pour l'évaluation de l'instabilité prothétique de l'épaule et un instrument pour l'évaluation fonctionnelle du membre supérieur et en particulier de son espace atteignable. Pour les deux instruments, une évaluation rigoureuse en laboratoire est proposée, comprenant une évaluation du premier outil par la modélisation de trois patients porteurs de prothèses et la comparaison avec leurs résultats cliniques, et pour le deuxième outil, d'une évaluation de sa sensibilité et fiabilité sur seize patients enregistrés directement dans une salle de consultation d'hôpital.

Dans la première partie de cette thèse, un simulateur robotique offrant cinq degrés de liberté est développé pour reproduire les forces nettes agissant sur l'articulation glénohumérale, ainsi que la majeure partie de son amplitude articulaire. Ce robot est particulier car il utilise de véritables prothèses pour former l'articulation glénohumérale et n'offre aucun mécanisme permettant d'éviter les luxations de cette articulation. Tous les éléments du robot sont expliqués, de sa conception mécanique à son contrôle. Ses performances sont ensuite évaluées dans plusieurs cas, par ordre de complexité croissante. D'abord en utilisant des mouvements simples pour évaluer sa précision et son comportement dynamique. Deuxièmement, afin de reproduire un test robotisé pour l'évaluation de l'instabilité GH utilisé lors des tests d'usure standardisés pour prothèses commerciales. Troisièmement, pour reproduire les patterns de force enregistrées *in vivo* par une prothèse instrumentée, en utilisant à la fois une approche quasi statique et une approche dynamique. Tous ces tests ont montré que le simulateur robotique est capable de reproduire avec précision et fiabilité les instructions demandées.

Ensuite, le robot est adapté pour évaluer le risque d'apparition d'une instabilité prothétique chez trois patients ayant une opération de remplacement total de l'épaule prévue dans les prochains mois. Les tomodensitogrammes et la planification chirurgicale de ces

patients sont utilisés pour construire un modèle musculosquelettique spécifique à chaque patient, incluant l'implant prothétique prévu pour chacun d'entre eux. Des données telles que la section transversale de leurs muscles, leurs points d'origine et d'insertion ainsi que leurs morphologies osseuses sont prises en compte par ce modèle, développé grâce à un partenariat avec le laboratoire d'orthopédie biomécanique (LBO - EPFL). Les forces glénohumérales prédites et les orientations relatives de l'implant prothétique sont ensuite transmises au simulateur robotique qui, en utilisant une copie exacte de l'implant prothétique du patient, reproduit trois mouvements de la vie quotidienne susceptibles de déclencher un comportement luxant dans le complexe de l'épaule. Bien que le modèle se soit montré capable de simuler les données des patients dans les trois situations demandées, le modèle a indiqué beaucoup plus d'instabilité que les résultats cliniques. Les causes présumées de cette différence ainsi que les possibles débouchés que cette méthodologie pourrait proposer pour de futurs projets de recherche sont rapportées.

Dans la deuxième partie de cette thèse, un instrument pour l'évaluation de l'espace atteignable du membre supérieur est développé à l'aide de technologies conçues pour le grand public. Cette approche offre une solution économique, rapide et plus simple d'utilisation par rapport aux instruments disponibles dans les laboratoires de capture de mouvement, tout en fournissant des métriques comparables. L'instrument proposé est la composition d'un kit de réalité virtuelle, le HTC Vive, d'un sac à dos modifié et de deux capteurs montés aux poignets et fixés au moyen de bracelets de montre. Après une courte calibration, le sac à dos permet d'enregistrer les mouvements du thorax en trois dimensions, tandis que les capteurs au poignet permettent, grâce à un modèle à segments rigides, de suivre les positions du coude et du poignet en temps réel. Ces informations sont ensuite utilisées pour construire un avatar du corps du patient, qu'il aperçoit à travers le casque de réalité virtuelle. Un ensemble de tâches simples est ensuite proposé pour mettre à l'épreuve la mobilité des membres supérieurs du patient, tout en le distrayant du contexte de l'examen clinique, en l'amenant dans un environnement plus naturel. À la fin du test, un rapport sur les performances du patient est généré automatiquement et les résultats principaux sont affichés sur l'écran de l'examineur, en incluant une évaluation de l'espace atteignable du patient, calculée à l'aide d'un algorithme conçu dans le cadre de ce projet, expressément dans ce but. La précision et la fiabilité de cet instrument sont évaluées en laboratoire, obtenant des résultats satisfaisants sur un ensemble de dix sujets en bonne santé effectuant un protocole de test-retest.

Cet instrument est ensuite évalué sur une population de patients âgés présentant différents types de pathologies impliquant des limitations fonctionnelles du membre supérieur, directement dans la salle de consultation de l'hôpital local. Les premiers résultats ont indiqué que le test était inapproprié pour la population étudiée, principalement en raison de l'accumulation excessive de fatigue chez les patients et de leur manque de souplesse dans la nuque, les empêchant de voir certaines des cibles. Une version adaptée du test est alors proposée, comprenant moins d'exercices et fournissant des consignes plus claires aux patients. Ce nouveau test est évalué dans un protocole de test - retest impliquant 16 nouveaux patients. Tous les patients ont réussi à terminer le test deux fois, dans le cadre de ce protocole de test - retest. La répétabilité de l'évaluation des amplitudes articulaires et de l'espace accessible était excellente (ICC = 0,94; ICC = 0,91 respectivement) et tous les scores proposés ont réussi à différencier le côté du membre supérieur pathologique du côté sain. De plus, l'espace atteignable des membres supérieurs du côté sain affichait des valeurs similaires à celles enregistrées avec la version plus longue du test sur des sujets complètement sains.

Cette thèse propose deux instruments innovateurs pour l'évaluation et la simulation robotique de l'articulation glénohumérale. Elle offre un outil pour reproduire les forces et les mouvements physiologiques au sein de l'articulation glénohumérale, ouvrant de nouvelles pistes pour l'étude de l'instabilité glénohumérale. Parallèlement, elle propose également un deuxième outil permettant d'évaluer la déficience fonctionnelle du membre supérieur des patients de manière objective et fiable; en extrayant des informations qui, par le passé, nécessitaient un déploiement de ressources irréalistes pour un examen clinique.

Mots-clés

Évaluation Clinique, évaluation fonctionnelle, instabilité glénohumérale, capture du mouvement, volume atteignable, biomécanique de l'épaule, chirurgie, arthroplastie totale d'épaule, évaluation du membre supérieur, réalité virtuelle, cinématique 3D, simulations robotiques, simulations musculosquelettiques.

Contents

Acknowledgements	vi
Abstract.....	ix
Keywords.....	x
Résumé.....	xi
Mots-clés.....	xii
Chapter 1 Introduction	19
1.1 Anatomy and function of the upper limb	19
1.2 Diseases affecting the shoulder complex	23
1.2.1 Glenohumeral instability	24
1.2.2 Glenohumeral osteoarthritis	24
1.2.3 Inflammatory arthritis.....	25
1.3 Treatments of the shoulder complex.....	25
1.3.1 Non-surgical treatments.....	25
1.3.2 Surgical treatments.....	26
1.4 Glenohumeral instability after TSA	27
1.5 Functional evaluation of the shoulder complex.....	27
1.6 Objectives	28
1.7 Outline	29
Chapter 2 State of the art.....	31
2.1 Introduction	31
2.2 Shoulder complex simulations.....	31
2.2.1 Numerical models	31
2.2.2 Robotic models	32
2.3 Clinical functional evaluation of the upper limb	33
2.3.1 Clinical questionnaires	33
2.3.2 Physical evaluation	34
2.4 Standard motion-lab based evaluation	35
2.5 Instrumented functional tests	37

Chapter 3	Robotic Glenohumeral Simulator for Investigating Prosthetic Implant Subluxation	39
3.1	Abstract.....	39
3.2	Introduction	39
3.3	Materials and Methods.....	40
3.3.1	Mechanical structure and actuation design.....	40
3.3.2	Sensors and Actuators.....	42
3.3.3	Controller	42
3.3.4	General performance evaluation	43
3.3.5	Standardized test for dislocation force estimation	44
3.3.6	Simulation with realistic forces.....	44
3.4	Results	45
3.4.1	Dynamic performance.....	45
3.4.2	Static performance	46
3.4.3	Standardized test for dislocation force estimation	47
3.4.4	Simulation with realistic forces.....	48
3.5	Discussion	49
3.6	Conclusion.....	50
3.7	Acknowledgments	51
3.8	Funding	51
3.9	Appendix A: Ramp response of the hydraulic actuators.....	51
3.10	Appendix B: Frequency response of the hydraulic actuators	55
Chapter 4	Patient Specific Robotic Evaluation of the Glenohumeral Translations in Total Shoulder Arthroplasty Patients	57
4.1	Abstract.....	57
4.2	Introduction	57
4.3	Materials and Methods.....	58
4.3.1	Subjects.....	58
4.3.2	CT Measurements.....	58
4.3.3	Musculoskeletal model for estimation of GH joint reaction force and kinematics.....	59
4.3.4	Input data processing.....	63
4.3.5	Simulating the GH translations of the patients	66
4.3.6	Estimation of GH translation	67
4.4	Results	68
4.5	Discussion	77
4.6	Conclusion.....	79
4.7	Acknowledgments	80
4.8	Funding	80
4.9	Appendix F: Modifications to the robotic simulator	81

4.10	Appendix A: User Manual to perform a patient's simulation	81
4.10.1	Expected inputs from the MS model.....	81
4.10.2	Matlab conversion script: GenerateSOGIpatientCommandsV2.m	82
4.10.3	MTS actuators control.....	84
4.10.4	Maxon Motors control	87
Chapter 5	Development of a Framework for the Instrumented Evaluation of the Functional Volume.....	91
5.1	Abstract.....	91
5.2	Introduction	91
5.3	Materials and Methods.....	92
5.3.1	Lighthouse based Tracking solution	92
5.3.2	System configuration	93
5.3.3	Anatomical calibration	94
5.3.4	VR guided test	95
5.3.4.1	Test procedure	96
5.4	Data analysis and Scores estimation	98
5.4.1	Estimation of the reachable space	98
5.4.2	Volumetric symmetry.....	99
5.4.3	Spherical volumetric estimator.....	99
5.4.4	Range of motion	100
5.4.5	End-Effectors comparison	100
5.4.6	Sensitivity of the reachable volume to the number of targets.....	100
5.5	Results	100
5.5.1	Test Retest.....	100
5.5.2	End-Effectors comparison	102
5.5.3	Sensitivity of the reachable volume to the number of targets.....	104
5.6	Discussion	104
5.7	Conclusion.....	106
5.8	Acknowledgments	107
5.9	Funding	107
5.10	Appendix A: Evaluation of the HTC tracker accuracy	107
5.10.1	Aim.....	107
5.10.2	Method	107
5.10.3	Results.....	108
5.10.4	Discussion and conclusion	108
Chapter 6	Use of the Functional Volume for the Evaluation of Patient's Impairment Following a Humeral Fracture	109
6.1	Abstract.....	109
6.2	Introduction	109

6.3	Methods.....	110
6.3.1	VR guided test	111
6.3.2	Test procedure	111
6.3.3	Data analysis and Scores estimation	112
6.4	Results	115
6.5	Discussion	119
6.6	Conclusion.....	120
6.7	Acknowledgments	121
6.8	Funding	121
6.9	Appendix A: Preliminary evaluation of the Volfon test on clinical patients.....	121
Chapter 7	Conclusions and Perspectives.....	125
7.1	Achieved results	125
7.1.1	Robot for the simulation of Glenohumeral instability.....	125
7.1.2	Volfon: A system for the instrumented functional evaluation of the upper limb.....	126
7.2	Perspectives	127
7.2.1	Robot for the simulation of glenohumeral instability.....	127
7.2.2	Volfon: A system for the instrumented functional evaluation of the upper limb.....	128
	References.....	129
	Glossary.....	138
	Curriculum Vitae.....	140

Chapter 1 Introduction

1.1 Anatomy and function of the upper limb

The upper limb's (*UL*) main function is to move the hand in space with a controllable position and orientation, so that it may perform a specific task (e.g. grasping of an object, typing on a keyboard, turning a handle, etc.). This function is achieved by the combined action of the shoulder, the elbow and the wrist. Within the scope of this work I will focus on the problems encountered by the shoulder, which is the most complex and fragile of these three articulations.

The shoulder articulation (Figure 1) is composed of three bones: the scapula (Figure 2), the humerus (Figure 3) and the clavicle (Figure 4). The anatomy of each bone is important both to understand the points of insertion of tendons and ligaments, but also in the field of motion analysis to locate precise positions (called *anatomical landmarks*) that are common to any patient and to define precisely the referential frames attached to each bone.



Figure 1: Representation of the three bones of the shoulder. Modified with permission from *Parker_West*.

The most important anatomical features of the scapula (Figure 2) are: (i) the glenoid cavity, which will receive the humeral head; (ii) the acromion and the coracoid process, that will provide superior support to the humeral head, while providing insertion points for

a large number of muscles and tendons; (iii) the Angulus Inferior (*AI*) or inferior angle of the scapula, commonly used as a landmark in motion analysis, together with (iv) the Trigonum Spinae (*TS*), which is the medial end of the scapular's spine.

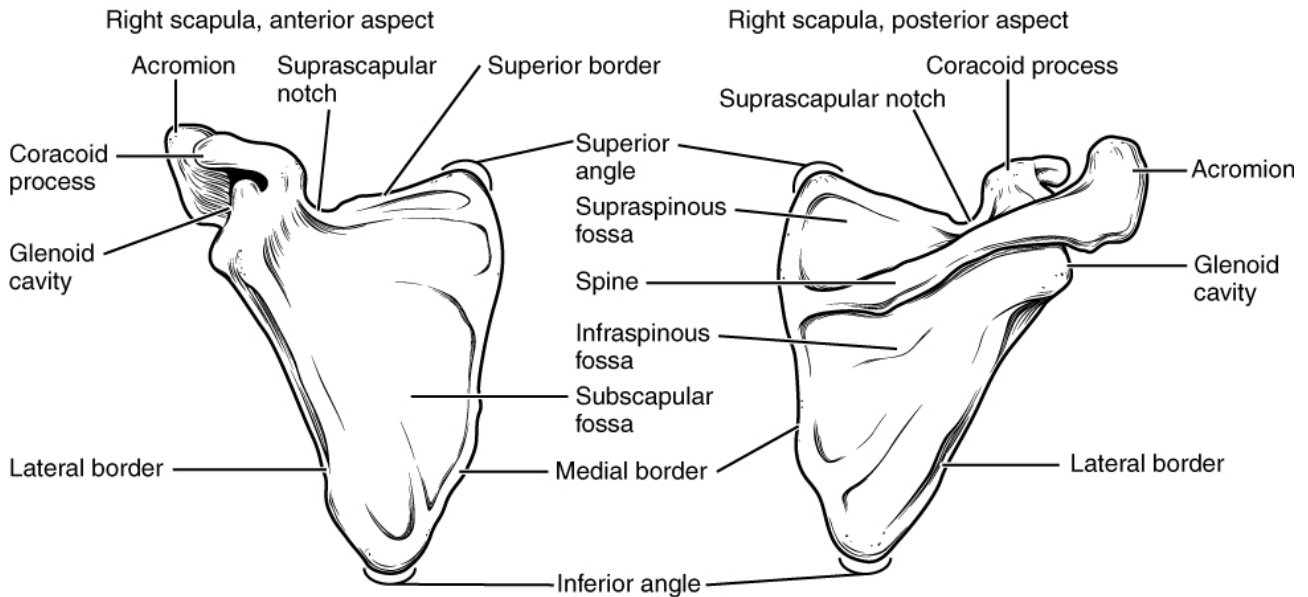


Figure 2: Anatomy of the scapula. Modified from Wikimedia. This file is licenced under the Creative Commons 3.0 license.

On the humerus (Figure 3) the main landmarks will be (i) the head of the humerus; (ii) its body; (iii) the lateral epicondyle (*EL*) and (iv) the medial epicondyle (*EM*).

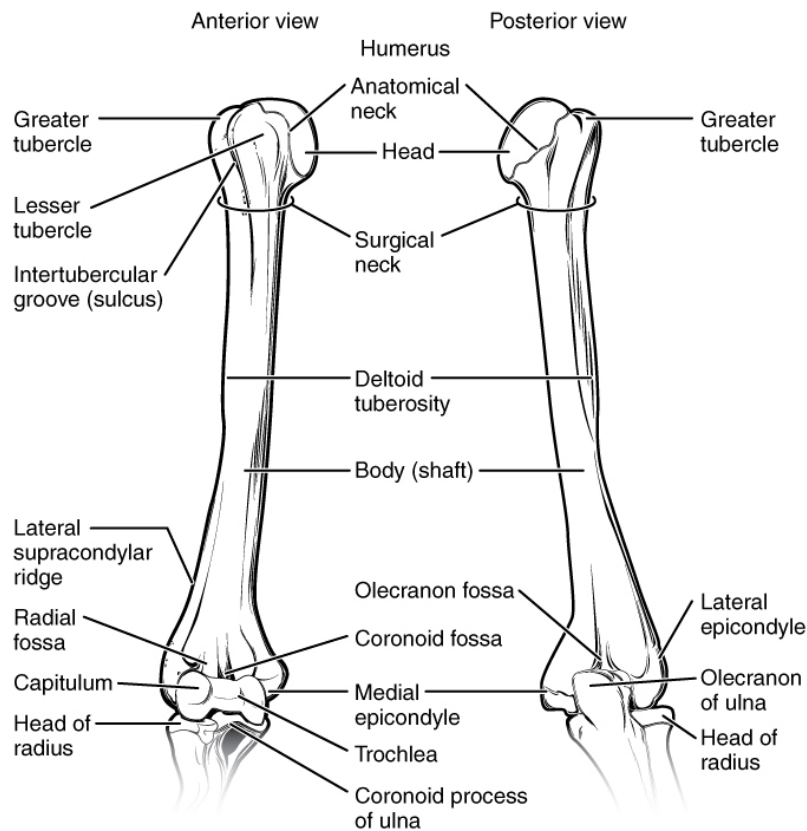


Figure 3: Anatomy of the humerus. Modified from Wikimedia. This file is licenced under the Creative Commons 3.0 license.

The clavicle (Figure 4) presents less features, mostly with its medial or sternal end and the lateral or acromial ends.

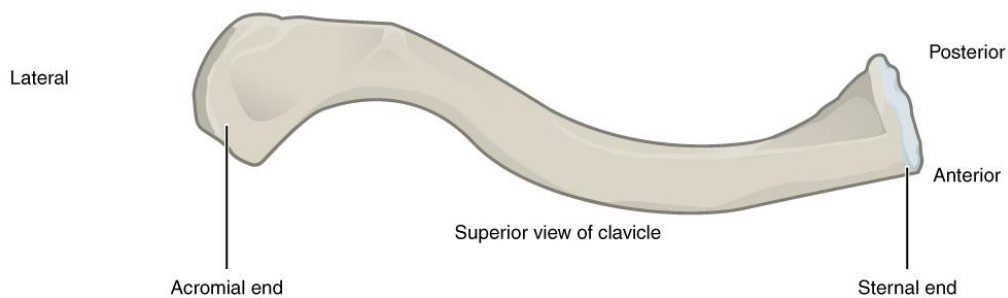


Figure 4: Anatomy of the clavicle. Modified from Wikimedia. This file is licenced under the Creative Commons 3.0 license.

These three bones are interconnected by three synovial joints (Figure 5): (i) the glenohumeral (*GH*) joint: an enarthrodial joint connecting the glenoid cavity of the scapula with the head of the humerus; (ii) the acromioclavicular joint: connecting the acromion with the acromial extremity of the clavicle; (iii) the sternoclavicular joint: an enarthrodial joint with a reduced range of motion (*RoM*) connecting the sternal extremity of the clavicle with the sternal manubrium. It allows to raise and lower the glenoid part of the scapula, to move it frontward and backward, as well as circumducting it.

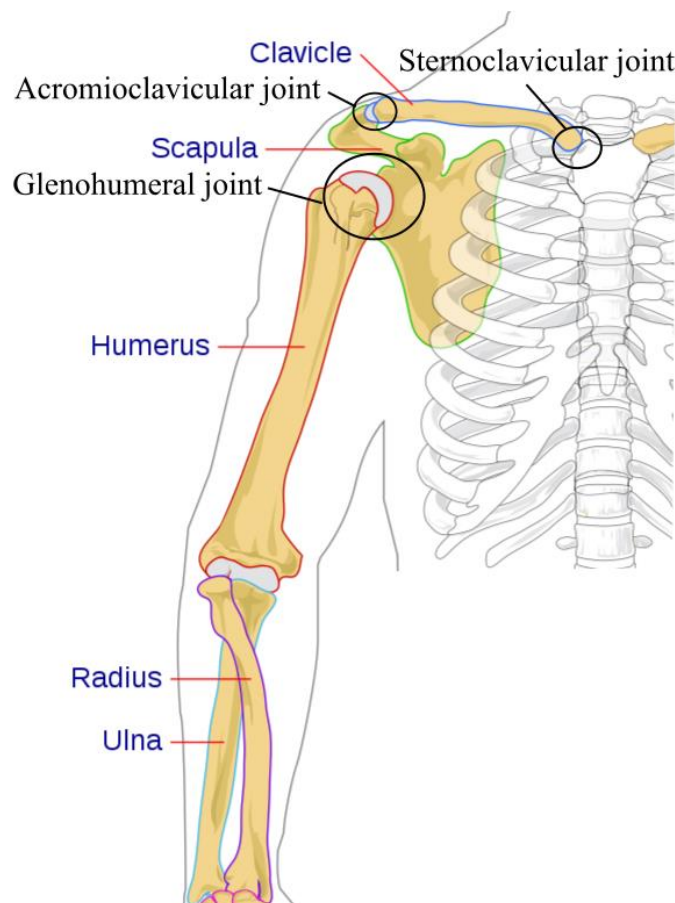


Figure 5: Bones of the upper limb (*UL*) and the three joints of the shoulder complex. Modified with permission from Mariana Ruiz Villarreal.

During a rotation of the upper arm, all of these structures must work in a coordinated way to be functional. The largest motions are provided by the GH joint, but the scapula itself rotates to accompany and facilitate the movement. During a typical elevation of the arm, the scapula barely moves for the first 30° of rotation, then it accompanies the rotations following a 2:1 ratio, called the scapulohumeral rhythm. Therefore, if the arm is raised by 60°, 40° are provided by the rotation of the GH joint and 20° by the rotation of the scapula. The role of the clavicle with the two joints attached to it, is to allow the rotations of the scapula while maintaining the glenoid distant from the thorax.

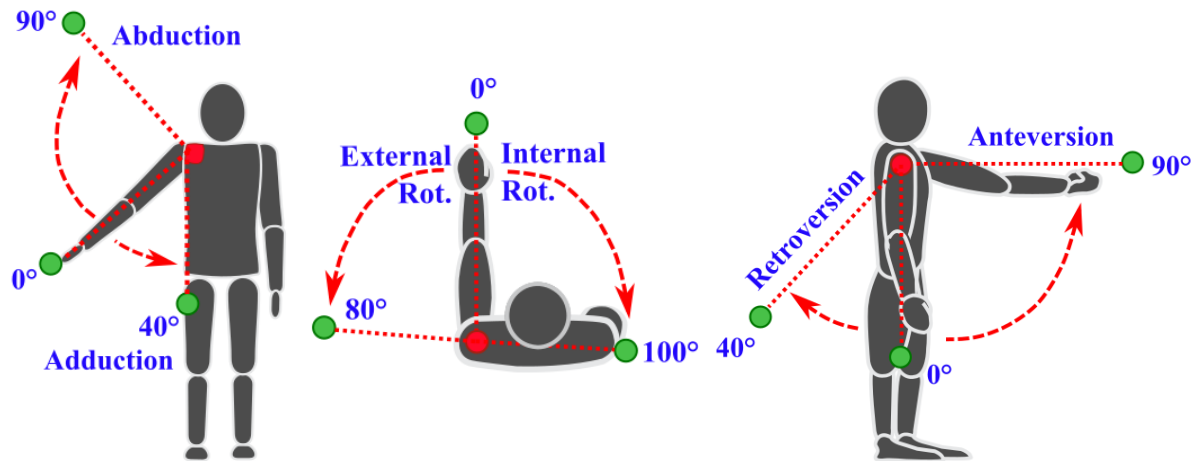


Figure 6: Articular ranges of the GH joint.

In this work I focus mostly on the GH joint (Figure 8), since it can be the source of many shoulder affections, including shoulder instability, osteoarthritis and inflammatory arthritis, as further developed in the next section. The *GH* joint is able to provide the largest ranges of motion of the whole body (Figure 6), with the ability to perform external rotations of 80°, internal rotations of 100°, anteversions of 90°, retroversions of 40° abduction of 90° and adduction of 40° (Bommas, Teubner, & Voss, 2008). By acting similarly to a ball and socket joint, this ample RoM requires a relatively small socket. Conversely, such a socket is not enough to stabilize the joint and additional structures are necessary to achieve this goal. Those structures can be divided in two different categories: active and passive stabilizing structures. The active stabilization is provided mostly by the rotator cuff muscles and more specifically by:

- supraspinatus muscle that connects the supraspinous fossa of the scapula to the greater tubercle of the humerus, contributing to the abduction movements of the arm;
- infraspinatus muscle that connects the infraspinous fossa of the scapula to the greater tubercle of the humerus, contributing to the external rotation of the arm;
- teres minor muscle that connects the lateral boarder of the scapula to the greater tubercle of the humerus, contributing to the external rotation of the arm;
- subscapularis muscle that connects the subscapular fossa of the scapula to the lesser tubercle of the humerus, contributing to the internal rotation and adduction of the arm.

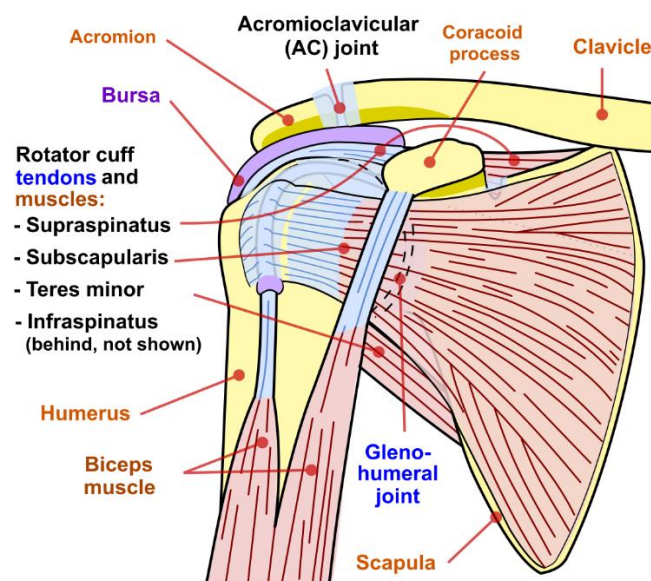


Figure 7: Depiction of the rotator cuff muscles. Image courtesy of the National Institute of Arthritis And Musculoskeletal And Skin Diseases

The passive stabilization (Figure 8) is provided by (i) two bursae: the subacromial and the subdeltoid bursae, whose role is to dampen the collisions between the humeral head and the structures above it; (ii) the glenoid labrum: a fibrocartilaginous structure expanding and deepening the boarder of the glenoid fossa, which by itself would only cover for a quarter of the humeral head's articular surface; (iii) the GH capsule: which connects on one side the edge of the glenoid cavity and on the other side to the surgical neck of the humerus, it also contains the synovial fluid lubricating the joint; (iv) and mostly by three types of ligaments:

- the coraco-acromial ligaments connecting the coracoid process with the acromion to form a vault for the superior stabilization of the humeral head;
- the coraco-humeral ligament that arises from the lateral border of the coracoid process and open in two bands, attaching it with the greater and lesser tuberosities of the humerus;
- the GH ligaments that are three ligaments on the anterior side of the GH joint. They are divided into the superior, middle and inferior ligaments and stabilize the humeral head anteriorly and inferiorly, depending on the position of the arm.

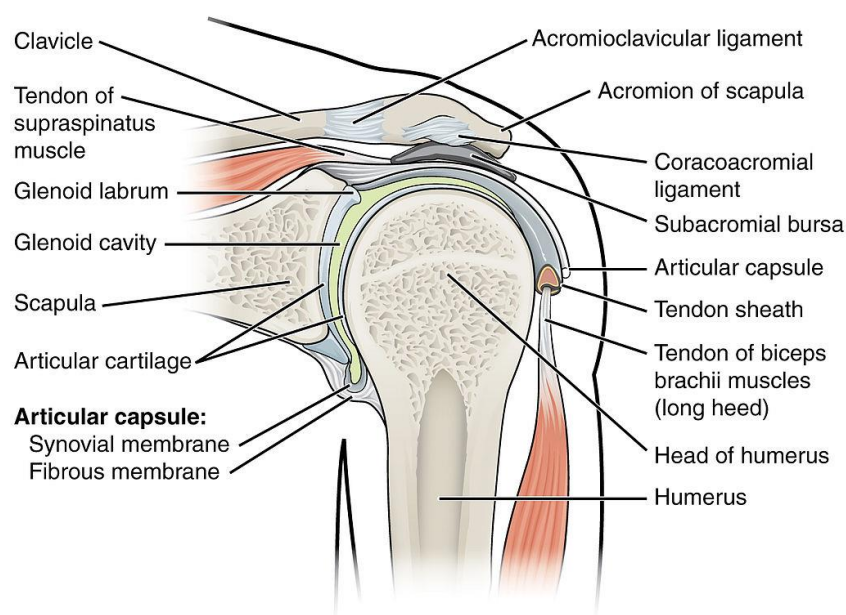


Figure 8: Passive structures involved in the glenohumeral joint stability. Image courtesy from Wikimedia. This file is licenced under the Creative Commons 3.0 license.

As a consequence of the large number of structures involved in its stabilization, different pathologies can indirectly cause shoulder instability, as explained in the next section.

1.2 Diseases affecting the shoulder complex

Shoulder problems are common and represent a major social burden. They account for 2.4% of all general practitioner consultations in the UK and more than 4 million visits to physicians annually in the USA (Linsell et al., 2006; Thomas et al., 2016). In 2000, the direct cost of the treatment of shoulder dysfunctions in the USA was estimated to \$ 7 billion, of which 2 to 5% was associated to Glenohumeral osteoarthritis (*GH OA*) (Meislin, Sperling, & Stitik, 2005). Inflammatory arthritis, and in particular Rheumatoid arthritis is also common, with a prevalence of 1% in caucasian men (Crowson, O'Dell, & Romain, 2019). When these pathologies progress to a highly painful and handicapping state, the most efficient way to deal with both, consists in replacing the brittle diseased articular surfaces with prosthetic ones, an operation called Total Shoulder Arthroplasty (TSA). However, avoiding GH instability after the surgery on an already fragile joint is challenging and may require a secondary corrective surgery, fragilizing the bone even further. In the following sub-sections, we will discuss about these two pathologies, as well as GH instability, then we will discuss about the treatments available and the potential impact of this thesis on the evaluation and treatment of these pathologies.

1.2.1 Glenohumeral instability

The literature commonly refers to three types of instability. *GH dislocation* is defined as the moment when the humeral head loses contact from the glenoid cavity by sliding away. The term *subluxation* is used with a large number of different meanings, causing confusion (Gatterman, 2005). *GH subluxation* commonly refers to the situation when a joint briefly pops out of its stable position but returns to its normal position without the need for external manipulations. During this thesis, GH instability will refer to the presence of this last definition of GH subluxation or to the more severe GH dislocations. However, in the prosthetics field GH subluxation is used to describe excessive eccentric movements of the humeral head over the surface of the glenoid cavity. This eccentric motion can be expressed as the displacement of the humeral head relative to a centered position in the glenoid cavity in millimeters or as a percentage, normalized by the humeral head diameter (Jacxsens, Van Tongel, Henninger, Tashjian, & De Wilde, 2017). Chapters 3 and 4 of this thesis discuss about instability in patients wearing prostheses, therefore this prosthetics definition of GH subluxation is used. In the absence of prosthesis, GH instability will maintain the previously defined, non-prosthetic sense.

The symptoms of GH instability are pain and a sense of displacement, which appear, in most cases (96%, (Warner & Caborn, 1992)) after a traumatic event. However, this condition can also arise as the consequence of a minor injury or repetitive use. The most common pathologies, causing GH instability can be structural, such as, lesions to the capsulolabral complex, to some of the rotator cuff muscles or to the GH articular surface or non-structural, such as an affection in the proprioceptive system of the shoulder or a perturbation in the neuromuscular control. Therefore, GH instability is subdivided in three types (Lewis, Kitamura, & Bayley, 2004):

- type I, traumatic structural instability: generally caused by a disruption in the capsulolabral complex or lesions to the rotator cuff muscles.
- type II, atraumatic structural instability: This pathology is mostly found in athletes practicing sports with the hands working overhead, such as throwing sports. It typically presents excessive external GH rotations, and a deficit of range on the internal rotation. This can be related to anterior capsular laxity, tight posterior capsule, scapular dyskinesis, muscular imbalance and congenital labral pathology (Braun, Kokmeyer, & Millett, 2009).
- type III, neuromuscular dysfunction or muscle patterning: is characterized by an aberrant activation of large muscles (latissimus dorsi, pectoralis major, anterior deltoid) and simultaneous inhibition of the rotator cuff activation (Jaggi & Lambert, 2010). In some cases, the muscular imbalance can cause dislocations of the shoulder and damage the capsulolabral complex in the process. For this reason, before performing a corrective surgery for a structural problem leading to GH instability, it is important to control that there is not a problem of muscle patterning, which might void the effect of the surgery.

The clinical assessment of GH instability is based on the patient's history and functional examination (more informations about the functional examination are available into a dedicated section below). If structural damages are suspected, imaging techniques are used to validate the extent of the damages, and, if needed, plan the surgery. The treatments following ther diagnosis of GH instability, will be discussed in the dedicated section.

1.2.2 Glenohumeral osteoarthritis

Glenohumeral osteoarthritis (*GH OA*) is caused by the degeneration of articular cartilage and subchondral bone within the joint. Since the role of cartilage is to protect the bone its degeneration causes a progressive worsening of the symptoms, as the GH cavity gets narrower, resulting in a less protected bone. Usually the progression of the pathology and its symptoms can be reduced using an array of different treatments and changes to the lifestyle, but the damage to the joint cannot be reversed. An active lifestyle, maintaining a healthy weight, physiotherapy and several analgesics can be used to improve both pain and joint function.

The typical signs and symptoms indicative of GH OA are the following: (i) pain in the affect joint, in particular during and after some movements; (ii) joint stiffness, typically upon awakening or after being inactive; (iii) the joint might feel tender while applying light pressure to or near it; (iv) the patient might not be able to move his/her joint through its full RoM; (v) the patient might feel a grating sensation, as well as popping and crackling, when using the joint; (vi) bone spurs, which feel like hard lumps, might form around the affected joint; (vii) swelling might be observed as a consequence of soft tissue inflammation around the joint.

These signs and symptoms, together with the presence of several risk factors such as: (i) older age; (ii) obesity; (iii) an history of injuries to the suspected joint; (iv) repeated stress on the joint, related to the job, sport or other elements of the lifestyle; (v) genetics; (vi) bone deformities; (vii) some metabolic diseases, such as diabetes and hemochromatosis (a condition in which the body has an iron excess).

Since GH OA cannot be cured, the treatments usually address pain reduction, restoration of the RoM and reduction of the duration of the symptoms, while taking in consideration the specific needs of each patient (age, need to perform some movements for his/her work, hobbies, daily routines, etc.)

1.2.3 Inflammatory arthritis

Inflammatory arthritis (IA) designs a group of diseases characterized by inflammation of the joints and potentially other tissues. Many forms of inflammatory arthritis are caused by an auto-immune disfunction, where the immune system will start attack some tissues in the joints or other tissues. The causes of this disfunction requires a favorable genetical background, but other poorly understood elements are required to develop the pathology ('Inflammatory Arthritis', 2019).

A large number of different types of inflammatory arthritis have been recognized, including rheumatoid arthritis, psoriatic arthritis, ankylosing spondylitis, juvenile idiopathic arthritis, systemic lupus erythematosus. In this thesis, only rheumatoid arthritis is discussed as one of the reasons leading to the use of TSA (Collins, Harryman, & Wirth, 2004). Rheumatoid arthritis is characterized by an inflammation of the joints, causing a thickening of the synovium (the tissue lining the inner surface of the joints and producing the synovial fluid) to thicken. As a consequence, the joints will be swollen and painful. If the inflammation doesn't get treated in time, it will damage the cartilage and the bones themselves, leading to OA ('What is Rheumatoid Arthritis?', 2019).

The diagnosis is usually based on medical history and physical examination. For some forms of IA, the diagnosis may be validated using imaging techniques.

1.3 Treatments of the shoulder complex

Treatment for OA and IA depends on the severity of the signs and symptoms, and on the degree of restriction in professional, leisure and daily activities. For most patients (78% of OA patients in the UK, based on (Thomas et al., 2016)), non-surgical care provides sufficient support to the patient, while avoiding the risks and the costs associated with the surgical approach. It typically involves the use of some of the following treatments: (i) activity modification; (ii) physical therapy; (iii) analgesic/non-steroidal anti-inflammatory drugs (NSAIDs); (iv) disease-specific drugs; (v) local injections and (vi) acupuncture (Chillemi & Franceschini, 2013; Thomas et al., 2016). Those treatments are preferred for patients with mild to moderate GH OA or GH IA, when pain and functional limitations are moderate, even in the presence of more advanced radiographic evidence.

In the presence of more severe GH OA or IA, in particular in cases where the patient still experiences high levels of pain and a handicapping reduction in his/her RoM, a need for a surgical intervention becomes necessary. Depending on the patient's age, occupation, activity level, expectations for functional recovery and the features of the disease (such as lesion size, amount and distribution of the damages to the cartilage, weaknesses of the rotator cuff muscles, ...) the following treatments are possible: (i) glenohumeral debridement; (ii) arthroscopic resurfacing arthroplasty; (iii) hemiarthroplasty; (iv) anatomic total shoulder arthroplasty; (v) reverse total shoulder arthroplasty.

For cases of instability, the type of instability will determine the choice of the treatment, with serious structural defects requiring surgical correction, while type III instability and some cases fo type II (such as muscular imbalance and scapular dyskinesis) will be corrected mostly through physical therapy.

1.3.1 Non-surgical treatments

Lifestyle and occupational modifications are often the first steps in the process. These changes attempt to reduce situations resulting in the pain in the shoulder. Physiotherapy is useful for nearly all GH patients to prevent atrophy and contractures, while maintaining a well-balanced musculature helps to stabilize the joint. Typical exercises include gentle RoM as well as isometric strengthening of the rotator cuff and scapulothoracic muscles.

In mild to moderate cases, the use of paracetamol–acetaminophen has been demonstrated to be an efficient solution with minimal adverse effects (Bijlsma, 2002). If the patient shows insufficient response to paracetamol–acetaminophen, alternative or additional pharmacologic agents may be considered, such as NSAIDs, or tramadol.

If no effective oral medication proved to be sufficient to mitigate the pain, intra-articular injections of corticosteroids are commonly used and are effective as a short-term solution. However, because of the lack of evidence supporting their efficacy, it is recommended to perform no more than three injection per joint (Denard, Wirth, & Orfaly, 2011).

Alternative treatments such as sodium hyaluronate injection, autologous platelet preparations, acupuncture, suprascapular nerve block or ablation are also commonly used techniques, which, depending on the conditions, may prove beneficial for the patients (Thomas et al., 2016). For IA patients, disease-modifying antirheumatic drugs are also available, depending on the type of IA contracted.

1.3.2 Surgical treatments

1.3.2.1 *Glenohumeral debridement*

This surgery aims at removing loose bodies and osteophytes, treating damage to the cartilage using the microfracture technique, and releasing a contracted capsule. In addition, the operation allows the surgeon to directly address some of the common pain generators such as biceps tenotomy or tenodesis and the removal of suture points. There is strong evidence (Namdari, Skelley, Keener, Galatz, & Yamaguchi, 2013) that this technique reduces pain and improves the RoM of the joint with minimal damages to the tissues with a faster recovery than most of its alternative surgical procedures. Since it does not involve the placement of an internal prosthesis, which, in time, may need a replacement, this procedure is particularly appropriate for younger patients.

1.3.2.2 *Arthroscopic resurfacing arthroplasty*

Several resurfacing methods are available in the literature, using different types of graft materials for the resurfacing (meniscal allografts, Graftjacket, Restore patch, metallic implants, ...) (Anderl, Krieglleder, Neumaier, Laky, & Heuberger, 2015; de Beer, Bhatia, van Rooyen, & Du Toit, 2010; N.Bhatia, van Rooyen, du Toit, & de Beer, 2006; Pennington & Bartz, 2005; Savoie FH, Brislin, & Argo, 2009). These procedures are appealing in terms of preserving the bone structure in younger patients, but none of these procedures are supported by strong evidence of the benefits yet.

1.3.2.3 *Hemiarthroplasty*

Hemiarthroplasty consists of replacing the humeral head with a prosthetic metallic equivalent (usually titanium or cobalt-chrome alloy). This allows to preserve the glenoid bone-stock, while consistently improving the RoM and pain levels of the patient. This also prevents loosening of the glenoid component, a common problem in total shoulder arthroplasty (TSA). However, the long term results are not comparable with those of the TSA, with large studies demonstrating good 5-years survivorship of the implant, but low satisfaction of the patients (47% of the patients declared having “unsatisfactory results”) (Bartelt, Sperling, Schleck, & Cofield, 2011). Moreover, other studies documented early improvements in joint mobility and pain, followed by long term failures related to the onset of glenoid arthritis (Bartelt et al., 2011; Dillon, Inacio, Burke, Navarro, & Yian, 2013; Hammond et al., 2013).

1.3.2.4 *Anatomic total shoulder arthroplasty*

Anatomical total shoulder arthroplasty (TSA) consists of the complete replacement of the physiologic humeral head with a metallic prosthetic implant, as in the hemiarthroplasty and the glenoid cavity with a polyethylene implant. This procedure represents the most recurring and reliable solution for the treatment of advanced GH OA and IA. In patients younger than 50 years old survivorships of the prostheses of 97% at 10 years and 84% at 20 years have been reported (Sperling, Cofield, & Rowland, 2004). In another study comparing the results of TSA to those of hemiarthroplasty (Gartsman, Roddey, & Hammerman, M., 2000) patients reported a significantly greater pain relief ($p=0.002$) and RoM ($p = 0.003$) after TSA. A meta-analysis over 112 patients confirmed these results (Bryant et al., 2005) at two years post-operatively. However, TSA comes with the risk of glenoid loosening. A review of 33 published studies found that glenoid component loosening accounted for 39% of all post-TSA complications (Bohsali, Wirth, & Rockwood Jr., 2006). Another study (Sperling et al., 2004) also reported declining prostheses survival after 5 to 8 years, in particular in individuals younger than 50 years old. The cause of glenoid aseptic loosening was not always clear, but prosthetic instability and soft tissue failure were considered as the most probable causes (Bonnevialle et al., 2013). Unfortunately, glenoid revision surgery resulted in poorer outcomes than the primary TSA (Bonnevialle et al., 2013). Therefore, understanding the causes of glenoid loosening and offsetting its onset will allow to improve the survivorship of GH prosthesis, improving its usability in younger patients and the outcomes in the overall patient’s population. Since abnormally large displacements of the humeral head over the glenoid surface are believed to be one of the main causes of loosening (Vani J. Sabesan et al., 2015), and are clearly a cause of prosthetic instability (the second most common cause of prosthetic failure in the shoulder), two chapters of this thesis (Chapter 3 and 4) will focus on the modelling of these GH displacements in post-TSA patients.

1.3.2.5 *Reverse total shoulder arthroplasty*

Reverse total shoulder arthroplasty consists of a prosthesis where the prosthetic “glenoid cavity” is placed on the proximal extremity of the humerus and a spherical implant is placed instead of the physiological glenoid cavity of the scapula. This method, although it results in a reduced RoM and an “unnaturally-looking” shoulder, is preferred in the presence of massive rotator cuff tears or ruptures, since it allows a much more effective stabilization of the joint and increased prosthetic survivorship for these patients (Cuff, Clark, Pupello, & Frankle, 2012; Guery et al., 2006).

Chapter 3 and 4 of this thesis focus on the creation of a combined numeric and robotic model, to model the onset of GH instability after TSA. Chapter 3 describes the creation and evaluation of the robotic model, while Chapter 4 combines it with a numeric model and assess its ability to evaluate the stability of a set of three local TSA patient.

1.4 Glenohumeral instability after TSA

Due to the very large RoM of the GH joint the support from many structures is needed to maintain its stability, as explained in section 1.1. Many of these sensitive structures might get damaged or altered during the surgery, or shortly after, when the shoulder is still fragile. A variety of injuries and pathologies, which could already be present before the surgery can also affect the joint stability.

Weaknesses, tear, tendonitis or laxity of the rotator cuff muscles may negatively affect the ability of these muscles to stabilize the shoulder and must be treated. If the rotator cuff cannot be restored to a good level of function, such as in the cases of massive tissue tears or advanced age-related laxity, a reverse TSA may be considered (Guery et al., 2006; Labriola, Lee, Debski, & McMahon, 2005). Tears to the labrum, in particular below the middle of the socket or to the inferior glenohumeral ligament (called Bankart lesion) are associated with shoulder instability and usually require surgical intervention (Singapore Sports and Orthopaedic Clinic, 2019).

During the surgery, the surgeon must pay particular attention to minimally damage the muscles and ligaments, and in particular the rotator cuff muscles. For this reason, the local hospital, the *Centre hospitalier universitaire vaudois (CHUV)* prescribes the use of the delto-pectoral entry approach, where the surgeon will pull the pectoralis major down and the deltoid muscle up, in order to create an access route to the GH joint. The placement of the humeral head implant will focus mostly on reaching a stable fixation to the bone, while remaining as close as possible to the original morphology of the bone. The placement of the glenoid implant, on its own, will be more delicate, and is known to affect the joint stability. The surgeon will try to place it in a way that minimizes bone resection, provides optimal bone support, and maintains a potentially stable orientation. Based on the local practices, a potentially stable glenoid orientation is defined as any orientation within $\pm 10^\circ$ of retroversion and of inclination angle. The size of the humeral head implant, and the size of the glenoid implant will be selected to match the original dimension of their biological counterparts, while the curvature of the glenoid implant will be selected to achieve a good fit of the implant in the glenoid cavity, while minimizing bone resection. At present, the surgeon has no tools other than these general rules and his own experience to evaluate if the planned surgery will result in a stable joint. Therefore, many authors are attempting to build models to improve the understanding of this phenomenon and to evaluate if a specific surgery on a specific patient would cause GH instability. A review of these models is provided in section 2.1, but none could be used to evaluate the GH translations in a reliable and patient-specific way. Therefore, in the Chapter 4 of this thesis, a patient-specific model for the evaluation of GH instability will be built and evaluated, based on the informations available during the surgical planning.

OA and joint instability are often connected. OA may cause a degradation of the glenoid articular surface, causing eccentric movement patterns and therefore promoting instability. On the other hand, cyclic off-center GH displacements with indexes greater than 5% posteriorly or anteriorly are associated with higher risks of glenoid aseptic loosening through promotion of abnormal stresses on the glenoid surface and through overuse of specific parts of the articular surface (Walch, Badet, Boulahia, & Khoury, 1999). Walch 2016 (Bercik et al., 2016) proposed to subdivide OA glenoids in seven categories: A1: centered humeral head with minor erosion; A2: centered humeral head with major central glenoid erosion and in which a line drawn from the anterior to the posterior rims of the native glenoid transects the humeral head; B1: posteriorly subluxated head with no bony erosion; B2: posteriorly subluxated head with posterior erosion and a biconcave glenoid; B3: monoconcave and posteriorly worn glenoids, with at least 15° of retroversion or at least 70% posterior humeral head subluxation; C: dysplastic glenoid with at least 25° of retroversion not caused by erosion; D: glenoid with any level of anteversion or with humeral head subluxation of less than 40% anteriorly.

The possibility to use modified glenoid implants backing to better accommodate different types of glenoids may improve the stability of the joint post-TSA, allowing to better accommodate the trade-off between an optimal prosthetic orientation and minimizing bone resection on the glenoid side. However, the tools to evaluate the impact of such implants on patients are still missing. The simulation framework that is developpend in Chapter 4 of this thesis could provide a platform to evaluate if one of these implants would be recommended or counter-indicated for a specific patient thanks to the combination of a patient-specific simulation based on the data normally recorded during the surgical planning.

1.5 Functional evaluation of the shoulder complex

After most shoulder surgeries the patient goes through a rehabilitation process. Based on the practices of the local hospital (CHUV) there is a recovery in 4 phases. In phase 1, the patient's shoulder is immobilized to allow the implant to consolidate. In phase 2, passive mobilization of the shoulder starts with a therapist checking if the shoulder is able to move fluidly. Once these two objectives

are reached (usually after a period of about 1 month), the patient enters phase 3. In phase 3, the patient slowly restarts using his/her shoulder actively. He/she is still not allowed to exert the shoulder (no sports, no overhead activities, no impacts, respect of the pain). In phase 4, the patient can progressively return to his/her normal lifestyle (usually 3 to 4 months after the surgery). During this last phase, it is useful to evaluate the functional recovery of the patient, both to assert if the surgery was successful and to better orient the patient toward the correct stretching or strengthening exercises.

However, the tools for the functional evaluation of the shoulder are very limited. The most common approaches consist of the discussions with the patient to establish a clear medical history, his/her progresses and perceived problems. A more formal approach consists in questioning him/her with a written clinical questionnaire (Angst, Schwyzer, Aeschlimann, Simmen, & Goldhahn, 2011). For a more objective and quantifiable evaluation, the articular ranges can also be measured in the three anatomical planes (Figure 9) using a goniometer. However, the goniometer represents a small set of planar measurements, not fully demonstrating the abilities of the shoulder, while the clinical questionnaires are very subjective and may lead to large biases related to the patient's personality and perception of his/her impairment (Ragab, 2003).

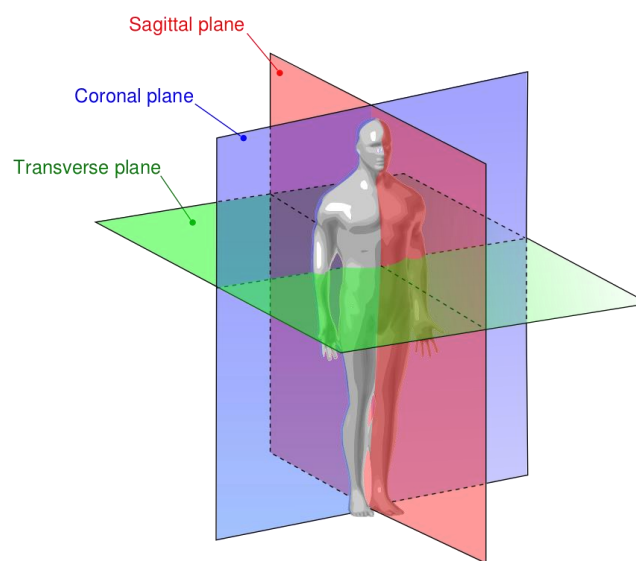


Figure 9: Representation of the human anatomical planes. Image credits to Juan Pablo Bouza under the terms of Creative Commons 3.0

For these reasons, more complex tests have been and are still being developed (Zhou & Hu, 2008). An array of motion tracking technologies (inertial sensors, stereophotogrammetry, electromagnetic trackers and others) have been used to monitor different aspects of the human motions. Camera-based technologies are used to measure precisely the motions in the laboratory, while the internal forces need to be estimated using numerical models (Ehsan Sarshari, 2018). A review of the existing numerical and robotic models for the shoulder is presented in section 2.2, a review of the tools available for the evaluation of the shoulder in a laboratory, in section 2.4. At present, many of these systems display high clinical potential, but none of them are commonly used in the clinics. The reasons vary between systems, ranging from impracticality to reliability issues. Wearable inertial sensors have shown the benefits of a simple test, that can take place anywhere (Pichonnaz et al., 2015). On the other side, more complex tools were used to provide a more complete evaluation of the shoulder mobility. Since the aim of the upper limb (UL) is to place and orient the hand in the space surrounding the trunk, for the later to perform a particular action, the evaluation of the volume where the UL can place the hand is of particular interest, and appears in several studies. A detailed presentation of the tests for the instrumented functional evaluation of the UL is available in section 2.5. However, no test provides a reliable and clinically usable evaluation of the R_{Space} . Toward this goal, a new tool named *Volfon* was developed in Chapter 5 and adapted to the clinical use in Chapter 6.

1.6 Objectives

The shoulder is a particularly important and complex joint system. It offers the largest RoM of any human joint systems, through a complex mechanism based on three joints. Moreover, as indicated in section 1.2.1, shoulder problems are common and due to its anatomy are difficult to understand and solve. For a severely compromised shoulder, TSA is particularly effective (Sperling et al., 2004). Unfortunately, TSA suffers from two main drawbacks (Bonneville et al., 2013): (i) the risk of aseptic loosening, leading to the

detachment of the glenoid implant from the scapula and a need for a revision surgery offering a less reliable prosthetic joint than the one installed during the primary surgery, and (ii) GH instability, which in moderate cases is believed to lead to aseptic loosening (through a phenomenon surnamed the “rocking horse effect” (Vani J. Sabesan et al., 2015)), and in stronger cases leads to regular joint dislocation and potential pain.

Previous studies built numerical models to study GH instability, mostly using numerical muscle-driven simulations (Favre et al., 2012; C Quental, Folgado, Ambrósio, & Monteiro, 2016; Ehsan Sarshari, Farron, Terrier, Pioletti, & Mullhaupt, 2017; Sins, Tétreault, Hagemester, & Nuño, 2015; Alexandre Terrier, Larrea, Malfroy Camine, Pioletti, & Farron, 2013). One of the main limitations of these simulations being the difficulty to model the physical interactions between the two articular surfaces and to achieve reliable validation of the outcome of such simulations. For prosthetic patients the interaction of the articular surfaces can also be assessed *in vitro* using the real prosthesis (Debski, Yamakawa, Musahl, & Fujie, 2017). However, there is currently no robotic model able to reproduce GH dislocation situation while correctly reproducing the rotation of the prosthetic components and the physiological ranges of force.

The first objective of this thesis is to build a model that will help understanding how GH displacements occurs and how to reduce them, in order to evaluate and reduce the risks of both glenoid loosening and GH instability (Chapters 3 and 4). Such robotic model will be able to reproduce the physiologic orientations and forces of the human shoulder. It will also be able to reproduce GH dislocation scenarios and will try to reproduce (Chapter 4) patient specific situations, through the coupling with patient specific numerical models of TSA patients.

After the surgery, it is also important to be able to measure how much of the shoulder function has been restored, and where it could be improved. Several tools exist and are discussed more in depth in Chapter 2, but their main limitations can be summarized as follows:

1. clinical questionnaires are subjective, leaving too much room to self-interpretation (Ragab, 2003);
2. standard laboratory motion capture systems are accurate and precise, but they are difficult to use within the clinical context. Their main problems are price, complexity and being time-consuming and cumbersome to use for the patients (Aminian & Najafi, 2004);
3. observational kinematic analysis relies on the therapist’s expertise and displays poor reproducibility (Bernhardt, Bate, & Matyas, 1998).

To address these limitations, there is a need for an objective evaluation tool for the assessment of UL function, usable in the clinical context. The system should be robust, easy to use, time-efficient, informative and reliable.

One metric of particular interest for the functional evaluation of the upper limb would be to measure the volume reachable by the hand while using only the UL motions. This metric called the reachable space (R_{space}) was proposed and evaluated using several methods in the past (N. Klopkar, Tomsic, & Lenarcic, 2007; Nives Klopkar & Lenarcic, 2005; Kurillo, Chen, Bajcsy, & Han, 2013; Kurillo et al., 2012; Lenarcic & Umek, 1994). Yet an accurate, reliable and clinically usable system for the evaluation of the R_{space} is still missing. The second part of this thesis (Chapters 5 and 6) will focus on the development and evaluation of such a tool.

In summary, the aim of this thesis is to develop new tools to improve the evaluation and simulation of instable GH joints.

1.7 Outline

This thesis is organized in seven chapters that are described in the following paragraphs. Chapters 1 and 2 provide the background information needed to understand the objectives of the project and the solutions that already exist. Chapters 3 and 4 focus on the modelling of GH stability in TSA conditions, while chapters 5 and 6 focus on the development of a new tool for the functional evaluation of the UL. Both chapters 3 and 5 present the development of new instruments, while the chapters immediately following them (4 and 6) deal with the clinical applications of these new tools.

Chapter 1 explains the anatomy of the shoulder, the impact that GH OA has on the overall population, the treatments available, and introduces the methods for its functional evaluation. Finally, it presents the objectives and outline of this thesis.

Chapter 2 presents the state of the art about the main topics that are discussed within this thesis, namely: GH instability after TSA, existing shoulder simulators, and the available tests for the functional evaluation of the UL.

Chapter 3 describes the development of a novel robotic simulator designed specifically for the study of prosthetic GH stability. It also presents its control strategy, and its evaluation using a public dataset recorded *in vivo* using instrumented prostheses (Bergmann, 2009).

Chapter 4 combines the robotic simulator developed in chapter 3, with a numerical musculoskeletal simulator in an effort to evaluate the GH stability of three TSA patients from the local university hospital (CHUV).

Chapter 5 focuses on the development of a new instrument called *Volfon* for the evaluation of the reachable space (R_{space}) of the UL, as a metric for its functional evaluation. This instrument was developed with the aim of being used in the clinic. It was then evaluated on ten healthy volunteers.

Chapter 6 shows tests and adaptation of *Volfon* for the use with patients in clinic, and evaluates it on sixteen patients through a test-retest protocol.

Chapter 7 concludes this thesis by summarizing the contributions of this work and discussing the perspectives for further work on the aforementioned topics.

Chapter 2 State of the art

2.1 Introduction

The goal of this thesis is the evaluation and robotic simulation of the GH joint. To understand the context of this work, it is important to understand the work that has been done for the simulation of the shoulder complex. A large number of numerical simulations are available, using different approaches, and presenting different limitations. Section 2.2.1 provides a summary of the methods available and their main results and limitations. At present, some problems cannot be solved using numerical models and require a verification on the real structures. For this, a set of robotic shoulder models were developed and are presented in section 2.2.2.

Here, the robotic simulation is designed to avoid the onset of problems to the GH joint, but to evaluate the presence of problems, and decide of an optimal treatment, several clinical tools can be used, as presented in section 2.3 with a focus on the functional approach. Those tools however tend to be partial and biased. Evaluation based on imaging technique is an important complement to the functional evaluation of the shoulder, providing more quantifiable data, but was not studied within the scope of this thesis and is therefore not presented here. More accurate tools for the functional evaluation of the UL are available in motion-laboratories, but have a tendency to be large, expensive and difficult to use. Section 2.4 will present the standard tools used in the laboratory for the functional evaluation of the shoulder. Between the complex motion-lab solutions and the subjective methods used in most clinics, instrumented functional test are gaining in popularity. Section 2.5 will present the main instrumented functional tests available for the evaluation of the UL, in order to offer to the reader a clear understanding of the motivations of this thesis to create a new device that should satisfy an unmet need.

2.2 Shoulder complex simulations

To evaluate the effects that a novel prosthetic implant or a modified treatment may have on a patient's shoulder, it is important to evaluate the effects on one or more models first to decrease the risks of installing a suboptimal implant on a patient, which may not last for as long as a standard implant or cause other undesirable effects. For biomechanical applications to the human shoulder, animal models are generally inappropriate due to very different morphologies. Nonetheless, many models of the human shoulder are available and can be divided in three main categories: (i) purely numerical simulations; (ii) cadaveric simulations and (iii) robotic simulations. Each category has both advantages and disadvantages.

2.2.1 Numerical models

Numerical models allow investigating aspects that are otherwise difficult or impossible to quantify due to technical or ethical reasons (necessity to place sensors inside the patient, tissue deterioration, etc). They offer several advantages: once the model is built, replication of experiments is generally simple and reliable. All the involved parameters are perfectly controllable, and the model can be passed on, replicated and modified easily, and without ethical concerns, as it would be for an experiment involving cadaveric specimens. Thanks to the progresses of semi-automatic segmentation in medical imaging techniques, the idea of using patient-specific models in the clinical routine is also starting to emerge as a realistic option.

For shoulder research, three main categories of numerical models are used: (i) rigid body models, which are usually employed to simulate kinematics, collisions between different elements as well as the wrapping of the muscles over the bones; (ii) muscle force estimation techniques, based on solving an inverse kinematic problem through optimisation and in some cases electromyographic (EMG) data and (iii) deformable finite elements models evaluating the stress-strain distributions in some of the components of the shoulder, to study implant failure, muscle or tendon rupture or articular degeneration.

Rigid body models assume rigid non-deformable bodies (typically bones) connected by different types of mechanical joints (typically hinge joints allowing rotation around a single axis or perfect ball and socket joints allowing 3D rotations around a single point). They are typically used to evaluate how a set of forces (input) would affect the kinematic behaviour of the UL (output) or the opposite. Within the context of improving the clinical treatment of the shoulder, rigid body models have been used to assess the range of shoulder motions in rehabilitation, in ergonomics applications, and to evaluate the effect of mispositioning a shoulder implant ('Conformis.com', n.d.; 'Shoulder Subluxation - Glenohumeral subluxation explained', n.d.; Favre, Moor, Snedeker, & Gerber, 2008;

N. Klopčar et al., 2007). This modelling approach has also been used in commercially-available models for the whole musculoskeletal system and in software such as AnyBody (AnyBody Technology A/S, Aalborg, Denmark), SIMM (MusculoGraphics Inc., Santa Rosa, USA). Customized versions of these software programs were used in several shoulder studies (I W Charlton & Johnson, 2006; 'Conformis.com', n.d.; 'Shoulder Subluxation - Glenohumeral subluxation explained', n.d.). At present, most of these models employ limited representations of the GH joint, simplifying it to either three hinges with defined axes of rotation or by defining it as an ideal ball-and-socket joint. These simplifications prevent the study of GH stability since they do not take GH translations into account. In addition, accounting for physical contact between muscles, bones and other soft tissues is mostly neglected, thus limiting the accuracy in modelling muscle actions over large ranges of motions. This is a major problem as it directly affects the muscle movement moment arm and line of action (Iain W. Charlton & Johnson, 2001). Moreover, rigid body models neglect tissue deformation, thus making such models improper for the study of some important problems in shoulder biomechanics, such as the aseptic loosening of glenoid implants.

A complementary approach to the modelling of the shoulder consists of simulation of a large number of muscles or muscle fascicles on top of a rigid body model and computation of the activation patterns (outputs) that lead to the requested kinematic patterns (inputs). Since in most cases the number of muscles is much larger than the number of DoFs, the set of equations present an infinite number of mathematical solutions. Therefore, the muscle activation is determined by filtering out unrealistic options and using optimisation techniques to minimize a selected cost function (such as muscle force, stress, fatigue, energy expenditure and others). In some cases, surface EMG data can be used to drive the activation pattern of the muscles recorded, but these activations cannot be recorded for deep muscles and do not translate well to other experimental settings. This modelling approach can help to study the onset of tendon tears, as well as their functional impact on the patient (Engelhardt et al., 2016; Lemieux, Nuño, Hagemester, & Tétreault, 2012). It was also used to investigate how GH joint stability could be achieved through the evaluation of the direction of the net force applied by the humerus to the glenoid cavity (Ehsan Sarshari et al., 2017; Van der Helm, 1994a).

The third approach to modelling consists in building a finite elements (FE) model of the shoulder. This method consists in subdividing a complex mechanical structure into a finite number of separate components with simple geometry called "elements". This allows to discretize and numerically solve problems that originally were very difficult or impossible to solve as a whole. This method is often used to study stress and strain distributions in the bones and soft tissues or the interactions between geometrically-complex structures. It can receive different types of entries (inputs), such as a stress, a strain, a set of forces or a forced displacement, depending on the hypothesis, and will compute the propagation of this phenomenon within the structure, typically providing maps of stress, strain or deformations within the elements (outputs). To study GH contact stresses, with varying glenoid cavities and humeral heads morphologies and orientations, (Büchler, Ramaniraka, Rakotomanana, Iannotti, & Farron, 2002) used a FE model involving the major muscles of the rotator cuff and the bones. In another study (Alexandre Terrier, Reist, Vogel, & Farron, 2007) investigated the consequences of supraspinatus deficiency and proposed a 3D FE model of the shoulder with a focus on GH stability. They calculated the contact point on the glenoid to measure joint stability, while (Büchler et al., 2002) used an average of the contact area between the humeral head and the glenoid toward this scope and ('Conformis.com', n.d.; Favre et al., 2012) compared the shear force to the compressive force applied to the joint to evaluate its stability. However, there is no comparison between these different approaches, therefore the validity is unclear. Further validation and standardisation of these metrics is still needed (Zheng, Zou, Bartolo, Peach, & Ren, 2017).

2.2.2 Robotic models

Initially, physical models were mostly used for the direct quantification of the properties of cadaveric specimens (Bigliani et al., 1992). However, the need to apply forces on different elements of the cadaveric samples, led to the use of more complex mechanical setups, first using pulleys and weights to generate the wanted forces on the muscles (Hughes, Niebur, Liu, & An, 1998) then using sets of pneumatic actuators to generate and control the forces (Kedgley et al., 2007), therefore creating robotics model of the shoulder. At present, some robotic models are able to provide similar results without the need for cadaveric specimens (Baumgartner et al., 2014; Christian Gerber, Snedeker, Baumgartner, & Viehöfer, 2014).

Robotic models are also frequently used to test surgical prostheses, in conditions that would reflect the *in vivo* conditions. To model the shoulder, Karduna (Karduna, Williams, Williams, & Iannotti, 1997) used a simple 2 Dofs robotic model for a first assessment of GH instability. Shortly later, several authors (Baumgartner et al., 2014; Kido, Itoi, Lee, Neale, & An, 2003; Wuelker, Korell, & Thren, 1998) developed wire and pulley robotic models to achieve motions that would be closer to an anatomical shoulder, where the wires would be connected to actuators and replicate the action of the muscles. However, this type of simulators is unable to reproduce the action of the large number of muscles fibers acting on the shoulder as a numerical simulation would do and work on a highly reduced number of simulated muscles. Moreover the forces generated at the GH joint from these models are below 300 N, and do not reach the amplitude of the forces measured *in vivo* (Bergmann, 2009).

A second approach (Debski et al., 1999; Hurschler, Wülker, Windhagen, Plumhoff, & Hellmers, 2001; McMahon, Burkart, Musahl, & Debski, 2004; Patzer et al., 2011) was to use general purpose robotic arms to manipulate shoulder specimens and evaluate their properties. It offers the benefits of using already built state of the art robotic systems for the evaluation of the specimens, but generally suffers from an overly complex system, with non-linear control properties and is generally able to apply only low forces on the shoulder specimen.

A third approach was designed to simulate the wear of the prosthesis after large number of cycles, while using physiologically realistic forces, as required by market regulations, such as the ASTM F2028-14 standardized test (International, 2014). These simulators (C Anglin, Wyss, & Pichora, 2000; Gregory et al., 2009; Virani et al., 2008) are very efficient toward this scope, but unadapted to evaluate complex motions, such as the rotations of the arm. Moreover, due to their high number of cycles, these simulators are built to avoid GH dislocations in order not to damage the system.

Specialized models focusing on the net GH force and on the orientation of the prosthetic components, were also developed for the evaluation of GH stability. Favre (Favre, Sussmann, & Gerber, 2010) proposed a simple solution with one DoFs being actuated and 3 which can be manually fixed to different values, while Debski (Debski et al., 2017) proposed a simulator with 6 actuated DoFs for the evaluation of diarthrodial joints. However, both these two models were not reported to work with forces higher than 300N, whereas *in vivo* measurement report much larger forces in the GH joint (up to 1.8 kN).

Within the context of Chapter 3, a new robotic simulator is developed for the study of GH instability after TSA. The robotic approach allows it to reproduce the real contact properties between the two prosthetic components, a problem that has generally been avoided in numerical models due to its complexity. This robotic simulator will use a structure of orthonormal actuators, similarly to the solution proposed by Debski (Debski et al., 2017), but will also be able to reproduce the full range of force recorded in the GH joints of TSA patients. In Chapter 4, this novel robotic model is combined with a patient-specific numerical model of the shoulder, to model the GH stability of three TSA patients from the local university hospital (CHUV).

2.3 Clinical functional evaluation of the upper limb

During the recovery of a patient it is important to monitor the progresses and to adapt the exercises. Several tools exist for the functional assessment of the patient. The most prominent ones are presented here along with some interesting tools that are still in development, but whose first evaluations can already be found in the scientific literature.

2.3.1 Clinical questionnaires

A large number of clinical questionnaires are available. OrthoToolKit ('OrthoToolKit', n.d.) provides a summary of the available scores and questionnaires that are currently in use. Only for the UL it gives 12 options reflective of their importance in the clinical practice. Five of the most relevant ones for this thesis are:

1. *Simple Shoulder Test (SST)* (Lippitt, 1993) was designed to provide a measure of the shoulder function as perceived from the patient's perspective. It consists of a list of 12 items with "Yes" or "No" answers, leading to an outcome measurement between 0% (low functionality) and 100% (normal functionality). Its simplicity being considered as one of its main strengths;
2. *Disabilities of the Arm, Shoulder and Hand (DASH)* (Hudak & et al., 1996) was designed to evaluate the function of the UL in patients with MS disabilities. It is composed of 30 items, each evaluated on a 5-point Likert scale. The outcome score ranges from 0% (no disability) to 100% (most severe disability). It evaluates the function of the whole UL, with the first 23 items evaluating the ability to perform daily life activities, followed by 6 items on the patient's perceived symptoms. In a systematic review by (Bot et al., 2004) several functional scores were evaluated for their clinimetric properties (validity, reproducibility, responsiveness and practicality) and the SST was judged as the best out of the sixteen questionnaires evaluated. However, the length of the DASH was criticized. For this reason, in 2005, (Beaton et al., 2005) developed a reduced version with only 11 items (8 on the patient's ability to perform daily life activities, and 3 on his perceived symptoms) out of the original 30, called the *QuickDASH*, which is commonly used nowadays;
3. *Constant-Murley Shoulder score* (Constant & Murley, 1987) was designed around 10 items to evaluate four domains of the shoulder's function: (i) pain (15 possible points); (ii) activities of daily living (20 possible points); (iii) mobility (40 possible

points); and (iv) strength (25 possible points). The first two parts of the test are completed by the patient, while the third and fourth are completed by the clinician. The final score ranges from 0 (most disability) to 100 (least disability).

4. *Western Ontario Shoulder Instability Index (WOSI)* (Kirkley, Griffin, McLintock, & Ng, 1998) was designed to target patients with shoulder instability. It is based on 21 items and is divided in four domains: (i) physical symptoms (10 items); (ii) sports, recreation, work (4 items); (iii) lifestyle (4 items) and (iv) emotions (3 items). Each item is evaluated from 0 through 100 using a visual analog scale. Overall score ranges from 0 (best shoulder function) to 2100 (worst shoulder function).
5. *Shoulder Pain and Disability Index (SPADI)* (K. E. Roach, Budiman-Mak, Songsiridej, & Lertratanakul, 1991) was designed to reflect the disability and pain associated with the clinical syndrome of painful shoulder, as well as to monitor the pain evolution over time. It is composed of 13 items, divided in two domains: (i) pain (5 items) and (ii) disability (8 items). Each item is evaluated by a visual analog scale, resulting in a score between 0 (easy/no pain) and 10 (difficult/worst pain). The final score is then obtained by summation of all the previous scores and expressed as a percentage, between 0% (unaffected shoulder) and 100% (worst possible shoulder condition).

Overall, many of these tests overlap in function and no single test emerges as a gold standard (Angst et al., 2011). Moreover, the scores obtained from these tests directly depends on the patient's interpretation and psychological status at the time of the evaluation (Ragab, 2003). Even though the perceived handicap is a very important part of the pathology, and there are no better ways to measure pain, the development of more objective and reliable tools to complement these tests are necessary.

2.3.2 Physical evaluation

A large number of techniques are used for the physical evaluation of a patient (as reviewed extensively in (May, Chance-larsen, Littlewood, Lomas, & Saad, 2010)). In this section the most common tests related to GH instability are described, mostly evaluating the GH instability or laxity.

The laxity of a joint is defined as a capacity for symptom-less translations; when the translations reach a pathologic level (damaging or painful), the joint is referred to as unstable. The five most common tests are the *sulcus sign*, the *load-and-shift*, the *apprehension relocation and release test* and the *anterior and posterior drawer test*.

Sulcus sign test (Christian Gerber & Ganz, 1982; Tzannes, Paxinos, Callanan, & Murrell, 2004) starts with the patient sitting with his arms relaxed by his side. The examiner grasps the patient's elbows and pulls down on them. If a sulcus appears in the subacromial area of the patient's shoulder should be measured (in centimeters). This test is an indicator of inferior GH instability.

Load-and-shift test has been described under several variations (Tzannes et al., 2004), for brevity here I present only one of the options. The patient starts in supine position with the center of the scapula of the tested limb on the edge of the examining table to allow free movement of the GH joint while providing a degree of fixation to the scapulothoracic joint. The examiner sits by the head of the patient and grasps the patient's elbow with his/her corresponding hand. The other hand of the examiner grasps the patient's upper arm. The examiner then positions the patient's arm to 90° abduction in the scapular plane in neutral rotation. He/she then centers the patient's humeral head on the glenoid by applying a load along the axis of the humerus with the hand that was grasping the patient's elbow. The examiner then attempts to shift the patient's humeral head off the glenoid in the anterior, posterior and inferior directions. The result is then graded on a scale from 0 to 3 as follows: grade 0, little to no movement of the humeral head; grade 1, the humeral head could be shifted so that it started to ride up onto the glenoid labrum; grade 2, the humeral head could be shifted off the glenoid, but spontaneously relocated once the pressure was eased; grade 3, the humeral head could be shifted off the glenoid and remained dislocated once the pressure was eased.

Apprehension relocation and release test (Lo, Nonweiler, Woolfrey, Litchfield, & Kirkley, 2004) is performed in three manoeuvres:

1. the *Apprehension maneuver*, where the patient is placed in supine position, with the arm at 90° of abduction. The arm is then stressed by the application of an external rotatory force. If the patient communicates the impression that the shoulder will come out, the test is positive, if the patient communicates that the maneuver causes pain, it is a sign of a more subtle anterior instability;
2. the *Relocation maneuver* starts from the apprehension maneuver, with the arm abducted at 90° and rotated externally, then a posteriorly-directed force is applied to the proximal humerus. Its role is to differentiate pain arising from an instable joint from pain related to other reasons. If the patient expresses relief in this second maneuver, then he/she suffers from GH instability, otherwise, the cause is probably different;

3. the *Release maneuver* is a final verification of the instability, it consists in removing the posteriorly-directed force to verify if the signs and symptoms observed in the apprehension maneuver reappear. If they do, the test confirms an unstable GH joint.

Anterior and posterior drawer tests (Christian Gerber & Ganz, 1982) are two tests that can be applied when the apprehension relocation and release test provides unclear results. The *anterior drawer test* is performed with the patient supine and the examiner standing in front of the affected shoulder. Assuming that the right shoulder is being tested, the examiner fixes the right hand of the patient under his/her own right axilla by adducting his/her humerus. The patient should maintain his/her UL relaxed and should not grasp the examiner's arm. The affected shoulder is held in 80° to 120° of abduction, 0° to 20° of forward flexion and 0° to 30° of lateral rotation. Then the examiner holds the patient's scapula with his/her right hand, pressing the scapular spine forward with his/her index and middle fingers, while his/her thumb applies a counter-pressure on the coracoid process, therefore holding the scapula firmly. Then, with his/her left hand, the examiner grasps the patient's left upper arm and draws it anteriorly with a force comparable to that used in the knee in Lachman's test. The examiner uses this manoeuvre to evaluate the relative movement between the scapula and the humeral head and therefore decide about the presence of anterior instability. The *posterior drawer test* also starts with the patient lying supine, with the examiner next to the affected UL (for convenience the right UL is assumed). He/she grasps the patient's proximal forearm with his/her right hand, flexes the elbow at about 120° and positions the shoulder at 80° to 120° abduction and 20° to 30° forward flexion. As in the previous manoeuvre, examiner then grasps the scapula with the left hand, placing the index and middle fingers along the scapular spine and the thumb lateral to the coracoid process. Then with the right hand the examiner slightly rotates the upper arm medially and flexes it to about 60° to 80°. During this manoeuvre, the examiner's thumb subluxates the humeral head posteriorly, while evaluating the displacement achieved by the humeral head.

Additional tests may be useful for the evaluation of tears in one of the four muscles of the rotator cuff, if such an injury is suspected. Many tests are available and only a quick overview is provided here:

1. *Jobe's test* starts with the arm of the patient flexed forward at 90°, and the thumb pointing downwards. The examiner then pushes gently the arm downwards and the patient should be able to counter the push. If patient is unable to resist, a tear in the supraspinatus muscle is probable;
2. test starts with patient positioning both elbows along the body, flexed at 90° and both arms externally rotated by 60°. The examiner holds both forearms in position and asks the patient to perform an external rotation. Inability to perform on the presumed pathologic side is indicative of a lesion to the infraspinatus muscle;
3. the *maneuver de Patte* starts with the patient's arm abducted at 90°, with no forward flexion and about 30° external rotation. The examiner then stabilizes the patient's elbow and forearm and asks him/her to perform a countered external rotation. Inability to perform is indicative of a lesion in the teres minor muscle;
4. *lift-off test of Gerber* starts with the patient staying upright, with the back of his/her hand on top of his/her back pocket. Patient is then asked to move the hand posteriorly in order to detach it from the pants. Inability to perform this motion is indicative of a lesion in the subscapularis muscle.

The reliability of the main physical examination methods for shoulder laxity and instability was evaluated by 4 different examiners, with different backgrounds (an orthopaedic shoulder specialist, an orthopaedic fellow, a sports medicine registrar, and a medical student), reporting the intra-class correlation coefficient (ICC) values for 22 tests, including the *Apprehension relocation and release test*, the *Sulcus sign test* and the *Load-and-shift test* (Tzannes et al., 2004). Only two variations of the inferior *load and shift test* reported a good inter-rater agreement (0.79) and one for the posterior *load and shift test* reported an excellent inter-rater agreement, with no difference between any of the examiners. Of the remaining evaluations, 8 scored moderate inter-rater agreement ($0.5 < \text{ICC} < 0.75$) and 11 scored poor inter-rater agreement ($\text{ICC} < 0.5$). A later systematic review (May et al., 2010) also concluded that "the majority of studies indicated poor reliability for all procedures investigated" and "There is no consistent evidence that any examination procedure used in shoulder assessments has acceptable levels of reliability. Alternate methods of classification, which are reliable should be used to classify patients with shoulder problems". On the other hand, the number of tests available underlines the importance of the functional evaluation of the UL for the clinicians and the lack of instruments being both reliable and clinically usable.

2.4 Standard motion-lab based evaluation

Conventional stationary systems generally represent the best tracking technologies available, with few compromises on costs and complexity. This makes these systems great for research and as validation tools, but they are generally not well-adapted for routine clinical use and rarely used within this context. Within these systems, five technologies are broadly used and described, their application to the evaluation of the shoulder is also explained.

1. *Stereophotogrammetric marker-based motion capture systems* measure the trajectory of passive markers fixed to specific locations of the body in order to tag and track several segments of the body. A set of cameras placed at different locations in space to track these markers together with specialized processing software provide the three-dimensional reconstruction of the motion of the markers in space and consequently of the kinematics of the marked segments. Excluding soft tissues artefacts, position and orientation of the segment can be tracked with an accuracy of <0.2 mm and $<0.6^\circ$ using the Vicon motion capture system (Windolf, Götzen, & Morlock, 2008). The downsides of this method are: (i) the costs of the setup; (ii) the need for a large dedicated room to perform these measurements; (iii) the need to place a lot of marker on the patient's skin; (iv) the need for a long calibration procedure; (v) the sensitivity of the setup to very small accidental motions of any camera, voiding the results; (vi) the sensitivity to occlusions of the markers and (vii) the need, in many cases, for a time-consuming post-processing step in order to analyze the recorded data.
2. *Optoelectronic motion capture systems with active markers* work by the same principle as the *Stereophotogrammetric marker-based motion capture systems* but replace the passive markers by a set of active markers each equipped with a blinking infrared light. Based on the blinking pattern of the light the marker can be recognized removing the need to label it manually in post-processing (one of the most time-consuming parts of the post-processing for the systems using passive markers). Based on the data from producer of one of these systems the accuracy of the Optotrack Certus is of 0.1 mm (NDI Measurement Sciences, n.d.). Therefore, compared to the passive markers, the use of active markers allows a more precise positional tracking, and a faster post-processing, at the cost of an even more complex initial setup.
3. *Electromagnetic tracking systems* are composed of an electromagnetic source and a set of trackers to be fixed on the segments to track. Each of these trackers contain a 3D magnetometer that allows the tracker to compute its position with respect to the electromagnetic source. The declared static accuracy varies depending on the distance from the source but should remain below 1.5 cm (Polhemus, 2010) in noiseless conditions. The advantages of such a system are: (i) compact form-factor; (ii) ease of installation and short calibration time; (iii) fast post-processing and (iv) occlusions resistance. The downsides are: (i) high costs; (ii) high sensitivity to the presence of any ferromagnetic element in proximity of the system, corrupting the measurement quality and (iii) limited accuracy and precision. Based on our laboratory experience with the Polhemus G4, the presence of metallic elements in the floor caused disturbances of more than 50 cm while performing static recordings 50 cm above the floor.
4. *X-ray fluoroscopy* uses a bi-plane fluoroscope to reconstruct the 3D position and orientation of the bones over time while the patient is moving. It can also be used to track metallic implants and metallic beads inserted into the patient. This measurement is particularly interesting since it does not suffer from soft-tissues artefacts like all previous methods. However, it exposes the patient to the ionizing radiation of the X-rays and should therefore be used only when no other method is appropriate.
5. *Surface Electromyography (EMG)* uses sets of electrodes on the patient's skin to sense the electrical activity produced by several chosen muscles. This "electrical activity" is generated by the summation of the action potentials from the motor units of the muscles and depends on the number of activated motor units, on the frequency of their activation and on their distance from the electrode (Konrad, 2005). Through accurate selection of the position of each electrode this method allows to record an approximation of the pattern of activation of the muscles. This information can also be used to estimate the force generated by the muscles, but this method is challenging and its reliability is often contested (Staudenmann, Kingma, Daffertshofer, Stegeman, & Dieën, 2006). Additionally, part of the information on the muscle activation cannot be measured with surface EMGs since they can only record the electrical activity of the superficially-located, but not deeply-located muscles.

There is a large number of research applications where these technologies are employed. (Micera, Sabatini, Dario, & Rossi, 1999) used statistical techniques and fuzzy logics to predict UL kinematic motions from EMG data. To evaluate the predicted outcome, the kinematics of the exercises were co-recorded by surface EMGs and by a stereophotogrammetric motion tracking system for concurrent comparison (six subjects participated to this study), showing that the classifier was able to correctly identify all of the different movements.

(Ehsan Sarshari, 2018) used the same technologies to record the kinematics and muscular patterns of a single volunteer during a set of pure motions and activities of daily living in order to build a MS model able to simulate those tasks.

(Charbonnier, Chagué, Kolo, Chow, & Lädermann, 2014) used a stereophotogrammetric motion tracking system system to evaluate the GH translation *in vivo*. Comparison with fluoroscopic data for six subjects indicated large RMSE values (>3.5 mm) for the different tasks evaluated but the patterns of humeral translation were in good agreement with published data.

(Magermans, Chadwick, Veeger, & Van Der Helm, 2005) took advantage of the faster post-processing proposed by electromagnetic trackers to evaluate the RoMs of a larger set of 24 experimental subjects during a set of activities of daily living in a controlled laboratory environment.

(Zulkarnain et al., 2017) used an optoelectronic motion capture system as reference system to evaluate if the RoM of the shoulder and smoothness of the UL motions of ten subjects could also be evaluated reliably with a recent commercial tracker.

All these studies are only a fraction of the research projects that took advantage of these advanced lab evaluation tools. However, due to the constraints of these systems (expensive and time consuming), most studies are limited to ten patients or less. Although, the usage of these technologies for clinical assessment is limited, they are generally used as a reference to evaluate other instruments due to their good performance.

2.5 Instrumented functional tests

Even though conventional stationary systems are mostly used for research applications, progress in tracking technology allows transition of the use of instrumented motion analysis to the clinic. The use of goniometers for the evaluation of the articular ranges in the anatomical planes has already been used for a long time. The evolution of microelectromechanical systems, such as accelerometers, gyroscopes and magnetometers allowed the development of compact, low-power inertial measurements units (IMUs). Such sensors are able to record 3D accelerations, angular velocities and changes in the magnetic field (typically to identify their orientation with respect to the magnetic north), while remaining extremely compact (many modern smartphones contain such sensors). Using these sensors to perform measurements in daily living condition was shown to provide more natural motions than in the clinic or laboratory framework (Bonato, 2005). For the evaluation of the UL mobility, (Coley, 2007) attached 4 IMUs, on both arms, on the trunk and on the scapular's spine. He developed several tests and kinematic scores based on those recording for the functional evaluation of the shoulder. In particular (Coley, 2007) proposed a first instrumented version of the SST score, offering a more reliable evaluation of the shoulder's function through the kinematic recording of 9 short tests. This test was then refined and simplified to use only a single IMU on the arm in 7 short tests (Duc, 2013). Two more studies (Pichonnaz et al., 2017, 2015) demonstrated that most of the information is in 2 of the 7 tests, proposing a very short and convenient score called the B-B score, where patients have to "put hand to the back" for the first test and put the "hand to the ceiling as to change a bulb" for the second. This test is responsive, offering excellent diagnostic power on patients suffering from rotation cuff conditions (N=20), fractures (N=23) and capsulitis (N=22) and reliability (ICC = 0.92). However, this test is not able to discriminate patients with instable GH joints from control subjects.

Recent developments in consumer-grade low-cost, marker-less optical tracking are opening new possibilities for the clinical functional evaluation of the UL. The Kinect camera (Microsoft, Seattle, WA, USA) is particularly relevant in this field and is used to perform simple measurements such as the articular RoMs (Lee et al., 2015) and to motivate and monitor children during physical UL rehabilitation using videogames controlled by their own UL motions (Parry et al., 2014). The accuracy and reliability of Kinect has been compared to a standard stereophotogrammetric marker-based motion capture systems during a set of UL movement for the evaluation of the RoM by (Bonnechère, Jansen, Salvia, Bouzahouene, Omelina, et al., 2014). The results indicate good reliability ("no significant difference was found between the test and the retest session for any of the movements tested") and the ICC's for the test-retest were moderate to high (>0.66) for the Kinect system, but accuracies varied strongly depending on the movements chosen.

Considering that the primary function of the UL is to place and orient the hand in space for it to perform an action, it is interesting to evaluate the volume where the hand can be placed in space by moving only the UL. This volume is called the reachable space (R_{space}) of the UL. This approach was initially proposed by (Lenarcic & Umek, 1994) and was first assessed using the Vicon motion capture systems, then in a following paper by the Optotrak motion capture (Nives Klopkar & Lenarcic, 2005). Both papers focused on building a model of the UL that would complete the point-cloud of the reachable positions, in order to evaluate the volume of the R_{space} using a voxelization algorithm. As a result, in both cases, the feasibility of computing the R_{space} was shown. However, Lenarcic did not apply his test to any patient, and Klopkar 2005 evaluated a single patient with a diaphyseal fracture of the humerus, indicating that the R_{space} of the later was his smaller. Finally, to make the test relevant for clinical use, the articular ranges of motion recorded using simple goniometers were used as input for the evaluation of the R_{space} (N. Klopkar et al., 2007), and used to record the R_{space} from 6 frozen shoulder patients. No information was provided about the discriminative power of the test or its reliability. Nonetheless, using only the four standard articular ranges to build the model may cause it to miss localized abnormalities of the R_{space} which may not have a significant impact on the motions in the anatomical planes, but could still cause a significant handicap in daily living conditions (Kurillo et al., 2012).

In a further study by (Kurillo et al., 2012) an optoelectronic motion capture system was used to evaluate the R_{space} without completing the R_{space} with tens of thousands of model-based and potentially wrong reachable positions, as it was done in the previous studies. However, with this Kurillo was not able to reliably compute the R_{space} but successfully developed a method to evaluate the envelope of the R_{space} . Then he evaluated his method on a set of 20 healthy subjects and 9 patients with different neuromuscular disorders of the UL (5 with Becker muscular dystrophy, 1 with Duchenne muscular dystrophy, 1 with facioscapulohumeral dystrophy and 1 with Pompe disease). Out of the 9 patients, data from only one was not statistically different from the control group. In a further study (Kurillo et al., 2013), the same protocol was repeated, but to simplify the test, the results from the optoelectronic motion capture system were confronted to the same test as recorded by a single low-cost marker-less motion capture system, the Microsoft Kinect device. It demonstrated a less robust tracking, but still produced meaningful data from the 10 healthy volunteers who participated to the study, indicating that the Microsoft Kinect is a viable solution for the evaluation of the envelope of the R_{space} ($\text{ICC} > 0.86$).

In Chapter 5 a new method to track the motions of the UL is developed and used to measure the R_{space} of a set of ten healthy volunteers. In an effort to make the recording easy to use, cost-effective and fully automatic, a tracking solution is developed as a customized version of the consumer-based tracking technology *Lighthouse*, normally employed by the *HTC Vive* virtual reality (VR) setup. In order to ensure clear and easy understanding of tasks, the exercises were guided by a custom-made virtual reality exergame. The use of virtual reality was shown beneficial to similar application by (Shin et al., 2016).

In Chapter 6 the test developed in Chapter 5 named *Volfon*, is adapted to the use with patients through direct evaluation on a set of patients. The performance of the final version is then evaluated on a set of sixteen patients displaying different functional affections of their UL (capsulitis, post-traumatic stiffness, rotator cuff reinsertion or other) during a test-retest protocol. From the recordings, different metrics are assessed and compared for discriminative power and reliability evaluation.

Chapter 3 Robotic Glenohumeral Simulator for Investigating Prosthetic Implant Subluxation¹

3.1 Abstract

Total shoulder arthroplasty is an effective treatment for glenohumeral osteoarthritis. However, it still suffers from a substantial rate of mechanical failure, which may be related to cyclic off-center loading of the humeral head on the glenoid. In this work, we present the design and evaluation of a glenohumeral joint robotic simulator developed to study glenohumeral translations. This five-degree-of-freedom robot was designed to replicate the rotations ($\pm 40^\circ$, accuracy 0.5°) and 3D forces (up to 2kN, with a 1% error settling time of 0.6sec) that the humeral implant exerts on the glenoid implant. We tested the performances of the simulator using force patterns measured in real patients. Moreover, we evaluated the effect of different orientations of the glenoid implant on joint stability. When simulating realistic dynamic forces and implant orientations, the simulator was able to reproduce stable behavior by measuring the translations less than 3 mm of the humeral head with respect to the glenoid implant. Simulation with quasi-static forces showed dislocation in extreme ranges of implant orientation. The robotic glenohumeral simulator presented here was able to reproduce physiological glenohumeral forces, and may therefore be used to further evaluate the effects of glenoid implant design and orientation on joint stability.

3.2 Introduction

As the population ages cases of shoulder osteoarthritis increase, leading to an increased demand for total shoulder arthroplasty (TSA). In 2007, about 650'000 shoulder prostheses were implanted in the USA, representing a 3.7-fold increase over the last 14 years (Day et al., 2015). Following the increase in shoulder implantations along with the increased longevity of the population, the number of revision surgeries ramped up by 431% over the same time period (Day et al., 2015). Identifying the underlying causes of these prosthetic failures and developing new methods to enhance the implant quality and survival can thus improve the patients' quality of life and decrease medical costs.

The two main problems instigating a frequent need for revision surgeries after TSA are glenoid implant aseptic loosening followed by glenohumeral (GH) joint instability (Alexandre Terrier, Ramondetti, Merlini, Pioletti, & Farron, 2010). Aseptic loosening of the glenoid component is mainly associated with cyclic off-center GH joint loading with subluxation indexes greater than 5% posteriorly or anteriorly (Walch et al., 1999). GH subluxation is defined by the displacement of the humeral head relative to a centered position in the glenoid cavity (Walch et al., 1999), or more recently, to its position with respect to Friedman's scapular axis, termed scapulohumeral subluxation (Alexandre Terrier, Ston, & Farron, 2015). In the present study, due to the lack of an actual scapula in the robot, we used the GH definition of subluxation. Humeral head subluxation is usually measured as the eccentricity of the humeral head center relative to the midpoint of the glenoid cavity (Bercik et al., 2016; Kidder et al., 2010; V.J. Sabesan, Callanan, Youderian, & Iannotti, 2014; Alexandre Terrier et al., 2015; Walch et al., 1999). According to Walch's classification, osteoarthritic glenoids are labeled A to D depending on the level of static subluxation (Bercik et al., 2016; Walch et al., 1999). This 2D measurement of the humeral head subluxation has been widely used. Recently, humeral head subluxation was measured relative to the scapula, first in 2D (Kidder et al., 2010), then extended in 3D (V.J. Sabesan et al., 2014; Alexandre Terrier et al., 2015). Subluxation can occur in any orientation, and may or may not be associated with rotator cuff tendon tears or osteoarthritis (C. Gerber & Nyffeler, 2002). Rotator

¹ This chapter is published in Mancuso, M., Arami, A., Becce, F., Farron, A., Terrier, A., & Aminian, K. (2020). A Robotic Glenohumeral Simulator for Investigating Prosthetic Implant Subluxation. *Journal of biomechanical engineering*, 142(1).

cuff muscle degeneration may induce joint instability and eventually asymmetric glenoid loading after anatomic TSA (Franklin, Barrett, Jackins, & Matsen, 1988; A. Terrier, Ston, Dewarrat, Becce, & Farron, 2017; Wirth & Rockwood, 1996).

Over the last 20 years, numerical models have been developed to study the shoulder joint and its stability (I W Charlton & Johnson, 2006; Prinold, Masjedi, Johnson, & Bull, 2013; Carlos Quental, Folgado, Ambrósio, & Monteiro, 2013). GH instability is generally evaluated by constraining the load and estimating GH reaction forces (Van der Helm, 1994b). However, most of these models cannot quantify GH translations. To the best of our knowledge, there are only few studies (Favre et al., 2012; C Quental et al., 2016; Ehsan Sarshari et al., 2017; Sins et al., 2015; Alexandre Terrier et al., 2013) that account for the GH translation in numerical modeling of shoulder stability. These numerical predictions are however limited by variations in glenoid implant deformation as well as the absence of stiction and friction.

The limitations of numerical modeling and the difficulties of in-vivo measurements have led to in-silico research with mechanical or robotic simulators. Commercial simulators or multi-station shoulder joint simulators are used for wear simulation (Smith, Li, Johnson, & Joyce, 2012). These simulators (e.g. www.amti.biz) are able to reproduce a wide range of motions while applying realistic forces. However, such systems were designed for testing prostheses under stable conditions where it is not possible to push the prosthesis towards dislocation, i.e. an excessive translation of the humeral implant over the glenoid implant.

Several machines were built to apply physiologically relevant forces on shoulder prostheses to study GH stability, implant wear and aseptic loosening, or to evaluate the load and translations which result in GH subluxation (Gregory et al., 2009; Smith et al., 2012; Virani et al., 2008). Favre et al. (Favre et al., 2010) designed a similar simulator with the ability to impose an incident angle on the humeral shaft to study the stability of reverse TSA and how to best position the implant to prevent dislocation. A mechanical simulator was also used with cadaveric shoulders to study the radial mismatch effect on subluxation load force (Karduna et al., 1997) and translation after applying displacement forces on the deltoid and rotator cuff muscles of cadaveric samples (Wuelker et al., 1998). Moreover, the contribution of the deltoid muscle to subluxation was also simulated, while varying the force levels (from 0 to 50 N), and the capsule condition (healthy, vented, and Bankart lesion) (Kido et al., 2003).

Even though all those robotic simulators can contribute to a better understanding of the shoulder function, none are able to provide a fully-controlled and physiologically relevant simulation of GH instability after anatomic TSA. Cadaver-based experiments are unable to reproduce force and movement patterns of the GH joint. To address these issues, few bio-mimetic robots (Mizuuchi et al., 2002; Y. Sodeyama et al., 2008; Yoshinao Sodeyama, Yoshikai, Nishino, Mizuuchi, & Inaba, 2007) were built with modified structures to avoid experiencing joint instability. Moreover, due to their high structural complexity their control is challenging and reproducing the internal force patterns of an anatomical human shoulder while maintaining controlled movements would be complex and costly.

Fujie et al. (Fujie et al., 1993) proposed to use actuators orthogonally placed around a diarthrodial joint, in order to have simpler control schemes and an improved accuracy during their simulations. Combining their simulator with cadaveric joints, they were able to evaluate the force exerted by most of the ligaments of the GH capsule during different levels of arm abduction (Debski et al., 2017). However, this simulator was demonstrated to work only with low loads (200 N), whereas *vivo measurements* (Bergmann, 2009) displayed larger loads, raising beyond 500 N in most cases.

One of the main outcomes of a robotic simulator is to provide the surgeon with preoperative information for better TSA. Among different surgical features, glenoid implant orientation has already been proposed to balance potential eccentric loadings (Suárez et al., 2009; Alexandre Terrier, Merlini, Pioletti, & Farron, 2009; Wong, Gallo, Kuhn, Carpenter, & Hughes, 2003); however, there are currently no tools to determine if one orientation is more stable than another. In this study, to model and quantify prosthetic GH instability and dislocation, we aimed at developing a GH joint robotic simulator capable of controlling joint forces while measuring humeral head translations over the glenoid cavity in stable and unstable conditions by changing GH orientation. Different tests were performed with the robot to evaluate both its static and dynamic performances, its effectiveness in controlling physiological GH forces and to measure GH translations in normal and subluxation/dislocation conditions by changing the glenoid implant orientation.

3.3 Materials and Methods

3.3.1 Mechanical structure and actuation design

There is a large number of muscles of different sizes acting on the shoulder. Most large muscles can be split into subgroups of muscle fibers with similar functions. However, building a robotic simulator with a dozen of actuators pulling on strings to replicate the natural process is impractical. Moreover, we were interested in the measurement of GH subluxation, i.e. displacement due to the net force acting on the prosthesis. Therefore, our robot had to work directly with the net forces exerted by the combination of these muscles on the prosthesis. Consequently, the number of actuators and mechanical complexity were also reduced.

Usually, the referential frames of the humerus and scapula are defined following the International Society of Biomechanics standard (Wu et al., 2005). However, in this study, the referential frames were slightly different in order to express directly the motions of the prosthetic components by the simulator measures. We considered 5 degrees of freedom (DoF) for the prosthetic GH joint, oriented with respect to the prosthetic humeral head: three translations (along X: anteroposterior; along Y: inferior-superior; and along Z: axial or mediolateral, with XY plane being parallel to the planar surface lying at the back of the metallic hemisphere, and Z being perpendicular to XY plane) and two rotations (internal-external α (around Y) and abduction-adduction β (around X)), applied sequentially (first α , second β), as shown in Figure 10a. By considering the prosthetic humeral head as perfectly spherical, we assumed its rotations about the axis of the glenoid implant had no effect on the position of the humeral head with respect to the scapula or the geometry of the joint. Therefore, this rotation was not simulated. The three forces that the humeral head exerts on the glenoid implant were actuated along the three axes (X, Y, Z). As shown in Figure 10b, the simulator presented rotated but equivalent axes with respect to the anatomical ones. The forces were expressed in the referential system of the prosthetic humeral head, and the humeral rotations were replicated by an equivalent reversed rotation of the glenoid implant. The ($\alpha = 0^\circ$, $\beta = 0^\circ$) coordinate indicated the configuration at which the axis of the glenoid implant was aligned with the axis of the humeral head.

The robot was designed and simulated using Solidworks (SOLIDWORKS®) (Figure 10b). This process led to a final assembly of 177 components to form the robot as shown in Figure 10c.

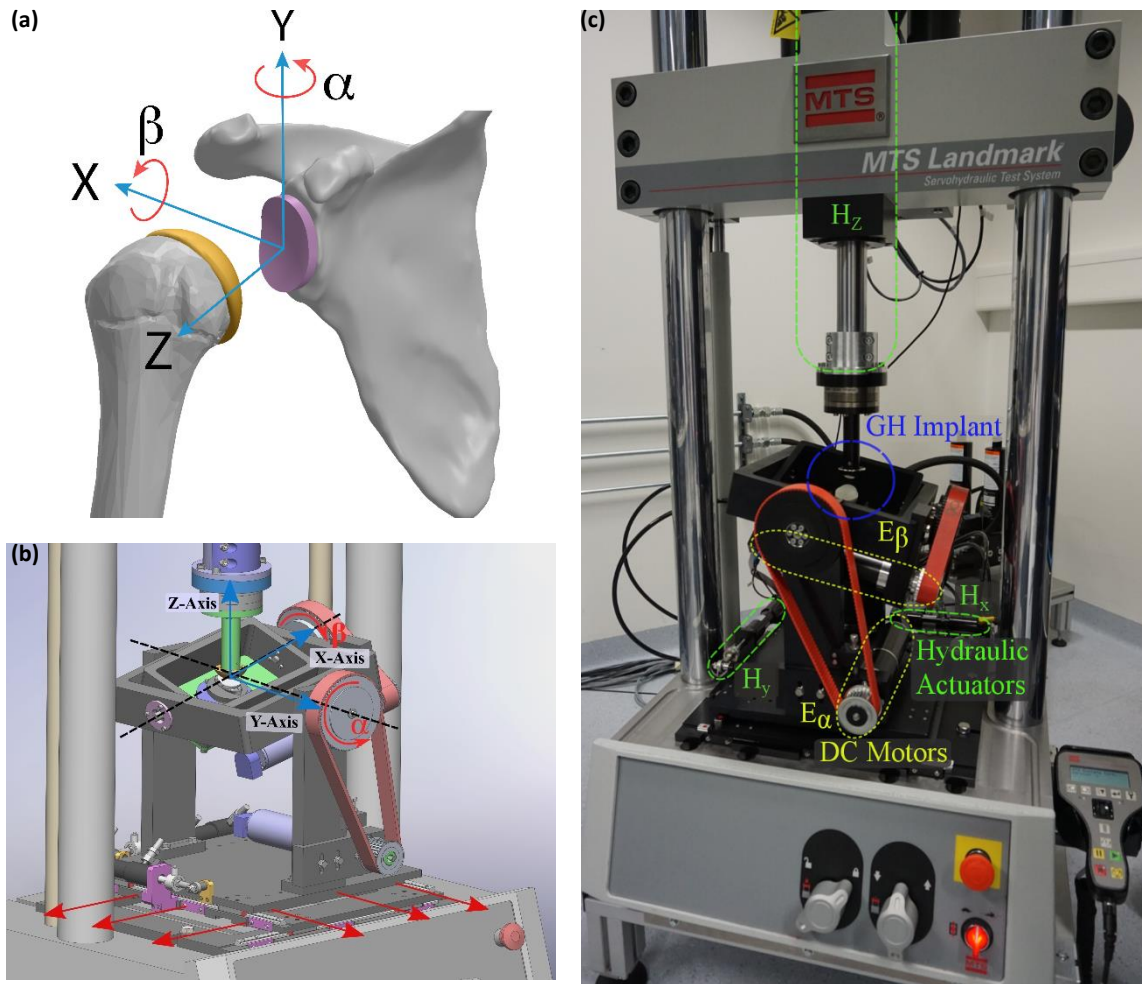


Figure 10: (a) Referential system of the shoulder fixed on deepest point of the glenoid implant, X: anteroposterior; Y: inferior-superior; and Z: axial or mediolateral. The angles between the humeral head and the glenoid implant were represented by α and β . (b) Computed Aided Design (CAD) simulation of the robotic simulator and its referential system. (c) Realized robotic simulator with three hydraulic actuators (H_x , H_y , H_z) and position and force sensors. X and Y translations were transmitted to the glenoid joint using ball bearing rollers mounted on two linear rails. α and β rotations were assured with two DC motors (E_α , E_β) equipped with encoder and customized with a planetary reducer and a transmission belt.

3.3.2 Sensors and Actuators

The axial compression was provided by an MTS Bionix® load unit (dynamic and static load capacity of ± 15 kN), which was completed by two smaller hydraulic cylinders (Custom Actuator Products Inc. (CAP) model: AA3/4X3-1-3-4M6(3)-1D; maximum compression 5.8 kN, maximum tension 4.4 kN) to account for the anterior-posterior and inferior-superior force components. These three hydraulic actuators (H_x , H_y , H_z) were equipped with position and force sensors. The position was measured through an embedded resistive sensor. Both translations are transmitted to the glenoid joint using 4 ball bearing rollers (Schneeberger AG, Wagen MN12-G3) mounted on two linear rails (Schneeberger AG, Schiene MN 12-370-G3-V0). The precision for position measurement was of $25.4 \mu\text{m}$.

In order to maintain the glenoid orientation even when the humeral head is applying a high load on the glenoid rim, strong rotary motors were needed. Considering that the forces should not exceed the most extreme cases found with the instrumented prosthesis (Bergmann, 2009) of 180% bodyweight (BW), with an assumed BW of 100 kg, the force should not exceed 1.8 kN. Placing such a force on the edge of the glenoid prosthesis would, therefore, generate a torque of $1.8 \text{ kN} \times 2.5 \text{ cm} = 45 \text{ Nm}$. For dynamic simulations, it was also assumed that the subject did not exceed speeds of 30 rpm (half a revolution per second). To fulfill these constraints, two identical electrical brushed DC motors (RE50, 200W, Maxon Motor AG, Sachseln, Switzerland) were chosen (E_α , E_β). Both motors were customized with a planetary reducer (1:74) and a transmission belt, further reducing the speed by a ratio 1:2.4. This allowed the motor to develop moments up to 45 Nm. With this level of reduction, the final rotation speed was still adequate, with 31 rpm in the free rotation (theoretical value).

E_α and E_β were equipped with a 500-impulsion encoder on the motor shaft. Since a turn of the prosthesis corresponded (due to the transmission system) to 177.6 turns of the motor shaft, it was equivalent to $355'200$ impulsions (4×500 quadcounts $\times 74 \times 2.4$ tours after transmission system) and therefore a theoretical resolution of 0.001° . Nonetheless, the errors due to internal contact motions between all the components of the transmission chain were factored in, reducing this theoretical precision.

3.3.3 Controller

H_x , H_y and H_z were controlled through MTS proprietary software (FlexTest 793.00) using a PID controller with feedforward (FF) compensatory term (PID-FF). During most tests the actuators were used in displacement control mode to place the humeral head 1 cm above the center of the glenoid component. Then, the axial actuator H_z was switched to force control with a command of 10 N to push at the center of the glenoid implant. Next, the simulation started and all hydraulic actuators were switched to force control in order to replicate the internal 3D force of the simulated subject. The range of the H_x and H_y was programmed to keep the glenoid implant within $[-17.1; 21.1]$ mm and $[-20.1; 32.1]$ mm respectively which was enough to study the stability of the implant.

The force control PID gains were manually fine-tuned to obtain a settling time less than 0.2 seconds and critically damped or overdamped, but close to critically damped behavior when tested with a number of control commands from different initial states. Two FF gains were added to improve the tracking. The following gains obtained for different actuators control; axial actuator: P: 30; I: 5; D: 0.1; F: 0.5; inferior-superior actuator: P: 20; I: 5; D: 0.1; F: 0.3; F: 0.4; anterior-superior actuator: P: 20; I: 5; D: 0.1; F: 0.3; F: 0.4.

The rotary motors E_α and E_β were position-controlled using a customized software developed in LabVIEW™ 2015 version 15.0f2 (National Instruments, Austin, United States). The control was done with two PIDs, using the gains: P: 271; I: 165; D: 1417 and P: 688; I: 1477; D: 1565 for the rotations about the inferior-superior axis (angle α) and the anterior-posterior axis (angle β), respectively. To avoid oscillatory behaviors the motor speeds were limited to a maximum value of 4000 rpm on the motor shaft, allowing for the prosthesis to rotate at top speeds of 22.5 rpm ($135^\circ/\text{s}$) on the shaft of the glenoid implant. The maximum acceleration and deceleration of the motors were limited to $10'000 \text{ rpm/s}$ on the motor shaft ($337.8^\circ/\text{s}^2$ on the shaft of the glenoid implant). To avoid internal impacts within different components of the simulator the E_α and E_β was limited to $\pm 40^\circ$.

The control interface (Figure 11) offered several advantages: (i) correction of the homing offset; (ii) recording the angular value of the glenoid shaft in an external file for further analysis; (iii) ability to reconfigure the controller while running in order to reproduce a complex motion sequence.

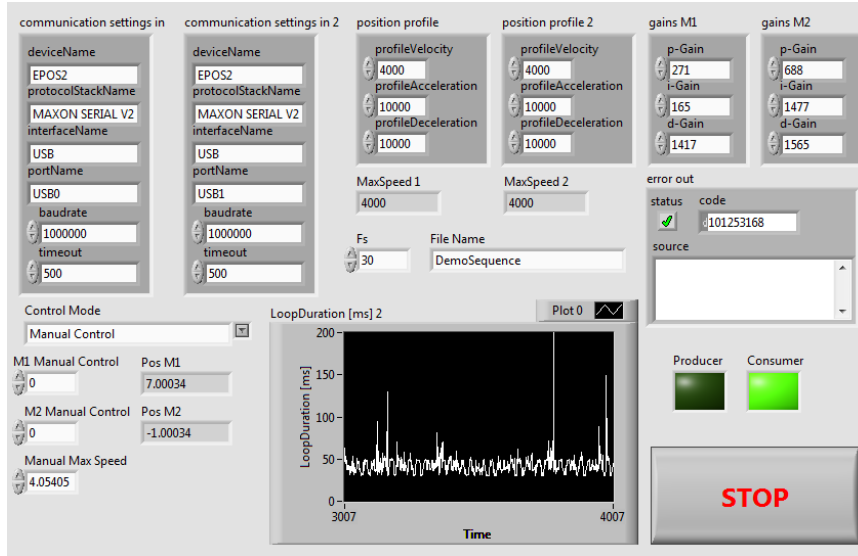


Figure 11: Customized LabVIEW interface for the control of the rotary motors allowing the control of forces, positions and rotations with adjustable gain and window to monitor relevant value.

For practical reasons the control of the hydraulic actuators was decoupled from the control of the electric motors and managed by two different computers and different controllers (Figure 12). On both setups the computers sent target positions or forces to the controllers, as well as the control parameters (PID-FF / PID gains). Then, the controllers ran the control loop with the actuators at 1 kHz frequency.

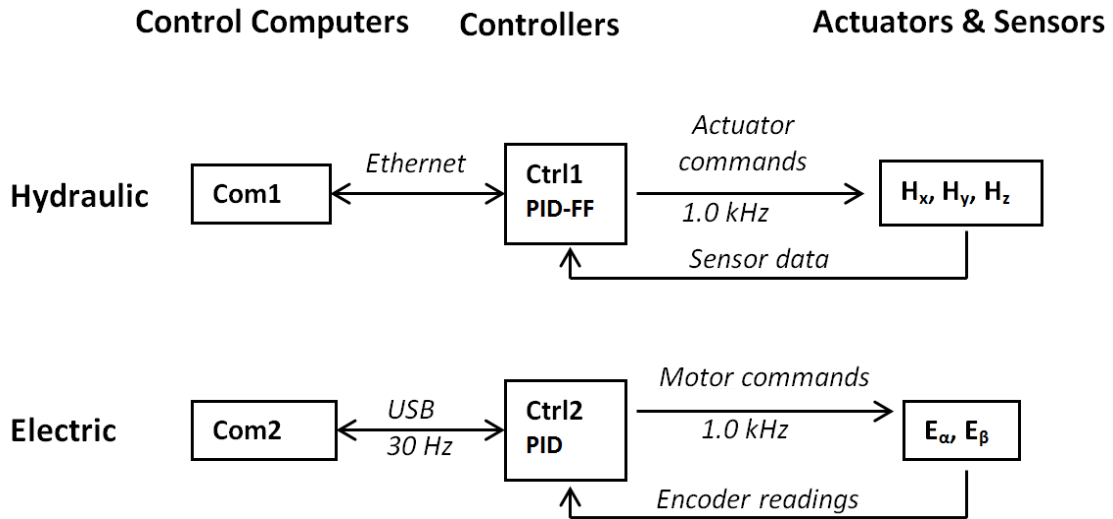


Figure 12: Control diagram of the robot. Com1, Com2: Control Computers; Ctrl1: MTS controller; Ctrl2: 2xMaxon Motor controllers; Ax: Axial Actuator; IS: Inferior-superior actuator, AP: Anterior-posterior actuator, M1, M2: Rotatory motors

3.3.4 General performance evaluation

The robustness of the robot's control was assessed through the ability to replicate a step response and maintain a specified position under varying torques. For the step response the hydraulic actuators (H_x , H_y , H_z) were evaluated independently through the application of a pre-load of 10 N, followed by steps of different amplitudes (± 50 N, ± 100 N, ± 150 N), every time returning to 10 N before applying the next step. The ability of the rotatory motors (E_α , E_β) to maintain a specified position under varying torques was tested. After applying a short pre-loading of 0.1 Nm on the glenoid implant larger torques were applied as a sequence of forces with magnitudes of (± 0.5 Nm, ± 1 Nm, ± 1.5 Nm), respectively (every time returning to 0.1 Nm before applying the next step). These torques were obtained by using similar forces (± 50 N, ± 100 N, ± 150 N) and pre-loading of 10 N applied at ± 0.01 m of the glenoid implant center. The prosthesis rotation caused by these sudden torques was recorded by the motor's encoders.

Since the transmission chain between the rotatory motors and the glenoid implant degrades the angular measurement accuracy, the latter was concurrently tested against a reference system: the motion-capture system VICON (Vicon Motion Systems, Oxford, United

Kingdom). This test was performed by comparing the angular command value with the value measured on the platform supporting the glenoid implant through a set of VICON markers. The difference (i.e. the angular accuracy of the system) was tested for static angles with all the 81 combinations of motors' rotation between -40° and $+40^\circ$ by steps of 10° .

3.3.5 Standardized test for dislocation force estimation

The ASTM F2028-14 standardized test (International, 2014) was applied on the Aequalis Perform + M35 pegged glenoid implant (Tornier-Wright Medical, Montbonnot-Saint-Martin, France) to measure how much an anatomical glenoid component rocks or pivots following cyclic displacements of the humeral implant, here the Aequalis™ Humeral Head ($\Phi=46$ mm, $H=17$ mm, $Ecc=1.5$ mm, Type=CoCr). The first part of the test consisted of quantifying the magnitude of the lateral force (F_x , F_y) that could cause prosthetic dislocation. Dislocation was defined as the case where the humeral head left the glenoid cavity and slid away from the glenoid implant.

In standardized conditions, the axis of the glenoid implant and the humeral head component had to be aligned ($\alpha = \beta = 0^\circ$). The procedure was as follows:

- Application of an axial force of 750 N
- Shifting the humeral head laterally until dislocation
- The force needed to cause the luxation was then retained as dislocation force

To avoid mixing the effects of the robot's inertia with the dislocation force in our simulator shifting the humeral head sideways was replaced by the application of a slowly increasing force until the center of the humeral head passed over the edge of the glenoid implant.

This protocol was repeated three times to test for the anterior, superior and inferior directions of dislocation. Since the prosthesis is symmetric about its inferior-superior axis, the force associated with posterior dislocation was assumed to be the same as the anterior one.

3.3.6 Simulation with realistic forces

Three series of tests were performed to assess the simulator performance in reproducing shoulder contact force patterns and joint translations. First, a pattern of 3D joint contact forces as recorded by in-vivo instrumented prosthesis (Orthoload patient S1R_300605_1_20 (Bergmann, 2009)) during a countered external rotation of the arm with no humerus movement was modelled using Fourier series of order 20. Then, the patterns were fed to the PID-FF controller and reproduced by the simulator. Force tracking performance was evaluated using the embedded force sensors. During this test the unconstrained displacements of the humeral head over the glenoid cavity were measured using the linear resistance transducers of E_α and E_β actuators. The first test was performed at the arbitrary orientation $\alpha=0$ and $\beta=0$. However, the test in the Orthoload database has been performed in a posture close to anatomical position but no information about GH orientation was available.

Therefore, in the second test, the values of α and β were measured from a set of 11 TSA patients using postoperative shoulder CT scans performed in the anatomical position. Approval from the institutional ethics committee was obtained (CER-VD protocol 395/15), and all patients gave written informed consent. Based on these measurements ($\alpha: 41.7^\circ \pm 7.3^\circ$ and $\beta: -10.2^\circ \pm 17.6^\circ$), the GH was set to $\alpha= 40$ deg and $\beta= -10$ deg.

In the third test, we checked the possibility to detect dislocation by changing GH orientation. For this purpose, five samples of force data from the Orthoload dataset were selected and used in a quasi-static test where for each force, GH orientation was changed from $(0^\circ, 0^\circ)$ to $(\alpha_{stable}, \beta_{stable})$ corresponding the dislocation or transducer range. A dislocation was detected when the estimated point of contact of the humeral head reached out of the glenoid rim, therefore switching from a stable equilibrium to an unstable one.

3.4 Results

3.4.1 Dynamic performance

In Figure 13 the step responses of the three linear actuators are presented. Results showed that transient errors lower than 1% of the command position could be reached in less than a second of settlement time (Table A1). As shown in Figure 13, no overshoot or oscillatory behaviors were observed in any condition, further validating this controller for the use of static simulations.

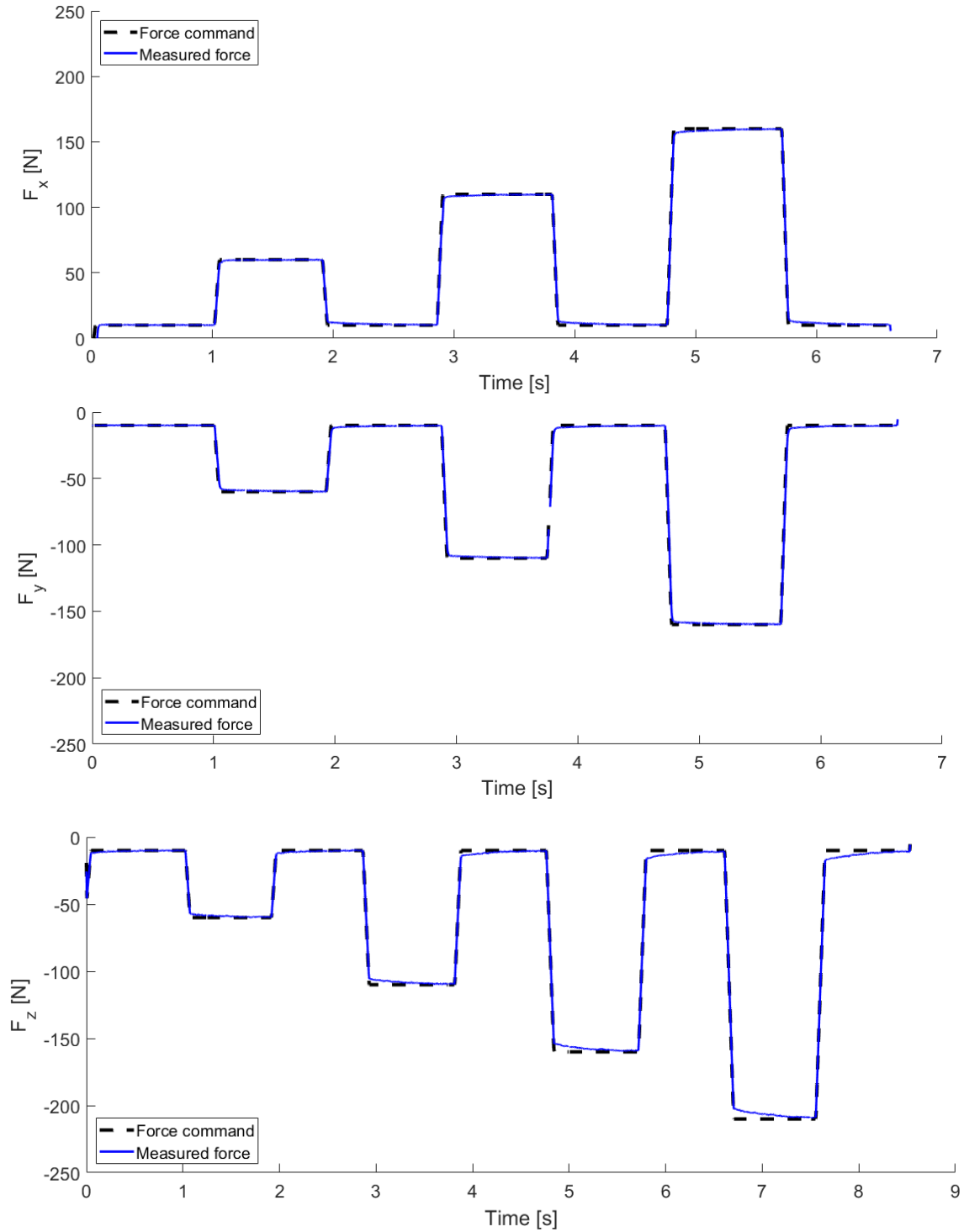


Figure 13: Step response of each of the three hydraulic actuators (Hx, Hy, Hz).

Table A1: Step response of the linear actuators

Force [N]		Rise Time [s]				Delay Time [s]	
		95% Up	95% Down	99% Up	99% Down	Up	Down
H_z	50	0.077	0.051	0.559	0.364	0.029	0.028
	100	0.061	0.058	0.525	0.369	0.037	0.036
	150	0.074	0.076	0.529	0.574	0.044	0.058
	200	0.088	0.088	0.589	0.552	0.053	0.051
H_x	50	0.041	0.043	0.094	0.587	0.026	0.026
	100	0.052	0.044	0.291	0.361	0.029	0.029
	150	0.043	0.042	0.290	0.300	0.032	0.031
H_y	50	0.048	0.047	0.506	0.414	0.028	0.026
	100	0.047	0.053	0.252	0.266	0.019	0.034
	150	0.052	0.053	0.165	0.182	0.034	0.033

3.4.2 Static performance

In addition to the linear actuators, the rotatory motors were evaluated (Table B1 and Table B2). The steady state errors were consistently low, with both the mean and median in the order of 0.1° for α and 0.5° for β .

Table B1: Angular error for the control of angle α expressed in degree. The overall mean and median error were 0.10°

$\alpha \backslash \beta$	-40	-30	-20	-10	0	10	20	30	40
-40	-0.187	-0.187	-0.204	-0.165	-0.133	-0.080	0.007	0.185	-0.146
-30	-0.131	-0.181	-0.164	-0.184	-0.143	-0.067	-0.166	-0.068	-0.153
-20	-0.138	-0.196	-0.178	-0.149	-0.113	-0.053	0.059	0.158	-0.155
-10	-0.074	-0.175	-0.163	-0.150	-0.120	-0.057	-0.077	-0.021	-0.072
0	-0.072	-0.196	-0.178	-0.151	-0.114	-0.055	-0.020	0.188	-0.053
10	-0.091	-0.182	-0.165	-0.151	-0.122	-0.075	-0.107	-0.068	0.146
20	-0.123	-0.195	-0.174	-0.153	-0.116	-0.060	-0.099	0.260	-0.112
30	-0.108	-0.185	-0.145	-0.171	-0.132	-0.079	-0.130	-0.109	-0.112
40	-0.131	-0.204	-0.167	-0.148	-0.127	-0.077	0.057	0.190	-0.067

Table B2: Angular error for the control of angle β expressed in degree. The overall mean and median error were 0.52°

α β	-40	-30	-20	-10	0	10	20	30	40
-40	0.235	0.371	0.503	0.905	0.520	1.121	0.619	0.794	0.921
-30	0.836	0.871	0.379	0.643	0.381	0.356	0.654	1.142	1.119
-20	0.774	0.469	0.532	0.514	0.510	0.419	0.415	0.495	0.036
-10	0.550	0.336	0.369	0.354	0.374	0.418	0.507	0.458	0.553
0	-0.388	0.382	0.436	0.443	0.447	0.476	0.481	0.615	0.471
10	0.632	0.347	0.441	0.499	0.532	0.562	0.514	0.555	0.631
20	0.509	0.486	0.512	0.506	0.417	0.554	0.573	0.650	0.893
30	0.571	0.358	0.434	0.529	0.535	0.534	0.643	0.711	0.847
40	0.532	0.476	-0.180	0.311	0.337	0.599	0.736	0.817	0.460

The ability of the robot to maintain a requested angle independent from the application of external moments of force is an important characteristic of the system. No perturbation was able to significantly alter the angular position (Table B3), with angle variations never larger than 0.005°.

Table B3: Maximum deviation (in degree) from the target angle while perturbed by an external torque. The torque was obtained by applying force with different norm (F_{norm}) at position (Pos) corresponding ± 1 cm from the glenoid implant center ($X=0$, $Y=0$) representing a lever arm

F_{norm} Pos	+50N	-50N	+100N	-110N	150N	-150N
x+1cm	0	0	0.003	-0.006	0.005	-0.001
x-1cm	0	0	0	0	0	0
y+1cm	0	0	0	0	0	0
y-1cm	-0.001	0.001	-0.001	0.001	-0.001	0.001

3.4.3 Standardized test for dislocation force estimation

Under a compressive force of 750 N, horizontal forces of 1300 N and 1250 N were necessary to cause prosthetic dislocation in the anterior-posterior and superior directions, respectively (Figure 14 A). Aiming to induce a dislocation in the inferior direction, forces up to 1750 N were applied but no dislocation was observed. The application of these forces over the rim of the glenoid implant also caused large non-reversible deformations of the polyethylene (Figure 14 B).

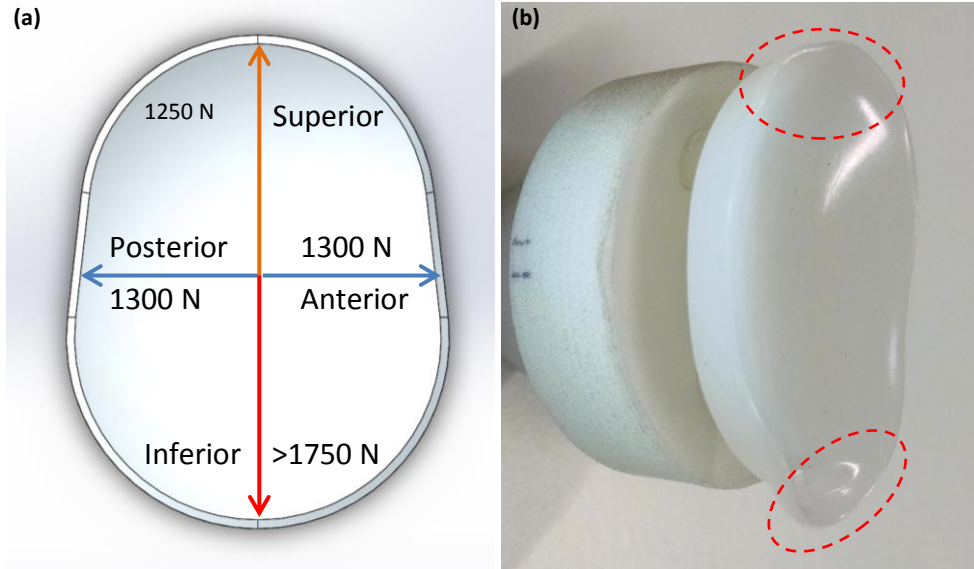


Figure 14: Results of the ASTM F2028-14 test on a M35 glenoid implant. (a) the forces required to cause a dislocation; (b) the implant deformations after passing through the test

3.4.4 Simulation with realistic forces

Dynamic test- The robot was able to reproduce the requested pattern in real time with a coefficient of correlation (R) of more than 0.98 and a root mean square error (RMSE) of 6.2 N for the H_z actuator and less than 5 N for the H_x and H_y actuators (Figure 15 A). Figure 6 B shows the GH translation of the humeral head over the glenoid cavity for $[\alpha = 0^\circ; \beta = 0^\circ]$. Using more realistic GH orientations of $[\alpha = -10^\circ; \beta = 40^\circ]$ still resulted in a clean control of the forces ($R > 0.95$, $RMSE < 11.5$ N, Figure 16 A) and GH translations of less than 3.0 mm (Figure 16 B). In both situations the prosthesis had a stable behavior. The range of translations were $[-0.1$ mm; 1.25 mm] for $[\alpha = 0^\circ; \beta = 0^\circ]$ and $[-0.1$ mm; 3.0 mm] for $[\alpha = -10^\circ; \beta = 40^\circ]$.

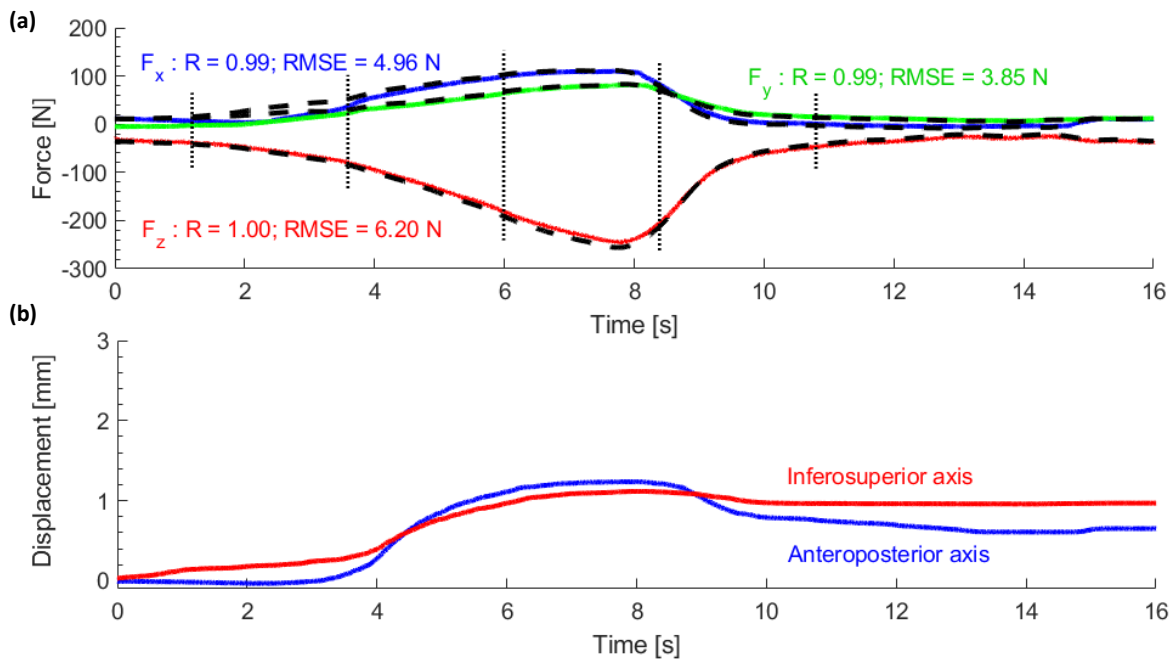


Figure 15: (a) Reproduction of the prosthetic internal net force based on in-vivo measurements with a perpendicular GH orientation ($\alpha = 0^\circ$, $\beta = 0^\circ$). The dashed lines represent the motor command; the red, blue and green solid line represent the axial, anteroposterior and inferosuperior forces, respectively, as measured by their respective force sensors, RMS error (RMSE) are reported for each case. The dotted line correspond to the force data used in quasi-static realistic force test. (b) GH translation of the humeral head over the glenoid cavity along the anterior-posterior axis and the superior-inferior axis.

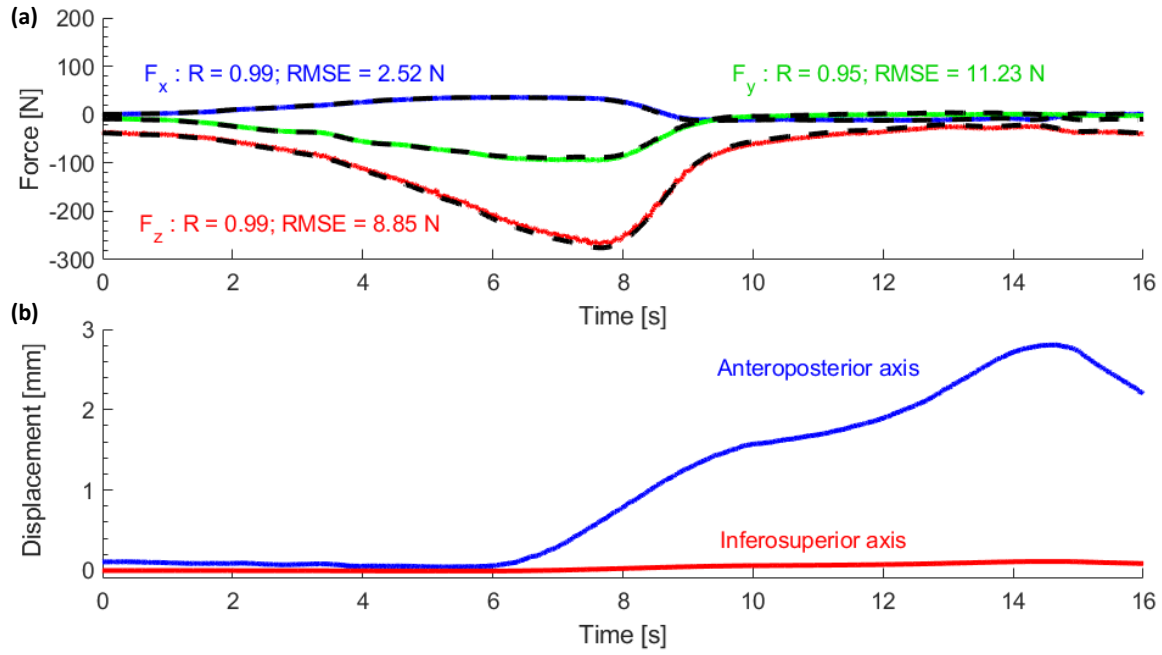


Figure 16: (a) Reproduction of the prosthetic internal net force based on in-vivo measurements with a realistic GH orientation ($\alpha = -10^\circ$, $\beta = 40^\circ$). The dashed lines represent the motor command; the red, blue and green solid line represent the axial, anteroposterior and inferosuperior forces, respectively, as measured by their respective force sensors, RMS error (RMSE) are reported for each case. The dotted line corresponds to the force data used in quasi-static realistic force test. (b) GH translation of the humeral head over the glenoid cavity along the anterior-posterior axis and the superior-inferior axis.

Quasi-static test- The limit of stability (α_{stable} , β_{stable}) of GH orientations during the application of realistic force was explored for 5 static sample forces extracted at a regular sampling interval from the previous force patterns (Figure 15 A): $F_1(-7.9, -14.9, -42.0)$, $F_2(-21.2, -39.7, -93.6)$, $F_3(-88.4, -68.4, -238.9)$, $F_4(-26.6, -2.0, -57.5)$, $F_5(-4.2, -0.5, -21.3)$ N. For each of these forces, GH orientation was changed while keeping one or the other angle (i.e. α or β) at zero degrees. The range of stable angle found for every combination is reported in Table C1. In general α_{stable} was in the range of $[-40^\circ; +40^\circ]$ and β_{stable} within $[-39^\circ; +38^\circ]$ which was also close to the limit of the actuators (Table C1).

Table C1: Stable angular range for GH orientation (α and β) when samples (F_1, \dots, F_5) of dynamic realistic force (F_1, \dots, F_5) in Figure 15 A were applied as static forces. * indicates the limit of angular range of transducer. ** indicates the limit of displacement range of the transducer

Applied force	$\alpha_{stable}, \beta=0^\circ$	$\beta_{stable}, \alpha=0^\circ$
F_1	-40deg*/+40deg*	-39deg/+31deg
F_2	-40deg*/+40deg*	-35deg**/+32deg
F_3	-37deg/+37deg	-23deg**/+32deg
F_4	-31deg/+31deg	-36deg**/+38deg
F_5	-40deg*/+40deg*	-39deg/+38deg

3.5 Discussion

A 5-DoF robotic simulator was designed and built to model GH instability. The system was able to reproduce the internal net force of the joint for 3D forces up to 2 kN, which are sufficient to reproduce most activities of daily living of the shoulder. Moreover, the simulator was able to control the rotations about the inferosuperior and anteroposterior axes. The mediolateral (or axial) axis was neglected as equivalent to rotations around the centerline of a perfectly hemispheric prosthetic humeral head. As far as linear motions are concerned, the simulator was able to test the stability of an anatomic GH implant composed of a humeral metallic (CoCr) head and a polyethylene glenoid implant when applying realistic force and replicate GH possible dislocation when some particular combinations of orientations and trajectories were set.

Using three hydraulic actuators, the triaxial forces could be controlled with a settling time (within 1% error) of 0.6 sec and translation could be measured with a high precision (25.4 μm), which is quite enough to simulate shoulder stability in most activity of daily life. Testing for the effective angular accuracy of the simulator against a reference system demonstrated expected errors less than 0.5°, even in the presence of external perturbations. Hence, this resulted in reliable control of the simulated GH angles.

Compared to existing simulators, this novel simulator used a set of orthonormal actuators, as suggested by (Fujie et al., 1993), but in addition had the ability to generate actuated rotations over two axis, which were not produced with some other robotic simulators (Gregory et al., 2009; Smith et al., 2012; A. Terrier et al., 2017). Moreover unlike existing simulators (Debski et al., 2017; Favre et al., 2010) where the force was limited (e.g. to 200N) it was possible to produce enough load on the prosthesis (e.g. up to 2kN) to simulate situations found in diverse activities of daily living. Actually, the force range of the proposed simulator fit the same range as observed in real patients (Bergmann, 2009) allowing to simulate better activities of daily living.

Ideally, the robotic simulations should be compared to actual situation measured with real subjects. Due to difficulty of measuring GH forces or translations in vivo a direct comparison is practically impossible. Therefore, we designed several tests to verify if the outcomes of the simulator are meaningful and consistent in extreme situations leading to dislocation and in realistic movement where shoulder stability is expected. The first test as defined by ASTM F2028-14 (International, 2014) aimed at determining the dislocation force (minimum force needed to push the humeral head out of the glenoid rim) while maintaining the joint under a constant axial load of 750 N. It also aimed to determine the extent of the robotic simulator achievement of the similar results as those of a wear test machine used by shoulder prosthesis manufacturers. It measured higher amplitude of force, with 1250 N and 1750 N for superior and inferior dislocation, compared to the measurements of Tornier-Wright Medical (Montbonnot.Saint_Martin, France) which were 351.1 N and 442.3 N respectively (Tornier's_Test_Laboratory, 2018). The reasons for this difference may be related to a stiffer support for the prosthesis (polyamide 2200 in our case vs. a cemented block of polyurethane foam in the case of Tornier-Wright Medical), allowing for less compression under the edge of the glenoid implant. Moreover, in the case of Tornier-Wright Medical the glenoid component had a 5-mm larger curvature radius (keeled M40 glenoid) than us (keeled M35 glenoid). More trials with different support materials are needed to point out the potential impact of the quality of the support material under the glenoid implant on joint stability.

In the second and third test a force-tracking task was executed at natural speed with realistic data. An excellent performance (RMSE < 6 N, $R^2 > 0.98$ for all actuators) was obtained, indicating that the motor control is reliable in these conditions. Moreover, this test allowed us to measure GH translations at an arbitrary position [$\alpha = 0^\circ$; $\beta = 0^\circ$] and a realistic position [$\alpha = -10^\circ$; $\beta = 40^\circ$]. The measured translations were small and close to the center of the glenoid (less than 1.25 mm at $\alpha=0$ and $\beta=0$ and less than 3.0 mm at $\alpha=-10^\circ$ and $\beta=40^\circ$). As expected in the case of a stable shoulder joint, the results were consistently stable when realistic forces and GH orientation were applied.

In the third test, the joint was pushed to the extreme values of GH orientation to determine possible dislocations. The robotic simulator was able to replicate dislocation situations, showing that the choice of the GH angles, which are underreported in the literature, play an important role in GH translations. Even though more tests will be necessary to draw a definitive conclusion, this result puts forward the importance of choosing correctly the version and inclination angle of the glenoid implant to maintain joint stability. For this reason, a patient-specific set of GH forces and angles will be necessary for future simulations.

One of the main applications of this robotic simulator is to evaluate the importance of glenoid implant orientation to better balance potential eccentric loadings in a subject specific case. For this purpose, a customized numerical patient-specific simulator for the prediction of internal forces (Ehsan Sarshari et al., 2017) may be coupled with the robotic simulator for the overall predictions of implant stability before surgery. This robot may also become useful for other applications, such as simulation of the causes of GH subluxation/dislocation or the design of new prostheses by evaluation of the shoulder stability behavior and tuning of relevant parameters used for the design purpose.

3.6 Conclusion

A novel 5 DoFs robotic simulator for the modeling of the GH joint was designed and realized. The simulator was able to control the net forces and orientations of a prosthetic GH joint and measure accurately the GH translation associated with prosthesis stability. The simulator controlled and reproduced realistic force patterns derived from in vivo measurements. The results open new possibilities to study the impact of different GH angles on joint stability, and to measure GH translations resulting from the application of specific GH contact forces and angles. Combined with a numeric simulator, this robotic model could have the potential to be used as a tool to improve the surgical planning and outcome in TSA, as well as the prosthetic design.

3.7 Acknowledgments

The authors would like to thank Pascal Morel for his valuable help in the design of mechanical components. Additionally, the authors would like to thank Tornier-Wright Medical for donation of all shoulder prosthetic implants used in this study.

3.8 Funding

This work was supported by grant CR3212_162766 from the Swiss National Science Foundation, and Lausanne Orthopedic Research Foundation.

3.9 Appendix A: Ramp response of the hydraulic actuators

To gauge the behavior of the dynamic control of the hydraulic actuators in the presence of non-linear behaviors, the ramp response was recorded both for a slow (0.1 Hz) and a fast (6 Hz) ramp command. The fast ramp (450 N/s, ramp Amplitude: 75 N, ramp duration: 1/6 s) representing the behavior of the system on the fast and short bouts of the movements such as observed in patients, and the slow ramp (50 N/s, ramp amplitude: 500 N, ramp duration: 10 s) representing the larger and slower parts of natural motions. As displayed in Figure 17, the Fourier reconstruction of the signal caused the shape of the signal to become much smoother, and the actuator was struggling to follow that command, smoothing the signal even more into a sinusoid. As indicated by Figure 19, the lag displayed negligible delays ($d_x = -1$ sample, $d_y = -1$ sample, $d_z = -3$ samples, sampling frequency: 1643 Hz).

The slower ramp command displayed on Figure 18 showed no significant deformation, its tracking was accurate as well and the cross correlation found no lag at all, with all the computed delays being of exactly 0 samples, as indicated on Figure 19.

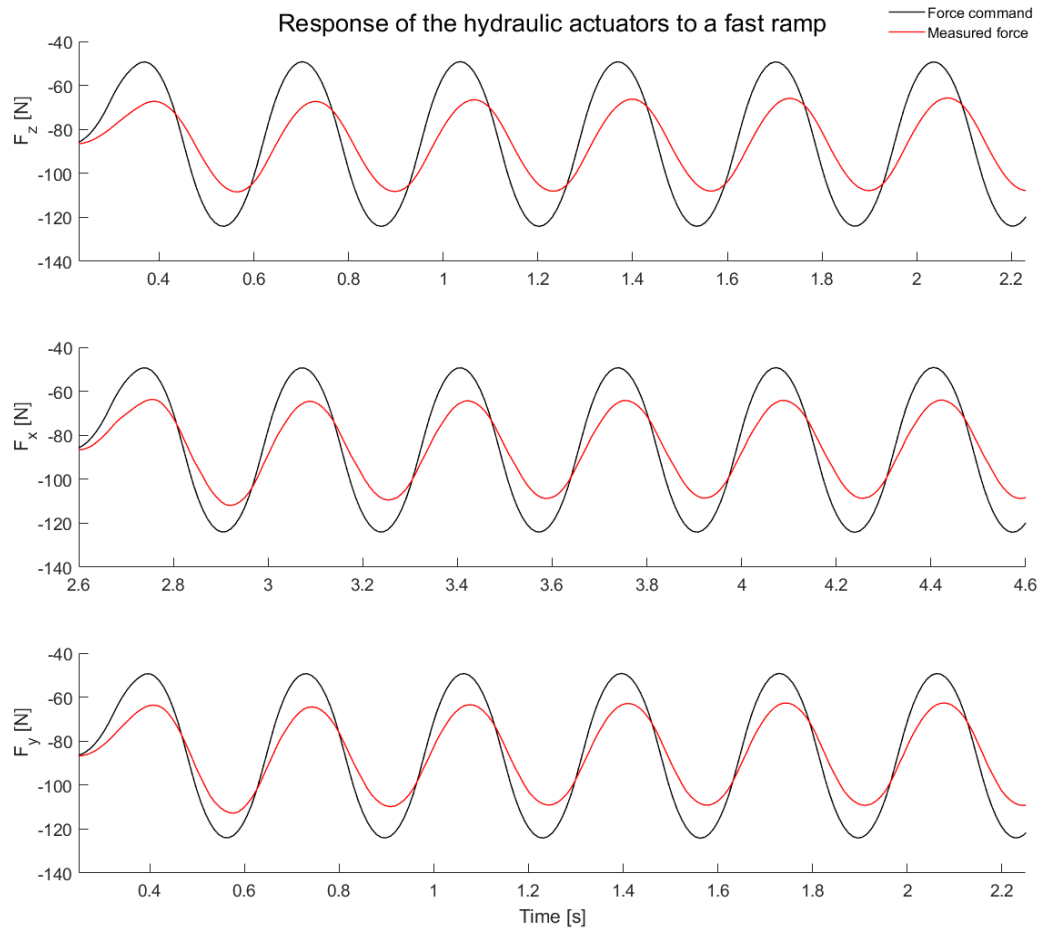


Figure 17: Response of the hydraulic actuators to a ramp periodic command of frequency 6 Hz and amplitude 75 N

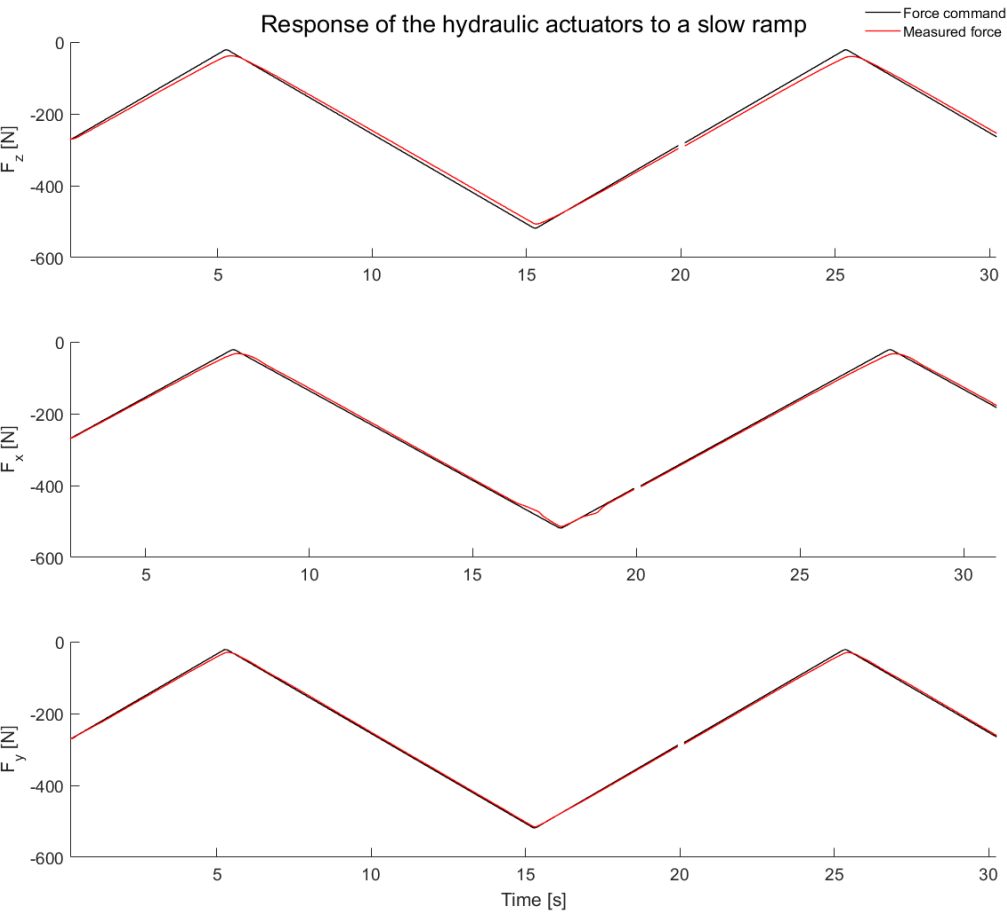


Figure 18: Response of the hydraulic actuators to a ramp periodic command of frequency 0.1 Hz and amplitude 500 N

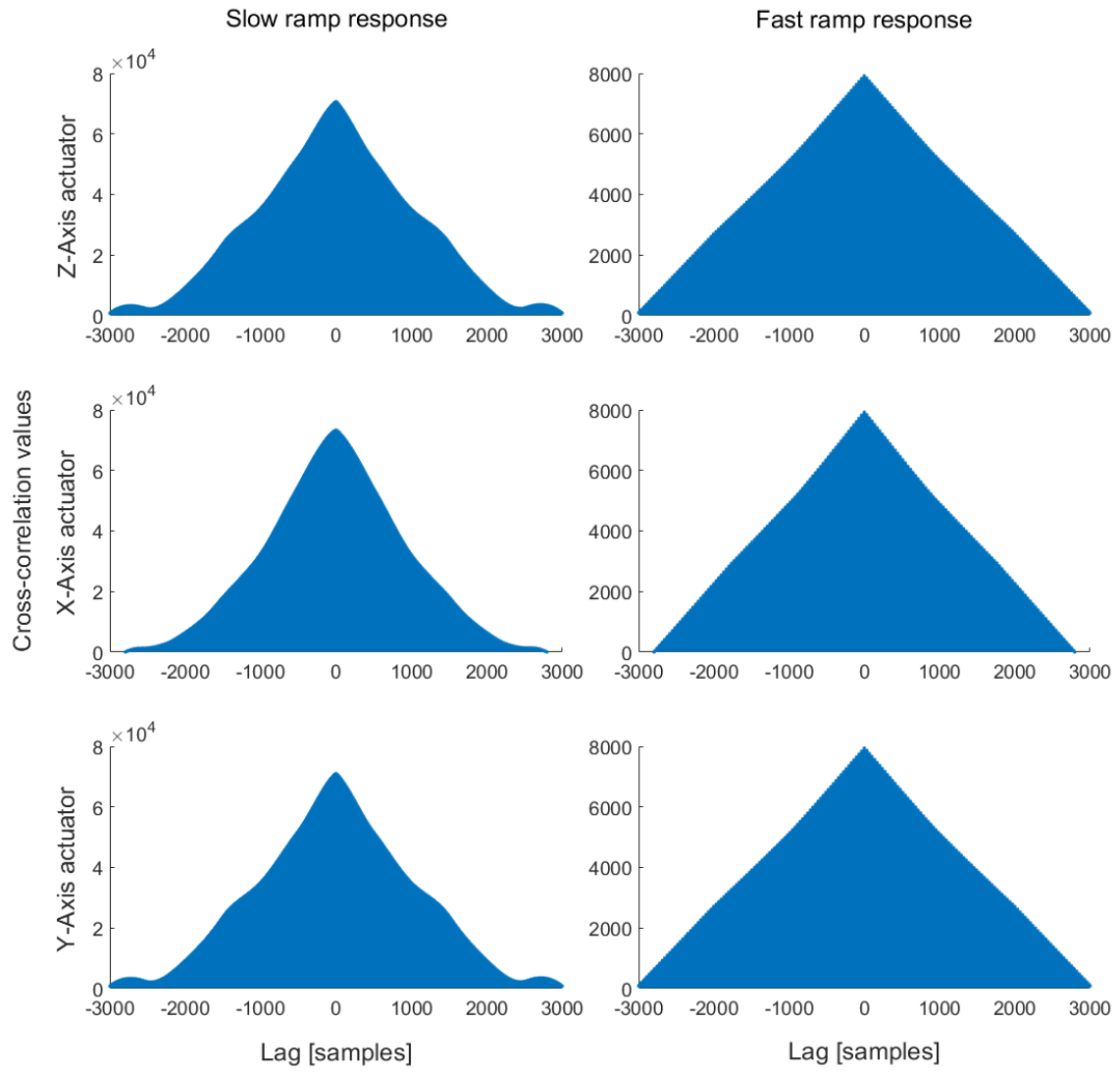


Figure 19: Cross-correlation of the ramp commands with their responses as measured on their respective actuators.

3.10 Appendix B: Frequency response of the hydraulic actuators

Another approach to evaluate the behavior of an actuator consists in evaluating its behavior while tracking a pure sinusoid signal at varying frequencies (Figure 20), here the test started at 0.1 Hz and ended at 3 Hz. From these measurements, the frequency response of the actuator was computed (Figure 21).

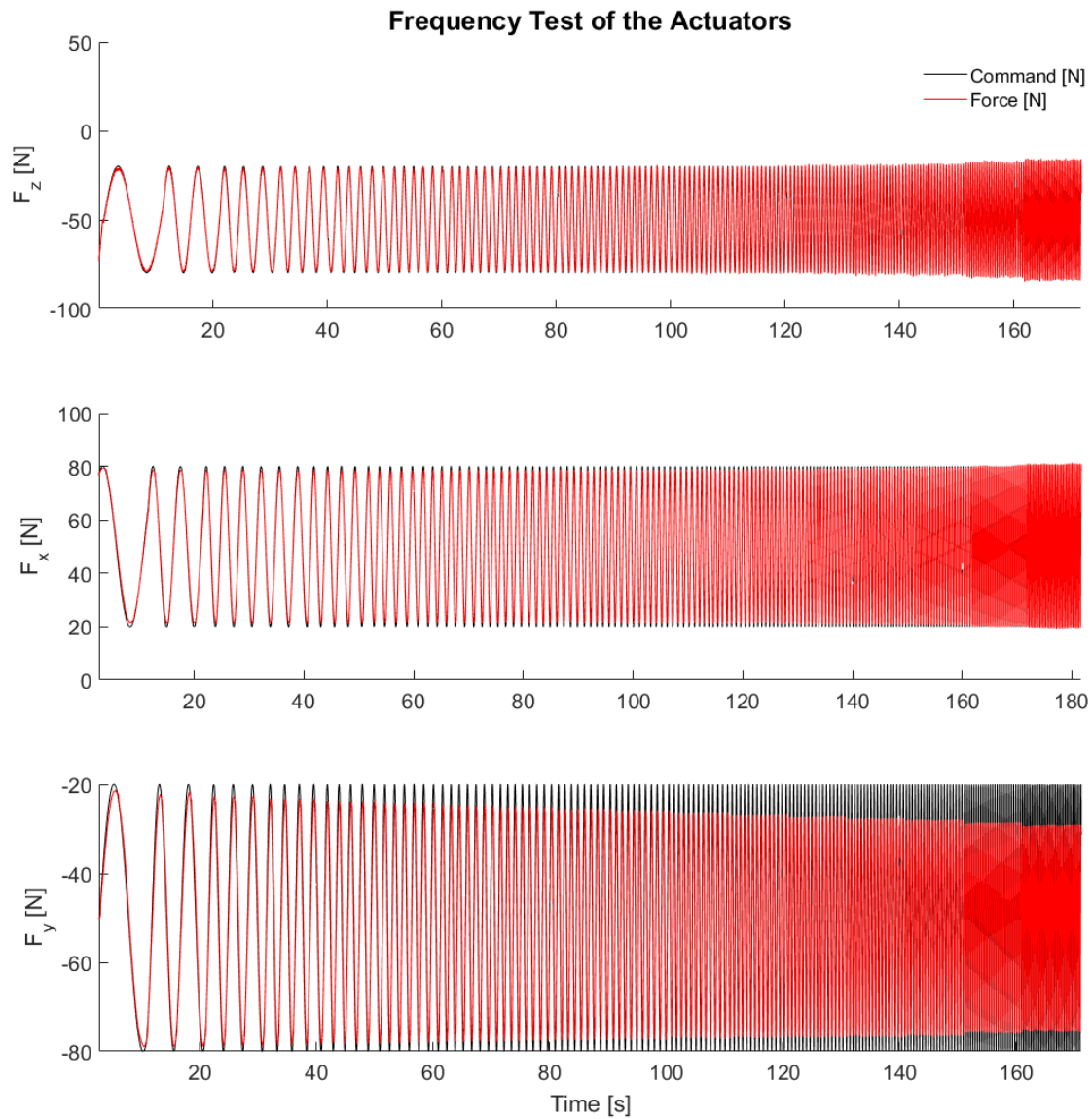


Figure 20: Testing the actuators' response to sinusoidal waves with an increasing frequency.

All the actuators remained within a ± 3 dB interval at every frequency, except for the y-axis actuator, that was observed to misbehave at more than 0.6 Hz.

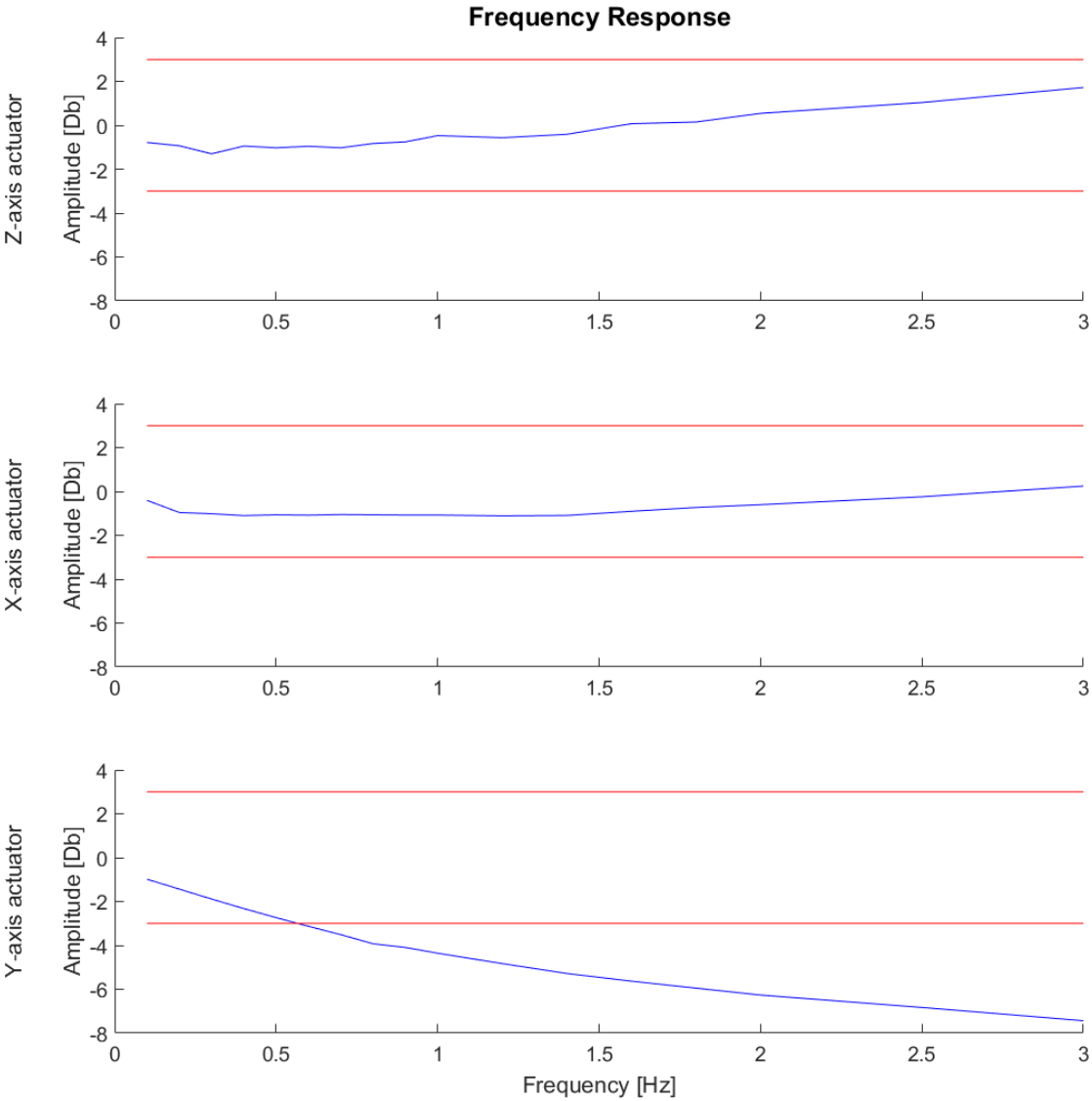


Figure 21: Frequency response of the three hydraulic actuators, with the ± 3 dB interval.

Chapter 4 Patient Specific Robotic Evaluation of the Glenohumeral Translations in Total Shoulder Arthroplasty Patients²

4.1 Abstract

The shoulder is the joint with the largest range of motion of the human body. For this reason, it is one of the most difficult to stabilize while using a prosthetic joint. This study aims at predicting the stability of the glenohumeral joint, by modelling the translation of the humeral head over the glenoid surface for three total shoulder arthroplasty patients. It combines a patient-specific musculoskeletal numerical model for the assessment of the internal forces and the orientations of the prosthesis during three different tasks, with a robotic model evaluating the glenohumeral translations on the real prosthesis. The results indicate that modelling the muscles and bones alone is not sufficient to explain the stability of the shoulder, as a significant number of superior dislocations were observed in the joint model, but absent in the patients. This might be a consequence of the absence of other structural elements (subacromial bursas, glenohumeral capsule, ...) of the shoulder, absent in the model, but preventing this type of dislocations in the patients.

4.2 Introduction

The incidence rate of shoulder arthroplasty in 2012 was evaluated to 20 procedures/10⁵ people, with a 6-fold increase between the highest (Germany) and the lowest (United Kingdom) countries analysed (Lübbeke et al., 2017). As the population ages, the number of primary and secondary surgery has been growing steadily (Day et al., 2015). Identifying the underlying causes of these prosthetic failures, and developing new methods to enhance the implant quality and survival would therefore improve the quality of life of a large number of patients and decrease medical costs.

The two main problems instigating a frequent need for revision surgeries after TSA are glenoid implant aseptic loosening followed by glenohumeral (GH) joint instability (Alexandre Terrier et al., 2010). Aseptic loosening of the glenoid component is mainly associated with cyclic off-center GH joint loading with subluxation indexes greater than 5% posteriorly or anteriorly (Walch et al., 1999). GH instability may be symptomatic of subluxation, defined as the excessive displacement of the humeral head relative to a centered position in the glenoid cavity (Walch et al., 1999), or more recently, to its position with respect to Friedman's scapular axis, termed scapulohumeral subluxation (Alexandre Terrier et al., 2015). Higher instability may produce GH dislocation, defined as translations of the humeral head that are large enough for the two articular surfaces to loose contact. GH dislocations accounts for 50 % of all major joint dislocations (Sherman, 2015), with the anterior dislocation being the most common form of GH dislocation (95 to 97 % of the cases), followed by posterior dislocation (2 to 4 %) and inferior dislocation (0.5 %) (Sherman, 2015). Due to the superior stabilizing structures such as the subcoracoid and subacromial bursas, the acromion itself and the coracoacromial ligament, superior dislocations are nearly inexistent.

For these two reasons, a better understanding on the mechanism controlling GH translation, should positively affect the clinical outcomes of many TSA patients. However, most musculoskeletal models for the upper extremity are generic models, developed on the anthropometric data of a single subject (Martelli, Kersh, & Pandey, 2015), whereas for this study, inter-individual differences are necessary to understand why some individuals display larger than normal GH translations. Therefore, the model presented below was designed as

² This chapter is written as a journal paper for further possible publication. Section 4.3.3 is based on the contribution of Ehsan Sarshari from the Laboratory of Biomechanical Orthopedics of École Polytechnique Fédérale de Lausanne (EPFL).

a patient-specific model, using the standard preoperative CT-scans and surgical planning to adapt a generic model to each patient's musculoskeletal system.

This patient-specific Musculoskeletal (*MS*) model was then used to extract the internal forces acting on the GH joint and to estimate the relative orientations of its prosthetic components, in order to simulate a set of motions that the patient's might do in his daily life, using the robotic simulator presented in Chapter 3.

Over the last 20 years, numerical simulations have been developed to study the GH joint and its stability (I W Charlton & Johnson, 2006; Prinold et al., 2013; Carlos Quental et al., 2013). In most cases, GH instability is assessed by constraining the load and estimating GH reaction forces (Van der Helm, 1994b). However, most of these models cannot quantify GH translations. To the best of our knowledge, there are only few studies (Favre et al., 2012; C Quental et al., 2016; Ehsan Sarshari et al., 2017; Sins et al., 2015; Alexandre Terrier et al., 2013) that account for the GH translation in numerical modeling of shoulder stability. These numerical predictions are however limited by variations in glenoid implant deformation, as well as the absence of stiction and friction.

The limitations of numerical modeling and the difficulties of in-vivo measurements have led to in-silico research with mechanical or robotic simulators as presented in Chapter 3. However, such systems were designed for testing prostheses under stable conditions where it is not possible to push the prosthesis towards dislocation, i.e. an excessive translation of the humeral implant over the glenoid implant. The simulator developed in Chapter 3 was able to undergo GH dislocation in any direction, therefore allowing to study the GH stability.

In this study, we aim to simulate GH translation through our robotic simulator, as presented in Chapter 3. For this purpose musculoskeletal model (Ehsan Sarshari, 2018) was scaled and adapted to each patient using their pre-operative CT scans and informations from the surgical planning. This patient-specific model was used to estimate the internal forces and GH orientations during specific movements that are believed to cause some large values of GH translations. Internal GH forces orientations were input to robotic simulator to test in quasi-static conditions GH translations and quantify possible prosthetic GH instability and dislocation.

4.3 Materials and Methods

4.3.1 Subjects

Three patients (P1 to P3, Table 2) with a total shoulder arthroplasty participated in this study. Implantation was based upon diagnosis of GH OA. The surgical approach was delto-pectoral. Approval from the institutional ethics committee was obtained (CER-VD protocol 395/15), and all patients gave written informed consent. Follow-up consultation was performed at 12 months, revealing no sign of GH instability.

Table 2: Shoulder prosthesis implanted in the patients

Patient	Glenoid implant	Humeral head implant diameter
P1	S40	46 mm
P2	S30	43 mm
P3	S40	46 mm

4.3.2 CT Measurements

Measurements were performed by a senior radiologist from the Department of Diagnostic and Interventional Radiology and comprised the collection of a preoperative CT-scan (in-plane spatial resolution: 488 μ m, Discovery CT750 HD, GE Healthcare, Waukesha, WI, USA) performed in anatomical position, with an elbow flexion of 0°. An anthropomorphic thorax phantom (QRM, Moehrendorf, Germany) was used for bone density calibration. Additionally, blueprint surgical planning (BLUEPRINT™ 3D Planning, Tornier-Wright Medical, Montbonnot-Saint-Martin, France) was performed for every patient by a senior shoulder surgeon from the Service of Orthopedics and Traumatology. This planning was used to produce patient specific guides and to help the surgeon in the choice of the prosthesis as well as its final configuration. Additionally, the CT-images were segmented and used to model the bone morphology, the physiological cross section area (*PCSA*) of the muscles involved in the *MS* model and their insertion points. The blueprint surgical planning was also used to evaluate the position and orientation of the glenoid implant in the *MS* model, and to evaluate the inclination angle of the humeral head, as detailed in section 4.3.4.

4.3.3 Musculoskeletal model for estimation of GH joint reaction force and kinematics

Electromyography (EMG) and motion data were recorded on the right shoulder of a healthy male subject for three activities. These recordings combined with MRI data were used to develop a generic MS model of shoulder and elbow joints. This model was then scaled and adapted to every patient using their preoperative CT scans and surgical planning in order to create patient-specific estimations of their GH joint reaction forces and kinematics.

4.3.3.1 Measurements

EMG and motion data were recorded on the right shoulder of a healthy male subject (29 years old, 186 cm, 85.5 Kg) for three activities (Figure 22). The activities included maximum abduction in the scapular plane with 2 kg weight in hand ($task_{abd}$), placing the hand behind the head ($task_{hand}$), and touching the opposite shoulder ($task_{should}$). All the activities were repeated for ten trials each.

EMG signals of fifteen superficial muscles were measured at 1500 Hz sampling frequency using AgCl Disposable EEG electrodes (Zak Kendall ARBO Disposable EEG electrodes H124SG Ø 24 mm, Johnson Controls, Milwaukee, WI, Stati Uniti) and recorded by a 16 channel Desktop DTS system (Noraxon, Arizona, USA). The muscles included the deltoid clavicular/acromial/scapular, trapezius C7/T1/T2-T7, pectoralis major sternal, infraspinatus, teres major, triceps brachii long/lateral, biceps brachii short/long, brachialis, and flexor carpi ulnaris. Maximum EMG values were also recorded by performing maximum voluntary contractions (MVC).

The measured EMG signals were transformed to muscle excitations by high-pass filtering, rectifying, and consequently low-pass filtering the EMG signals. Eighth order zero-phase Butterworth filters were used. Their cut-off frequencies were set by residual analysis and were crosschecked with the harmonic analysis. The resulting EMG signals were normalized for each muscle using the maximum of its associated MVC signal. They were then parted per activity and per trial. Their means and standard deviations associating to the ten trials were obtained.

Trajectories of eleven palpable bony landmarks were measured by tracking their associated skin-fixed markers using an 8 camera VICON videogrammetry system (Vicon Motion Systems, Oxford, United Kingdom) at 100 Hz sampling frequency. The bony landmarks included incisura jugularis (IJ), processus xiphoideus (PX), 7th cervical vertebra (C7), 8th thoracic vertebra (T8), Center of Acromioclavicular articulation (AC), Angulus Acromialis (AA), Medial Epicondyle (EM), Lateral Epicondyle (EL), radial styloid (RS), and ulnar styloid (US). The center of rotation of the humeral head into the GH joint was defined as landmark GHC and the center of the glenoid implant surface was defined as landmark GC.

The recorded trajectories were low-pass filtered using an 8 order zero-phase Butterworth filter. Its cut-off frequency was obtained following the same procedures as the EMG signals. The resulting trajectories were parted for each activity and per trial. Then, their means corresponding to the ten trials were obtained.

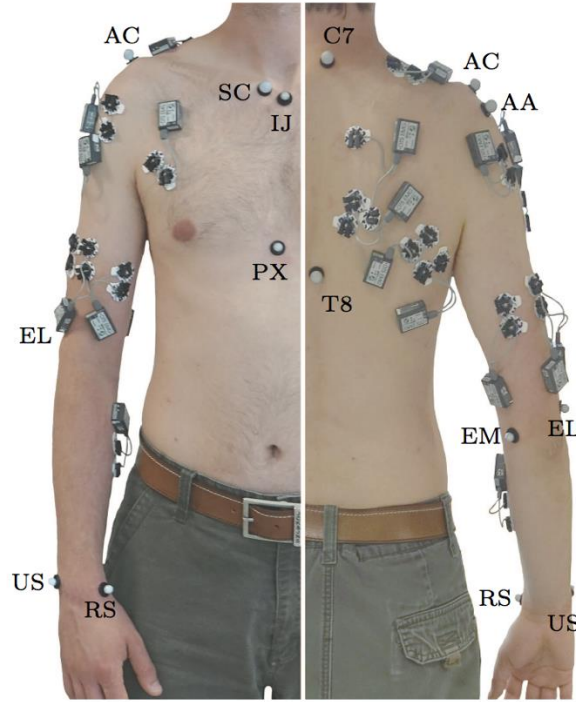


Figure 22: Recording EMG and motion data on the subject (Ehsan Sarshari, 2018).

4.3.3.2 Musculoskeletal model

A MS model of shoulder and elbow (Ingram, 2015; Ehsan Sarshari, 2018) that was validated with *in vivo* measurements of (Bergmann, 2009) was used to provide estimations of the GH joint reaction force and kinematics. The MS model was developed from MRI scans of the right shoulder of the same subject. It consisted of six rigid bodies including thorax, clavicle, scapula, humerus, ulna, and radius (Figure 23a). The hand was assumed to be rigidly tied to the radius. It had nine degrees of freedom (DOF) attributed to three ball-and-socket joints associated with sternoclavicular, acromioclavicular, and glenohumeral joints and two hinge joints for humeroulnar and radioulnar joints and two holonomic constraints. Two constraints restricted trigonum scapulae (TS) and angulus inferior (AI) on the scapula medial boarder to glide over two ellipsoids approximating the thorax and their underlying soft tissues. The configuration of each bony segment was defined using at least three non-collinear bony landmarks. The medial epicondyle (EM), lateral epicondyle (EL), and their middle point (HU) on the humerus were borrowed for the ulna and the radius. The ISB recommendations (Wu et al., 2005) were followed to define six bone-fixed frames. In particular, the frames of the thorax, scapula, cone and humerus were defined as follows:

- i. Thoracic Referential Frame
 - Center: IJ.
 - \vec{X}_{Thorax} : normal to the plane defined by the IJ, C7, $(T8+PX)/2$ -IJ pointing to the right.
 - \vec{Y}_{Thorax} : normal to the X and Z axis pointing forward
 - \vec{Z}_{Thorax} : parallel to the line between the points $P_1 = \frac{PX+C7}{2}$ and $P_2 = \frac{T8+IJ}{2}$
- ii. Scapular Referential Frame
 - Center: AC.
 - \vec{X}_S : parallel to the line defined by AA - TS, pointing to the right.
 - \vec{Y}_S : normal to the plane defined by the x-axis and the AI-TS axis, pointing forward.
 - \vec{Z}_S : normal to the x and y axes, pointing upwards.
- iii. Humeral Referential Frame
 - Center: GHC.
 - \vec{X}_H : normal to the Y and Z axes, pointing to the right.
 - \vec{Y}_H : normal to the plane defined by GHC, EL and EM, pointing forwards.
 - \vec{Z}_H : parallel to the line between the points $P_3 = \frac{EL+EM}{2}$ and GHC, pointing upwards.
- iv. Cone Referential Frame
 - Center: GC.

- \vec{X}_{Cone} : parallel to GHC-GC, pointing to the right.
- \vec{Y}_{Cone} : parallel to $\vec{Z}_{Thorax} \times \vec{X}_{Cone}$ pointing forward.
- \vec{Z}_{Cone} : parallel to $\vec{X}_{Cone} \times \vec{Y}_{Cone}$ pointing upward.

The joints coordinates coincided with the bone-fixed frames. An Euler angle sequence of $X - Y - Z$ was used for both the sternoclavicular and the acromioclavicular joints, but $Z - Y - Z$ was considered for the GH joint.

The MS model equations of motion were derived using the Lagrange's equations by considering bones as rigid bodies, joints as ideal mechanical joints (with no translations), and muscles as massless elastic strings. Mass and inertial properties were attributed to the bone segments according to (Garner & Pandy, 2001). The muscles moment arms were obtained using the geometric definition of moment arm and crosschecked with the tendon excursion method (Ingram, Engelhardt, Farron, Terrier, & Müllhaupt, 2015). To this end, the muscles paths were approximated using the obstacle set method (Garner & Pandy, 2000). The origins/insertions, via points, and wrapping objects of 42 muscles spanning the upper extremity joints were defined from the MRI scans. They included subclavius, serratus anterior upper/middle/lower, trapezius C1-C6/C7/T1/T2-T7, elevator scapulae, rhomboid minor/major T1-T2/major T3-T4, pectoralis minor/major clavicular/major sternal/major ribs, latissimus dorsi thoracic/lumbar/Iliac, deltoid clavicular/acromial/scapular, supraspinatus, infraspinatus, subscapularis, teres minor/major, coracobrachialis, triceps brachii long/medial/lateral, biceps brachii short/long, brachialis, brachioradialis, supinator, pronator teres, flexor carpi radialis/ulnaris, and extensor carpi radialis long/radialis berris/ulnaris. Each muscle group of the model could be represented by up to 20 strings (Figure 23b).

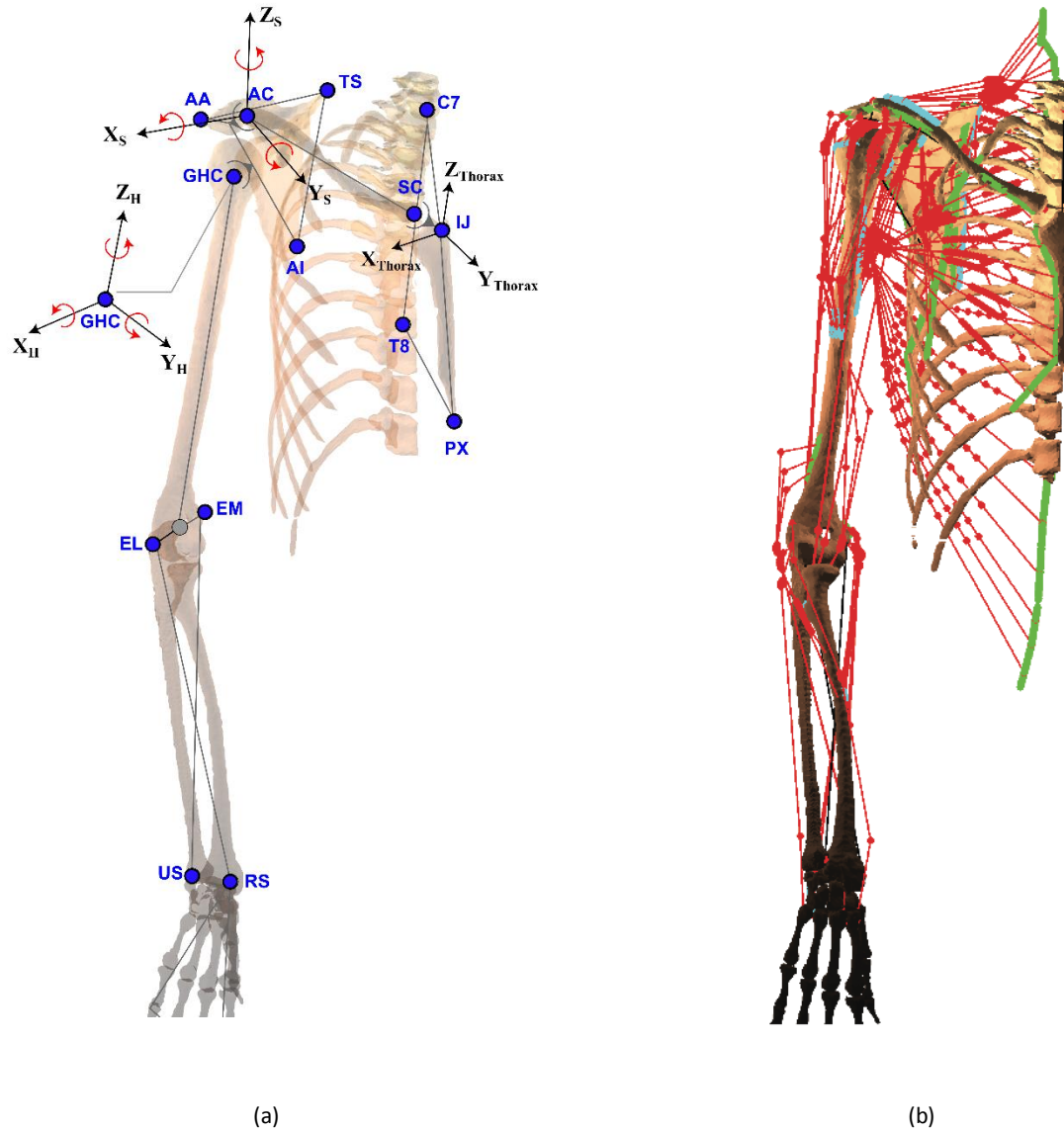


Figure 23: (a) bone fixed frames and joint coordinate systems. (b) MS model with 42 muscle groups represented by strings (Ehsan Sarshari, 2018)

The measured motion was reconstructed in terms of the generalized coordinates using multi-segment optimization providing the GH joint kinematics. A method developed in (E. Sarshari et al., 2019) was applied to estimate GH, TS, and AI trajectories, given that they were masked under thick layers of soft tissues and therefore not traceable using videogrammetry.

The equations of motion provided eleven second order differential equations for the resulting generalized coordinates obtained from the multi-segment optimization. There were more unknowns (42 muscles times number of strings per muscle) than the number of equations. Therefore, we casted an EMG assisted load sharing (EALS) to find the muscle forces and consequently the GH joint reaction forces. The EALS found the muscles forces such that the sum of squared muscle stresses was minimized while the muscle forces were within their lower and upper bounds and a so-called stability constraint was satisfied. The muscle lower and upper bounds were defined as zero and $k \cdot a$, where k was the Fick constant (E. Sarshari et al., 2019) and a was PCSA of muscles obtained for a similar subject from (E. Sarshari et al., 2019). For muscles with measured EMG signals, $\pm 5\%$ of their EMG-based muscle forces from a musculotendon model were used as the lower and upper bounds. A validated Hill-type musculotendon model was used to estimate the muscle forces associated to the measured EMG signals (Ehsan Sarshari, 2018). The stability constraint also restricted the GH joint reaction force to always point toward a cone approximating the glenoid fossa.

4.3.3.3 Simulation of the musculoskeletal model

Three patients (67 to 74 years old, 1M/2F) planned for total shoulder arthroplasty (TSA) were included. The measured kinematics were scaled for each patient according to their height. The measured EMG data were scaled according to each patient's body weight. The MS model also featured scaling routines that allowed scaling the segments' inertia, lengths, and muscle architectures according to gender, weight, and height of each patient (Figure 24). The PCSA values of rotator cuff muscles were also adapted in the scaled MS model to account for degenerations measured on preoperative CT scans of each patient. The glenoid implant version/inclination angles were also obtained from the preoperative planning software for each patient to adapt the corresponding parameters in the MS model. We then replicated the three scaled measured activities using the scaled/adapted MS model based on each patient. The GH joint reaction force and kinematics were obtained. The following outputs were also obtained from the MS model in order to transform the GH joint reaction force and kinematics to consistent values for the test setup (See Next Section).

- ${}_{\text{Cone}}^{\text{Scapula}}R_0$: rotation matrix from cone to scapula coordinate system.
- ${}_{\text{Scapula}}^{\text{Thorax}}R_0$: rotation matrix from scapula to thorax coordinate system.
- ${}_{\text{Humerus}}^{\text{Thorax}}R(t)$ and ${}_{\text{Scapula}}^{\text{Thorax}}R(t)$: time varying rotation matrix from humerus and scapula to thorax coordinate system.
- ${}_{\text{Thorax}}F_{GH}$: GH joint reaction force in the thorax coordinate system.

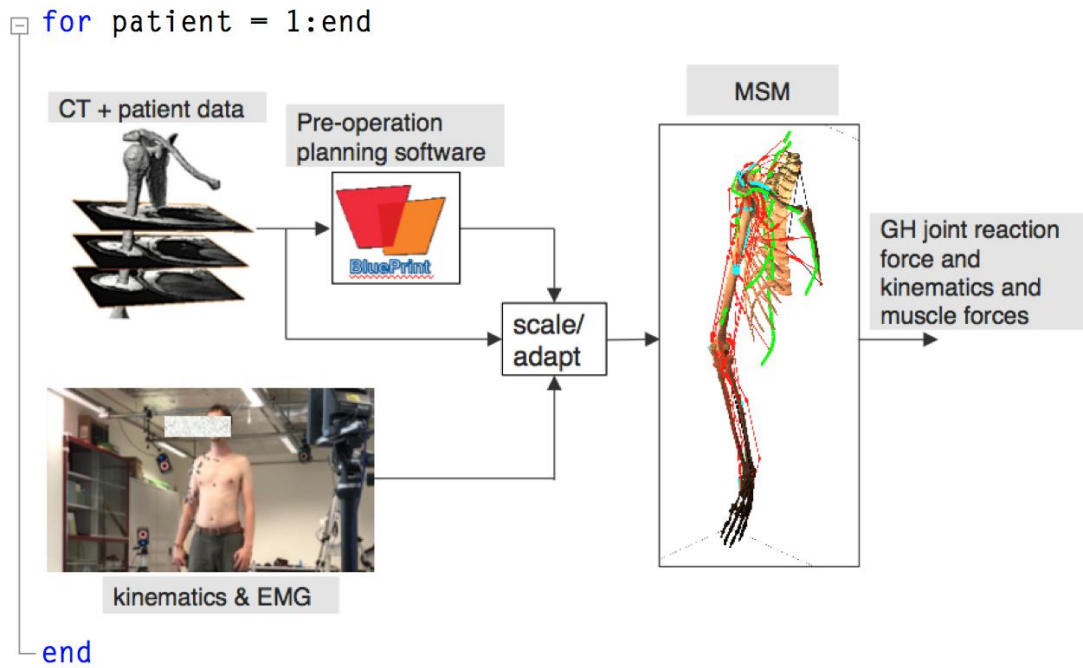


Figure 24: Scaling/adapting the MS model (MSM) to each patient and simulation of each measured activity (Ehsan Sarshari, Boulanaache, Becce, Farron, & Terrier, 2019).

4.3.4 Input data processing

To evaluate the prosthetic stability, it was important to know the orientation of the glenoid implant with respect to the humeral head implant under specific loading. Nonetheless the MS model, had its referential frames at the level of the bones. Here an approach was proposed to convert the bone-based referential frames of the MS model to the referential of the respective prosthesis proposed on Figure 26. This allowed expressing internal-external rotation angle (α) and abduction-adduction angle (β) and the force acting on the implant (${}_{HI}F_{GH}$) in the humeral implant frame (HI), in order to perform robotic simulation (Figure 25).

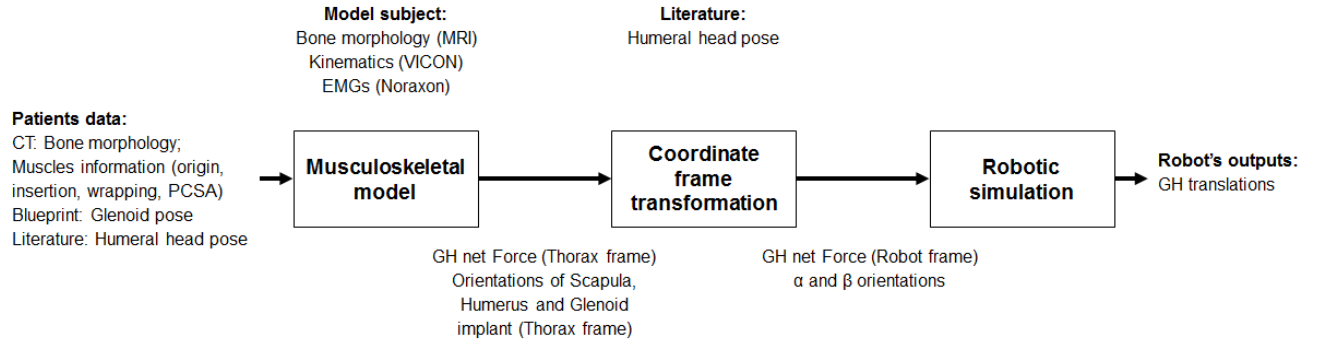


Figure 25: Schema block of the successive transformations of the data recorded from the patients, through the MS model, their conversion through the software for the "Coordinate frame transformation" and finally their use to control robotic simulations and record the GH translations for specific patients and tasks.

HI was defined as:

- P_{HI} : the plane of the humeral head prosthesis, defined by the planar surface lying at the back of the metallic hemisphere.
- Z-axis (Z_{HI}) the normal vector to P_{HI} pointing in the lateral direction (away from the glenoid).
- Y-axis (Y_{HI}) the flipped projection of the Y-axis of the thorax (Y_T) onto the plane P_{HI} .
- $\vec{X}_{HI} = \vec{Y}_{HI} \times \vec{Z}_{HI}$
- The origin was GHC .

And the referential of the glenoid implant (GI) was defined as:

- Z-axis (Z_{GI}) parallel to X_{Cone} , pointing towards the humeral head.
- Y-axis (Y_{GI}) the axis going from the most superior boarder of the glenoid implant toward the most inferior boarder. This axis was projected on the glenoid implant plane.
- $\vec{X}_{GI} = \vec{Y}_{GI} \times \vec{Z}_{GI}$
- The origin O_{GI} was the center of the implant, defined as the point of the glenoid surface with the smallest Z_{GI} value.

Note: Both referentials were made orthonormal (by normalization).

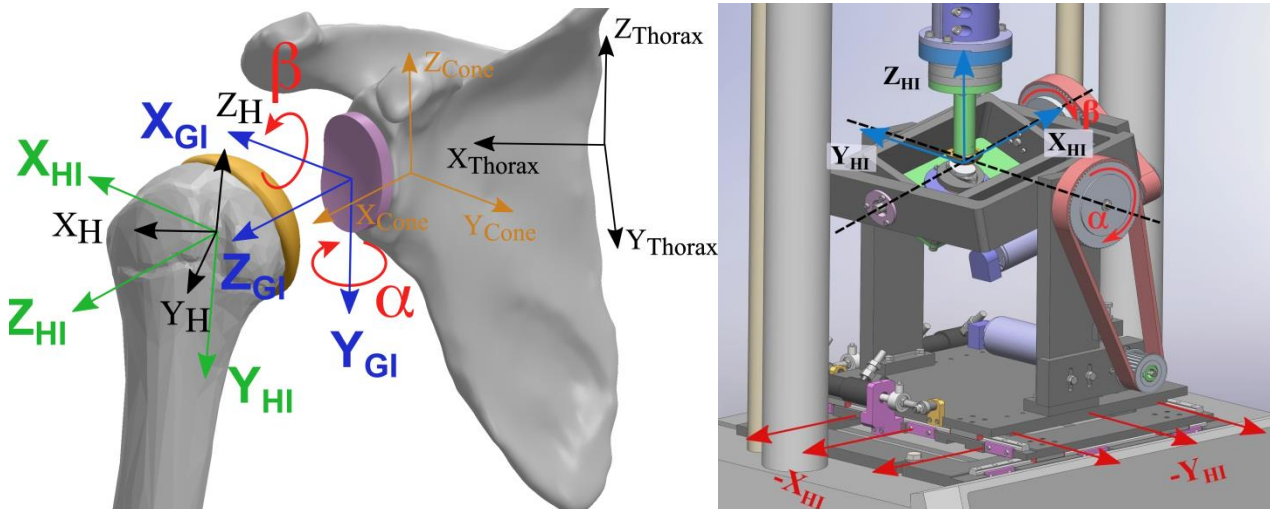


Figure 26: (a) Prosthetic referential frame of the Humeral Implant (HI) and of the glenoid implant (GI); (b) Prosthetic referential transposed to the robotic simulator's axes.

The rotation matrix between the two prosthetic components was expressed as the product between two rotation matrices:

$${}^{HI}_{GI}R(t) = {}^{HI}_{Thorax}R(t) \cdot {}^{GI}_{Thorax}R(t)^{-1} \quad (1)$$

${}^{HI}_{Thorax}R(t)$ was found as follow:

$${}^{HI}_{Thorax}R(t) = {}^{HI}_{Humerus}R_0 \cdot ({}^{Thorax}_{Humerus}R(t))^{-1} \quad (2)$$

With ${}^{HI}_{Humerus}R_0$ the rotation matrix from the humeral referential frame to the humeral implant referential frame.

The orientation of the humeral head prosthesis with respect to the humeral referential was defined by the inclination (γ) and the torsion angle (v). The inclination angle indicating the rotation of the humeral head around X_{HI} and the torsion angle around Z_H . Based on the surgical planning, the inclination angle (Figure 27b), was the same for every patient $\gamma_{P1} = \gamma_{P2} = \gamma_{P3} = 132.5^\circ$.

Based on the literature (Patil, Sethi, & Vasudeva, 2016), the Torsion angle (Figure 27a) of the humeral head implant was assumed to be $v=64\pm 7^\circ$ for every patient.

Therefore, the rotation matrix from the humeral referential frame to the humeral implant referential frame was approximated as:

$${}^{HI}_{Humerus}R_0 = R_\gamma \cdot R_{ax} \cdot R_v = \begin{pmatrix} 1 & 0 & 0 \\ 0 & \cos(\gamma - 90) & -\sin(\gamma - 90) \\ 0 & \sin(\gamma - 90) & \cos(\gamma - 90) \end{pmatrix} \cdot \begin{pmatrix} 0 & -1 & 0 \\ 0 & 0 & -1 \\ 1 & 0 & 0 \end{pmatrix} \cdot \begin{pmatrix} \cos(v) & -\sin(v) & 0 \\ \sin(v) & \cos(v) & 0 \\ 0 & 0 & 1 \end{pmatrix} \quad (3)$$

And ${}^{GI}_{Thorax}R(t)$ was found as follows:

$${}^{GI}_{Thorax}R(t) = {}^{GI}_{Cone}R_0 \cdot {}^{Cone}_{Thorax}R(t) \quad (4)$$

With:

$${}^{GI}_{Cone}R_0 = \begin{pmatrix} 0 & -1 & 0 \\ 0 & 0 & -1 \\ 1 & 0 & 0 \end{pmatrix} \quad (5)$$

And:

$${}^{Cone}_{Thorax}R(t) = ({}^{Thorax}_{Cone}R_0)^{-1} \cdot {}^{Thorax}_{Scapula}R_0 \cdot ({}^{Thorax}_{Scapula}R(t))^{-1} \quad (6)$$

$${}^{GI}_{Thorax}R(t) = {}^{GI}_{Cone}R_0 \cdot ({}^{Thorax}_{Cone}R_0)^{-1} \cdot {}^{Thorax}_{Scapula}R_0 \cdot ({}^{Thorax}_{Scapula}R(t))^{-1} \quad (7)$$

Using Eq.1-7, ${}^{HI}_{GI}R(t)$ was calculated:

$${}^{HI}_{GI}R(t) = R_\gamma \cdot R_{ax} \cdot R_v \cdot ({}^{Thorax}_{Humerus}R(t))^{-1} \cdot {}^{Thorax}_{Scapula}R(t) \cdot ({}^{Thorax}_{Scapula}R_0)^{-1} \cdot {}^{Thorax}_{Cone}R_0 \cdot ({}^{GI}_{Cone}R_0)^{-1} \quad (8)$$

α and β were found from ${}^{HI}_{GI}R(t)$ using the Euler sequence around the Z, Y, X axes. The first rotation (around Z-axis) was neglected since the glenoid implant was centered and aligned under the humeral head and the rotations around its center-line had no effect on the geometry of contact. Then the rotation around the Y-axis corresponded to the angle α . The one around the X-axis corresponded to the angle β . Matlab function `rotm2eul(${}^{HI}_{GI}R(t)$, 'ZYX')` was used for this calculation.

Finally, the forces were provided in the thorax referential frame and needed to be rotated to the humeral implant referential frame (HI):

$${}^{HI}F_{GH}(t) = {}^{HI}_{Thorax}R(t) \cdot {}^{Thorax}F_{GH}(t) = R_\gamma \cdot R_{ax} \cdot R_v \cdot ({}^{Thorax}_{Humerus}R(t))^{-1} \cdot {}^{Thorax}F_{GH}(t) \quad (9)$$

Through a customized Matlab script these forces were then converted into the coefficients of a Fourier series of order 20 and converted automatically in code for the controller of the linear actuators.

Similarly, two other text-files were generated with the instructions for the DC motors, to be imported into custom-made Labview control software.

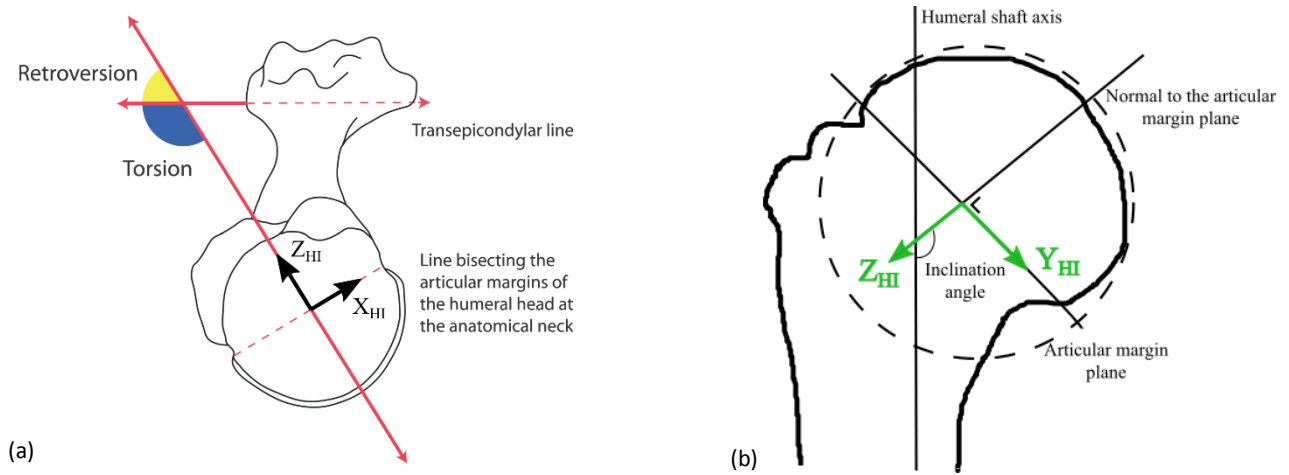


Figure 27: (a) Representation of the torsion angle (ν). Image courtesy from N. Roach & Al. 2012 (N. T. Roach et al., 2012) (b) Representation of the inclination angle (γ)

4.3.5 Robotic simulation of the GH translations of the patients

Initialization phase- In this phase GI frame was aligned and centered with HI frame. The simulator was first equipped with the same prosthesis as the one installed in the patient. Second, the glenoid implant was set to the neutral orientation $\{\alpha = 0^\circ; \beta = 0^\circ\}$ and manually centered under the center of the humeral head prosthesis (while using displacement control on all the actuators). Third, a finer centering was performed by switching on the Axial actuator to a force control until contact was achieved, with a value of ${}_{HI}F_{GH,z}(t) = -100$ N. Next, the X and Y-axis actuators were switched to force control with a force of 0 N each, leaving the glenoid implant free to align its lower point under the center of the humeral head implant. Once no further movement was observed, the X-Y displacements were recorded as the new origin of frame HI and used as the starting point for every recording sequence for that patient. Then the actuators were switched back to displacement control, the humeral head was raised about 1 cm above the glenoid surface and the glenoid was centered underneath.

Simulation phase- In this phase the task to simulate was first selected, then reproduced using a quasi-static simulation. The signal processing and control strategy developed in Chapter 3, section 3.3.6 for dynamic tests was used here. Each force sequence was described using a series of Fourier of order 20. Since every movement started with the UL at neutral position and finished in the same position, forces and orientations were assumed periodic. In order to avoid ripples between two repetitions of the sequence, each sequence was repeated three times, inserting a 1 second linear transition between the last point of a cycle and the first one of the next. Next the data, sampled uniformly at 100 Hz, were smoothed with a truncated Gaussian average sliding window of 15 samples. The first and last cycles were then truncated, and the remaining pattern was reconstructed with Series of Fourier of order 20. In the previous Chapter, this signal was used to control a dynamic simulation. However, due to the presence of larger movements in this simulation, a dynamic simulation would be affected by the inertia of the machine, which is very different than the inertia of a natural shoulder. To avoid this problem, the simulation was performed in a quasistatic way, decomposing the signal in N timeframes and assuming that the equilibrium of the forces must be reached on every frame. Therefore, the forces were down-sampled to 5 Hz using cubic spline interpolation resulting in N time samples of force (${}_{HI}F_{x,i,N}$, ${}_{HI}F_{y,i,N}$, ${}_{HI}F_{z,i,N}$) for each patient and each task.

The GH orientations α and β , by deriving from the motions simulated in the MS model, were observed to be natively smooth. Being read by the customized Labview interface used for the rotatory motors, no conversion into a Fourier Series was needed. Therefore they were directly down-sampled to 5 Hz using cubic spline interpolation resulting in the GH orientation commands GH orientations ($\alpha_{i,N}$, $\beta_{i,N}$).

During the simulation, the rotary motors actuating α and β were always controlled in displacement control using their own encoders, as described in the Chapter 3, while the linear actuators were used in displacement control during the initialization phase, and in force control during the simulation phase controlling the force ${}_{HI}F_{GH}(t)$. Starting from the neutral position, with all the linear actuators in displacement control, the humeral head was set 1 cm above the glenoid surface and the glenoid implant was centered underneath. Then, the humeral head was lowered to contact, by switching the axial actuator to apply a constant force of -10N. After contact, the control was left some seconds to stabilize the integrator component. Next the vertical force was increased progressively until it reached and maintained $F_{z,i}$. Next, the Y linear actuator was set to apply a constant force $F_{y,i}$, followed by the X linear actuator, set to $F_{x,i}$. The joint was left free to move under these forces, until a stable position was found or for at least 30 seconds. Then the XY position was manually

recorded, and the GH orientation was increased by $\{+0.2 \cdot \alpha_i; +0.2 \cdot \beta_i\}$. The change in orientation was performed very slowly, by decreasing the maximum angular speed of the actuator to 0.04054 [Deg/sec]. After reaching the new orientation, the orientation was maintained for at least 30 seconds, to let the system's dynamic process settle down. Then the XY position was recorded. Next the platform was rotated, left 30 seconds to settle, the new XY position was recorded and the process was repeated until the platform reached $\{0.8 \cdot \alpha_i; 0.8 \cdot \beta_i\}$, then the angular steps were shortened to $\{+0.1 \cdot \alpha_i; +0.1 \cdot \beta_i\}$ until $\{\alpha_i; \beta_i\}$. After recording the position in this last orientation, the axial actuator was shifted to displacement control, and the humeral head was raised above the glenoid surface. The XY actuators were returned to displacement control and re-centered under the humeral head; the GH-orientation was restored to the neutral orientation and the process was repeated for the next time-point $i+1$, until all the time points were tested.

In case of GH dislocations, the orientations were recorded, and the simulation stopped for these orientations. To minimize the risk of damaging or consuming the prosthesis boarders, configurations that were considered as potentially unstable were tested last.

4.3.6 Estimation of GH translation

In order to convert the XY translations recorded by the robotic actuators, to the translations happening over the glenoid implant surface, a conversion equation was developed. In order to make this computation simpler, the surface of the glenoid was assumed planar instead of curved.

Modelling the glenoid surface by an inclined plane, one described three referential frames: $R = \langle e_x, e_y, e_z \rangle$ the referential of the glenoid plane, before applying any rotation; $R' = \langle e'_x, e'_y, e'_z \rangle$ the referential of the glenoid plane, after applying a rotation α around e_y ; $R'' = \langle e''_x, e''_y, e''_z \rangle$ the referential of the glenoid plane R , after applying a rotation α around e_y , followed by a rotation β around e'_x .

Consequently, for a point in space \vec{p} :

$$\vec{p}'' = M_\beta \vec{p}' = M_\beta M_\alpha \vec{p} = \begin{pmatrix} 1 & 0 & 0 \\ 0 & \cos(\beta) & -\sin(\beta) \\ 0 & \sin(\beta) & \cos(\beta) \end{pmatrix} \begin{pmatrix} \cos(\alpha) & 0 & \sin(\alpha) \\ 0 & 1 & 0 \\ -\sin(\alpha) & 0 & \cos(\alpha) \end{pmatrix} \begin{pmatrix} p_x \\ p_y \\ p_z \end{pmatrix} \quad (10)$$

The sensors of the robot measured p_x'' and p_y'' . Therefore \vec{p} was obtained by inverting the matrix:

$$\vec{p} = (M_\beta M_\alpha)^{-1} \vec{p}'' = \begin{pmatrix} \cos(\alpha) & \sin(\alpha)\sin(\beta) & -\sin(\alpha)\cos(\beta) \\ 0 & \cos(\beta) & \sin(\beta) \\ \sin(\alpha) & -\cos(\alpha)\sin(\beta) & \cos(\alpha)\cos(\beta) \end{pmatrix} \begin{pmatrix} p_x'' \\ p_y'' \\ p_z'' \end{pmatrix} \quad (11)$$

Finally, assimilating the glenoid implant surface to an inclined plane, with inclinations α and β , the value of p_z'' was extracted from the values of p_x'' , p_y'' and the equation of the plane. The equation of the plane was built as:

$$l_z = a \cdot l_x + b \cdot l_y + c \quad \text{where } a, b, c \text{ three constants and } l_x, l_y, l_z \text{ the coordinates of a point in the plane}$$

Solving for a, b, c , the values of three points in the plane were necessary. The three following points were employed:

$$\vec{l}_0 = (0 \ 0 \ 0)^t \quad \text{then} \quad 0 = a \cdot 0 + b \cdot 0 + c \quad c = 0 \quad (12)$$

$$\vec{l}_1 = M_\beta M_\alpha \cdot \begin{pmatrix} 0 \\ 1 \\ 0 \end{pmatrix} = \begin{pmatrix} 0 \\ \cos(\beta) \\ \sin(\beta) \end{pmatrix} \quad \text{then} \quad \sin(\beta) = a \cdot 0 + b \cdot \cos(\beta) + 0 \quad b = \frac{\sin(\beta)}{\cos(\beta)} = \tan(\beta) \quad (13)$$

$$\vec{l}_2 = M_\beta M_\alpha \cdot \begin{pmatrix} 1 \\ 0 \\ 0 \end{pmatrix} = \begin{pmatrix} \cos(\alpha) \\ \sin(\alpha)\sin(\beta) \\ -\sin(\alpha)\cos(\beta) \end{pmatrix} \quad \text{then} \quad -\sin(\alpha)\cos(\beta) = a \cdot \cos(\alpha) + \tan(\beta) \cdot \sin(\alpha)\sin(\beta) \quad (14)$$

$$a = \left(-\sin(\alpha)\cos(\beta) - \frac{\sin(\beta)}{\cos(\beta)} \cdot \sin(\alpha)\sin(\beta) \right) / \cos(\alpha) = -\tan(\alpha) \cdot (\cos(\beta) + \sin(\beta) \cdot \tan(\beta)) \quad (15)$$

$$\text{Finally, } p_z'' = \tan(\beta) \cdot p_y'' - \tan(\alpha) \cdot (\cos(\beta) + \sin(\beta) \cdot \tan(\beta)) \cdot p_x'' \quad (16)$$

and

$$\vec{p} = \begin{pmatrix} \cos(\alpha) & \sin(\alpha)\sin(\beta) & -\sin(\alpha)\cos(\beta) \\ 0 & \cos(\beta) & \sin(\beta) \\ \sin(\alpha) & -\cos(\alpha)\sin(\beta) & \cos(\alpha)\cos(\beta) \end{pmatrix} \begin{pmatrix} p_x'' \\ p_y'' \\ \tan(\beta) \cdot p_y'' - \tan(\alpha) \cdot (\cos(\beta) + \sin(\beta) \cdot \tan(\beta)) \cdot p_x'' \end{pmatrix} \quad (16)$$

Where p_x and p_y corresponded to the x and y displacements of the humeral head over the glenoid surface.

Since the surface of the glenoid prosthesis was slightly curved instead of planar, the maximum error on p_x and p_y caused by this simplification was computed on the CAD model (Figure 28) of one of the larger glenoid implants (size M) using Pythagoras theorem to compute the true : $p_{x,r} = \sqrt{p_x^2 + p_z^2}$ and $p_{y,r} = \sqrt{p_y^2 + p_z^2}$ with $p_{x,r}$ and $p_{y,r}$ being the linear distance between GC in the worst-case position of the humeral head on their respective axes. Using the measurements from the CAD file, the error along the x-axis (err_x) was of $err_x = \sqrt{12.6^2 + 2.5^2} - 12.6 = 0.2 \text{ mm}$ and along the y-axis (err_y) of $err_y = \sqrt{16.9^2 + 5.2^2} - 16.9 = 0.8 \text{ mm}$.

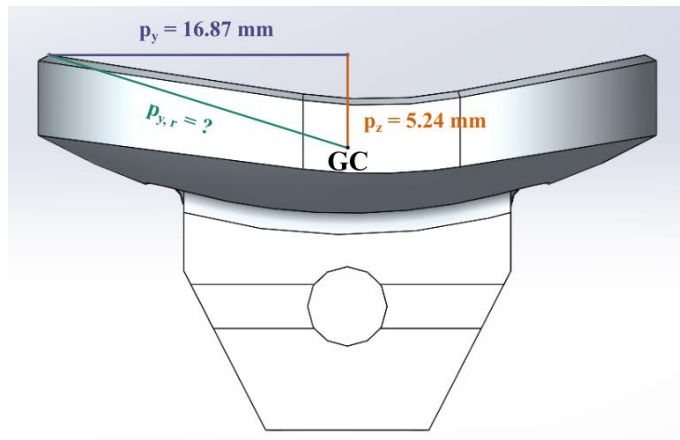


Figure 28: Side view of an M35 glenoid implant. $p_{y,r}$ indicating the distance between GC and the boardermost possible position of the humeral head on the y-axis. p_y and p_z its y and z components, as they would be recorded by the robot's sensors.

4.4 Results

The motions of patient P3 were simulated for three different tasks ($task_{abd}$, $task_{hand}$, $task_{should}$), resulting in the GH forces presented in Figure 29 (left). Those forces were then converted to the HI referential frame, resulting in the force commands of the robotic simulator, as shown in Figure 29 (right) and the implant's relative orientations α and β , as displayed in Figure 30 and reported in Table 5, Table 6, and Table 7. Due to the observation of large marks on the prosthesis in the presence of repeated high forces, and to protect the equipment, specific points in the simulation were not simulated if the compressive force F_z was higher than 750N.

Next, the inter-patient variability of $task_{hand}$ was evaluated on patients P1, P2 and P3 (Table 3, Table 4, Table 5).

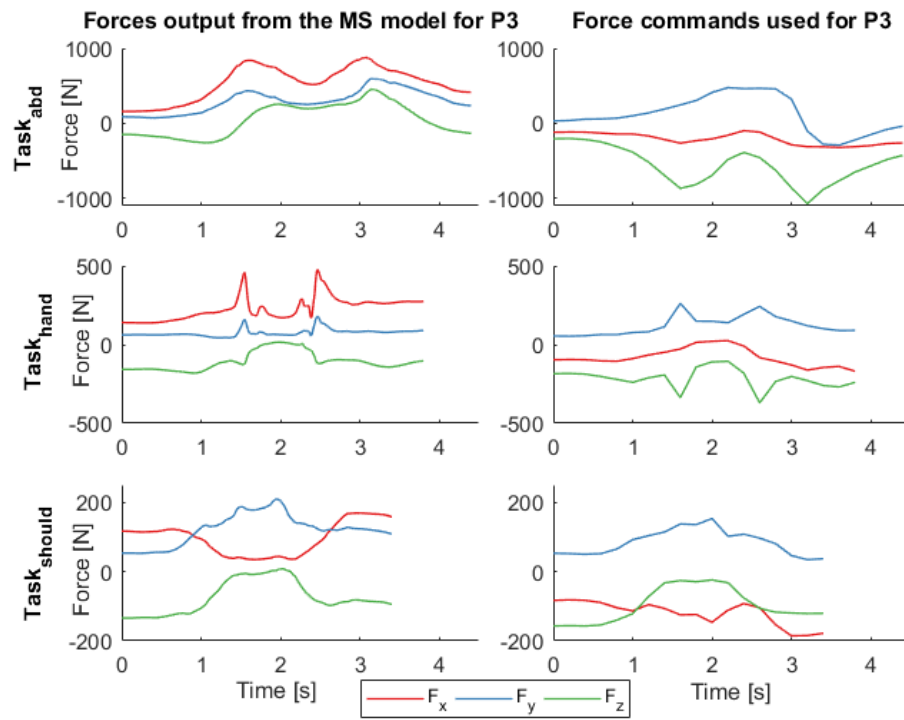


Figure 29: The left column presents the GH internal force as simulated by the MS model for patient P3 during task_{abd} , $\text{task}_{\text{hand}}$ and $\text{task}_{\text{should}}$. The right column presents the force commands for the robotic simulation obtained for patient P3 during those same tasks, expressed in the HI referential frame.

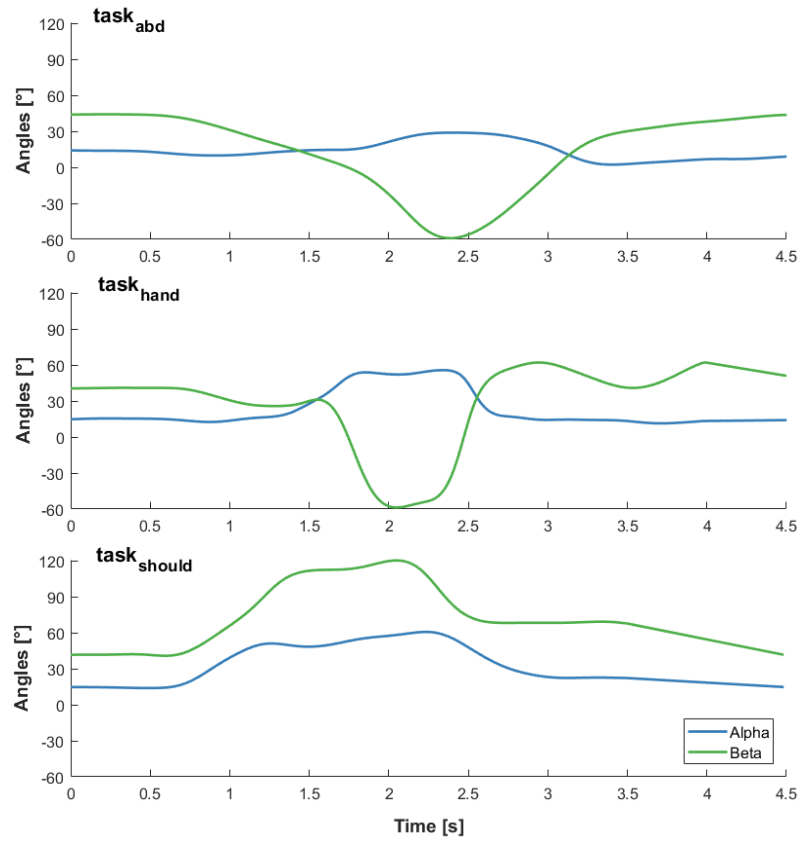


Figure 30: Prosthetic relative orientations obtained for patient P3 during task_{abd}, task_{hand} and task_{should}

Patients P1 to P3 were then simulated on task_{hand}. The measurements from the robotic simulation were then converted into the GI referential frame. The humeral head was considered as a point contact on its surface and its motions were presented in Table 3, Table 4 and Table 5. For all the simulations, the experiment had to be stopped before reaching the target angle, due to joint dislocation.

Table 3: GH translations (in mm) for patient P1, task_{hand}. “Sup. Lux.” indicates a case of dislocation directed superiorly. “Pos. Lux.” indicates a case of dislocation in the posterior direction. “Pos. Sup. Lux.” indicates a case of dislocation between the posterior and superior direction. “Sup. Lux. Slow” indicates a case of dislocation directed superiorly, that happened very slowly, 60 seconds after the position was reached. For every time step, the target values of α and β were defined, and the GH translations were recorded for different ratios of the target orientations, starting from $\alpha=0^\circ$, $\beta=0^\circ$ and increasing until a dislocation was observed.

F _x [N]	F _y [N]	F _z [N]	α	β	GH translations for patient P1, task _{hand}															
					0%·{α;β}		20%·{α;β}		40%·{α;β}		60%·{α;β}		80%·{α;β}		90%·{α;β}		100%·{α;β}			
					X	Y	X	Y	X	Y	X	Y	X	Y	X	Y	X	Y		
-387.0	-181.0	37.8	8.95	46.12	-3.09	0.30	-2.93	3.86	-2.27	8.98	Sup. Lux.									
-383.2	-179.9	35.7	9.62	46.50	-3.23	0.13	-2.85	4.08	-2.37	10.09	Sup. Lux.									
-386.4	-184.1	34.2	9.52	46.68	-3.26	0.14	-2.98	4.14	-2.41	9.81	Sup. Lux.									
-400.0	-191.4	36.4	9.01	46.66	-3.38	0.14	-3.12	4.15	Sup. Lux. Slow											
-427.1	-175.5	31.0	6.98	43.77	-3.22	0.13	-3.11	3.76	-2.64	8.43									Sup. Lux.	
-495.6	-134.3	59.5	6.63	36.12	-2.63	0.30	-2.55	3.33	-2.10	7.00									Sup. Lux.	
-485.6	-104.2	84.7	7.43	31.80	-2.31	0.31	-2.22	3.00	-1.65	6.34	Sup. Lux.									
-470.4	-120.7	131.3	9.62	33.21	-2.60	1.50	-2.24	4.54	-1.52	8.56	Sup. Lux.									
-718.3	-142.6	368.7	21.18	37.38	-2.93	3.49	-1.73	7.76	Sup. Lux.											
-545.5	-15.7	347.3	36.95	0.89	-1.45	3.48	1.50	3.33	5.53	3.51									Ant. Lux.	
-315.8	24.2	293.5	40.47	-32.29	-0.51	3.65	2.59	1.08	7.38	-1.31									Ant. Lux.	
-327.0	5.5	288.2	41.40	-30.86	-0.79	3.56	2.38	1.12	7.12	-1.19	Ant. Lux.									
-430.9	-5.6	307.2	39.60	-9.66	-1.09	3.24	1.93	2.94	6.62	2.21	Ant. Lux.									
-671.5	-237.3	286.1	13.63	49.25	-4.20	3.01	Sup. Lux.													
-501.6	-339.2	254.2	8.24	64.91	Pos. Lux.		Sup. Lux.													
-366.3	-301.6	185.8	8.07	66.69	Pos. Lux.		Sup. Lux.													
-591.8	-410.7	126.3	8.32	57.95	Pos. Lux.		Pos. Lux.		Sup. Lux.											
-658.6	-316.1	80.5	7.71	48.17	Pos. Lux.		Pos. Sup. Lux.													
-653.7	-277.7	58.2	5.60	46.42	Pos. Lux.		-4.42	4.70	Pos. Sup. Lux.											
-647.9	-387.9	59.2	6.08	56.09	Pos. Lux.		Pos. Sup. Lux.													

Table 4: GH translations (in mm) for patient P2, $\text{task}_{\text{hand}}$. “Sup. Lux.” indicates a case of dislocation directed superiorly. “Pos. Lux.” indicates a case of dislocation in the posterior direction. “Pos. Sup. Lux.” indicates a case of dislocation between the posterior and superior direction. “Ant. Lux.” indicates a case of dislocation in the anterior direction. “Ant. Sup. Lux.” indicates a case of dislocation between the anterior and superior direction. “Sup. Lux. Slow” indicates a case of dislocation directed superiorly, that happened very slowly, 60 seconds after the position was reached. For every time step, the target values of α and β were defined, and the GH translations were recorded for different ratios of the target orientations, starting from $\alpha=0^\circ$, $\beta=0^\circ$ and increasing until a dislocation was observed.

F _x [N]	F _y [N]	F _z [N]	α	β	GH translations for patient P2, task _{hand}													
					0%·{α;β}		20%·{α;β}		40%·{α;β}		60%·{α;β}		80%·{α;β}		90%·{α;β}		100%·{α;β}	
					X	Y	X	Y	X	Y	X	Y	X	Y	X	Y	X	Y
-310.81	-190.04	29.21	6.99	45.33	-3.8	0.18	-5.33	3.26	Sup. Lux.									
-304.33	-184.47	26.14	7.57	45.75	-3.49	0.03	-5.44	2.84	Sup. Lux.									
-303.93	-184.53	29.91	7.50	45.88	-3.73	0.20	-5.10	3.35	Sup. Lux.									
-318.41	-195.54	38.42	7.06	45.76	-3.94	0.29	-5.28	3.69	Sup. Lux.									
-363.48	-194.92	42.05	4.99	43.16	-3.57	0.12	-4.52	3.19	Sup. Lux. Slow									
-405.03	-163.38	68.78	5.39	35.75	-2.83	0.21	-3.19	2.89	-2.83	0.21	Sup. Lux.							
-393.25	-138.81	86.11	6.90	32.20	-2.37	0.33	-2.47	2.85	-2.37	0.33	Sup. Lux.							
-390.91	-166.13	119.24	10.41	33.94	-2.87	0.80	-2.92	3.79	-2.87	0.80	Sup. Lux.							
-688.96	-314.77	319.75	23.14	40.79	-5.20	3.78	-4.23	8.47	Sup. Lux.									
-672.90	-117.80	395.05	41.80	6.61	-2.80	4.39	0.45	5.10	Ant. Sup. Lux.									
-374.47	28.00	378.47	47.44	-34.52	0.01	3.95	5.63	3.25	Ant. Lux.									
-383.72	25.92	375.15	48.28	-31.90	0.33	4.52	7.30	3.97	Ant. Lux.									
-494.50	-58.42	343.84	44.82	-4.20	-0.81	4.12	2.99	4.13	Ant. Sup. Lux.									
-518.61	-314.47	219.95	16.65	49.83	Pos. Lux.		Pos. Sup. Lux.											
-383.20	-311.76	239.05	9.34	65.14	Pos. Lux.		Sup. Lux.											
-286.10	-287.47	178.81	7.92	67.60	Pos. Lux.		Sup. Lux.											
-403.34	-375.27	84.46	7.47	58.77	Pos. Lux.		Pos. Lux.		Sup. Lux.									
-498.60	-341.84	25.26	6.21	49.32	Pos. Lux.		Pos. Lux.		Pos. Sup. Lux.									
-522.50	-323.73	-4.27	4.17	47.50	Pos. Lux.		-6.02	3.46	Pos. Sup. Lux.									
-470.10	-386.49	26.18	5.06	56.76	Pos. Lux.		Pos. Lux.		Pos. Sup. Lux.									

Table 5: GH translations (in mm) for patient P3, task_{hand}. “Sup. Lux.” indicates a case of dislocation directed superiorly. “Ant. Lux” indicates a case of dislocation directed anteriorly. “Pos. Lux.” indicates a case of dislocation in the posterior direction. “Pos. Lux. S1” indicates a case of dislocation directed posteriorly that happened very slowly, 45 seconds after the position was reached. “Pos. Lux. S2”: indicates a case of dislocation directed posteriorly that happened very slowly, 90 seconds after the position was reached. “Pos. Lux. S3”: indicates a case of dislocation directed posteriorly that happened very slowly, 75 seconds after the position was reached. For every time step, the target values of α and β were defined, and the GH translations were recorded for different ratios of the target orientations, starting from $\alpha=0^\circ$, $\beta=0^\circ$ and increasing until a dislocation was observed.

F _x [N]	F _y [N]	F _z [N]	α	β	GH translations for patient P3, task _{hand}															
					0%·{α;β}		20%·{α;β}		40%·{α;β}		60%·{α;β}		80%·{α;β}		90%·{α;β}		100%·{α;β}			
					X	Y	X	Y	X	Y	X	Y	X	Y	X	Y	X	Y		
-185.0	-96.4	54.9	14.84	40.57	-2.12	0.35	-1.68	4.21	Sup. Lux.											
-183.1	-95.0	53.4	15.52	40.91	-2.21	0.46	-1.67	4.51	Sup. Lux.											
-187.2	-95.9	56.3	15.43	41.03	-2.19	0.41	-1.75	4.51	Sup. Lux.											
-202.8	-103.3	63.9	14.92	40.96	-2.44	0.91	-2.09	5.063	Sup. Lux.											
-221.3	-105.9	63.5	12.96	38.01	-2.25	0.71	-1.99	4.55	Sup. Lux. S1											
-239.7	-88.8	76.8	13.69	30.65	-2.16	1.13	-1.84	4.12	-1.08	3.93	Sup. Lux.		Sup. Lux.							
-210.5	-65.9	81.8	16.37	26.16	-2.05	1.25	-1.59	3.79	-0.38	6.46	0.73	9.80								
-193.0	-49.0	113.2	21.21	26.76	-1.96	1.95	-1.22	4.93	0.28	8.21	Sup. Lux.									
-336.7	-27.9	261.8	35.43	29.67	-1.83	3.66	Sup. Lux.													
-142.0	14.6	148.8	53.15	-18.53	-0.36	2.70	3.11	2.76											Ant. Lux.	
-109.8	21.1	148.5	52.44	-57.66	Sup. Lux.		3.80	0.25											Ant. Lux.	
-106.0	25.3	139.1	53.90	-54.82	Sup. Lux.		4.17	0.33											Ant. Lux.	
-181.6	-8.8	191.7	55.01	-30.21	Sup. Lux.		2.76	2.43											Ant. Lux.	
-369.8	-83.3	242.2	25.23	43.28	-2.09	3.47	Sup. Lux.													
-234.2	-104.4	177.6	16.60	58.70	Pos. Lux. S2		Sup. Lux.													
-202.8	-129.6	149.9	14.34	61.53	Pos. Lux.		Sup. Lux.													
-228.5	-161.7	119.5	14.47	53.19	Pos. Lux. S2		Sup. Lux.													
-260.0	-145.0	101.1	14.10	43.74	-2.94	2.16	Sup. Lux.													
-268.8	-138.5	89.1	12.13	41.73	-2.88	1.90	-3.02	6.77	Sup. Lux.											
-239.9	-169.2	90.3	11.79	51.31	Pos. Lux. S3		Sup. Lux.													

Additionally, the task_{abd}, task_{hand} and task_{should} were simulated for patients P3. The results are reported in Table 5, Table 6 and Table 7. For the task_{abd}, some specific time-points were not simulated due to the presence of compressive forces (F_z) higher than 750 N. Those time-points were labelled “EF” for excessive force.

Table 6: GH translations (in mm) for patient P3, task_{abd}. "EF" stands for "Excessive force" and describes situations where the axial force was higher than 750 N, posing a risk of damaging the prosthesis. "Sup. Lux." indicates a case of dislocation directed superiorly. "Ant. Lux." indicates a case of dislocation directed anteriorly. "Ant. Inf. Lux." indicates a case of dislocation with a direction that is between anterior and inferior. "Sup. Lux. Slow" indicates a case of dislocation directed superiorly that happened very slowly, 70 seconds after the position was reached. For every time step, the target values of α and β were defined, and the GH translations were recorded for different ratios of the target orientations, starting from $\alpha=0^\circ$, $\beta=0^\circ$ and increasing until a dislocation was observed.

F _x [N]	F _y [N]	F _z [N]	α	β	GH translations for patient P3, task _{abd}																		
					0%·{α;β}		20%·{α;β}		40%·{α;β}		60%·{α;β}		80%·{α;β}		90%·{α;β}		100%·{α;β}						
					X	Y	X	Y	X	Y	X	Y	X	Y	X	Y	X	Y					
-119.5	31.2	-205.4	14.15	43.99	-2.00	0.26	-1.80	4.74	-1.37	9.88	Sup. Lux.												
-116.0	37.6	-202.3	13.91	44.22	-2.18	0.31	-1.90	4.46	-2.02	1.18	Sup. Lux.												
-117.4	55.5	-215.6	13.60	44.08	-2.25	0.43	-2.04	4.96	Sup. Lux.														
-130.2	58.9	-246.9	11.96	42.89	-2.30	0.34	-2.20	4.73	Sup. Lux.														
-143.2	68.4	-309.5	10.16	38.53	-2.35	0.46	-2.27	4.38	Sup. Lux.														
-142.9	100.4	-384.7	10.11	31.20	-2.24	1.35	-2.09	4.41	-1.60	8.02	Sup. Lux.												
-168.2	139.2	-518.2	11.78	23.06	-2.37	1.80	-2.12	3.99	-1.24	6.35	-0.54	9.86							Sup. Lux.				
-216.4	190.2	-694.7	13.69	15.33	-2.84	2.16	-2.48	3.69	-1.22	5.15	-0.02	6.68							1.09	8.49	1.59	9.72	Sup. Lux.
-264.5	245.3	-868.0	14.57	6.72	EF	EF	EF	EF	EF	EF	EF	EF	EF	EF	EF	EF	EF	EF					
-231.6	305.5	-816.3	15.44	-3.50	EF	EF	EF	EF	EF	EF	EF	EF	EF	EF	EF	EF	EF	EF					
-207.6	412.9	-695.3	21.35	-22.43	-2.61	4.01	-1.24	3.27	0.77	0.91	3.20	-1.29	Ant. Lux.										
-158.9	475.7	-481.4	27.38	-48.53	-2.35	5.51	-0.14	1.93	3.29	-3.25	Ant. Lux.												
-97.8	462.6	-388.0	28.95	-58.96	-1.87	5.67	0.66	0.74	Ant. Inf. Lux.														
-117.5	466.9	-457.4	28.25	-49.50	-1.86	5.53	0.40	1.60	Ant. Inf. Lux.														
-205.6	459.9	-626.0	24.81	-29.48	-2.31	5.10	-0.72	3.44	2.33	0.30	Ant. Inf. Lux.												
-286.9	321.5	-861.2	17.90	-5.69	EF	EF	EF	EF	EF	EF	EF	EF							EF	EF	EF	EF	EF
-311.3	-104.1	-1071.6	6.72	16.67	EF	EF	EF	EF	EF	EF	EF	EF							EF	EF	EF	EF	EF
-313.6	-279.8	-882.0	2.31	27.58	EF	EF	EF	EF	EF	EF	EF	EF	EF	EF	EF	EF	EF	EF					
-321.9	-290.4	-766.5	3.66	32.06	EF	EF	EF	EF	EF	EF	EF	EF	EF	EF	EF	EF	EF	EF					
-311.1	-222.0	-651.3	5.26	35.60	-2.83	-2.34	-2.83	-0.42	-2.76	3.72	-2.97	8.49	Sup. Lux.										
-296.2	-149.2	-567.3	6.79	38.19	-3.29	-1.13	-3.12	1.78	-2.87	5.85	Sup. Lux.												
-269.6	-82.4	-483.6	6.97	40.65	-3.39	-0.38	-3.23	2.80	-3.09	7.44	Sup. Lux.												
-261.2	-36.4	-427.1	8.18	43.07	-3.61	-0.08	-3.36	3.87	Sup. Lux. Slow														

Table 7: GH translations (in mm) for patient P3, task_{should}. “Sup. Lux.” indicates a case of dislocation directed superiorly. “Pos. Lux.” indicates a case of dislocation in the posterior direction. “Pos. Sup. Lux.” indicates a case of dislocation between the posterior and superior direction. For every time step, the target values of α and β were defined, and the GH translations were recorded for different ratios of the target orientations, starting from $\alpha=0^\circ$, $\beta=0^\circ$ and increasing until a dislocation was observed.

F _x [N]	F _y [N]	F _z [N]	α	β	GH translations for patient P3, task _{should}													
					0%·{α;β}		20%·{α;β}		40%·{α;β}		60%·{α;β}		80%·{α;β}		90%·{α;β}		100%·{α;β}	
					X	Y	X	Y	X	Y	X	Y	X	Y	X	Y	X	Y
-157.0	-83.4	52.7	14.86	41.71	-1.71	0.29	-1.28	4.19	-0.46	8.60	Sup. Lux.							
-156.2	-81.7	51.7	14.65	41.84	-1.79	0.31	-1.36	4.21	-0.59	8.77	Sup. Lux.							
-157.1	-83.1	49.9	14.11	42.17	-1.87	0.37	-1.48	4.29	-0.74	8.91	Sup. Lux.							
-154.2	-89.6	51.6	14.44	40.92	-1.95	0.29	-1.69	4.20	-1.14	9.07	Sup. Lux.							
-140.0	-104.5	65.0	23.00	48.61	-2.28	0.68	-2.25	6.51	Sup. Lux.									
-121.5	-113.5	91.9	39.33	66.03	Pos. Lux		Sup. Lux		Sup. Lux									
-72.3	-95.5	103.4	50.39	88.14	Pos. Sup. Lux		Sup. Lux											
-32.9	-106.4	114.0	49.30	108.66	Sup. Lux													
-26.0	-125.0	137.3	49.51	112.53	Sup. Lux													
-29.4	-124.1	135.4	54.48	114.10	Sup. Lux													
-24.2	-146.3	152.7	57.57	119.84	Sup. Lux													
-32.5	-111.5	101.6	60.63	112.70	Sup. Lux													
-76.6	-92.5	107.7	55.41	83.56	Sup. Lux													
-106.3	-104.3	96.3	39.98	69.49	Pos. Sup. Lux		Sup. Lux											
-117.3	-153.7	80.5	28.41	68.34	Pos. Sup. Lux		Sup. Lux											
-119.6	-185.5	46.1	23.20	68.35	Pos. Lux.		Pos. Sup. Lux		Sup. Lux									
-121.2	-184.7	34.2	22.55	68.81	Pos. Lux.		Pos. Sup. Lux		Sup. Lux									
-120.6	-178.1	36.8	22.62	69.10	Pos. Lux.		Pos. Sup. Lux		Sup. Lux									

4.5 Discussion

A framework for the study and simulation of shoulder stability was built as a constructive combination of two different tools: (i) a patient-specific MS model that allows the estimation of GH forces and (ii) a custom-built robotic simulator where the estimated force was used to measure the GH translations. This combination allows getting a large number of simulated muscle strings, with corresponding forces and insertion points, through the patient-specific MS simulation, as well as, the mechanical behaviour that one would observe between two prosthetic components, through the robotic simulation. Additionally, in this study, the simulations were based on the surgical planning of a set of patients from the local university hospital (CHUV) in an attempt to predict whether these patients would, after surgery, have a stable prosthetic joint.

Based on the observations made in a previous work (Chapter 3), the material properties of the bone underlying the glenoid implant strongly affect the GH translations with stiffer supports requiring larger transverse forces to cause a GH dislocation (Chapter, 3, section 3.4.3). In this study we used a Sawbone (Sawbones Europe AB, Malmö, Sweden) foam (Solid Block, pcf 25) presenting mechanical properties close to those of the trabecular bone (young modulus of 317 MPa) of the scapula following the assumption that the cortical bone is usually removed while preparing the seat of the implant during the surgery. This made the joint easier to dislocate with respect to the experiments presented in Chapter 3. Unfortunately, the choice of the support properties was not easy since the literature provides variable approximate young modulus values for the trabecular bone of the scapula with values ranging from 105 to 411 MPa (Carolyn Anglin, Tolhurst, Wyss, & Pichora, 1999; Frich, 1994; Frich & Odgaard, 1995). The values reported in the literature are strongly affected by variations between patients and measurement protocol that explains this large range of possible values.

At the same time glenoid implants cemented in Sawbone displayed less wear and less damage to the glenoid surface during the tests than the prosthesis with a harder support material such as PA2200 (young modulus of 1700 MPa). Nonetheless, they displayed small plastic deformations of the glenoid implant, in particular during dislocations with forces above 500N. For this reason, the test was started with the time-frames presenting the smallest forces and finishing with the largest, in order to preserve the implants from damage as long as possible. As a side-effect the progressive central axial compression of the Sawbone should promote a harder support. Therefore, a more stable joint, while the repeated compressions on a particular side of the glenoid implant would cause a progressive tilting of the implant, and rounding of its edges, promoting more GH instability. As the comparison with a harder support material (PA2200, in Chapter 3, section 3.4.3) indicates, the destabilizing effect was stronger than the stabilizing one.

The force commands used for the simulation (Figure 29) displayed similar amplitudes (up to 1000 N) with the forces recorded *in vivo* (Bergmann, 2009) showing lower values at the beginning and at the end of the task and higher values during the exercises. Similarly, the relative prosthetic orientations at the beginning of the movement (α : $42.1^\circ \pm 1.7^\circ$ and β : $14.6^\circ \pm 0.4^\circ$) and at its end (α : $45.6^\circ \pm 5.0^\circ$ and β : $12.6^\circ \pm 3.3^\circ$) were very similar to the equivalent values recorded in Chapter 3, section 3.3.6, on 11 patients in anatomical position, thanks to the CT-scanner (α : $41.7^\circ \pm 7.3^\circ$ and β : $-10.2^\circ \pm 17.6^\circ$). Between the two positions, there should be no significant difference in abduction-adduction, since the elbow was in both cases against the body. However, a difference of about 25° in internal-external rotation was observed and might be related to a slight difference between the two postures (patients in the CT scanner were in supine position, while during the tasks simulated here, they should be standing).

As observed in all of the results (Table 3 to Table 7) the cases of severe prosthetic instability that resulted in the joint's dislocation were observed for every patient. However, all the patients with an implant proved to have stable prosthetic implants. Additionally, most of the dislocations observed within the simulator were directed superiorly, which in the clinical cases is one of the rarest types of dislocations (Sherman, 2015).). A possible explanation would be the absence of several natural superior stabilizers of the GH joint such as the GH capsule, the subcoracoid and subacromial bursas, the acromion itself and the coracoacromial ligament in this model. Those elements are difficult to simulate numerically since their mechanical properties are poorly understood and because their effect strongly depends on the GH translations, which are not yet available at that stage of the MS simulation. However, the robot could be adapted to fit cadaveric specimen of these structures. Next, by repeating some simulation of patients with a morphology similar to that of the available cadaver would allow verification of the importance of the presence of these passive stabilizers to achieve more realistic GH translations.

Additionally, for the robotic model presented here, it was assumed that every set of GH forces and orientations should be statically stable. It is actually not clear if this assumption is always valid, since the configuration of a specific time-frame could be unstable but not have the time to cause a dislocation before the next motion. A dynamical simulation that takes into account the temporality of the events as well as the inertia of the arm would probably alter the results of the current simulation. However, using dynamical movements with the inertia of the robot would result in excessive inertia since the robotic moving components are heavier than their human counterparts and a model should be used to compensate for this difference, making the model more complex and adding a potential source for errors. For static isometric motions, the robot already demonstrated its abilities in Chapter 3, sections 3.4.1 and 3.4.4.

Several hypotheses also affect the current results, for example the values of torsion and inclination angle of the humeral head are not the real values present in the patient but are a general approximation. The angle of torsion (ν) has been shown to be quite variable, therefore the real torsion angle of the patients simulated could be within 20° and 98° (Patil et al., 2016; Zhang et al., 2016; Zhou & Hu, 2008). Therefore, divergence between the model and the clinical case up to 45° are possible, altering the angular commands α and β and, in the worst-case scenario by the same angle. Similarly, the inter-patient range of the inclination angle of the humeral head reported in the literature as humeral neck/shaft angle was variable with reported values ranging between 109° and 159° (Dare & Godfrey, 2012). In the worst-case scenario this could cause errors of up to 50° on the angular commands. These two angles could by themselves alter the results between a stable and an unstable prosthesis in most simulations and a protocol to record them in a patient specific way will be necessary for future simulations.

Similarly, the version and inclination of the glenoid implant were defined from the clinical planning instead of the post-operative data, leaving room for some variations between the model and the clinical case. However, the glenoid implants were inserted using patient-specific 3D printed guides and should not present large errors such as those presented for the humeral head orientation. These differences between the planned and the realized placement of the glenoid implant affected directly the definition of the cone referential frame, and therefore both the MS numerical model and the robotic simulations through the matrix $^{Thorax}_{Cone}R_o$.

The remaining static rotation matrices ($^{Thorax}_{Scapula}R_o$ and $^{Thorax}_{Humerus}R_o$) were derived from the CT scans of every patient. Therefore, all these matrices were subject to small errors during the segmentation and manual placement of the anatomical landmarks on the models.

The reproduction of different tasks ($task_{abd}$, $task_{hand}$, $task_{should}$) was based on data recorded from a reference subject using the VICON camera system. This potentially adds the uncertainty of tracking errors from the cameras, soft-tissues artefacts (which are the errors related to different motions of the skin where the marker is attached relative to the underlying bony landmark that was targeted) and the natural differences in movement and morphology between the reference subject and the clinical patients, thereby altering the MS model and the robotic simulations through the matrices $^{Thorax}_{Scapula}R(t)$ and $^{Thorax}_{Humerus}R(t)$.

The quasi-static protocol assumed that each position needed to reach the equilibrium of the forces, by waiting for a long settling time. In a real case scenario, one position would probably not last for more than a second, and the joint might not have the time to dislocate. In the simulations presented, some cases of GH dislocations took more than 10 seconds to shift the humeral head out of its socket. However, all of these cases described the critical limit to instability, advancing the angle one step further always caused a fast and clear dislocation. Moreover, these cases were observed rarely (only 7 occurrences of dislocations appeared more than 10 seconds after the new values were set).

Another limitation of the current model was the use of a geometrical model to determine the displacements of the humeral head over the glenoid surface. To evaluate the point of contact between the two prosthetic implants the radius of curvature of the glenoid component was assumed to be very large that simplified the glenoid surface to a plane. However, the error induced by this hypothesis was shown to be low ($err_x < 0.2$ mm, $err_y < 0.8$ mm).

The current simulation was based on the pre-operative planning of each individual patient. In the present study, the difference between the real surgery and the planning were not evaluated. In a future study the use of post-operative CT-scans to configure the MS model should provide closer to reality simulations.

Another weakness of the current model would be the limited validation of the ability of the MS model to predict accurately the force patterns between the two components of the prosthesis (Ehsan Sarshari, 2018), which is an essential part of the robotic simulation. Further comparison with patients from Orthoload (Bergmann, 2009) would provide force patterns closer to the clinical reality.

Alternative test could be envisioned to better understand the actual mismatch between the robotic simulations and the clinical reality. One way would consist in working at a fixed GH orientation and varying the forces one by one to find stable ranges of each force for a given orientation. The differences between the expected forces and the stable forces could provide some insights on the contribution of the elements missing in this model.

Further research should also be done on the reasons for the plastic deformations observed on the glenoid implants, which either don't correspond to real clinical cases or are a consequence of the unnaturally large number of joint dislocations that those implants had to endure.

The actual shoulder simulation framework was the first implementation of a combined MS digital model of the GH joint working in synergy with a robotic simulator. Even if the actual system is not in its actual form able to accurately reproduce clinical patient data it offers an interesting tool for the study of how different elements of the human shoulder will affect the GH stability.

At the beginning of this project the idea was to use the data available during the surgical planning in order to build an MS model to replicate the internal net forces acting on the GH joint in a patient-specific manner, then to apply these forces as realistically as possible on a real copy of the prosthesis planned for implantation in order to evaluate the GH translation. This would have helped to reduce the amount of GH translation in the patients, therefore reducing the risks of GH instability and aseptic loosening. To validate this modelling approach, it was applied to a set of clinical patients from the local hospital (CHUV) in order to compare the results of the patients with the model. The abilities of the robot to follow the commands properly were satisfactorily assessed in Chapter 3. However, at present all the patients monitored displayed stable GH joints, whereas the models displayed unstable joints. The possible causes of this difference are explained above.

In its actual state the combination of the MS model with the robotic simulator could be used to study the elements affecting GH stability by quantifying the differences between the patients and the simulations to explore how changes in the force or angular commands would stabilize the simulation. This could provide insight on the elements that cause these differences and help to improve the general understanding of the processes that lead to stable GH joints.

If the model had been able or was modified in a way that would make it able to simulate the stable GH joint behaviour observed in patients a second validation would still be necessary since its ability to replicate a patient with an unstable implant would remain unverified raising the question on having an model that is more stable than its clinical counterpart.

Finally, if the model was able to replicate the behaviour of patients with both stable and unstable GH joints this model could be used on one hand pre-operatively to validate the surgical planning of patients (to reduce the risk of a failure of the implant) and on the other hand, to explore the possibility of using different implant designs or surgical planning to improve the surgical outcomes in patients with particular conditions, such as heavily eroded glenoid cavities.

If correcting the model proved to be too difficult, the robotic simulator still provides a controllable 5 DoFs platform for prosthetic evaluation, and could be adapted for the evaluation of other joints, such as the evaluation of prosthetic stability in knees with anterior cruciate ligament rupture, or for a study on the mobility of different hip prostheses.

4.6 Conclusion

To improve the understanding of the mechanisms underlying prosthetic GH stability, it is important to be able to simulate accurately the impact of different parameters on the final outcome. A framework for the study and simulation of shoulder stability was therefore proposed and tested against data from real patients. This framework consisted in three successive steps. First, data from the patients were gathered during their normal clinical routine that included their pre-operative CT-scans and their surgical planning. Second, a patient-specific MS model was built for every patient that computed both the net force that the two components of the prosthesis are applying one on each other, and the relative orientations of the two components during different tasks. Third, the same model of prosthesis as found on the patient was installed in a robotic simulator, which reproduced the conditions simulated in the MS model on the prosthesis in order to observe the stability of the joint during a set of different tasks.

Three tasks were simulated for one patient, and one task was simulated on three patients. The robotic simulation was able to reproduce most of the forces and orientation of the two GH implants. However, the results of the combined simulations were not in agreement with the clinical outcomes of the patients tested and displayed much higher rates of superior GH dislocation. Due to the complexity of the entire process the sources of this divergence are multiple and range from the absence of some anatomic elements in the model to the approximation of some of the parameters of the model or the errors caused by some of the hypotheses used during the simulations.

If the problems actually hindering the simulations were to be solved, this chained simulation process would provide a tool to the surgeon, allowing him to better adapt his surgical planning to the patient's shoulder, informing him when the choosen operatory parameters would pose a risk of prosthetic instability. Moreover, this tool could also be used for the evaluation of new prosthetic designs, providing a testing platform prior to human testing.

The authors believe that the actual simulation process even though unable to reproduce accurately the clinical situation in its actual state reproduces many of the fundamental phenomena that affect the shoulder stability and pave the way for a new methodology in the study of GH stability.

4.7 Acknowledgments

The authors would like to thank Pascal Morel for his valuable help in the design of mechanical components. Additionally, the authors would like to thank Tornier-Wright Medical for having donated us all shoulder prosthetic implants used in this study.

4.8 Funding

This work was supported by grant CR32I2_162766 from the Swiss National Science Foundation, and Lausanne Orthopedic Research Foundation.

4.9 Appendix A: Modifications to the robotic simulator

The robotic simulator was the same 5DoFs glenohumeral simulator as described in (Mancuso et al., 2020), with the exception of the glenoid implant support. This simulator was able to actuate the two components of a glenohumeral prosthetic implant, in order to reproduce physiologically relevant forces (up to 2kN, with a 1% error settling time of 0.6sec) and orientations (biaxial, $\pm 40^\circ$, accuracy 0.5deg). Following the conclusions of previous experiments, the rigid support (PA2200, young modulus of 1700 MPa) of the glenoid implant was replaced with a porous material mimicking the mechanical properties of the natural bone, called Sawbone (Solid Block PCF 25 with a young modulus of 315 MPa; produced by Sawbones Europe AB, Malmoe, Sweden).

For each glenoid implant, a customized Sawbone socket was created. Such socket was machined to allow for a 0.5 mm uniform tolerance around the keel and the back of the implant, in order to allow cementing in the prosthesis in conditions that would be similar to the surgical ones. Next, the glenoid implants were cemented, each into its specific socket using surgical cement (TBCem 3, Class IIb, European Medical Contract Manufacturing, Nijmegen, Netherlands).

The robot's socket itself was adapted to receive the Sawbone sockets (Figure 31), in a way that would prevent chiseling forces as well as torsion on the Sawbone support, by enclosing all of its faces but the top one, in a thigh aluminum (AlMgSi1) support structure.

Finally, a shock-absorbing foam was added around the prosthesis to protect the structures in cases of joint dislocations.



Figure 31: New glenoid implant receptacle. The glenoid implant is cemented in a Sawbone socket, which in turn is tightly fit into an aluminum structure. The black material around the edge is a shock absorbing foam, to protect the system during dislocations.

4.10 Appendix B: User Manual to perform a patient's simulation

4.10.1 Expected inputs from the MS model

- Patient reference number, for example *P354*
- *SSDATA.Rmat*: A concatenation of rotation matrices, respectively from Clavicle (C), Scapula (S), Humerus (H), Ulna (U), Radius (R) to Thorax (T) for all the time samples of the simulation, assembled as follows:

$$SSDATA.Rmat = [{}^T_C R_{t1}, {}^T_S R_{t1}, {}^T_H R_{t1}, {}^T_U R_{t1}, {}^T_R R_{t1}, \dots, {}^T_C R_{tN}, {}^T_S R_{tN}, {}^T_H R_{tN}, {}^T_U R_{tN}, {}^T_R R_{tN}]$$
 with N being the total number of time samples
- *DYDATA.ConeRb*: The rotation matrix going from the *Cone* referential frame to the Thoracic referential frame, constructed based on the MRI images: ${}^{T}_{Cone} R_0$
- *BLDATA.OriginalMatrices_L2A.Rs*: The rotation matrix going from the *Scapula* referential frame to the Thoracic referential frame, constructed based on the MRI images: ${}^T_S R_0$
- *Humeral Torsion angle*: ν . If not available use the value of $64 \pm 7^\circ$, as published in (Patil et al., 2016).

- *Humeral Inclination angle*: γ . If not available, use 132.5° , which is the value used in the surgical planning of Prof. Farron (the reference surgeon).

4.10.2 Matlab conversion script: GenerateSOGIpatientCommandsV2.m

This conversion script will load the data from the MS model and generate two files, with the instruction sets for the two sets of actuators moving the robotic simulator: (i) The two *Maxon motor* DC motors that control the prosthetic orientation; (ii) The three *MTS* hydraulic actuator that reproduce the 3D force between the two prosthetic components. Along the process it will also display a set of 14 plots, to control that the conversion process did not encounter any issue, and to help the experimenter to decide how to set up the experiment.

4.10.2.1 Overview

The script is composed of the following sections:

- Parameters: In this section you enter all the parameters to run the script properly.
- Load data: Imports the data from the external files.
- Structure and rotate imported data: This section will compute the GH forces and orientations over time from the informations available from the MS model. Then the GH forces, as well as the angles α and β are periodized, by adding a linear padding between the end of one period and the beginning of the next. The junctions of the padding can be smoothed using a moving average window (but aren't smoothed in the default scenario).
- Apply speed reduction: This section will adapt the sampling frequency and time scale, in order to decrease the execution speed of the simulation by the requested factor.
- Export for Unity visualisation: This section will generate an external file (*Angles.txt*) with instructions for the *Prosthetic Orientation* visualisation software (running under *Unity 2018.3.3f1*), allowing the rendering of the simulated motions of the two prosthesis (based only on the rotations) in a 3D simulation.
- Generate force commands: Process the GH Force to generate a set of three orthonormal Fourier series encoding for the force that each actuator will need to provide during the simulation. For each of the three 1D force the process is the following:
 - Gaussian bell-shaped average sliding window on the whole signal. (Of a length of 15 samples).
 - Fourier reconstruction of the sequence.
- Check concatenation: Displays a set of plots to show how the
- Generate code for MTS actuators: Generates three text files in the *Output* folder with the format **name of the patient*_act?_Axial.txt*; **name of the patient*_act?_LRT1.txt*; **name of the patient*_act?_LRT2.txt*. With Axial being the actuator responsible for the application of the F_z force, LRT1 for F_x and LRT2 for F_y . The code in these files can be used to control dynamic simulation on the MTS actuators (more informations on this process are available in the *Output files* subsection).
- Generate table for Labview: Generates two text files with the instruction for the Maxon Motor DC motors M1 (controls the orientation α) and M2 (controls the orientation β). These files are placed in the *Output* folder with the names: **name of the patient*_act?_M1.txt* and **name of the patient*_act?_M2.txt*. They can be read by the Labview control software *MaxonMultiMotorControl05.vi* to control the DC motors in a dynamic simulation.
- Frequency analysis of the different signals: To perform quasistatic simulations, it is important to know which frequency components compose the signal. The frequency analysis tool will automatically display the intensity of the FFT against the frequency.
- Downsample and generate table: This section will generate a downsampled version of the all the control commands at the frequency specified by *fs_down* (5 Hz by default). These results will be stored in the local variable *ExportAngles* and *ExportForces* and can be used to perform a quasistatic simulation using the manual control mode.

4.10.2.2 Parameterization

First, a folder with the name of the patient to be simulated, and containing the data for the different tasks should be added in the folder named *Data*. The tasks are named with a reference name as *act?.mat* where “?” is the reference number of the task, as indicated in Table 8.

Table 8: Reference names for the different types of tasks that can be simulated with the MS model

act1	Abduction frontal plane with 2 kg
act2	Elevation sagittal plane with 2 kg
act3	Abduction scapula plane with 2 kg
act4	Fast abduction scapula plane
act5	Slow abduction scapula plane
act6	Put 2 kg in a shelf at head height
act7	Hand behind the head
act8	Touch the other shoulder
act9	French canes
act10	Counter external rotation (static pose, no motion)
act11	Counter internal rotation (static pose, no motion)

Then, at the beginning of the script, there is a *Parameters* section (Figure 32).

In this section, the following parameters should be adapted to every patient:

- i. act: specifies the number of the task to be simulated.
- ii. patient: specifies the patient's code.
- iii. IncHum: specifies the humeral inclination of the patient's prosthetic humeral head.
- iv. TorHum: specifies the humeral torsion of the patient's prosthetic humeral head.

The following values have default values and should not be changed in the case of a normal simulation, but can be modified to deal with particular problems:

- i. *n*: Order of the Fourier series used to reconstruct the GH forces. Its value is a tradeoff between the resolution of the reconstruction and the control delay. Larger value will take more computational time on the control loop of the hydraulic actuators.
- ii. *RotMaxVel*: This is the maximal velocity allowed to the rotatory actuators. The default value is the highest safe value. Lower values could reduce vibrations in the system, but will result in a slower and less responsive control.
- iii. *PadDur*: Duration (in samples) of the padding added to smooth the transitions between the end of a cycle and the beginning of the next one.
- iv. *SmoothDur*: This sets the bilateral duration (in samples) of the moving average windows (MVA) smoothing at applied at the junction between the signal and the surrounding padding.
- v. *MVA_len*: Moving average window length, the longer the window, the stronger the smoothing. With a value of 1, no smoothing is applied.
- vi. *SlowMo*: Can be used to slow down the execution speed of the simulation by the factor indicated.

```

%% Parameters
act = 8;
patient = 'P354';
n= 20;           % Order of the Fourier series
RotMaxVel = 4.05405; % Maximum rotation velocity allowed for the electric motors
IncHum = 132.5;   % Inclination angle of the humeral head implant
TorHum = 64;      % Version angle of the humeral head implant
PadDur = 1;%10;    % Duration of the data padding in seconds
SmoothDur = 1;% 40; % Duration of the smoothing around jointures, in samples (bilateral)
MVA_len = 1; % 21; % Length of the moving average filter in samples
SlowMo = 1;       % Slows down the execution speed by "SlowMo" times
% EnableSlowMo = 1; % If 1: Slow Motion is enabled, if 0: Slow Motion is disabled

```

Figure 32: Parameter set of *GenerateSOGIpatientCommandsV2.m* script

4.10.2.3 Supervision tools

A list of plots is automatically generated to verify that every step of the process is working properly.

Figure 1 displays the angular trajectories before smoothing and padding. It allows detecting abnormal datasets from the MS model. Their ranges, continuity and meaningfulness should be assessed.

Figures 2, 3 and 4 indicate the differences between the smoothed and the raw force signals. This allows to fine-tune the smoothing aggressivity.

Figure 5 shows the differences between the force signals reconstructed from the Fourier series against their original version for three cycles; this is useful to select an appropriate order (parameter: n) for the series of Fourier and to make sure that the padding between two cycles was smooth enough.

Figure 6 displays the processed angular commands. Besides the plot, the file *Angles.txt* can also be loaded into a purpose built Unity software to display the requested GH rotations of the two prosthetic components, in a simulated 3D environment. This helps preventing robotic simulations that could be damageful for the hardware.

Figures 7, 8 and 9 display the spectral analysis of the different command signals. This is useful while designing a quasi-static experiment to decide the down-sampling frequency.

Figure 10 displays the force commands along with the selected samples from the down-sampling process. The same information is available for the angular values on Figure 6.

4.10.2.4 Output files

The files with names ending by *Axial.txt*; *LRT1.txt*; *LRT2.txt* contain code to control the three hydraulic actuators with these names, into performing a dynamic simulation of the patient and act contained in the name of the file.

These codes should be copy-pasted into the *Calculation editor* of the *MTS Station Manager* software from the *793.00 control suite*.

Two are the commands for the Maxon Motor DC motors and are named **name of the patient*_act?_M1.txt*³ and **name of the patient*_act?_M2.txt*. They contain a table of times and angles, for the motors. Those should be placed in the

Angles.txt

4.10.3 MTS actuators control

4.10.3.1 Powering up the station

To use MTS's hydraulic actuators, power up the compressor, the Eaton alternative power supply, the control computer and the press base station with the respective power buttons.


³ The character ? in a string is used to replace any one letter alphanumeric character.

On the compressor, you will need to setup the language every time you restart it, as well as performing a soft reset in *Main>Reset*.

On the control computer, go to *MTS 793.00 Control Software* and start the application called *Station Manager*. Then load the configuration file *Matteo_ShoulderDev_with_Maxon.cfg*, you should see the interface displayed on Figure 33.

Check the *Exclusive control* box; reset the *Interlock 2* safety warning and power up the station by turning on the power to the HPU T7-J25 unit (please wait that the unit reaches the low power level, and only when the button stops blinking set up the high power level). Turn on the power level to *Low* for the *HSM T4-J28A*, *HSM T4-J28B*, *HSM T6-J28A*. Then turn the power level of *HSM T6-J28A* to high power.

Next, calibrate the actuators. First, set the Axial actuator in Displacement mode (by setting *Displacement* in the *Control Mode* drop-down menu). Then set a *Target Setpoint* to a position where the Axial actuator will not touch anything (e.g. +40 mm). Make sure that the *Amplitude* parameter is set to 0, then press on *Play*. The actuator will start raising to the target setpoint.

In *Station Controls* click on the *autosetpoints* button . The *Signal Auto Offset* menu will appear. For *Axial Force*, *LRT 1 Force*, *LRT 2 Force* click the *Auto Offset* button next to each one of them, to calibrate them. Then close the *Signal Auto Offset* window and in *Station Manager* press on the *Stop* button to interrupt the command to the Axial actuator.

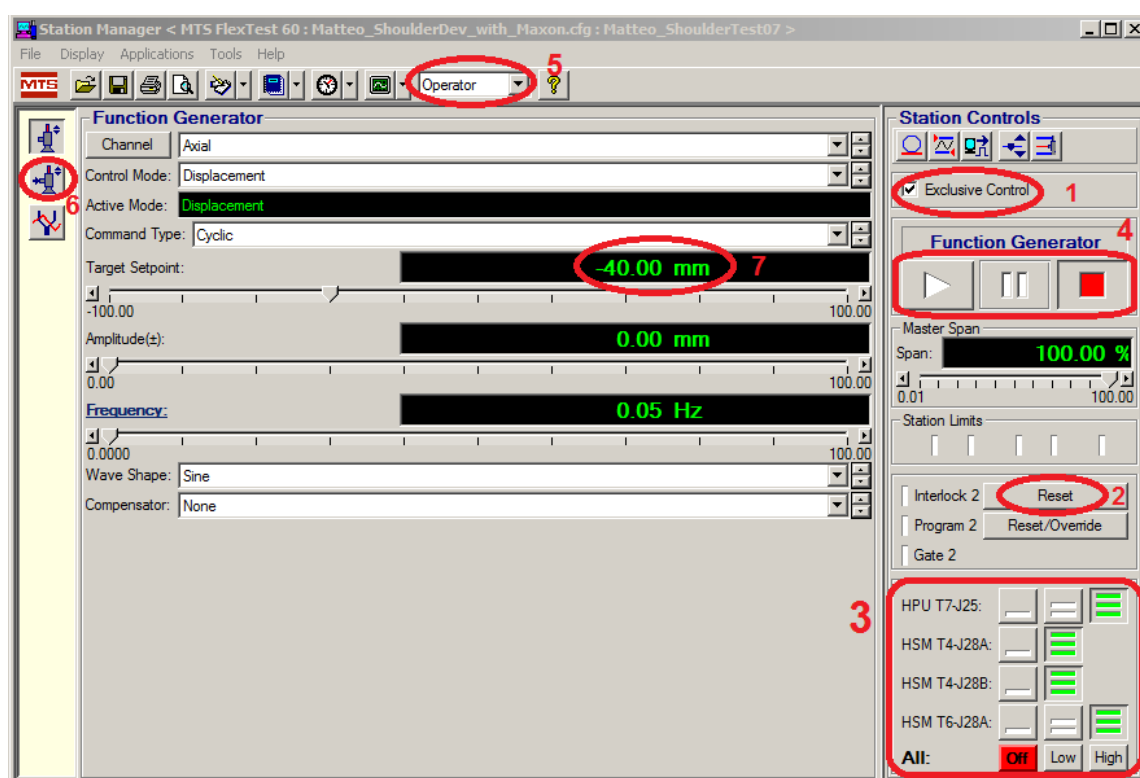


Figure 33: Station Manager Interface. 1. *Exclusive Control*; 2. *Interlock 2* reset button; 3. Buttons to power up the HPU and HSMs components; 4. Play, Pause and Stop buttons; 5. Menu to switch between different modes, mostly *Configuration* and *Operator* modes; 6. Button to open the *External command* menu.

Next, still in displacement control, move the humeral head prosthesis about 1 cm above the glenoid implant. (**IMPORTANT:** Avoid contact between the prosthetic components while in displacement control, as it would damage them.) To do this, press on *Play*. Then change the value of the *Target Setpoint* until the humeral head is approximately 1 cm above the glenoid plane, then press *Stop*. Under the *Channel* dropdown menu, select *LRT 2*. Make sure that the *Control Mode* is set to *Displacement*, then press *Play*. Change the *Target Setpoint* until the humeral head's center is visually aligned with the glenoid implant's center along the *y-axis*. Then press *Stop*, switch the *Channel* to *LRT 1* and repeat the process along the *x-axis*.

Next, the centering must be refined. Change the *Channel* to *Axial* and the *Control Mode* to *Force*. Set up a *Target Setpoint* of -100 N and wait for the prosthesis to make contact, and the force to stabilize. Change channel to *LRT 1* and *LRT 2*, switch each to *Force*

control, and insert a *Target Setpoint* of 0 N for each. Wait until the system stops moving and record the LRT1 and LRT2 displacement values as the centered position.

Switch back the Axial actuator to displacement control, and raise it back 1 cm above the glenoid surface. Then switch both LRT1 and LRT2 to displacement control, and place them to the centered values recorded earlier. Then switch back the Axial actuator to force control with a *Target Setpoint* of -10 N and wait until it makes contact with the prosthesis. This will be the *initial position* for every simulation, and we will refer to it as the *Initial position*.

Please note that during this whole process the platform should remain flat ($\alpha=0^\circ$; $\beta=0^\circ$).

4.10.3.2 Quasistatic control

To perform a quasistatic control simulation, the system is used in manual control. Then the target forces from the table *ExportForces* from *GenerateSOGIpatientCommandsV2.m* are taken line by line, and inserted as *Target Setpoints* in the different channels, following the order Axial, LRT2, LRT1. The system is left to stabilize, the LRT1 and LRT2 displacements are recorded at different values of α and β , then the system is returned to the initial position, and the next line is simulated similarly.

4.10.3.3 Dynamic control

To perform a dynamic simulation of the force pattern of a patient one should use the codes generated for this patient by the *GenerateSOGIpatientCommandsV2.m* script. He should go to *MTS 793.00 Control Software* and start the application called *Station Manager*. Then he should load the configuration file *Matteo_ShoulderDev_with_Maxon.cfg*, switch to *Configuration* mode (password: *Configuration*). Go to *Tools>Calculation Editor*. In the windows that opens, he should go to *Axial External Command2* and replace all of its content with the code from the file **_Axial.txt*⁴. Similarly, the code in *LRT1 External Command Force* and *LRT2 External Command Force* should be replaced with the contents of the files **_LRT1.txt* and **_LRT2.txt* respectively.

Then, the station should be powered up following the protocol described in the sub-section *Powering up the station*.

Next, the user should start the software *Multipurpose Elite*, go to *File>Open Test>OrtholoadTest02*. Then in *Test Runs* create a new *Test Run*. Edit the *Specimen* name, in a way that will be easy to retrieve. Continue through the menus and press *Start* to begin the test. At the same time as the *Start* button is pressed here, it should also be pressed on the labview interface *MaxonMultiMotorControl05.vi* to obtain a synchronised execution of the rotations and forces. No electronic synchronisation is available at the moment.

In the *Test Runs*, a test summary will be created with the recordings from the simulation. The best way to export it, is to copy-paste the table to MS Excel, since none of the export function actually works.

4.10.3.4 Additional considerations on MTS 793.00 Control suite

MTS Control Suite is not a reliable software and should be handled with care. The control parameters are saved with the configuration. However, it does occasionally happen that they get corrupted and the values change by themselves. Please make regularly check the following values to prevent any damage:

- Detectors:
 - o Axial Force: min. -2000 N; max. 2000 N
 - o LRT1 Force: min. -2000 N; max. 2000 N
 - o LRT2 Force: min. -2000 N; max. 2000 N
 - o LRT1 Displacement: min. -25.1 mm; max. 30.1 mm
 - o LRT2 Displacement: min. -22.1 mm; max. 22.1 mm
- Station Setup>Channels:
 - o Axial>Tuning>Adjustments
 - P Gain: 5.00
 - I Gain: 1.00
 - D Gain: 0.05
 - F Gain: 0.00
 - F2 Gain: 0.00
 - FL Filter: 512 Hz

⁴ The character * is used to replace any sequence of alphanumeric characters.

- LRT 1>Tuning>Adjustments
 - P Gain: 13.00
 - I Gain: 10.00
 - D Gain: 0.00
 - F Gain: 0.00
 - F2 Gain: 0.00
 - FL Filter: 512 Hz
- LRT 2>Tuning>Adjustments
 - P Gain: 10.00
 - I Gain: 5.00
 - D Gain: 0.00
 - F Gain: 0.00
 - F2 Gain: 0.00
 - FL Filter: 512 Hz

Be also aware that the mechanical structures of the robot were designed to support up to 3kN in any direction. Using larger forces may damage the structural integrity.

Finally, at the time when this document was written, the Axial actuator had an issue, most probably an electro-valve not opening fully, causing a decrease in its maximal force down to approx. 750 N. Please make sure that it is fixed, if you plan on using larger forces.

4.10.4 Maxon Motors control

4.10.4.1 The interface

The interface to control the Maxon motors was developed on Labview 15.0f2 under the form of *MaxonMultiMotorControl05.vi*. This interface (Figure 34) allows to control every parameter of the DC motors in real time (manual mode) or to follow a predefined trajectory using an external sourcefile, containing a table of times and angular positions to track.

All the menus are doubled, the first one controlling the DC motor 1, called M1 (rotating around the Y-axis), the ones ending with a 2 controlling the DC motor 2, called M2 (rotating around the X-axis). For most parameters, the default value will allow performing a proper simulation and should not be modified.

Since the encoder of the DC motors measures only displacements, every time the controller is turned on, the motors must be undergo a *homing* process. In order to perform that, first make sure that the platform is free to move, and in particular raise the Axial actuator as high as possible. Then, Run *MaxonMultiMotorControl05.vi*. The motors will move to their assumed zeros, then maintain this position. With the buttons *Offset M1* and *Offset M2* rotate the platform until it is flat. Check that the position is really flat by controlling that the outer platform is exactly aligned with the edge of the column supporting it, and that the inner platform is perfectly aligned with the outer platform. Then don't touch the offsets anymore and use the *M1 Manual Control* and *M2 Manual Control* to operate rotations of the platform.

The other important functions are:

- *Manual Max Speed*: Controlling the maximum speed that the motors are allowed to reach.
- *Fs*: Controls the frequency at which the controller will try to read external command files, while tracking a set of waypoints.
- *FileName*: Name of the file to track the waypoints from.
- *Control Mode*
 - *Manual Control*: Mode where you specify the angles to maintain
 - *Waypoints tracking*: Mode where the motors will follow the waypoints in the specified file.
 - *Waypoints Tot. Smoothed*: Is an experimental mode, where for every waypoint, the controller will adapt the maximum speed, in order to reach the target just in time, and minimize system's vibrations. However only small differences were found between this mode and the *Waypoints tracking* mode.
- *Reset*: Returns in manual control mode, and sets all the angles to 0.
- *Stop*: Stop the execution of the .vi and commands the DC motors to maintain the actual position.
- *Run*: On the top menu, starts the execution of the .vi. If this is not active, controlling the menus will not have any effect on the motors.

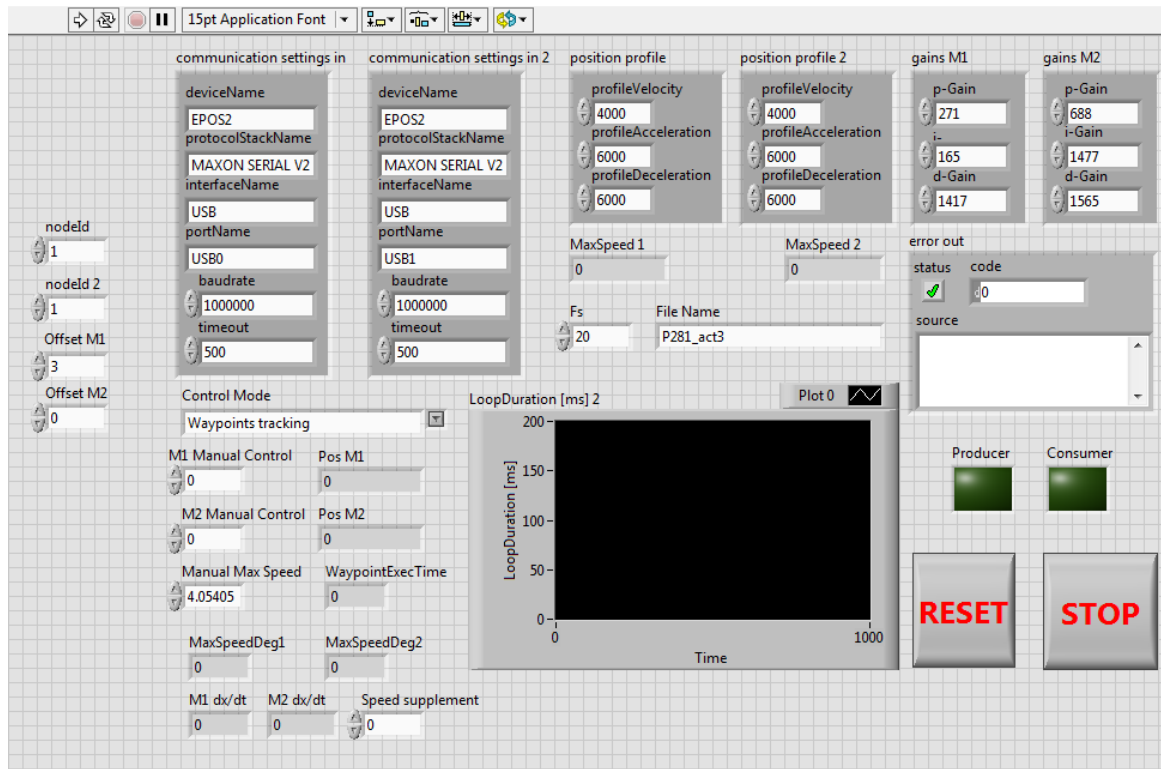


Figure 34: Labview interface to control the Maxon Motors DC motors

4.10.4.2 Quasistatic control

To perform a quasistatic control simulation, the system is used in manual control mode. Then the target forces from the table *ExportAngles* from *GenerateSOGIpatientCommandsV2.m* are taken line by line, and inserted as *M1 Manual Control* and *M2 Manual Control* to set the angles.

The quasistatic simulation presented in the report, were performed by setting the platform flat ($\alpha=0^\circ$, $\beta=0^\circ$), setting the *Manual Max Speed* to 0.0405 °/s, setting the force on the hydraulic actuators ($F_{x,i}$, $F_{y,i}$, $F_{z,i}$), waiting 30 seconds for the system to reach a stable equilibrium, then recording the position.

Next, the platform was rotated successively by 20%, 40%, 60%, 80%, 90% and 100% of α_i and β_i . After each rotation, a minimum of 30 seconds were left to the system to settle, then the XY displacements (more specifically LRT 1 and LRT 2 displacements) were recorded before proceeding with next rotation.

Once all the orientation were tested for the line i , the orientations were reset to 0, the humeral head was returned to its *Initial position*. Then the testing for the line $i+1$ was performed using the same procedure.

4.10.4.3 Dynamic control

In order to perform a dynamic simulation, the instruction files for the specified patient and act should be generated using *GenerateSOGIpatientCommandsV2.m*. The two files containing the instructions for the DC motors (those terminating by *_M1.txt* and *_M2.txt*) should be placed in the active directory *Maxon Motor Control\Labview\Saved_Data*. In the Labview interface, change *File Name* with the name of the files that you created, excepted for the terminal part. So if the files are *P354_act7_M1.txt* and *P354_act7_M2.txt*, then the *File Name* should be set to *P354_act7*. Next press on *Run*, then change the *Control Mode* to *Waypoints tracking* and the motors will immediately start performing the specified pattern. Once they will finish the whole pattern, they will immediately restart it from the beginning until the operator provides a new command.

4.10.4.4 Standard settings

These settings are inserted by default into the program. In the case they get corrupted, here is a list of what was found to be optimal for both the *communication settings* and the *controllers'* settings.

Communication settings:

- i. deviceName: EPOS2
- ii. protocolStackName: MAXON SERIAL V2
- iii. interfaceName: USB
- iv. portName: *USB0* for M1, *USB1* for M2.
- v. Baudrate: 1'000'000 bauds/s
- vi. Timeout: 500 ms

Controller 1 settings (managing M1):

- i. profileVelocity: 4'000 quads/s
- ii. profileAcceleration: 10'000 quads/s²
- iii. profileDeceleration: 10'000 quads/s²
- iv. p-gain: 271
- v. i-Gain: 165
- vi. d-Gain: 1417

Controller 2 settings (managing M2):

- vii. profileVelocity: 4'000 quads/s
- viii. profileAcceleration: 10'000 quads/s²
- ix. profileDeceleration: 10'000 quads/s²
- x. p-gain: 688
- xi. i-Gain: 1477
- xii. d-Gain: 1564

Chapter 5 Developement of a Framework for the Instrumented Evaluation of the Functional Volume⁵

5.1 Abstract

The main purpose of the human *Upper Limb (UL)* is to place and orient the hand in space so that it can perform a particular task. Most of the available diagnostic tools for the UL functional evaluation focus on a very restricted range of the UL mobility, mainly with 2D or subjective measurements. This study aims to provide a new metric for the functional evaluation of the UL by evaluating the volume of the reachable space (R_{Space}) of each side and comparing the pathologic against the healthy UL. The measurement relies on a customization of a recent technology developed for the video game industry and provides a simple, robust and cheap method to track and guide the movements of the UL in space. In this work a fully functional test named *Volfon* is developed, optimized and its early evaluation is presented on 10 healthy subjects. The new algorithm evaluates the R_{Space} with a bias <7% of the theoretical volume within a simulated context, and with reasonable volumes $0.17 \pm 0.06 \text{ m}^3$ as measured on ten healthy subjects. It presents a fair reproducibility, as indicated by its ICC = 0.5 and symmetric limits of agreement [-0.11; 0.12]. A new metric to evaluate the R_{Space} asymmetry is also proposed under the name of *Volumetric symmetry* and its accuracy and reliability are evaluated on healthy patients. The ranges of motions and two other scores are also proposed to support the quantitative analysis of the UL.

Current results pave the way to the development of a new set of tools and measurements for the functional evaluation of the *UL*.

5.2 Introduction

The human UL is defined as the combination of the shoulder, elbow and wrist joints. The main purpose of this complex sequence of joints is to place and orient the hand in space so that it can perform a particular task. When part or all of the *UL* is affected by a traumatic injury or by pathology, the space reached by the hand decreases.

Because of its intrinsic complexity, the *UL* joint is difficult to diagnose. There are mainly two approaches to diagnosis the UL limitation. First, is the *imaging technique*, where a scanner (X-ray, CT-scanner, MRI) is used in order to visualize the mechanical problem and allow the physician to evaluate it within the complex articular chain. This approach is very effective in some conditions such as fractures, but because of the inherent complexity of the *UL*, it is subject to an important number of incorrect diagnoses (Bencardino et al., 2000; Connor, Banks, Tyson, Coumas, & Alessandro, 2003; De Jesus, Parker, Frangos, & Nazarian, 2009; Jost, Zumstein, W. A. Pfirrmann, Zanetti, & Gerber, 2005; Read & Perko, 1998). The second approach, called the *functional approach*, consists in evaluating the impairment of the *UL* during functional tests based on UL movement. This is mainly based on (i) clinical questionnaires such as *Constant score* or the *Mayo score*, filled by the physician about the function of the patient's shoulder, based on direct observation and anamnesis (Angst et al., 2011); or *Quick-DASH* (Gummesson, Ward, & Atroshi, 2006) or Simple Shoulder test *SST* (Godfrey, Hamman, Lowenstein, Briggs, & Kocher, 2007) about the perceived limitations of their *UL* and (ii) Measuring the *Range of Motion*

⁵ This chapter is based on a system developed with the collaboration of Patrick Luca Sgrò from École Polytechnique Fédérale de Lausanne (EPFL), Dr. Patrick Goetti and Dr. Frédéric Vauclair from the service d'orthopédie et de traumatologie of the Centre Hospitalier Universitaire Vaudois (CHUV). Patrick Sgrò helped in the implementation of the software used for the tracking of the arm and forearm segments. Dr. Patrick Goetti and Dr. Frédéric Vauclair provided medical advice that helped orient the test in a direction that would be both relevant and usable in the clinical context. It is written as a journal paper for further possible publication.

(*RoM*) using goniometers (Hayes, Walton, Szomor, & Murrell, 2002). Clinical questionnaires are however subjective, and goniometer remain static and offers a limited insight of the shoulder mobility.

Research has been done toward the development of objective functional scores. The most straightforward approach consisting in the instrumentation of the exercises described in the clinical questionnaires, using different types of sensors and technologies. As an example, Coley et al. (Coley, 2007) instrumented the main tasks of SST recorded and analysed them using inertial sensors. These recordings were then simplified, refined and clinically validated by other researchers (Duc, 2013; Pichonnaz et al., 2015), resulting in a short and informative test, that is now used in several clinics using smartphone application (Pichonnaz et al., 2017). Nonetheless, this test is efficient for specific shoulder diseases where the space reaching is evaluated with few simple movements.

Considering that the main scope of the *UL* is to place its end effector (*EE*), i.e. the hand in space to allow it to perform a particular task, measuring the volume where the *UL* is able to place the *EE* would provide a very general score about the functional impairment of the *UL*. Toward this goal a numerical model was built to evaluate the volume that a subject's *UL* could reach (called the *reachable space* (R_{space})) based on the *RoMs* measured in the anatomical planes using a goniometer (N. Klopkar et al., 2007; Nives Klopkar & Lenarcic, 2005; Lenarcic & Umek, 1994). However, this method lacks resolution since it assumes limited possible locations of *UL* using an interpolation that was validated exclusively for healthy subjects. The method was improved by Kurillo et al. (Kurillo et al., 2013) who developed a protocol to evaluate the R_{space} using a Kinect (Microsoft, WA, USA). In this case the R_{space} is bound to be a portion of a perfect sphere which may not be the actual volume. Moreover, the Kinect suffers from limited precision and accuracy. Clément et al. (Clément, Raison, & Rouleau, 2017) refined the test using reflective markers placed on *EE* combined by stereo-photogrammetry cameras (the Optitrack system, NaturalPoint, Inc., OR, USA) and a slightly refined algorithm to estimate the edges of the R_{space} . However, this last method results in a test that could not be used for a routine examination in a typical hospital due to the complexity to use the stereo-photogrammetry cameras and the cost of the system. Although other motions capture systems, such as electromagnetic tracking systems provide a low-cost solution, they suffer from electromagnetic artefacts, due to the presence of iron and electrical equipment in hospital environment. Among consumer based tracking solutions the *Lighthouse tracking* technology (HTC, Taipei, Taiwan) offers good usability with high accuracy, reliability and robustness compared to other tracking solutions such as Kinect and PlayStation Move (Bonnechère, Jansen, Salvia, Bouzahouene, Sholukha, et al., 2014). This product was then adapted to the scope of this project, in order to provide tracking of the *UL*, as explained in the next section.

The computation of the R_{space} itself from the kinematics of *EE* is not a straightforward problem. It involves several steps such as recording the three-dimensional coordinates of *EE*, filtering, defining contour surface by polygon meshing of three-dimensional point cloud (vertices) and volume computation by considering concave and convex shapes. Each one of these operations will add some errors to the final outcome and needs to satisfy as much as possible a set of mathematical hypotheses.

Finally, we believe that a reliable measurement of the R_{space} requires the subject to scan almost homogeneously all portion of the space in order to have enough and almost same number of data within each portion. In order to guarantee a homogeneous distribution, in this study we propose to guide the subject to reach different part of the space by providing visual feedback through virtual reality (VR). Therefore, the main objective of this study was to design a VR guided test to measure the volume reachable (R_{space}). To this end, a new tracking system was developed extending the existing *lighthouse tracking technology*. It relies on a setup that can be used in a clinical environment within a reasonable cost and duration, without requiring the intervention of highly trained support personnel. This system, that we named *Volfon*, was designed to measure in an automated manner the motion of a set of bony landmarks placed on the shoulder, elbow and wrist joints, through a VR guided test. By comparing the *RoM* and R_{space} of left and right *UL* different scores were proposed and their reliability to be used in clinical field evaluated.

5.3 Materials and Methods

In this section first the Lighthouse-based tracking solution and body fixed markers configuration are described. Second, the system configuration and different body segment frames are defined based on anatomical calibration process. Third, the VR guided scenarios for space calibration are outlined. Fourth, the VR guided functional test of the *UL* is presented. Finally, this section ends with the description of two estimators of functional volume.

5.3.1 Lighthouse based Tracking solution

The Lighthouse based tracking system included: (i) the Head Mounted Displays (*HMD*), which displayed the virtual reality environment to the subjects as well as tracked their head's *pose* (position and orientation); (ii) the *Controllers* used to mark a set of landmarks on the subject and in one of the configurations, to track the movement of the hands; (iii) the *Trackers* (*SteamVR Trackers*) used to provide the positions of the body segments.

The tracking is based on the *Lighthouse tracking technology*, which uses a combination of inertial sensors and optical tracking. First, 1kHz tracking is performed using inertial sensors, then the position and orientation are reset using the *lighthouse constellation* optical sensors at 60 Hz and finally the pose is transmitted to the computer at variable frequencies (Kreylos, 2016; 'Lighthouse', n.d.). The *lighthouse constellation* tracking relies on a base-station acting as a reference position in the room and a set of photodiodes rigidly mounted to the tracked object, called a constellation. At first the base-station emits a pulse of infrared (*IR*) light, which, once it is detected by the photodiodes of the constellation, trigger the start of their timers. Then two lasers beam scan the room, one horizontally, the other vertically at 60 Hz each. The difference of time between the trigger of the IR pulse and the detection of the laser beam allows estimating the angular position of the laser. Using both lasers and the known distances between the photodiodes of a single object, a full pose is estimated and used to reset the drift of the inertial sensors. The overall accuracy of the system was evaluate by (Kreylos, 2016) to 1.9 mm (RMS) for the controllers. Additional tests performed on the Trackers are presented in Appendix A, which provide similar results.

In addition to the tracking technology, a *Head Mounted Display (HMD)* was used to display in 3D and in real time the positions where the subject should place his *EE*. This was used in order to guarantee a set of exercises that would be easy to understand, adapted to the patient and easily reproducible.

5.3.2 System configuration

For the evaluation of the *UL*, a kinematic chain of five rigid articulated segments was considered: the thorax, right and left arms, right and left forearms. The positions and orientations (*pose*) of these segments were measured using four Trackers. Two Trackers (T1 and T2) were placed on the straps of a modified backpack, in order to remain over the higher part of the *pectoralis major* muscle and two were placed on the right and left forearms (T3 and T4), using two watch straps and a 3D printed socked adapter (Figure 35). Each one of the trackers returned a full *pose* at a frequency of 60 Hz (Kreylos, 2016). Moreover, both wrists were immobilized using removable splints in order to maintain the feeling that the subject was pointing the hand toward the targets instead of the forearm.

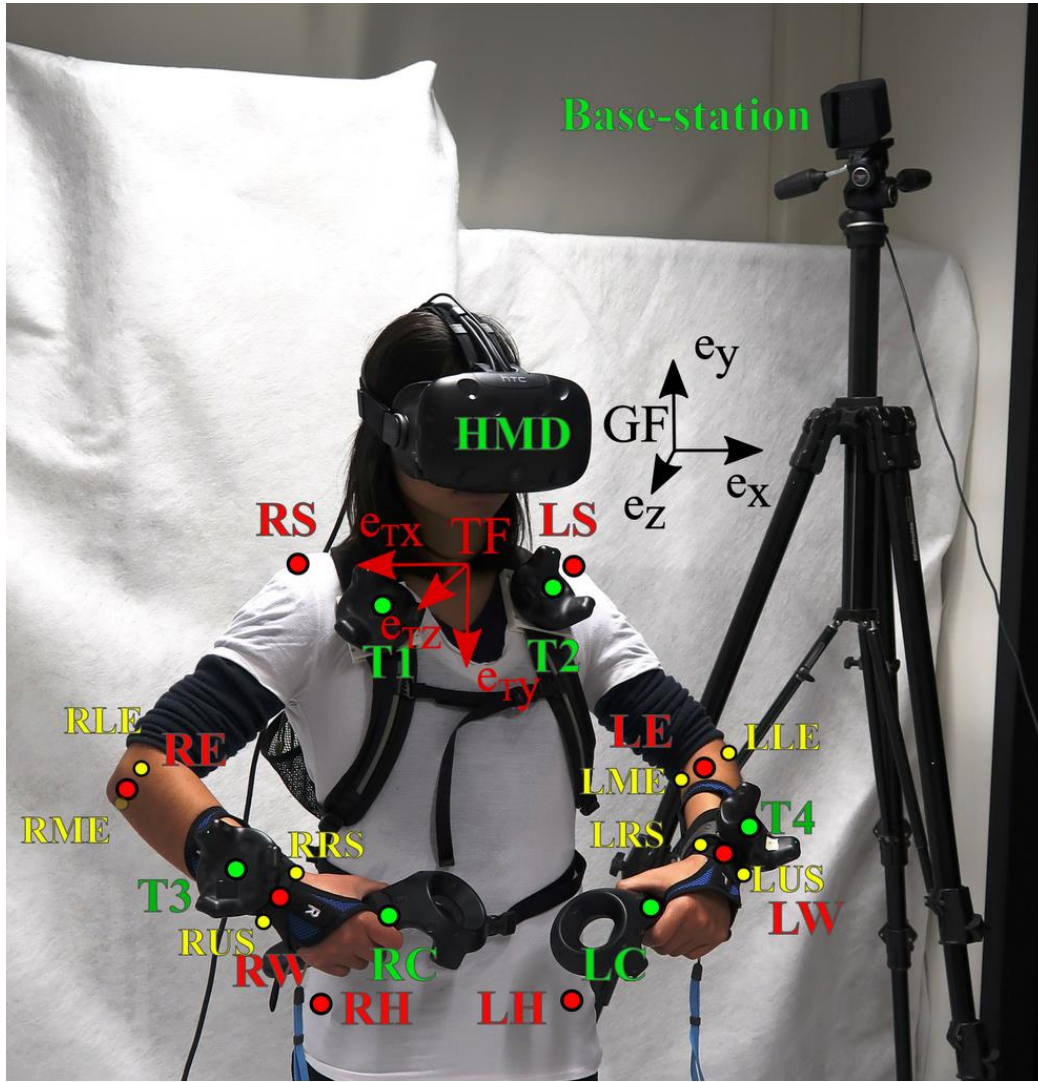


Figure 35: Subject with Trackers on backpack's straps (T1, T2), wrist Trackers (T3, T4), Headset (HMD), Controllers (RC, LC) and Base-station. Anatomical landmarks (RS: Right Shoulder, LS: Left Shoulder; RH: Right Hip; LH: Left Hip; RME: Right Medial Elbow; RLE: Right Lateral Elbow; LME: Left Medial Elbow; LLE: Left Lateral Elbow; RUS: Right Ulnar Styloid Process; RRS: Right Radial Styloid Process; LUS: Left Ulnar Styloid Process; LRS: Left Radial Styloid Process), which are localized using the Controller. The tracked position of the right and left wrists (RW, LW) and elbows (RE, LE) are indicated in red.

5.3.3 Anatomical calibration

After the trackers were placed on the subject, a calibration step (*Anatomical Calibration*) was necessary to align the Trackers' technical frame with the anatomical segments. Using the Controller the examiner marked the position of the following 12 anatomical landmarks into the technical frame of their respective tracker (T1 to T4): distal end of the right (T_1RS) and left *supraspinatus fossa* (T_2LS); right (T_1RH) and left (T_2LH) anterior superior iliac spine; lateral (T_3RLE , T_4LLE) and medial (T_3RME , T_4LME) epicondyles of the right and left elbow; radial (T_3RRS , T_4LRS) and ulnar styloid (T_3RUS , T_4LUS) of the right and left wrist. These landmarks allowed defining 3 anatomical frames: the thorax's frame; the right forearm frame; the left forearm frame.

The position of the right and left wrists (T_3RW , T_4LW) and elbows (T_3RE , T_4LE) were evaluated as the mean of the two anatomical markers used to localize them in the technical frame of the respective forearm trackers (T3 and T4), therefore:

$$T_3RW = \frac{T_3RUS + T_3RRS}{2}; \quad (1)$$

$$T_4LW = \frac{T_4LUS + T_4LRS}{2}; \quad (2)$$

$$T_3RE = \frac{T_3RLE + T_3RME}{2}; \quad (3)$$

$$T_4LE = \frac{T_4LLE + T_4LME}{2}. \quad (4)$$

Then these points were converted back in the global referential frame (GF) and used to display the hand and forearm (as a single rigid mesh) in the virtual reality environment. The length of each arm and forearm was then computed and the mesh was scaled to the anatomical dimensions and kept constants throughout the test (respectively A_R , A_L , F_R , F_L).

The anatomical referential of the thorax $TF(\vec{e}_x, \vec{e}_y, \vec{e}_z)$, was initially defined in GF using the positions of the landmarks RS, LS, RH and LH as follows:

$$\vec{e}_x = \frac{\vec{RS} - \vec{LS}}{\|\vec{RS} - \vec{LS}\|} \quad (5)$$

$$\vec{e}_{tmp} = \frac{(\vec{RH} + \vec{LH})/2 - (\vec{RS} + \vec{LS})/2}{\|(\vec{RH} + \vec{LH})/2 - (\vec{RS} + \vec{LS})/2\|} \quad (6)$$

$$\vec{e}_z = \vec{e}_x \times \vec{e}_{tmp} \quad (7)$$

$$\vec{e}_y = \vec{e}_z \times \vec{e}_x \quad (8)$$

The tracking of the thorax was granted from the two trackers mounted on the straps of the backpack (T1 and T2). The position of the shoulders (RS and LS) was considered as fixed within the technical frame of the respective trackers (T1 and T2). Its size was standardized for all the subjects, and its translations were defined as equal to the translations of the shoulder's midpoint $(\vec{GF}RS + \vec{GF}LS)/2$, while the changes in orientation were those of the shoulder not being used for the test, in order to limit unwanted rotations of the sensor, not corresponding to the motion of the thorax.

The arms were placed to rotate around RS and LS. Their flexion and abduction were set to point in the direction of the RE and LE respectively. This did not allow computing the internal-external rotation of the arm which was set arbitrarily in a way that would look natural in VR.

From these data a real-time avatar of the subject was displayed and animated in the scene, following the movements of the subject in real time.

5.3.4 VR guided test

The avatar of the subject was built and displayed in the *HMD* as well as on the computer display for control and supervision. The virtual reality scenario consisted in a large sandy plateau, surrounded by the sea, during a sunny day. The body of the subject was represented by the upper body of a humanoid character with a spear mounted on the forearm under the test as displayed in Figure 36. In front of the character, three large mirrors were displayed floating in the air allowing the subject to see his avatar (reinforcing the impression of embodiment (Slater, Spanlang, Sanchez-Vives, & Blanke, 2010)) and where the targets were located around him.

To isolate the motions of the *UL* from the motions of the rest of the body, the position of all of the targets was then defined within the referential TF. In this way, the targets would move together with the thorax, naturally filtering out the effects of unwanted motions, such as stepping forward to catch a target or turning around to better reach. Actually, these motions would result in the target moving back or turning with the subject and maintain the exercise at the same difficult as it would be without the unwanted motion.

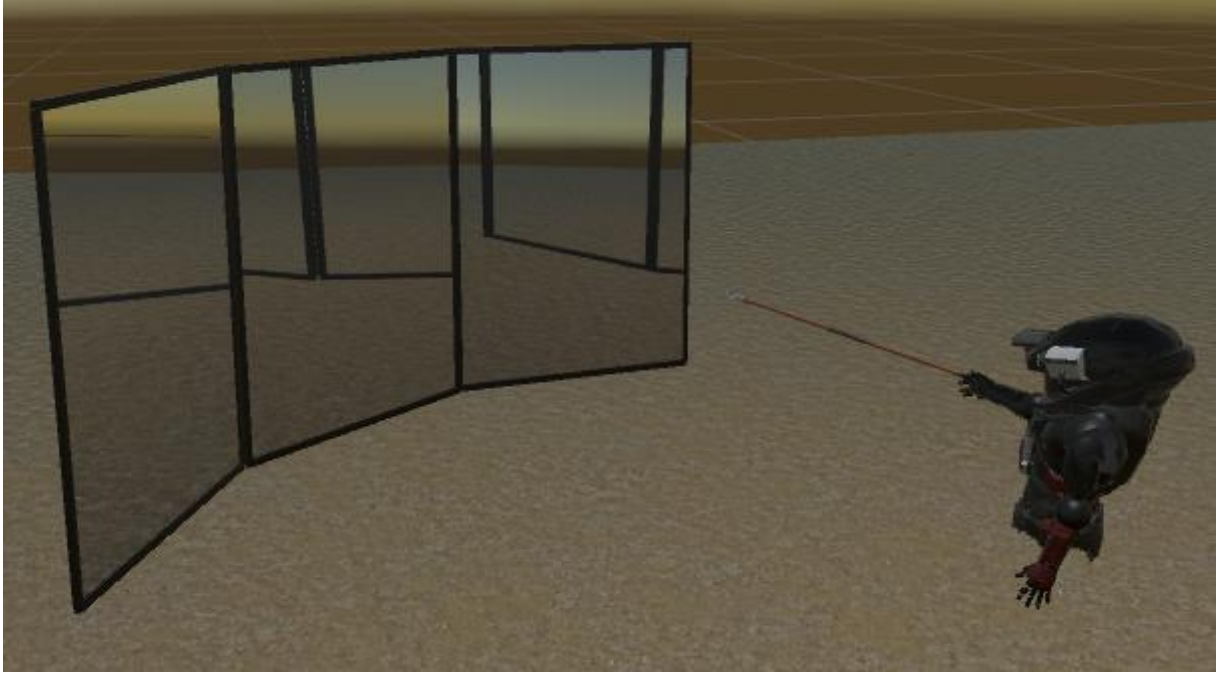


Figure 36: 3D Scene of the VR guided test

The test was developed mainly using the Unity 5.6.1f1 real-time engine in combination with C# scripting language. Within this framework, a virtual scene was designed using a combination of imported and customized 3D models as well as home-designed models, which were built using Solidworks 2017 and Unity scene editor. During the software execution, this scene was continuously rendered on three interfaces: (i) a first person view, three dimensional rendering was displayed on the subject's headset; (ii) a 2D rendering of what the subject was observing was displayed on the computer display; (iii) a lateral and movable third person view was also displayed on the computer screen to help the examiner to observe the scene and if the subject's EE had properly reached the target.

SteamVR plugin was used to interface Unity with the Controllers, Trackers and HMD, recovering poses, and button clicks as well as managing the HMD's display. Unity's interface was adapted to monitor and control the process execution, allowing the examiner to choose his angle of view, to validate a target's acquisition or to redo it. Moreover, at the end of the test an overview of the results was displayed on the computer screen, including a reconstruction of the volume that the subject could reach with each arm, its volume and the relative volumetric difference. Finally, all the results are exported to external text files including a summary of the results and a more detailed file, for an in-depth analysis on Matlab 2017a.

5.3.4.1 **Test procedure**

The test involved two phases: (i) *Ranges evaluation* (ii) *R_{Space} evaluation* Figure 37CD. In the *Range evaluation* the maximum RoM of the UL was estimated by requiring the subject to spear through two sets of arcs. The first set (Figure 37A) was composed of horizontal arcs placed at the height of RS or LS (depending on the side being tested). The subject was required to spear into the arc, right in front of his shoulder, and to rotate the *UL* first internally, measuring the range of internal rotation (H_{int}) then externally, measuring the range of external rotation (H_{ext}), as displayed in Figure 37A. These ranges were measured as the angle between the normal axis of the thorax \vec{e}_z and the vector going from the shoulder to the wrist ($\overrightarrow{RW} - \overrightarrow{RS}$ or $\overrightarrow{LW} - \overrightarrow{LS}$).

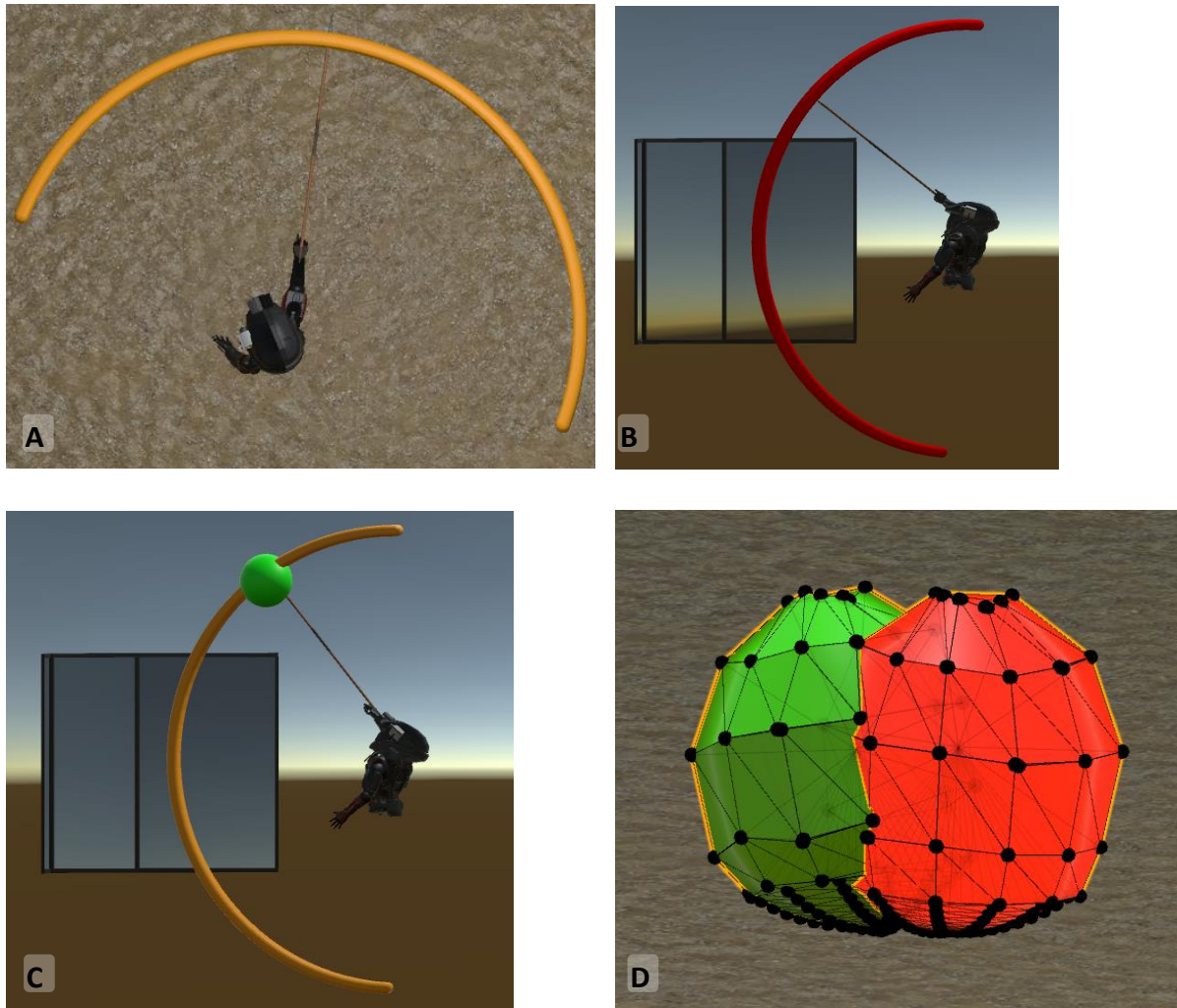


Figure 37: (A) Evaluation of the range of external rotation; (B) evaluation of the range of elevation of the arm; (C) R_{Space} evaluation; (D) Reconstructed R_{Space} : the black dots representing the positions reached by the wrist while the target was acquired, in green the right R_{Space} , in red the left R_{Space} .

Each arc of this set was recorded three times, and the mean values $(\bar{H}_{int}, \bar{H}_{ext})$ were computed for both the right and the left UL. The second set (Figure 37B), was composed of 8 vertical arcs distributed at regular intervals between \bar{H}_{int} and \bar{H}_{ext} . For each one of these arcs, the maximum elevation range was recorded as $V_{\{1, \dots, 8\}}$ with V_1 being the one on the maximum of H_{int} and V_8 being the one on the maximum of H_{ext} . The elevation range was computed as the angle between the axis \vec{e}_z of the thorax and the vector $\overrightarrow{RW} - \overrightarrow{RS}$ or $\overrightarrow{LW} - \overrightarrow{LS}$ depending on the side being tested. Each one of these ranges was evaluated three times and the average values $(\bar{V}_{\{1, \dots, 8\}})$ were recorded.

This allowed to customize the space to the mobility of each UL independently and to distribute virtual targets into potentially reachable positions. For right/left arm, in total 10 virtual targets $(RT_{\{1, \dots, 8\}, \{1, \dots, 10\}}/LT_{\{1, \dots, 8\}, \{1, \dots, 10\}})$, were displayed for each vertical arc, with the first representing an arm elevation of 20° and the last corresponding to the \bar{V}_i with i being the index of the arc being followed. In the second phase, each task consisted on spearing through each virtual target as deep as possible, reaching in this way the maximal articular range. For any of these tasks, the examiner had a third person view of the virtual reality scene on computer screen and decided when the subject reached his best stable position and validated the task by pressing a button. For each one of the targets (displayed altogether on Figure 38), the corresponding right/left wrist position was recorded as $RW_{\{1, \dots, 8\}, \{1, \dots, 10\}}/LW_{\{1, \dots, 8\}, \{1, \dots, 10\}}$.

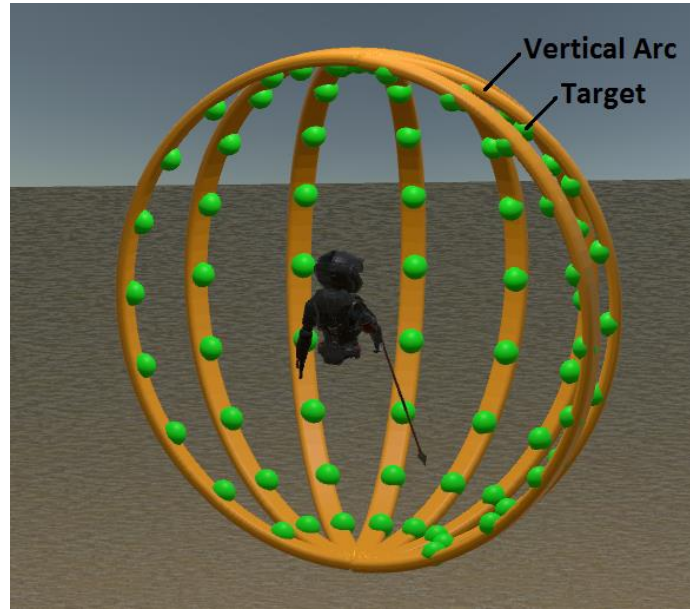


Figure 38: The 8 vertical arcs (V) each with its 10 targets displayed in front of a subject's avatar.

Computed scores were stored in an external file and results were displayed on the screen.

5.3.4.2 Test Retest

The reliability of this test was evaluated using a test retest protocol on ten healthy subjects, aged between 21 and 52, as allowed by the local ethical committee (CER-VD protocol 85/15). A five minutes break was inserted between the test and the retest for the subjects to rest their arms and the anatomical calibration was performed a second time from scratch during the retest protocol. The repeatability was then evaluated, though the differences between the scores of the test and the retest, the absolute reliability was indicated by the limits of agreement ($LoA = mean \pm 1.96 \cdot s_v$), the test reproducibility through the Intraclass Correlation Coefficient ($ICC_{x,y} = \frac{\sum_i (x_i - mean(x,y)) \cdot (y_i - mean(x,y))}{(N-1) \cdot s_v(x,y)}$) and the presence of a bias through the Wilcoxon rank sum test (Bruton, Conway, & Holgate, 2000). Finally, those results were also visualized using a correlation and a Bland and Altman plot.

5.4 Data analysis and Scores estimation

The main goal of the VR guided test was to estimate the *UL* functional volume and propose new scores related to the R_{space} .

5.4.1 Estimation of the reachable space

Starting from a 3D point cloud ($\overrightarrow{RW}_{i,j}$) representing the positions of the EE when it reached its target ($i=[1...8]$, $j=[1...10]$). This provided 80 points in space (called *vertexes*) around the right shoulder of the subject. These vertexes were expressed in the referential of the thorax and centered on the RS, taken at the time of their measurement:

$${}_{TS}\overrightarrow{RW}_{i,j} = {}^{Trunk}_{GF}R(t) \cdot {}_{GF}\overrightarrow{RW}_{i,j}(t_i) - \overrightarrow{RS}(t) \quad (9)$$

This process eliminated the effect of the motions of the thorax on the UL.

A 3D triangulation was then created from the ${}_{RS}\overrightarrow{RW}_{i,j}$ through a process called *meshing*. The back portion of the volume was connected to the origin (${}_{RS}\vec{0}$) to close the volume with the position of the shoulder. Here, the map of the targets allowed determining a map of how the vertexes (i.e. ${}_{RS}\overrightarrow{RW}_{i,j}$) should be interconnected to generate the volume's external surface. This surface was represented by a set of interconnected triangular surfaces called a *mesh* as shown in Figure 39. By construction the three vertexes forming each triangle were ordered so that the norm of the set would be pointing outside of the volume.

Once the surface was meshed, the contained volume could be estimated by voxelization ('Triangle Mesh Voxelisation', 2009) or by tetrahedral decomposition (Cook et al., 1980; Egons, 2011). Because of the lower computational cost, the second method was used for the online application. The tetrahedral decomposition was computed by connecting each triangle of the mesh with the centroid of the point-cloud (CM), generating a set of tetrahedrons. Then the volume was computed as the sum of the signed tetrahedrons:

$$V_R = \sum_k \frac{(\vec{a}_k \times \vec{b}_k) \cdot \vec{c}_k}{6}$$

where $\vec{a}_k, \vec{b}_k, \vec{c}_k$ are the vectors connecting the centroids of the volume $CM = {}_{RS}\vec{d} + \sum_{i,j}({}_{RS}\vec{RW}_{i,j})$ to each of the three vertexes of the tetrahedron number k , in the order provided by the mapping. Similarly V_L was computed using the LS and LW instead of RS and RW.

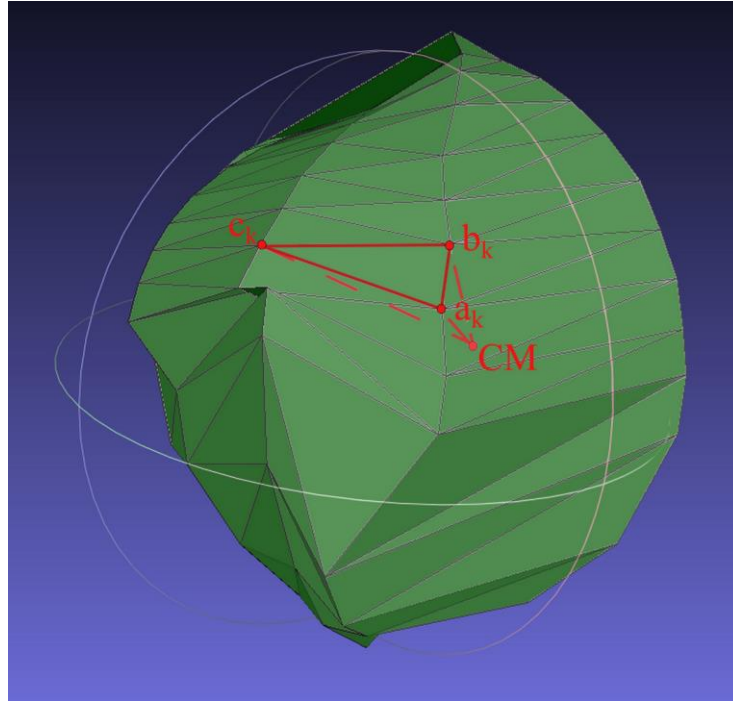


Figure 39: Mesh of the surface of the UL's R_{space} . In red, the tetrahedron "k", composed by three vertices on the surface of the mesh (a, b, c) and one at its centroid (CM)

5.4.2 Volumetric symmetry

By assuming that a healthy subject should be symmetric, one could compare the pathologic UL with the healthy one, in order to evaluate the decrease in R_{space} and therefore its decrease in function. The volumetric symmetry ($V_{\%}$) was therefore computed based on symmetry index (Robinson, Herzog, & Nigg, 1987) as:

$$V_{\%} = \frac{|V_H - V_P|}{V_P} \cdot 100 \quad (10)$$

Or for healthy subjects:

$$V_{\%} = \frac{|V_R - V_L|}{(V_R + V_L)/2} \cdot 100 \quad (11)$$

5.4.3 Spherical volumetric estimator

The *spherical volumetric estimator* was designed as an alternative score. To compute this estimator, a sphere was fitted to the point-cloud formed by ${}_{RS}\vec{RW}_{i,j}$, obtaining the center of the sphere and its radius. Next, the referential was shifted to the center of the sphere and the vertexes of ${}_{RS}\vec{RW}_{i,j}$ were projected on the surface of the sphere creating the set of projected vertexes. To this set of vertexes was added the center of the sphere. Since this set was granted to form a convex volume, it was meshed using the convex hull (*convhull* function of *Matlab 2017a*). The volume V_{Sph} was then computed by *tetrahedral decomposition*, using the same method as presented for the estimation of the R_{space} .

5.4.4 Range of motion

During the measurement protocol, for each UL, ten measurements of range ($\bar{H}_{int}, \bar{H}_{ext}, \bar{V}_{\{1,...,8\}}$) were recorded. A simple *elevation score* (Q_S) to evaluate the handicap on the ability to elevate the arm was proposed as by sorting $\bar{V}_{\{1,...,8\}}$ by order of magnitude, such as $q_1 = \max(\bar{V}_{\{1,...,8\}}); \dots; q_8 = \min(\bar{V}_{\{1,...,8\}})$, then dividing the two smallest values by the two largest ones: $Q_S = \frac{q_7+q_8}{q_1+q_2} \cdot \frac{q_4+q_5}{2}$. This value will decrease in case of inconsistent performances or in case of generally low elevation ranges.

5.4.5 End-Effectors comparison

Another important aspect of this test was the number of joints to include in the biomechanical model. Here we considered two joints: shoulder and elbow by fixing the wrist by splint. Actually, the shoulder being the most complex joint of the UL, and one of the most frequently injured, it had to be included. Elbow allows to place the hand in space properly by shortening and lengthening the UL. While adding wrist would give a better result reflecting the function of UL, it could hide some functional limitations of the shoulder by compensatory movement such as large flexion-extension to increase UL motion range. To investigate further on this topic, a test-retest was performed on 6 healthy subjects in two different conditions with and without wrist immobilization:

- i. The controller was placed in the hand and its position (RC or LC) was tracked as EE. Therefore, the spear moved together with the hand and the biomechanical chain included the shoulder, the elbow and the wrist joint.
- ii. The wrist was immobilized by the splint and the test was done without controller while the position of the wrist (RW, LW) was tracked as end-effector. Therefore, the spear moved together with the forearm and the biomechanical chain included the shoulder and the elbow joint.

The sequence of the tests was balanced by asking 3 subjects to start with wrist immobilized, then without immobilization and 3 subjects starting without immobilization, then with wrist immobilized.

Here the same metrics were used for both tests, simply considering the EE to be RW/LW for the configuration with splints and considering the EE to be RC/LC for the configuration with the controllers in the hands.

5.4.6 Sensitivity of the reachable volume to the number of targets

In our test we defined 80 targets dispatched through 8 vertical arcs, i.e. 10 targets per arc. The error for volume reconstruction can be reduced by increasing the number of vertex (i.e. the number of targets). However, this requires more effort from the subject who should hit more targets with the consequence of loss in the quality of movement due to fatigue. In order to evaluate the sensitivity of the volume estimation to the number of targets, a numerical simulation was performed to quantify the accuracy and precision of volume estimation as a function of the number of arcs and targets presented in space. The simulation consisted of a hemisphere of known radius (r) and volume ($Vol_{theo} = \frac{4\pi r^3}{3} \cdot \frac{1}{2}$), sampled with a number N_A of arcs including each N_T of targets, corresponding to the case of a subject with a spherical R_{space} performing the test. The vertexes sampled on the sphere were then summed up with a zero-mean Gaussian noise with variance equal to σ^2 . Then the vertexes were processed as described in section 3.5.1 to compute the estimated R_{space} as Vol_m . This experiment was repeated 100 times for each level of noise resulting in k -estimations of $Vol_m(k)$, ($k=1,...,100$). The relative bias (b_v) and standard deviation (s_v) of the volume ($b_v = \frac{1}{N} \sum_{k=1}^N \frac{Vol_{theo} - Vol_m(k)}{Vol_{theo}} \cdot 100$,

$$s_v = \sqrt{\frac{\sum_{k=1}^N \left(\frac{Vol_m(k) - Vol_{theo}}{Vol_{theo}} \right)^2}{N-1}} \text{ in the presence of varying } \sigma^2 \text{ (}\sigma^2 \in [0; 10] \text{ cm, varying by steps of 2 cm) were estimated.}$$

5.5 Results

5.5.1 Test Retest

Their respective ranges of motion are presented in Table 10, the horizontal ranges being presented only for eight of the ten subjects due to a technical issue with the recording software. Their *elevation scores* are presented in Table 11.

The achieved volumetric symmetries (Table 9) did not present significant differences between the first and the second test, with an average difference between the test and the retest of 2.3 ± 19.8 %. However, the mean (19.04 for the test and 16.77 for the retest), median (14.99 for the test and 11.51 for the retest) and standard deviation (13.53 for the test and 18.08 for the retest) were consistently lower on the second iteration of the test, indicating a probable effect of the training, muscular warm-up and general

level of confidence with the test and the environment. For this reason, it was believed that the subjects should receive a short training sequence before starting the final test.

Statistical testing on a small sample ($N=20$) is not reliable and will require more subjects to provide clear results. Comparing the calculation of the volume for the test against the retest classes, provided an ICC of 0.50 and an LoA of $[-0.11, 0.12]$. The Wilcoxon test did not demonstrate the test data to be statistically equivalent to the retest data, with a p-value of 0.68. The Bland and Altman plot (Figure 40) indicates a slight bias (-0.01) indicating that the patients were able to reach for a slightly larger volume during the retest. Only subject 1's left US had a data point and could be considered as an outlier.

The alternative volumetric estimator V_{sph} displayed a lower ICC of 0.37 and an LoAs of $[-0.18, 0.24]$. The Wilcoxon test did not demonstrate the test data to be statistically equivalent to the retest data, with a p-value of 0.07.

Table 9: Reachable right (V_R) and left volume (V_L) and volumetric symmetries ($V\%$) of ten subjects during the test (T) retest (R)

Subject:	$V_{L,T}$ [m ³]	$V_{R,T}$ [m ³]	$V_{L,R}$ [m ³]	$V_{R,R}$ [m ³]	$V\%,T$ [%]	$V\%,R$ [%]	$V_{sph,L,T}$ [m ³]	$V_{sph,R,T}$ [m ³]	$V_{sph,L,R}$ [m ³]	$V_{sph,R,R}$ [m ³]
1	0.38	0.25	0.19	0.17	42.5	11	0.47	0.42	0.31	0.38
2	0.14	0.16	0.13	0.13	14.5	1.6	0.28	0.33	0.2	0.33
3	0.13	0.1	0.11	0.21	23.1	60.8	0.15	0.15	0.12	0.43
4	0.21	0.21	0.18	0.23	0.7	21.2	0.3	0.39	0.25	0.39
5	0.16	0.19	0.17	0.17	14.6	1.3	0.2	0.21	0.21	0.23
6	0.08	0.09	0.09	0.09	15.4	1.1	0.52	0.27	0.21	0.26
7	0.16	0.16	0.19	0.17	1.1	8.5	0.21	0.3	0.22	0.25
8	0.13	0.2	0.12	0.18	41.3	38	0.29	0.4	0.2	0.35
9	0.24	0.19	0.28	0.25	24	12.2	0.34	0.4	0.34	0.4
10	0.16	0.19	0.15	0.17	13.3	12.1	0.31	0.41	0.34	0.37
Mean	0.18	0.17	0.16	0.18	19.1	16.8	0.31	0.33	0.24	0.34
s_v	0.08	0.05	0.05	0.05	14.3	19.1	0.12	0.09	0.07	0.07

Table 10: Mean reachable ranges (in degrees) for the horizontal internal (\bar{H}_{int}) and external (\bar{H}_{ext}) rotation, as well as the mean vertical reachable ranges ($\bar{V}_{\{1,...,8\}}$) for the 8 vertical arcs of the left arm. T stands for Test and R for Retest; the missing values are indicated with "-".

Subject	\bar{H}_{int}		\bar{H}_{ext}		\bar{V}_1		\bar{V}_2		\bar{V}_3		\bar{V}_4		\bar{V}_5		\bar{V}_6		\bar{V}_7		\bar{V}_8	
	T	R	T	R	T	R	T	R	T	R	T	R	T	R	T	R	T	R	T	R
1	-	-	-	-	101	103	98	100	96	97	96	96	95	95	93	95	93	92	101	100
2	-	-	-	-	107	108	107	108	105	106	105	104	103	99	97	96	98	91	105	101
3	81	65	110	105	100	101	97	98	96	98	96	95	95	95	97	95	98	94	106	98
4	63	60	115	129	106	107	103	103	100	101	95	98	90	95	88	95	87	92	103	103
5	84	72	130	127	104	102	103	99	97	94	97	91	95	92	85	90	92	91	102	102
6	73	69	123	128	100	100	101	100	99	100	100	101	99	101	100	100	100	100	100	99
7	56	65	107	105	103	104	101	101	99	98	97	97	94	95	94	93	94	93	101	103
8	80	69	112	114	98	102	97	99	95	95	95	96	96	95	97	94	96	95	100	101
9	71	77	127	123	106	101	104	101	99	99	93	96	91	95	90	95	92	95	102	100
10	63	65	113	115	105	104	103	103	101	99	96	97	92	71	91	91	90	91	103	101

Table 11: Elevation score (Q_s) of 10 healthy subjects during the test-retest for both the right (R) and the left (L) ULs.

Subject	Test		Retest	
	$Q_{s,L}$	$Q_{s,R}$	$Q_{s,L}$	$Q_{s,R}$
1	160.0	162.4	163.1	135.8
2	143.4	159.6	158.4	164.7
3	145.0	149.3	145.1	165.9
4	176.7	158.6	176.5	159.8
5	156.5	141.0	157.6	163.1
6	171.2	153.6	157.7	159.3
7	160.0	163.1	155.5	159.8
8	165.6	165.1	156.6	155.9
9	146.0	158.8	163.4	163.8
10	150.7	164.6	133.1	169.7
Mean	157.5	157.6	156.7	159.8
s_v	11.4	7.7	11.4	9.3

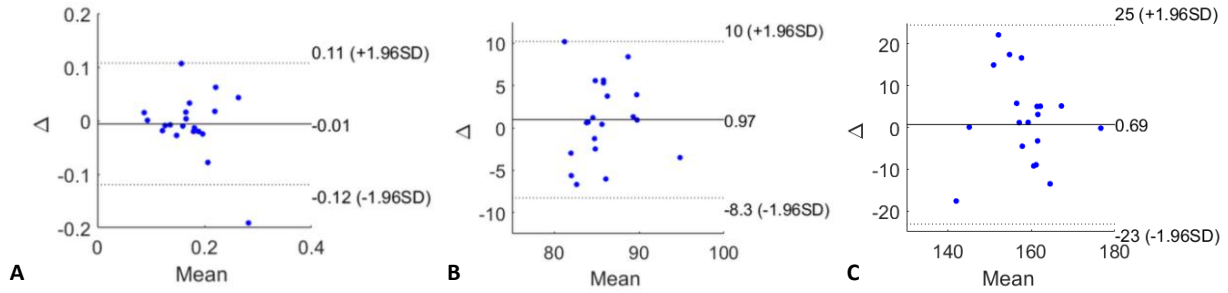


Figure 40: (A) Bland-Altman plot of the measurements of R_{space} between the test (V_T) and the retest (V_R). With Δ being the difference $V_T - V_R$ and $Mean$ representing $(V_T + V_R)/2$. (B) Bland-Altman plot of the measurements of the mean elevation between the test and the retest. (C) Bland-Altman plot of the measurements of Q_s between the test and the retest

5.5.2 End-Effectors comparison

The R_{space} obtained while considering the hand or the wrist as EE and their volumetric symmetries are presented in Table 12. Their respective ranges of motion are presented in Table 13 and their *elevation scores* in Table 14. The Wilcoxon rank sum test ($N = 12$ arms) did not show any statistical equivalence between the *elevation scores* of the hand and the wrist measurements (p -value > 0.9).

Table 12: Measured volumes of the R_{space} and volumetric symmetries of 6 subjects testing while using the hand (H) or wrist (W) as EE

Subject:	Wrist			Hand		
	$V_{L,W} [m^3]$	$V_{R,W} [m^3]$	$V_{\%,W} [\%]$	$V_{L,H} [m^3]$	$V_{R,H} [m^3]$	$V_{\%,H} [\%]$
1	0.11	0.15	31.0	0.15	0.14	7.3
2	0.17	0.17	1.7	0.48	0.23	69.1
3	0.20	0.18	11.2	0.29	0.43	38.0
4	0.17	0.18	9.0	0.30	0.34	13.7
5	0.11	0.15	34.2	0.24	0.26	9.0
6	0.06	0.08	23.6	0.08	0.19	77.2
Mean	0.14	0.15	18.5	0.26	0.27	35.7
s_v	0.05	0.04	13.1	0.14	0.10	31.1

Table 13: Reachable ranges (in degrees) of the left arm. W: standing for Wrist used as EE and H: standing for Hand used as EE

S	\bar{H}_{int}		\bar{H}_{ext}		\bar{V}_1		\bar{V}_2		\bar{V}_3		\bar{V}_4		\bar{V}_5		\bar{V}_6		\bar{V}_7		\bar{V}_8	
	W	H	W	H	W	H	W	H	W	H	W	H	W	H	W	H	W	H	W	H
1	69	66	123	139	103	88	98	83	89	83	88	80	78	83	56	84	72	86	94	92
2	66	62	114	59	110	94	91	94	62	90	88	92	83	90	82	85	85	85	93	90
3	84	72	128	121	99	101	95	103	88	97	91	83	85	78	85	79	85	79	87	96
4	72	72	115	107	99	98	94	93	94	85	87	79	82	78	83	78	84	76	89	92
5	60	45	108	103	94	81	87	79	111	83	99	80	90	81	77	83	81	80	87	88
6	47	35	96	96	95	66	87	80	91	89	89	66	92	85	91	84	95	83	101	92

 Table 14: Q_s of 10 healthy subjects during the test-retest for both the right and the left arms

Subject:	$Q_{s,HL}$	$Q_{s,HR}$	$Q_{s,WL}$	$Q_{s,WR}$
1	165.2	158.9	144.1	159.9
2	171.2	156.1	149.3	152.0
3	157.5	167.6	166.1	164.5
4	154.6	154.1	164.6	160.2
5	165.1	145.1	154.7	159.2
6	149.9	166.1	172.3	165.9
Mean	160.6	158.0	158.5	160.3
s_v	7.93	8.28	10.9	4.89

5.5.3 Sensitivity of the reachable volume to the number of targets

Table 15: Bias and standard deviation (in %) of a simulated reconstruction on a hemisphere of radius 0.5m with varying numbers of arcs and noise while using 10 targets per arc. All the values are expressed as a percentage of the theoretical volume of the hemisphere.

σ^2 Arcs	0		2		4		6		8		10	
	b_v	s_v	b_v	s_v	b_v	s_v	b_v	s_v	b_v	s_v	b_v	s_v
4	19.8	0.0	19.9	2.1	20.3	4.4	20.4	7.0	20.1	8.7	19.1	12.5
5	12.7	0.0	13.0	2.3	12.7	4.8	13.5	7.2	12.0	9.5	10.8	14.3
6	9.3	0.0	9.3	2.3	9.5	4.5	8.8	6.8	10.0	8.7	8.2	13.2
7	7.4	0.0	7.3	2.4	7.8	4.4	7.3	6.7	6.7	8.6	7.8	12.9
8	6.2	0.0	6.2	2.1	5.5	4.4	5.4	6.7	5.5	8.3	6.8	11.6
9	5.5	0.0	5.5	2.3	6.4	4.4	5.5	5.9	4.4	9.5	5.8	12.6
10	5.0	0.0	5.1	2.2	5.2	4.6	4.0	6.8	6.2	9.0	4.0	12.8

Table 16: Bias and standard deviation (in %) of a simulated reconstruction on a hemisphere of radius 0.5m with varying numbers of arcs and noise while using 15 targets per arc. All the values are expressed as a percentage of the theoretical volume of the hemisphere.

σ^2 Arcs	0		2		4		6		8		10	
	b_v	s_v	b_v	s_v	b_v	s_v	b_v	s_v	b_v	s_v	b_v	s_v
4	18.3	0.0	18.2	1.9	18.4	3.4	17.3	6.8	18.4	8.5	16.0	10.1
5	11.1	0.0	11.2	2.0	11.2	3.5	12.1	5.9	10.5	8.8	11.9	12.4
6	7.6	0.0	7.9	1.8	7.3	3.9	8.8	6.0	8.2	8.3	6.8	12.5
7	5.7	0.0	5.9	2.1	5.2	3.6	5.4	6.0	4.4	9.1	6.5	12.3
8	4.5	0.0	4.4	1.9	4.4	4.1	4.2	6.1	4.2	9.1	3.3	10.2
9	3.8	0.0	3.8	1.7	3.1	3.8	4.5	6.0	2.4	8.6	2.3	13.1
10	3.2	0.0	3.5	1.8	4.3	3.5	2.3	4.9	3.4	8.2	3.7	12.2

5.6 Discussion

In an effort to address the clinical need for a tool to objectively and efficiently evaluate the state of the UL function, we developed an instrumented test that is easy to use, cost-efficient and entertaining, while providing several evaluation scores of the UL, and in particular a novel volumetric evaluation of its R_{Space} . Using the HTC Vive headset in combination with a set of Trackers and customized straps, such a test demonstrated its usability on a set of 10 healthy subjects.

The use of VR was observed to help the subjects not to overthink about their pathologic limb and to get them to view the exercises more as a game or a challenge, in this way, increasing the subject's compliance. Moreover guiding clearly the motions of the subjects was shown in (Clément et al., 2017) to leads to marked improvements in the accuracy of the volumetric evaluation, this guiding was reinforced here through the use of clear targets in VR. The use of VR also allowed adapting the positions of the targets in function of the motions of the trunk and of the subject's performance over the previous tasks.

Looking at the scores, from a quantitative perspective, and assuming a subject with a shoulder-to-wrist distance of 0.5m and a R_{Space} varying between one quarter and one half of a sphere, the volume expected would be of $V_{\text{Theo,min}} = \frac{1}{4} \cdot \frac{4\pi}{3} \cdot r^3 = 0.13 \text{ m}^3$ and $V_{\text{Theo,max}} = \frac{1}{2} \cdot \frac{4\pi}{3} \cdot r^3 = 0.26 \text{ m}^3$. Subjects from the test-retest displayed on average a R_{Space} of 0.17 m^3 with a standard deviation of 0.06 m^3 , therefore indicating reasonable results in terms of overall volume. Based on the interclass correlation coefficient the reliability of the test was fair (ICC = 0.5, N = 20 arms), the LoA of [-0.11, 0.12] was symmetric indicating little bias, and the Wilcoxon rank-sum test (p-value = 0.68) did not demonstrate the data to be statistically equivalent.

The errors of the different steps of the protocol can be decomposed as the errors in the *Recording system*, *Anatomical calibration*, *Range Calibration*, *Target Acquisition* and *Volumetric Reconstruction*.

The error of the *Recording system* could not be measured during the VR test with any of the other motion-tracking systems available without causing interferences, but it's accuracy was evaluated to be generally lower than 3 mm in Appendix A and in (Kreylos, 2016).

During the *Anatomical calibration* the positions of the shoulder joint, elbow joint and wrist are calibrated by tagging a set of anatomical landmarks in order to reconstruct a model of these positions on top of the SteamVR trackers. From this information the length of the arm and forearm is computed and used throughout the test to scale the *UL* segments. Therefore, the precision of this calibration is evaluated by comparing the length of the arm and forearm between the test and the retest, showing results in the order of 1 to 2 cm (difference of length of arm: mean = 1.8 cm; s_v = 1.1 cm; difference of length of forearm: mean = 1.7 cm; s_v = 1.8 cm;). A single experimenter took all the measurements in this study. In a future study, the inter-experimenter error should also be evaluated.

During the *Range Calibration*, the ranges of rotations were estimated 3 times per arm and per test. Aggregating the data from the test and the retest for 8 subjects, the left arm presented on average $69.6^\circ \pm 7.9^\circ$ and the range of external rotation was of $117.75^\circ \pm 8.9^\circ$

The *Target Acquisition* suffered from the cumulated errors of the previous steps, as well as from varying target positions, due to different estimations of the ranges and could not be compared separately.

However, based on the measurements of the R_{Space} , the volumetric symmetry was computed to quantify the subject's level of asymmetry. All the subjects recorded were healthy; therefore, this score should be low. Its average value was of $17.9\% \pm 16.4$, with a slightly higher value for the test (19%) than for the retest (16.8%).

As indicated by the Bland and Altman plot (Figure 40), there was a little bias, indicating a slight increase in the R_{Space} during the retest. This could be viewed as an effect of training or chance. The Wilcoxon rank sum test did not demonstrate the test results to be equivalent to the retest results ($p = 0.68$), therefore we cannot exclude the presence of a training effect. Based on the Bland Altman test, subject 1 could also be considered as an outlier, since he achieved a very surprising result with his left arm on the test, greatly contributing to the generally large standard deviation. Removing subject 1 from the analysis as an outlier shifts the results, with a difference between the test and the retest data growing to $6.7\% \pm 3.25$. The average volume for the test would then be of $18.6\% \pm 15.1$ and $11.9\% \pm 11.8$ for the retest (Table 9). Nonetheless, this would still be insufficient to conclude about any difference between the test and the retest.

The choice of the *EE* was also an important decision. Considering that this test was designed to produce a set of natural reaching motions that should cover as much of the hand's R_{Space} as possible, only two possibilities were conceivable: (i) the hand; (ii) the wrist. Assuming that the space added by the wrist was negligible with respect to the reach provided by the rest of the *UL*, the effect of tracking the hand was mostly to provide a more natural movement. However, the achieved volumetric symmetries were larger (mean = 35.72, median = 25.85) and more variable (s_v = 31.14) while tracking the hand than they were while tracking the wrist (mean = 18.46, median = 17.41, s_v = 13.09). This choice caused a worsening of the reproducibility of the test, since this extra degree of freedom allowed them to reach the targets in different and less effective ways, leading to worse results. Therefore, it was decided to keep the illusion that the hand was being used to move the spear, but that the wrists were blocked by splints. Then the position of the wrists was tracked as *EE* position.

It is important to notice that the wrists could have been left free to move and the spear could have been mounted on the forearm nonetheless. However, as indicated in the literature, the placement and orientation of the hand in space is controlled differently than that of the forearm (Balakrishnan & MacKenzie, 1997). Consequently, the subject should keep the impression of orienting their hand in space instead of their forearm, which is why splints were used to mechanically couple the two.

Another important parameter of the test was the number of arcs and targets displayed, since on one hand it affected the accuracy of the volumetric reconstruction (more targets and arcs leading to better reconstruction) but on the other, it made the test longer and more difficult to perform for the subjects. Quantifying the phenomenon with numerical simulation indicated that the tuning the test with 8 arcs and 10 targets would provide a good trade between the test duration (<30 min) and the volumetric bias (< 7%), while remaining relatively robust to noise (s_v = 10% with a very high amount of noise on the data). Moreover, this result allowed to quantify the error of the *Volumetric Reconstruction* and confirmed that the novel algorithm is able to accurately measure the volume of a polygon with known shape.

Besides the measurement of the volumetric symmetry, other metrics can be extracted from this test, such as the ranges of motion of the subjects, the *elevation score* (Q_s) and the *spherical volumetric estimator* (V_{sph}).

Between the test and the retest, the ranges of motions had a mean difference of 4.75° for the horizontal arcs and 0.31° for the vertical ones. The higher differences on the horizontal ranges (Table 10) might be related to the incapacity of the subject to see their hand in the end-range and therefore to more variable final positions. As indicated by the Bland and Altman analysis, the mean difference of test retest for the *elevation score* was of 0.69° , while it was of 0.97° for the *mean elevation*. Moreover, all of its data-points were further away from the LoAs, indicating that the Q_s is more robust than the mean elevation angle.

The *spherical volumetric estimator* (V_{sph}), by simplifying the shape of the R_{space} displayed larger volumes ($\text{mean}(V_{sph}) = 0.30 \text{ m}^3$) than V ($\text{mean}(V) = 0.17 \text{ m}^3$), without showing any improvement in reliability ($s_v(V_{sph}) = 0.09 \text{ m}^3$ against $s_v(V) = 0.06 \text{ m}^3$, $\text{ICC}(V_{sph}) = 0.37$, LoA of $[-0.11, 0.12]$). Therefore, we do not suggest using this approach as an alternative to evaluate the R_{space} .

In its actual state, this instrumented test allowed to equip and instruct a new subject in about 5 minutes; the anatomical calibration that followed could be done within a minute; the evaluation of the reachable ranges as well as the target acquisition could last for 10 to 20 minutes, and the data analysis was totally automated, taking less than 5 seconds to compute and providing automatic reports for further offline analyses.

Moreover, the system Volfon does not require a large recording space, as a conventional motion-tracking setup would and a 2x2 m floor space is enough to install and perform it. The technology used, being originally developed for the mass consumer market is inexpensive, stable and easy to use. As a consequence, there should be no technical barrier for a normal clinical therapist to work with Volfon.

Overall, the final test was tuned to provide accurate and reliable results while limiting its duration to less than 30 minutes. The feasibility was demonstrated but a larger number of subjects will be necessary in order to verify the test reproducibility and the statistical validity of the new scores.

The next step of this study will be to record a larger set of subjects, in order to characterize the levels of R_{space} asymmetry of patients with different pathologies, and of healthy patients. This should demonstrate if this tool, combined with these new metrics is accurate and precise enough to be used for a routine evaluation of the shoulder. In future works, it would also be of interest to study how the R_{space} evolves during the recovery process following a surgery or an injury, and to evaluate the potential to adapt these tools for the patient's follow up. Another topic to explore would be to subdivide the R_{space} in subpart and by comparing the decrease of a subpart against the healthy reference side, determine if some patterns could be related to some particular pathology.

5.7 Conclusion

In this study, we examined the validity and reliability of a novel method for the instrumented assessment of the human R_{space} called Volfon. This test was based on a customized tracking solution build on top of the Controllers, Trackers and HMD from HTC Vive. With this platform was proposed a VR test to guide the subject's *EE* through his R_{space} . This allowed to map the subject's R_{space} and to evaluate the symmetry of his ULs. It is assumed that a healthy subject should display less asymmetry than one with a unilateral lesion or pathology, and therefore this asymmetry score, that we called *Volumetric symmetry* should be able to help in the evaluation of the functional state of the subject's *UL*.

The overall accuracy and reproducibility of the measurement of the R_{space} was assessed experimentally using a test-retest protocol on ten healthy subjects, displaying a sound average volume of $0.17 \pm 0.06 \text{ m}^3$, together with a fair reliability ($\text{ICC} = 0.5$, $N = 20$ arms). From these measurements, the *Volumetric symmetry* was computed finding an average ratio of $17.9\% \pm 16.4$ in healthy subjects and a difference of 2.3% between the test and retest.

Moreover, the technology employed, was selected and tuned to provide a relatively fast (30 min), easy to use and inexpensive setup, that could be, in the future, deployed in a normal medical cabinet with minimum hassle.

Even though Volfon displays great promises, clinical testing will be necessary to validate its ability to differentiate reliably pathologic from non-pathologic conditions, as well as to define the range of pathologies where such a test might be most informative.

This study showed the feasibility to measure the R_{space} of the *UL* with a relatively simple and fast test that displays great potential to add a new and powerful tool into the doctor's arsenal.

5.8 Acknowledgments

The authors would like to thank Nan Wang for his valuable help in the initial choice of the virtual reality platform as well as his help in getting the project started. Additionally, the authors would like to thank Andrea Crema for his advices on the test design.

5.9 Funding

This work was supported by the Lausanne Orthopedic Research Foundation.

5.10 Appendix A: Evaluation of the HTC tracker accuracy

5.10.1 Aim

The aim of this test was to verify if the Tracker's accuracy was the same as the accuracy of the Controllers.

5.10.2 Method

In order to perform this test, 4 trackers (T1-T4) were fixed to a table and equipped with VICON reflective markers. The position of the trackers was measured using 4 VICON T010 cameras. The distance between each pair of trackers was then measured as the distance between the centroid of the 4 VICON markers equally positioned on each tracker, resulting in measurements T_{V12} , T_{V13} , T_{V24} , T_{V34} . Next, the VICON system was turned off, to avoid infrared interferences with the VIVE system, and the Vive system was turned on and used to record the position of its trackers in space and to compute their pairwise distances T_{H12} , T_{H13} , T_{H23} , T_{H34} . The comparison of the difference in RMS distances between the 4 trackers' measurements and their equivalents measured from the VICON system were then used to provide an evaluation of the accuracy of the HTC Vive system. The measurement of the norms was repeated 5 times with the Trackers and the standard deviation of the Trackers was evaluated.

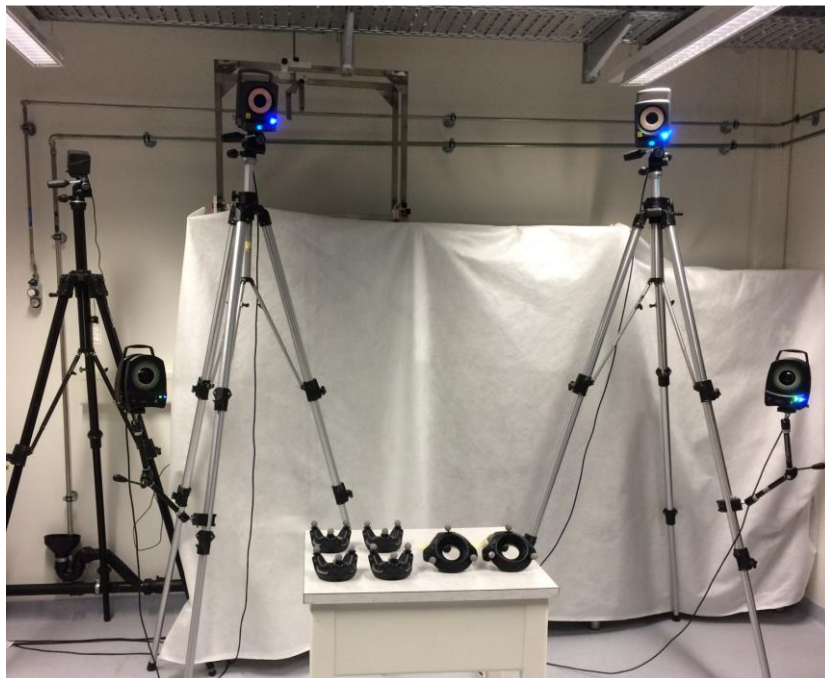


Figure 41: Recording of 4 Trackers with VICON cameras and the HTC Vive.

5.10.3 Results

Table 17: Root mean square (RMS) difference of distance between the positions measured by the Trackers (T12: distance between the trackers 1 and 2, T24: distance between the trackers 2 and 4, ...) and those recorded by VICON, as well as the standard deviation (s_v) and the limits of agreement (LoA)

	RMS	s_v
	[cm]	[cm]
T12	0.00	0.10
T13	0.86	0.02
T24	0.12	0.02
T34	0.17	0.03

5.10.4 Discussion and conclusion

Both the VICON and the HTC Vive system use infrared light and interfere one with each other, blocking us from performing a concurrent test in a situation with motions. However fixing all the sensors on a table, and performing the two sets of recordings successively allowed us to evaluate the static accuracy of the HTC Vive Trackers, resulting in similar results to those of (Kreylos, 2016).

Chapter 6 Use of the Functional Volume for the Evaluation of Patient's Impairment Following a Humeral Fracture⁶

6.1 Abstract

In the previous chapter, the functional test for the upper limb *Volfon* was developed using a customized state of the art tracking solution with a VR headset in conjunction with a set of exercises designed to explore the reachable space of the upper limb. The combination of the system, the test and the derived scores were shown to be usable on healthy subjects. In the current chapter, the test *Volfon* was shortened and adapted to the abilities of clinical patients displaying a broad range of functional impairments of the upper limb. Then, the test was performed by sixteen patients following a test-retest protocol. Results indicated both a good usability of the test, since all the patients were able to finish the test-retest protocol and a good reproducibility of the test, with ICC values of 0.94 for the evaluation of the reachable ranges, 0.91 for the volumes, 0.85 for the *volumetric symmetry* score, 0.87 for the *range score*. All the proposed scores were able to identify the pathologic case in a statistically significant manner. Additionally, the adapted test recorded similar reachable space for the healthy upper limb of clinical patients with respect to the reachable spaces recorded on healthy subject using the longer protocol explained in the previous chapter.

In the next step, the test *Volfon* should be evaluated against specific pathologies and compared against the state-of-the-art metrics, in order to demonstrate its clinical relevance.

6.2 Introduction

From a functional point of view, the *Upper limb (UL)*'s main goal is to place and orient its *end effector (EE)*, the hand, within its *reachable space (R_{space})*. The R_{space} being defined as the volume that the *EE* can reach thanks to the movements of the *UL*, without moving the thorax. Therefor R_{space} can be used as an objective evaluation of shoulder impairment. If one *UL* is affected by a pathology or traumatic injury, a decrease in function is often encountered and is expected to appear as an asymmetry between the R_{space} of the affected *UL* ($R_{space, p}$) and the R_{space} of the sound contralateral *UL* of the patient ($R_{space, c}$).

In the past, Lenarcic and al. (N. Klopčar et al., 2007) identified the R_{space} potential for the functional evaluation of the *UL*. However due to the limitations of the tracking tools available, their experimental work did not reach out to the clinical world. Besides the works on the R_{space} , the most common clinical tools for functional evaluation lack objectivity, since they mostly rely on patients' self-evaluation of their physical capacities (Angst et al., 2011). Other tools such as the *Action Research Arm Test* (Lyle, 1981; Weerdt & Harrison, 1985) or the *Wolf Motor Function Test* (Lyle, 1981) have no evaluation of the kinematics of *UL*, and mostly assess the speed of execution of a set of tasks or, in rarer cases the strength of the *UL* in a specific set of motions. Therefore, several studies (Clément et al., 2017; Coley, 2007; Duc, 2013; Kurillo et al., 2013; Pichonnaz et al., 2017) focused on the development of functional kinematic tests that would be both objective, and clinically usable. One of the unusual features that most of these studies shared, was the use of consumer-grade technologies (cellphone internal sensors, Microsoft Kinect camera), in order to maintain contained costs and a good usability of the system.

By joining the ideas of quantifying the R_{space} with the idea of developing a clinically usable tool for the functional kinematic evaluation of the *UL*, the *Volfon* test described in *chapter 5* was created. This test combined a Virtual Reality (VR) headset, with a motion tracking solution, the *SteamVR Trackers* and *Controllers*, that was adapted for the tracking of the torso and *UL*. The combination of these two

⁶ This chapter is written as a journal paper for further possible publication. Data were collected with the collaboration of Dr. Patrick Goetti, Dr. Nicolas Gallusser, Dr. Frédéric Vauclair.

technologies allowed the design of a sequence of reaching tasks, being adapted in real time to the patient's capabilities, and allowing an automatic and objective assessment of shoulder R_{Space} .

At the end of *chapter 5* the usability of this test was verified on ten healthy subjects, achieving satisfactory results. Next, a pilot study of the *Volfon* test with 5 clinical patients, demonstrated that the test was generally too long and tiresome for clinical patients. The *Volfon* test was therefore simplified by requesting less reaching task leading to some minor adjustments of the test, which shorten it while keeping same order of accuracy.

This new chapter will present this simplified version and its clinical evaluation on patients suffering from different shoulder pathologies limiting *UL*'s functional capabilities. Similar scores of *chapter 5* and more adapted one were evaluated here on patients and their reliability and accuracy were estimated and compared with the results achieved in the previous chapter with healthy subjects.

6.3 Methods

The system and testing protocol used in this chapter was an upgraded version of the one presented in Chapter 5. It uses the same hardware (the Head Mounted Displays (*HMD*); the *Controllers*; the *Trackers* (*SteamVR Trackers*)) mounted at the same body locations (the *HMD* on the head, one *Tracker* on each shoulder strap and one *Tracker* on each wrist, see Figure 35), calibrated using the same protocol (see Chapter 5, section 3.3 *Anatomical calibration*). However, the protocol was modified in order to offer a faster and more reproducible test.

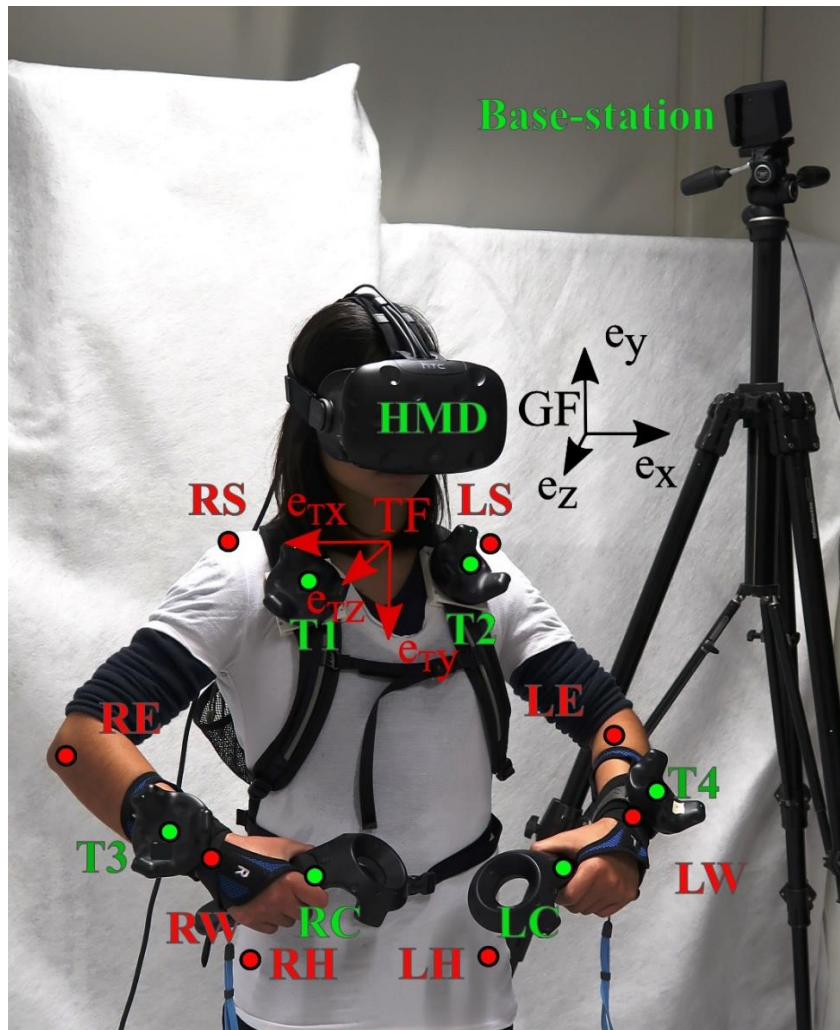


Figure 42: Subject with Trackers on backpack's straps (T1, T2), wrist Trackers (T3, T4), Headset (HMD), Controllers (RC, LC) and Base-station. Anatomical landmarks RS: Right Shoulder, LS: Left Shoulder; RH: Right Hip; LH: Left Hip, which are localized during the calibration process. The tracked position of the right and left wrists (RW, LW) and elbows (RE, LE) are indicated in red.

6.3.1 VR guided test

The setup was similar to the one described in Chapter 5. Shortly, it consisted of projecting the subject was into a virtual reality scenario where the body was replaced by an avatar composed of thorax, head and two ULs (arm, forearm, and hand rigidly attached to forearm using splinters). The avatar was animated in real time using the sensor mounted on the subject's body. Three large mirrors were maintained in the scenario to better search targets and to reinforce the impression of embodiment (Slater et al., 2010).

Both a video feed of what the subject was viewing, as well as a 3rd person view of the scene, were provided in real time to the experimenter who can supervise and control the activities of the patient during the test on his computer, as well as validate the task at the best of the patient's abilities before moving to the next task.

6.3.2 Test procedure

Similar to Chapter 5 (section 3.4.1), first, the maximum internal (H_{int}) and external rotation (H_{ext}) of the UL was estimated by requiring the subject to spear through horizontal arcs placed at the height of RS or LS (Figure 37A). The subject was required to spear into the arc, right in front of his shoulder, and to rotate the UL first internally, measuring the range of internal rotation (H_{int}) then externally, measuring the range of external rotation (H_{ext}). These ranges were measured as the angle between the normal axis of the thorax \vec{e}_z and the vector going from the shoulder to the wrist ($\vec{RW} - \vec{RS}$ or $\vec{LW} - \vec{LS}$).

Here H_{int} , H_{ext} were measured only twice to simplify the test and the mean values (\bar{H}_{int} , \bar{H}_{ext}) were computed for both the right and the left UL. Then 6 vertical arcs (instead of 8 in Chapter 5) were distributed at regular intervals between \bar{H}_{int} and \bar{H}_{ext} (Figure 37 B) while for each one, the maximum elevation range of the patient was recorded as $V_{\{1, \dots, 6\}}$, between \bar{H}_{int} (corresponding to V_1) and \bar{H}_{ext} (corresponding to V_6). The elevation range was computed as the angle between the axis \vec{e}_z of the thorax and the vector $\vec{RW} - \vec{RS}$ or $\vec{LW} - \vec{LS}$ depending on the side being tested. Each one of these ranges was evaluated twice and the average values ($\bar{V}_{\{1, \dots, 6\}}$) were recorded.

Once all internal/external and elevation ranges were estimated for each UL, targets were placed on the arcs. Here to simplify the test the patient was requested to reach only 30 targets (instead of 80 in Chapter 5). *Reached Targets (rTarg)*. It was assumed that the patients could reach easily elevation angle less than 45° and it was useless to tire them on these tasks. Therefore, between 45° of elevation and V_i (with i being the index of the tested arc), 5 targets were placed at regular intervals. They were displayed sequentially, as large green balloons, and the subject was requested to spear through each one of them, as far as he could go, without moving his trunk

Other targets were estimated or interpolated as described below:

- i. *Estimated Targets (eTarg)*: Between an elevation angle of 0° and 45° 10 targets were placed at regular intervals on the vertical arcs between 0° and 45° of elevation and it was estimated that the subject could reach with his *EE* exactly in their direction, with an extension of the UL computed as: $UL_{ext} = A + F$ where A and F are the length of the subject's arm and forearm respectively, as measured during the anatomical calibration (as reported in chapter 5, section 3.3).
- ii. *Interpolated Targets (iTarg)*: Between every two *rTarg* ($rTarg_{i-1}$ and $rTarg_{i+1}$) another target was interpolated. This target was placed at the crossing between the vertical arc and the bisector line cutting the angle formed between $rTarg_{i-1}$, RS/LS and $rTarg_{i+1}$. The UL_{ext} for an interpolated target i was computed as:

$$UL_{ext,i} = (UL_{ext,i-1} + UL_{ext,i+1})/2 \quad (1)$$

This way for each UL, in total 19 targets ($RT_{\{1, \dots, 6\}, \{1, \dots, 19\}}/LT_{\{1, \dots, 6\}, \{1, \dots, 19\}}$), were generated for each vertical arc. The targets were ordered based on their angle of elevation, with $RT_{\{1, \dots, 6\}, \{1, \dots, 1\}}/LT_{\{1, \dots, 6\}, \{1, \dots, 1\}}$ having an elevation angle of 0° and $RT_{\{1, \dots, 6\}, \{1, \dots, 19\}}/LT_{\{1, \dots, 6\}, \{1, \dots, 19\}}$ having an elevation angle of $\bar{V}_{\{1, \dots, 6\}}$. For each of these targets, the position of the wrist was evaluated (estimated, measured or interpolated) and recorded as an *EE* position: $RW_{\{1, \dots, 6\}, \{1, \dots, 19\}}/LW_{\{1, \dots, 6\}, \{1, \dots, 19\}}$, with $RW_{\{1, \dots, 6\}, \{1, \dots, 10\}}/LW_{\{1, \dots, 6\}, \{1, \dots, 10\}}$ corresponding to the *eTarg*; $RW_{\{1, \dots, 6\}, \{11, 13, 15, 17, 19\}}/LW_{\{1, \dots, 6\}, \{11, 13, 15, 17, 19\}}$ corresponding to the *rTarg* and $RW_{\{1, \dots, 6\}, \{12, 14, 16, 18\}}/LW_{\{1, \dots, 6\}, \{12, 14, 16, 18\}}$ corresponding to the *iTarg*.

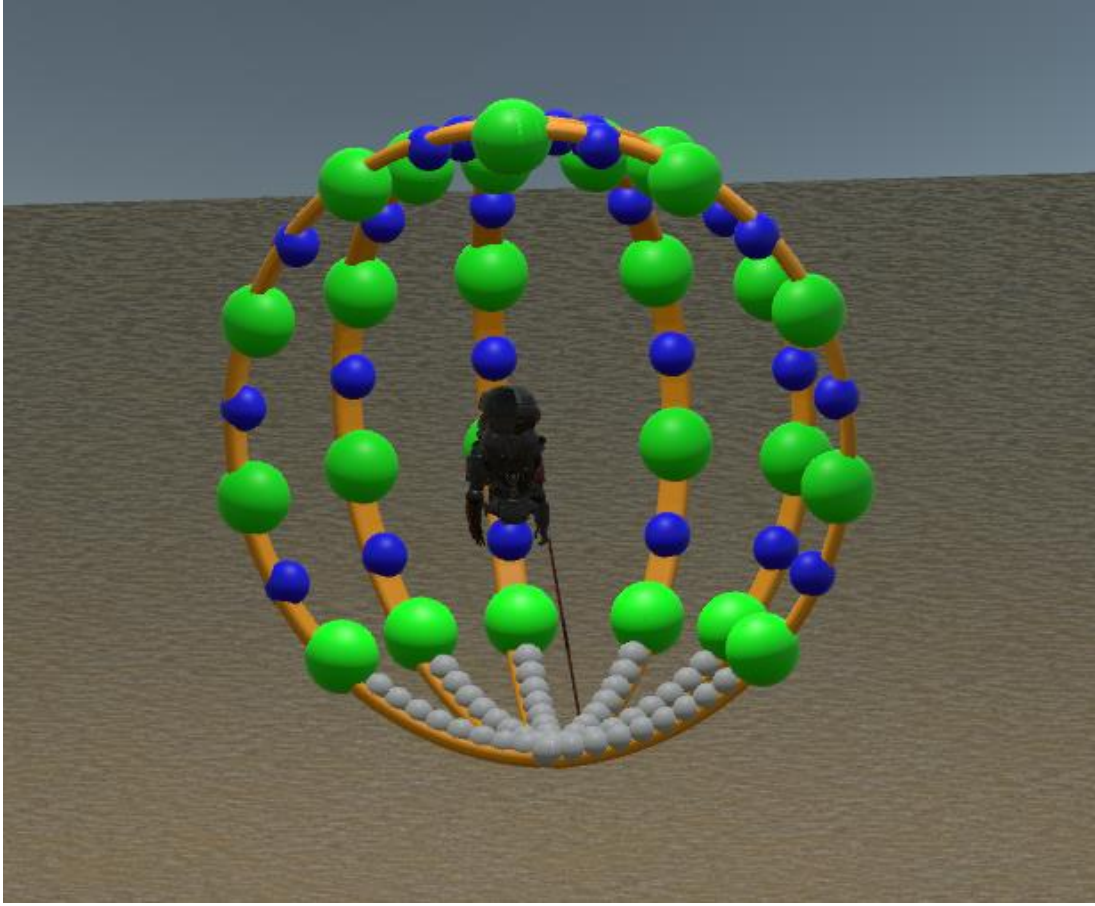


Figure 43: The 6 vertical arcs (V) are displayed in orange, each with its 19 targets displayed in front of a subject's avatar. In grey, are the *eTarg*, in green the *rTarg* and in blue the *iTarg*.

From the evaluation of these ranges of motions and the movements of spearing through the targets, several scores were computed, stored in an external file for further recovery and the results of the different scores were displayed on the experimenter screen.

6.3.3 Data analysis and Scores estimation

In addition to the values of \bar{H}_{int} , \bar{H}_{ext} and \bar{V}_i which express the RoM in horizontal and vertical planes, and their combination (*range score*: R_S), other score related to the R_{space} were estimated as explain in the following sections.

6.3.3.1 Range score

During the measurement protocol, for each UL, eight measurements of range ($\bar{H}_{int}, \bar{H}_{ext}, \bar{V}_{\{1,...,6\}}$) were recorded. A *range score* (R_S) to evaluate the handicap on the ability to elevate the arm was proposed as by sorting $\bar{V}_{\{1,...,6\}}$ by order of magnitude, such as $q_1 = \max(\bar{V}_{\{1,...,6\}})$; ...; $q_6 = \min(\bar{V}_{\{1,...,6\}})$, then dividing the two smallest values by the two largest ones and pondering the score by the median value and the horizontal range resulted in the following definition:

$$R_S = \frac{q_5 + q_6}{q_1 + q_2} \cdot \frac{q_3 + q_4}{2} \cdot \frac{|\bar{H}_{int}| + |\bar{H}_{ext}|}{1000} \quad (12)$$

This value should decrease in case of inconsistent performances or in case of generally low ranges.

6.3.3.2 Reachable volume

Similar to Chapter 5 (section 3.5.1) *RW* locations were used to estimate the right and left *UL* reachable volume (V_R and V_L). However, in this case the both inferred and interpolated *RW* were added to the calculation. To this end, a 3D point cloud composed of the positions of all $RW_{\{1,...,6\}, \{1,...,19\}}$ types, was expressed in the referential of the thorax and centered on the RS, generating a set of 114 vertices:

$${}_{RS}\overrightarrow{RW}_{i,j} = {}^{Thorax}_{GF}R(t) \cdot {}_{GF}\overrightarrow{RW}_{i,j}(t_i) - \overrightarrow{RS}(t) \quad (13)$$

This process eliminated the effect of the motions of the thorax on the UL.

A 3D triangulation was then created from the ${}_{RS}\overrightarrow{RW}_{i,j}$ for *meshing*. The back portion of the volume was connected to the origin (${}_{RS}\vec{o}$) to close the volume with the position of the shoulder. Here, the map of the targets allowed determining a map of how the vertexes (i.e. ${}_{RS}\overrightarrow{RW}_{i,j}$) should be interconnected to generate the volume's external surface. This surface was represented by a set of interconnected triangular surfaces (*mesh*) as shown in Figure 39. By construction the three vertexes forming each triangle were ordered so that the norm of the set would be pointing outside of the volume. Once the surface was meshed, the contained volume was estimated by tetrahedral decomposition (Cook et al., 1980; Egons, 2011), which gave for the right UL:

$$V_R = \sum_k \frac{(\vec{a}_k \times \vec{b}_k) \cdot \vec{c}_k}{6} \quad (14)$$

where $\vec{a}_k, \vec{b}_k, \vec{c}_k$ are the vectors connecting the centroids of the volume $CM = {}_{RS}\vec{o} + \sum_{i,j} ({}_{RS}\overrightarrow{RW}_{i,j})$ to each of the three vertexes of the tetrahedron number k , in the order provided by the mapping. Similarly, V_L was computed using the LS and LW instead of RS and RW. By considering pathological (subscript P) and healthy UL (subscript C as control), V_R and V_L was named V_P or V_C .

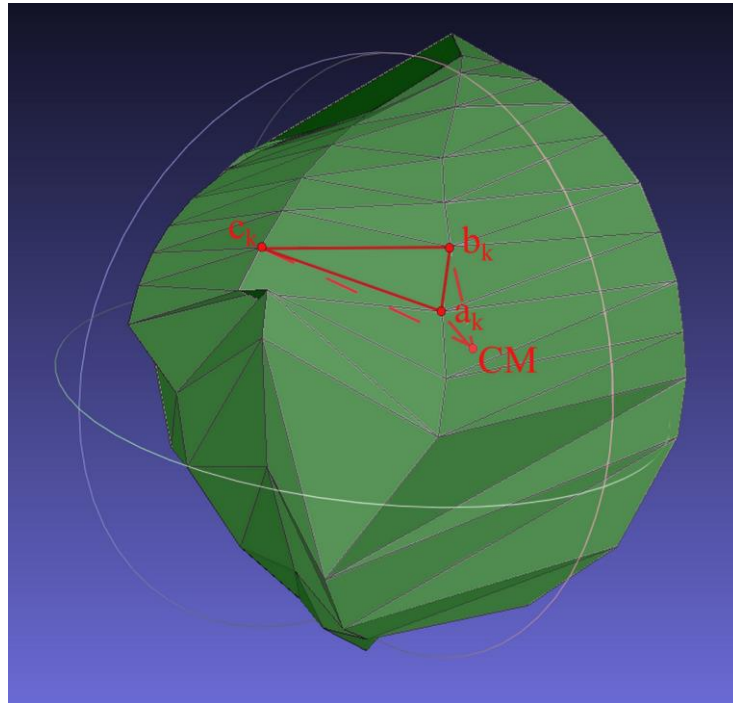


Figure 44: Mesh of the surface of the UL's R_{space} . In red, the tetrahedron "k", composed by three vertices on the surface of the mesh (a, b, c) and one at its centroid (CM)

6.3.3.3 Spherical volume estimator

The *spherical volumetric estimator* was designed as another score for reachable volume. It corresponded to the volume of sphere fitted to the point-cloud formed by ${}_{RS}\overrightarrow{RW}_{i,j}$ and obtaining its center and radius. Next, the referential was shifted to the center of the sphere and the vertexes of ${}_{RS}\overrightarrow{RW}_{i,j}$ were projected on the surface of the sphere creating the set of projected vertexes. To this set of vertexes was added the center of the sphere. Since this set was granted to form a convex volume, it was meshed using the convex hull (*convhull* function of *Matlab 2017a*). The volume V_{Sph} was then computed by *tetrahedral decomposition*, using the same method as presented for the estimation of the R_{space} .

6.3.3.4 Volumetric symmetry

By assuming unilateral shoulder pathology, one could compare the pathologic UL with the healthy one, in order to evaluate the decrease in R_{space} and therefore its decrease in function. The volumetric symmetry ($V_{\%}$) was therefore computed based on symmetry index (Robinson et al., 1987) as:

$$V_{\%} = \frac{|V_H - V_P|}{V_P} \cdot 100 \quad (15)$$

6.3.3.5 Patients and experiences

The simplified *Volfon* test was evaluated on sixteen clinical patients, aged between 21 and 69, displaying a variety of shoulder pathologies restricting its mobility (as reported in Table 1. The protocol was approved by the local ethical committee (CER-VD protocol 85/15), whenever useful the articular ranges of motions were also recorded by the resident surgeon.

Table 18: List of patients, together with their gender, age, pathology or trauma

	Gender	Age	Affected side	Pathology or Trauma
P1	Male	57	Left	Capsulitis
P2	Male	57	Right	Post-traumatic stiffness
P3	Male	41	Right	Capsulitis
P4	Male	47	Right	Retractile capsulitis
P5	Female	54	Right	6 weeks after an open reduction and internal fixation
P6	Female	53	Left	10 weeks after a rotator cuff reinsertion
P7	Male	48	Right	23 weeks after an open reduction and internal fixation, and a cure for pseudoarthritis
P8	Male	51	Left	18 weeks after a rotator cuff reinsertion
P9	Female	69	Right	Capsulitis in inflammatory phase
P10	Male	42	Right	Reinsertion of the supraspinatus muscle
P11	Female	65	Left	Humeral fracture; 27 weeks after an open reduction and internal fixation; joined with necrosis of the humeral head and stiffness
P12	Female	21	Left	Dysplasia of the proximal humerus
P13	Female	47	Right	Rotator cuff reinsertion
P14	Male	43	Left	Rotator cuff reinsertion
P15	Female	55	Right	Fracture of the distal clavicle
P16	Female	53	Left	Retractile capsulitis

Test and retest of simplified *Volfon* were performed on all patients, by respecting few minutes break between the test and the retest. Anatomical calibration was performed a second time from scratch during the retest protocol. The repeatability was then evaluated, though the differences between the scores of the test and the retest, the absolute reliability was indicated by the limits of agreement ($LoA = \mu \pm 1.96\sigma$), the test reproducibility through the Intraclass Correlation Coefficient ($ICC_{x,y} = \frac{\sum_i (x_i - \mu_{x,y}) \cdot (y_i - \mu_{x,y})}{(N-1) \cdot \sigma_{x,y}}$) and the presence of a bias through the Wilcoxon rank sum test (Bruton et al., 2000). Additionally, those results were also visualized using a correlation and a Bland and Altman plot. The hypothesis that the scores between the pathologic and control *UL* side were statistically equivalent for the different scores were assessed using the Wilcoxon rank-sum test. The hypothesis that the *volumetric symmetries* of the healthy subjects presented in chapter 5 were equivalent to those of the patients presented in this chapter were evaluated using the two-tailed Mann-Whitney-Wilcoxon test (Nachar, 2008).

6.4 Results

All the patients in this pool were able to complete the test, and most understood the instructions easily and were able to perform a repetition of the test within 15 minutes, including the time to equip them and to explain them the tasks that they would have to perform.

The ranges of motions of the patients are presented on Table 19 for the test and Table 20 for the retest. It displayed an excellent ICC of 0.94. In average mean differences of 22.5° and 51.9° were observed for H_{int} and H_{ext} between pathologic and sound side. These differences were in average of 63.4° for the V_i .

Table 19: Mean values of RoM (in degrees) in horizontal (\bar{H}_{int} , \bar{H}_{ext}) and vertical plane ($\bar{V}_{\{1,\dots,6\}}$) for pathological *UL* side (P) and healthy side (C) considered as control *UL* side.

Patients	\bar{H}_{int}		\bar{H}_{ext}		\bar{V}_1		\bar{V}_2		\bar{V}_3		\bar{V}_4		\bar{V}_5		\bar{V}_6	
	P	C	P	C	P	C	P	C	P	C	P	C	P	C	P	C
1	19	95	54	102	138	192	147	170	145	168	191	164	133	166	139	167
2	48	86	27	87	128	185	128	168	122	168	232	166	156	162	164	168
3	49	64	77	113	122	181	114	259	85	167	99	168	129	191	112	182
4	51	64	46	102	125	196	123	186	125	174	188	168	144	170	118	172
5	59	58	49	80	29	150	33	161	30	153	38	179	29	143	38	136
6	28	51	34	108	75	196	79	193	71	181	75	173	76	174	70	173
7	62	56	42	128	59	183	42	167	25	174	49	193	32	166	29	171
8	62	62	47	67	34	124	43	96	36	99	38	102	51	115	41	127
9	36	72	62	83	75	203	79	181	68	169	69	167	74	172	68	167
10	42	58	38	101	161	162	154	164	152	156	159	159	144	172	154	165
11	60	60	66	108	122	163	119	158	106	158	112	198	127	180	172	181
12	33	53	30	74	174	156	156	158	148	157	151	157	143	155	139	116
13	51	48	27	86	55	169	51	178	60	167	54	170	46	171	41	173
14	60	56	24	95	76	143	82	143	63	142	73	149	67	168	50	184
15	63	100	61	113	177	180	174	174	172	173	167	180	172	180	170	174
16	22	99	69	110	154	188	153	179	128	172	190	167	110	179	140	170

Table 20: Mean reachable ranges (in degrees) for the horizontal internal (\bar{H}_{int}) and external (\bar{H}_{ext}) rotation, as well as the mean vertical reachable ranges ($\bar{V}_{\{1,...,6\}}$) for the 6 vertical arcs during the retest. S stands for subject, P for pathological *UL* side and C for control *UL* side.

S	\bar{H}_{int}		\bar{H}_{ext}		\bar{V}_1		\bar{V}_2		\bar{V}_3		\bar{V}_4		\bar{V}_5		\bar{V}_6	
	P	C	P	C	P	C	P	C	P	C	P	C	P	C	P	C
1	35	94	55	110	154	208	175	189	175	181	158	167	159	169	170	168
2	53	85	50	95	143	188	125	180	126	169	172	172	155	168	151	170
3	35	61	43	90	67	173	97	175	65	166	63	155	76	164	69	163
4	50	76	49	106	131	195	130	183	121	179	117	177	136	162	127	163
5	55	51	28	78	18	139	28	135	46	131	26	175	27	136	27	134
6	30	58	61	114	80	208	103	194	73	181	85	179	126	169	111	174
7	71	61	29	113	42	184	48	175	23	169	48	196	25	175	28	170
8	58	86	54	73	59	62	41	115	43	87	41	85	57	122	60	101
9	60	70	65	112	79	190	66	192	53	177	58	164	68	171	65	168
10	52	60	34	110	181	168	179	165	159	155	167	163	154	174	155	172
11	36	76	51	119	122	161	120	161	87	159	104	223	126	168	149	180
12	57	68	56	106	219	170	180	180	176	165	147	178	147	177	123	191
13	30	34	49	103	53	174	51	169	31	171	60	175	50	167	55	169
14	63	64	45	99	66	160	64	155	57	154	73	161	77	176	63	170
15	59	100	64	122	197	175	183	175	167	170	163	192	172	174	165	178
16	18	102	70	109	146	195	147	186	109	168	124	168	113	178	71	169

The *Range* scores which express a combination of different RoM are presented on Table 21. In average the mean differences of 10.8 was observed for Rs between pathologic and sound side. This difference was 12.3 in average for retest.

Table 21: Test and retest values of Range score (R_s) of 16 patients comparing pathological *UL* side (P) and healthy side (C) considered as control *UL* side.

Patients	R_s			
	Test, P	Test, C	Retest,P	Retest, C
1	11.5	22.2	18.6	22.6
2	10.4	15.8	14.6	19.5
3	8.8	21.7	4.2	19.2
4	8.8	20.9	13.9	22.9
5	2.8	14.6	1.1	10.7
6	6.1	21.6	5.5	25.3
7	1.9	25.0	2.3	21.4
8	3.4	10.1	4.8	6.2
9	6.5	19.0	5.7	25.9
10	13.9	20.2	15.1	22.6
11	9.6	23.8	7.9	20.2
12	11.4	12.2	11.6	23.5
13	3.7	17.5	2.1	24.5
14	4.9	12.4	6.5	21.1
15	27.2	28.8	22.4	29.1
16	10.2	28.4	6.9	25.7
Mean	8.8	19.6	8.9	21.3
s_v	6.05	5.57	6.33	5.72

Comparing the calculation of the V_P and V_C of the test against the retest classes ($N=32$) provided an ICC of 0.93 on the pathologic side and an ICC of 0.85 on the control side, LoA of [-0.15, 0.00]. No significant equivalence was observed between test and retest based on the Wilcoxon test ($p=0.2$). The Bland and Altman plot (Figure 45) indicates a slight bias (0.01). All values are reported in Table 22.

The volumetric symmetries (Table 22) did not present a significant difference between the test and the retest ($p=0.80$), with an ICC of 0.85 between the test and the retest.

The alternative volumetric estimator V_{Sph} displayed a slightly lower pair of ICCs, with 0.93 on the pathologic side and 0.80 on the control side, and LoAs of [-0.16, 0.00]. No statistical equivalence was observed between test and retest ($p=0.21$).

Visual evaluation of the reconstructed R_{space} of every patient is also possible through a custom-built Unity script, as illustrated on Figure 46. This figure allows to clearly see a functional handicap in the patient's ability both to elevate the right arm as well as to rotate it toward the internal and external directions.

Table 22: Reachable pathologic side (V_p) and control side volume (V_c) and volumetric symmetries ($V_{\%}$) of ten subjects during the test and retest.

Patients	V_p, m^3	V_c, m^3	V_p, m^3	V_c, m^3	$V_{\%}, \%$	$V_{\%}, \%$	V_{Sph, P, m^3}	V_{Sph, C, m^3}	V_{Sph, P, m^3}	V_{Sph, C, m^3}
	Test	Test	Retest	Retest	Test	Retest	Test	Test	Retest	Retest
1	0.12	0.21	0.14	0.16	43.38	15.85	0.12	0.21	0.15	0.18
2	0.18	0.16	0.17	0.22	-10.88	21.26	0.20	0.18	0.17	0.24
3	0.10	0.20	0.07	0.14	52.46	49.48	0.11	0.30	0.07	0.16
4	0.13	0.16	0.16	0.17	18.38	7.28	0.14	0.20	0.16	0.20
5	0.04	0.14	0.01	0.12	73.59	88.91	0.03	0.15	0.03	0.11
6	0.08	0.14	0.10	0.20	43.13	48.79	0.08	0.16	0.11	0.23
7	0.02	0.15	0.02	0.16	88.04	86.67	0.03	0.16	0.03	0.16
8	0.04	0.09	0.05	0.08	60.45	33.63	0.04	0.08	0.05	0.08
9	0.13	0.19	0.17	0.20	34.64	15.57	0.13	0.22	0.17	0.23
10	0.15	0.27	0.21	0.30	46.04	30.67	0.16	0.29	0.22	0.31
11	0.15	0.23	0.12	0.24	36.14	48.73	0.15	0.24	0.13	0.24
12	0.10	0.10	0.13	0.19	1.26	32.96	0.11	0.10	0.16	0.20
13	0.02	0.10	0.02	0.13	77.74	84.49	0.03	0.10	0.02	0.14
14	0.05	0.11	0.06	0.15	54.60	59.17	0.05	0.11	0.06	0.15
15	0.25	0.34	0.23	0.31	25.86	25.63	0.29	0.35	0.27	0.33
16	0.26	0.33	0.22	0.32	21.63	30.41	0.27	0.37	0.24	0.37
Mean	0.11	0.18	0.12	0.19	41.7	42.5	0.12	0.20	0.13	0.21
s_v	0.07	0.08	0.07	0.07	26.8	26.0	0.08	0.09	0.08	0.08

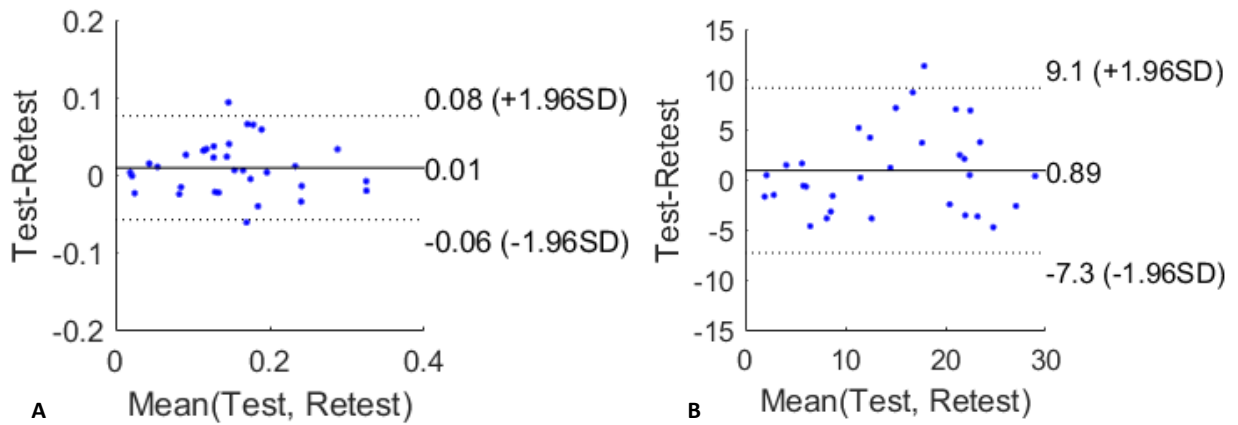


Figure 45: (A) Bland-Altman plot of the measurements of R_{Space} between the test and the retest. With Δ being the difference Test-Retest and $Mean$ representing the mean value of the test and retest measurements (V_R, V_L). (B) Bland-Altman plot of the measurements of R_S between the test and the retest.

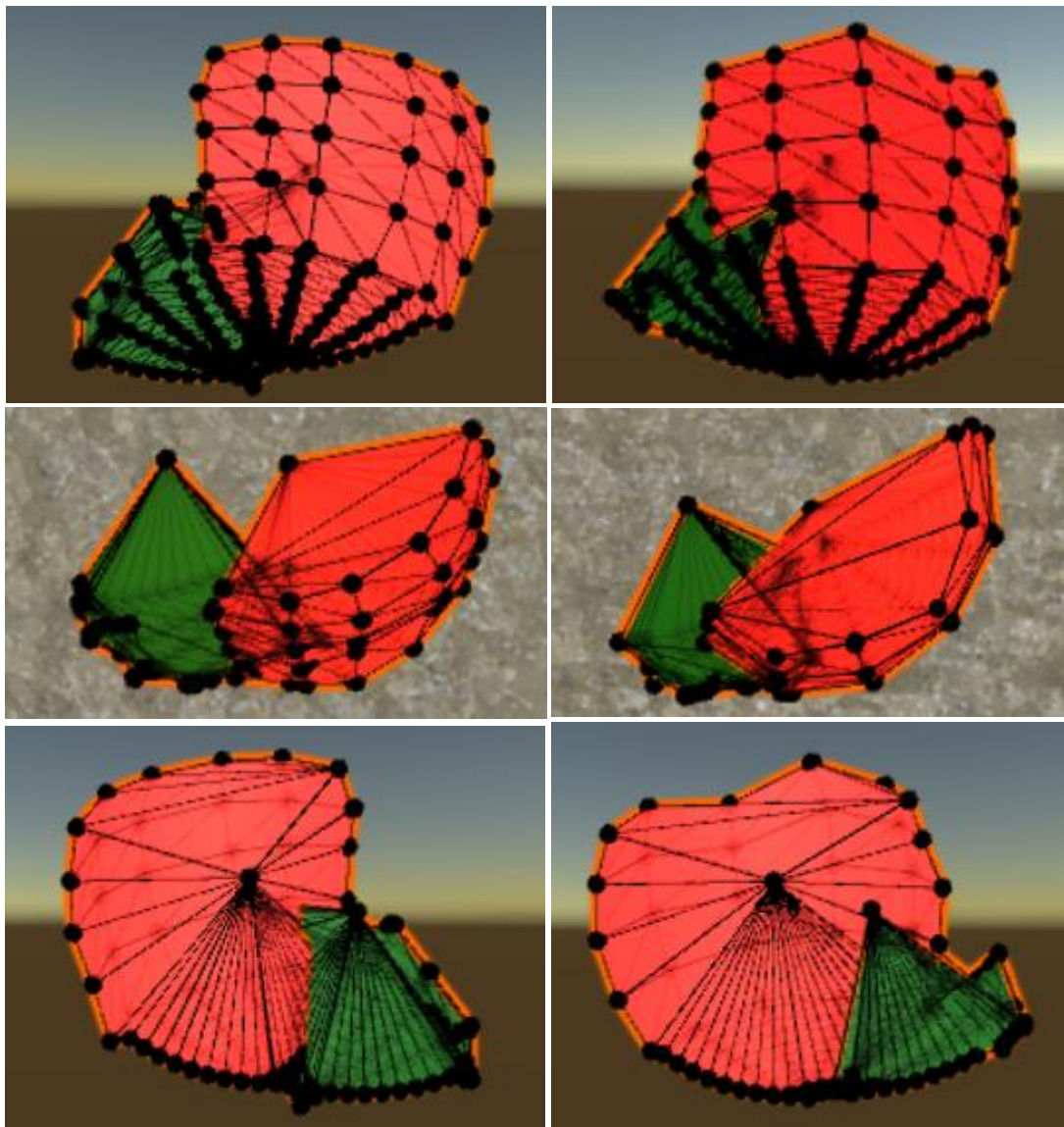


Figure 46: The volume in green represents the right R_{space} , while the volume in red represent the left R_{space} . The black dots represent positions that where recorded, estimated or interpolated during the test. Left column: reconstructed R_{space} of patient P10 during the test. Right column: reconstructed R_{space} of patient P10 during the retest. The first line displays the frontal view, the second, the top view and the third the back view.

6.5 Discussion

In the previous chapter (Chapter 5) we developed a VR based measurement system *Volfon* for estimation of the functional mobility of the shoulder based on volume reached by the arm. While the system shown was simple and convenient to use, inexpensive, objective and reliable it was not adapted for clinical use due mostly to the high number of reaching task and duration of the measurement. Actually, patients were observed to be easily confused in front of the virtual reality setup, and quickly tired (Appendix A). Therefore we adjusted the test for a more efficient use with clinical patients by reducing the test duration by half (10 to 15 minutes instead of 20 to 30 minutes), improving the guidance of the patients, decreasing the number of movement and reaching task (30 instead of 80), while compensating this deficiency with estimated and interpolated targets in order to maintain enough vertices in the point-cloud to perform a proper volumetric evaluation.

The *simplified Volfon* was evaluated on 16 clinical outpatients in a regular medical cabinet at the local university hospital in order to provide a technical validation of the system usability, in the clinical context, for a wide range of UL pathologies. The patients were able to perform the test and quickly understood the tasks they were required to perform. We observed however, the vertical arcs on the extrema of external and internal rotation, were sometimes difficult to see and the related tasks, difficult to perform. This was

particularly problematic in patients with neck stiffness. An improved visual strategy is needed to guide them toward these targets, such as an arrow floating in front of the subject and indicating him where to search for the target, might be of use.

We proposed two type of quantitative scores to evaluate shoulder disabilities based on RoM and R_{space} . For the first type we proposed two scores: Elevation score (Q_s) and Range score (R_s). The RoMs as expressed by horizontal and vertical movement ($\bar{H}_{int}, \bar{H}_{ext}, \bar{V}_{\{1,...,6\}}$) were significantly lower ($p < 0.001$) on the pathologic side, than on the control one, as indicated on Table 19 and Table 20. However, in some cases, such as \bar{V}_1 for the test of P12, we observed the opposite, most probably due to a sound RoM in that direction on the pathologic side (\bar{V}_1 for the pathologic side: 174° , and for the control side: 156°). This inversion was also found in the equivalent retest measure (\bar{V}_1 for the pathologic side: 219° , and for the control side: 170°). The other score, the *Range score* (R_s) obtained by aggregating different RoMs was able to systematically detect the pathologic side. Its value was significantly lower ($p < 0.01$) on the pathologic side (mean($R_{s,p}$) = 8.9; $s_v(R_{s,p})$ = 6.2) than on the control one (mean($R_{s,c}$) = 20.5; $s_v(R_{s,c})$ = 5.6). Its reproducibility was good, with an ICC of 0.86 on the pathologic side and 0.62 on the control side but LoA was large [-23.64, 0.49]. The Wilcoxon test demonstrated the test data to be statistically equivalent to the retest data with a p-value of 0.47.

The second type of score was based on the evaluation of the R_{space} , the variability of the estimated volumes ($s_v(V_p) = 0.073 \text{ m}^3$, $s_v(V_c) = 0.074 \text{ m}^3$) was similar between the pathologic and the control UL, yet higher than the variability of previous healthy subjects ($s_v(V_{healthy}) = 0.057 \text{ m}^3$, see Chapter 5). Comparing the test-retest measurement provided good ICC, with 0.93 for the pathologic side and 0.85 for the control side. Higher age and disability of the patients may be the causes for this higher variability of the R_{space} . The Bland-Altman plot (Figure 45) also indicated that the volumes on the second test tended to be slightly smaller than those of the first test, suggesting a fatigue effect and the fact that the test should not be made longer. As expected, the *volumetric symmetry* ($V_{\%}$) was shown to be significantly higher ($p < 0.001$) by the Mann-Whitney test, and more variable in the patients ($V_{\%} = 42.1 \pm 26.4\%$), than in the healthy subjects ($V_{\%, healthy} = 17.9 \pm 16.7\%$). However, the reproducibility was not always good, with patients sometimes doing errors on the first test, or getting tired and less involved in the retest phase. Designing a very short training phase to help them perform the tasks correctly without observing the effects of fatigue, might be useful. The *spherical volumetric estimator* (V_{sph}) performed in a comparable way than the *Volume estimator* (V), estimating slightly larger volumes (mean(V_{sph}) = 0.16 m^3 ; mean(V) = 0.15 m^3) and displaying a slightly higher standard deviation ($s_v(V_{sph}) = 0.082$; $s_v(V) = 0.074$), but still show significant difference between pathological and sound UL ($p < 0.001$). Its ICC values were slightly lower, with 0.93 for the pathologic side and 0.80 for the healthy one.

Further comparison between the healthy subjects recorded in chapter 5 shows that the mean R_{space} is similar between the healthy subjects (mean($V_{healthy}$) = 0.174 m^3) and the control side of the patients (mean(V_c) = 0.188 m^3) of this experiment. The R_{space} on the pathologic side was significantly ($p < 0.001$) smaller (mean(V_p) = 0.115 m^3). The *volumetric symmetry* was significantly higher ($p < 0.001$) in the patients ($V_{\%} = 42.1 \pm 26.4\%$) than in the healthy subjects ($V_{\%, healthy} = 17.9 \pm 16.7\%$). This allows a good discrimination, but due to the high standard deviation, misclassifications are possible, in particular if the patient has only a small functional impairment, such as P2 (the only misclassified patient). The author would suggest not to consider *volumetric symmetries* lower than 20% as indicators of a pathology while using this test.

In the future, to further reduce the execution time and improve the execution reliability, the virtual reality scene could be further improved, in order to better guide the patients through the tasks, with extensions like an indicator warning both the user and the therapist when the motions are not performed properly (for example, an indicator detecting when the elbow gets flexed). Additionally, the clinical environment (hospitalisation, testing equipment, ...) may alter the natural behaviour of the patients and could have an impact on the performed test. Further work on the virtual reality scenario could improve the esthetics of the scenario and gamify it, to better distract the patient from their environment while increasing patients' involvement and motivation. Additionally, the explanation that the therapist provides to the patients at the beginning of the test have not been standardized and are still evolving. They may become clearer with more practice, decreasing the initial learning phase and therefore decreasing the scores' variability. Then, a clinical validation of the use of this tool for specific pathologies would be necessary prior its clinical deployment. From a clinical perspective, follow up studies of patients, monitoring the evolution of the R_{space} , would allow to better understand the return to function of patients' affected ULs, and could be used to better advise them on the treatment. Finally, creating a database, displaying typical R_{space} for different pathologies of the UL, would allow more in depth analysis of the measurements performed by this tool potentially improving its diagnostic power.

6.6 Conclusion

In this chapter, we presented the clinical adaptation and technical evaluation of the functional test for the UL: *Volfon*. This test combines a customized state of the art tracking solution with a VR headset, to guide the patient through his tasks, evaluate his performances in real time, and adapt the tasks difficulties to the patient's performance. It was created and assessed on healthy

subjects in previous work, but later, it had to be adapted to the endurance of clinical patients, by reducing the number of reaching motions, required from each patient to complete the test. This was achieved while maintaining similar volumetric scores ($\text{mean}(V_{\text{healthy}})=0.174 \text{ m}^3$; $\text{mean}(V_C) = 0.188 \text{ m}^3$) and improving the reliability ($\text{ICC}_{\text{lab}} = 0.5$; $\text{ICC}_{\text{clinical}} = 0.91$), by replacing some of the motions with estimated and interpolated evaluation of the subject's performance on the targets that were not measured anymore. The test provided similar R_{space} between the healthy UL side of clinical patients and healthy subjects, as measured within Chapter 5. Moreover, the test was able to discriminate in a statistically significant manner between the healthy and pathologic side of patients, as long as the pathology caused a decrease of more than 20% of the R_{space} on the affected side. The test-retest protocol indicated an excellent reproducibility for the evaluation of the R_{space} with ICCs of 0.93 and 0.85 for the pathologic and control sides respectively, and a good reproducibility for the $V_{\%}$ score ($\text{ICC} = 0.85$). It was also able to assess the reachable ranges of the patients ($\text{ICC} = 0.94$) and to compute a *range score* with excellent reliability ($\text{ICC} = 0.86$ and 0.62 for the pathologic and healthy sides respectively).

Comparing the healthy UL of clinical patient with the healthy UL of healthy subjects in the laboratory provided similar results with the mean volume for healthy subjects being of 0.174 m^3 with the previous protocol, and slightly larger for the non-affected side of the clinical patients on the new protocol, with an average reachable volume of 0.188 m^3 . At the same time, the R_{space} on the pathologic side was consistently smaller, with a volume of 0.115 m^3 . This led to a *volumetric symmetry* being much higher in the patients ($V_{\%}=60.3\pm46.8\%$) than in the healthy subjects ($V_{\%, \text{healthy}}=17.9\pm16.7\%$). However, one of the patients displayed a close to functional performance, indicating that with *volumetric symmetries* lower than 20%, no conclusion should be drawn about the affected side.

This test, thanks to its versatility, high degree of automation, convenient deployment and accurate results, could be adapted for different use cases, including the study of the effect of different pathologies on the kinematic of the UL, as well as the development of a follow-up tool for the monitoring of the progresses of patients during functional UL rehabilitation.

6.7 Acknowledgments

The authors would like to thank Nan Wang for his valuable help in the initial choice of the virtual reality platform as well as his help in getting the project started.

6.8 Funding

This work was supported by the Lausanne Orthopedic Research Foundation.

6.9 Appendix A: Preliminary evaluation of the Volfon test on clinical patients

The test protocol presented in Chapter 5, section 3.4.2 was evaluated on 5 clinical patients for a test-retest protocol. Many patients encountered difficulties in performing the full test-retest protocol:

- Patient P5 was scared by the idea of putting on the virtual reality helmet and refused to perform the test. Therefore, he was excluded from the test.
- Patient P2 got frustrated during the test by not being able to understand easily where the targets to reach for where and after some trials declined to continue. Due to an insufficient amount of data recorded, P2 was excluded from the test.
- Patient P3 finished the test but refused to stay for the retest because he was too tired.

The ranges of motion recorded for every patient are presented in Table 23 and

Table 24, the *Elevation scores* in Table 25 and volumetric scores in Table 26. Unavailable data were noted as “-”.

Table 23: Mean values of RoM (in degrees) for 3 subjects (S) in horizontal (\bar{H}_{int} , \bar{H}_{ext}) and vertical plane ($\bar{V}_{\{1,...,8\}}$) for pathologic UL side (P) and the control side (C).

S	\bar{H}_{int}		\bar{H}_{ext}		\bar{V}_1		\bar{V}_2		\bar{V}_3		\bar{V}_4		\bar{V}_5		\bar{V}_6		\bar{V}_7		\bar{V}_8	
	C	P	C	P	C	P	C	P	C	P	C	P	C	P	C	P	C	P	C	P
1	-	66	-	101	185	163	176	151	166	152	175	152	166	147	163	157	163	128	186	178
3	35	-	60	-	165	49	161	60	160	69	166	79	167	79	163	83	166	85	174	85
4	58	-	65	-	180	142	170	160	168	161	166	153	164	154	164	161	167	177	175	169

Table 24: Mean reachable ranges (in degrees) for the horizontal internal (\bar{H}_{int}) and external (\bar{H}_{ext}) rotation, as well as the mean vertical reachable ranges ($\bar{V}_{1,...,8}$) for the 8 vertical arcs during the retest. S stands for subject, P for pathologic UL side and C for control UL side.

S	\bar{H}_{int}		\bar{H}_{ext}		\bar{V}_1		\bar{V}_2		\bar{V}_3		\bar{V}_4		\bar{V}_5		\bar{V}_6		\bar{V}_7		\bar{V}_8	
	C	P	C	P	C	P	C	P	C	P	C	P	C	P	C	P	C	P	C	P
1	-	65	-	95	182	152	178	156	169	148	169	147	155	149	168	158	162	165	180	179
3	-	-	-	-	-	-	-	-	-	-	-	-	-	-	-	-	-	-	-	-
4	47	-	67	-	183	132	203	160	178	163	173	155	174	155	173	154	172	141	180	173

 Table 25: Test and retest values of *Elevation* score (Q_s) of 3 patients comparing control UL side (C) and pathologic (P) UL side.

S	Q_s			
	Test, C	Test, P	Retest, C	Retest, P
1	90.5	72.1	101.4	73.3
3	80.8	137.5	-	-
4	78.6	138.9	77.7	135.2

 Table 26: Reachable pathologic side (V_P) and control side volume (V_C) and volumetric symmetries ($V_{\%}$) of three subjects during the test and retest.

S	V_C, m^3	V_P, m^3	V_C, m^3	V_P, m^3	$V_{\%}, \%$	$V_{\%}, \%$
	Test	Test	Retest	Retest	Test	Retest
1	0.16	0.07	0.13	0.03	74.0	125.7
3	0.07	0.02	-	-	126.0	-
4	0.15	0.09	0.10	0.08	50.3	17.4

An error was encountered while exporting the right horizontal ranges ($\bar{H}_{int}, \bar{H}_{ext}$), therefore the recorded value was not available for offline analysis.

Many patients struggled to finish the test-retest protocol, complaining of its duration, and of the difficulty to find the targets that they should reach for. Therefore the actual test protocol was considered improper for usage with clinical patients, as presented in Chapter 6, section 3.

Chapter 7 Conclusions and Perspectives

7.1 Achieved results

The main goal of this thesis was to develop new tools to improve the evaluation and simulation of instable GH joint. Toward this objective two systems were developed and evaluated. The first is a robotic, custom-designed system for the simulation of the glenohumeral instability in prosthetic joints. The second, *Volfon*, is the combination of a VR headset with a customized system for the tracking of the UL's motions that was used for the functional evaluation of the UL, and in particular of its R_{space} . The main results and contributions for both systems are summarized in the following sections.

7.1.1 Robot for the simulation of Glenohumeral instability

A 5-DoF robotic simulator was designed and built to model GH instability. The simulator is equipped with 3 linear hydraulic actuators, allowing it to reproduce the internal net forces present in a physiological shoulder during activities of daily living (with forces up to 2kN in any direction). Additionally, the prosthetic GH joint mounted within can perform GH translations both on the inferosuperior and on the anteroposterior axes, with ranges sufficient to provoke dislocations. The simulator is also able to control the rotations about these two axes, using two rotary DC motors, while rotations about the mediolateral axis have been neglected, due to the perfectly hemispheric prosthetic humeral head. The prosthetic joint mounted in the simulator is easily detachable and different commercial shoulder prostheses can be mounted in the robot to be tested. It is also possible and recommended to use a material which mimics the properties of the natural bone to fix the glenoid in the machine. Indeed, experiments performed in Chapter 3 (section 3.4.3) indicated that mounting the glenoid implant in a stiff socket would make the joint more stable than it would be in natural conditions. Therefore, for most of the subsequent experiments, the glenoid was cemented in a material with mechanical properties similar to those of the natural glenoid bone (called Sawbone foam), creating a set of inserts composed by the Sawbone, where the glenoid implant was cemented, before mounting the whole insert in the simulator's socket.

A control strategy for the robot was implemented and fine-tuned, achieving satisfactory performances. On the linear actuators, the settling time (within 1% error) was of 0.6 sec in force control. The displacements of the implants were measured with high precision ($<0.1\text{mm}$), by sensors placed on the axes of the actuators themselves. The rotatory motions were also measured by highly accurate encoders, but due to the transmission mechanism between the motor axes and the prosthesis, the final angular accuracy was evaluated to be of 0.5° in the worst conditions (by comparison against an external reference system).

The performance of the simulator was evaluated in five different case scenarios:

1. Reproducing the first part of the wear test ASTM F2028-14 (International, 2014), to identify the force needed to cause a dislocation of the joint in a clear context. The joint was found to be much more stable in our own simulator with respect to the robotic wear test of Tornier-Wright Medical (Montbonnot-Saint-Martin, France), resulting in the adoption of a softer Sawbone sockets under the glenoid prostheses instead of the initially stiff PA2200 socket.
2. Using the 3D contact force pattern recorded *in vivo* in a patient with a total shoulder replacement during a countered external rotation of the arm (Orthoload patient S1R_300605_1_20 (Bergmann, 2009)) as a reference. The force pattern was reproduced on a prosthesis mounted in the simulator. We hypothesized only the forces and the GH translation should vary since the arm was not moving. Since the orientation of the glenoid relatively to the humeral head was not known, it was arbitrarily decided to have both axes aligned ($\alpha=0^\circ$ and $\beta=0^\circ$). The test resulted in a stable joint (with small GH translations, close to the center of the joint) with a reliable dynamic force tracking ($\text{RMSE} < 6 \text{ N}$, $R^2 > 0.98$ for all actuators).
3. The previous test had an unrealistic orientation of the two implants, one with respect to each other. Based on the radiographic measurement of 11 patients, a more realistic GH orientation was selected ($\alpha=40^\circ$ and $\beta=-10^\circ$) and tested with the same force pattern as presented in the previous test. The results were similar: a clean dynamic force tracking ($\text{RMSE} < 6 \text{ N}$, $R^2 > 0.98$ for all actuators) and a stable and well centred joint.

4. In this test, the previous force pattern was sampled at regular intervals to extract five samples. For each of the five situations, the GH joint was set flat ($\alpha=0$ deg and $\beta=0$ deg) and centered. Then the force sample was applied as a continuous force, and the orientation of the joint was slowly modified to identify, within what range of orientations the joint would remain stable (in the sense that no dislocation would occur). This test provides an idea of the sensibility of the patient to different orientations of the glenoid within the scapula. This test allowed to verify the ability of the simulator to safely deal with dislocations, as well as to show the sensibility of the joint, not only to the force being applied, but also to the joint orientation, which is underreported in the literature.
5. The robotic simulator was coupled with the patient specific MS models of three clinical patients with TSA, in order to evaluate numerically, the expected force patterns and GH orientations present in those patients during three tasks (task_{abd} , task_{hand} , task_{should}). The force and angular commands computed from the MS model were reasonable and could be evaluated using the same quasi-static simulation as presented in point 4. The robotic simulator was able to reproduce the commands properly but demonstrated levels of GH instability that were not present in the patients. Moreover, the majority of dislocations were directed superiorly. Superior dislocations are virtually inexistent in real patients, due to the presence of a set of passive stabilizing structures (the acromion, the bursae, the coraco-acromial ligament, etc). Their absence could have been compensated in previous experiment by a rotation of the glenoid component that would compensate for these eccentric motions. However, in this last experiment, all the DoFs were controlled and could not be used to stabilize the model. Therefore, the absence of the superior passive stabilizers of the shoulder could be a reason for this unexpected result. However, by chaining the MS model with the robotic model, many other potential sources for errors were created, which may lead to the same problematic behaviour. The orientation of the glenoid implant was available in the surgical planning and should present minimal errors, but the orientation of the humeral head implant was not specified, and due to the large inter-patient variability of the humeral bone morphology, using average values, as was done in this study could cause errors in the computed orientations of the GH implants of up to 45° . As indicated by the tests in point 4, such errors could change the implant's stability profile. Additionally, the support under the glenoid implant was softened for this last set of tests through the use of Sawbone's sockets. However, the compressive properties of the bone in the glenoid cavity are poorly defined, with large variations being presented in the literature. As indicated by previous experiments, the use of a stiffer support would have provided more stability to the joint. Measurement or evaluation errors on any of the parameters of the MS model or of the software could cause biases in the simulation and negatively affect its final outcome, without compromising any of the previous tests. A detailed review of the possible sources of error present in this experiment is available in Chapter 4, section 4.5.

In its actual state, this robotic GH simulator is able to reproduce force patterns and GH orientations reliably. However, it is not yet able to predict GH instability, and will need more work before being used as a tool for surgical planning.

7.1.2 Volfon: A system for the instrumented functional evaluation of the upper limb

An instrument for the measurement of the R_{space} was developed as a combination of a set of seven objects tracked in space using the lighthouse technology, of which two were mounted on the shoulder-straps of a backpack to track the movement of the thorax, two were mounted as watches (one on each wrist of the subject) to track the movements of the forearms, two were handheld controllers used for the calibration of the subject and one was the tracked headset for the position and orientation of the head over time. Based on these tracked objects and on a patient-specific rigid body model of his/her upper body (built automatically during the calibration phase), the upper body of the subject could be tracked in space in real-time, as a scaled rigid body model composed by 6 segments: one thorax, 2 upper arms, 2 forearms and one head. This model combined with a VR headset allowed the creation of a real-time avatar of the subject, projected instead of his/her own body, and following his/her movements. A VR environment was then created to guide the subject through a set of motor tasks that are continuously adapted to his/her scores in the previous tasks.

Using this technology, the subject was guided first through the evaluation of his/her reachable ranges, following a set of arcs in space, reaching as far as he/she could go. Then, a set of targets in space, placed to map his/her estimated R_{space} . The whole exercise was guided externally by a minimally trained clinician, through an intuitive computer interface or a remote. Since all the motions of the patient were precisely recorded, a map of his/her R_{space} was then built using customized algorithms, meshed and the contained volume was measured.

Several metrics were developed and tested to evaluate the R_{space} , including 2 algorithms to compute the R_{space} volume ($V_{R/L}$ and V_{sph} , R/L), the volumetric symmetry was defined to compare the healthy and the pathologic R_{space} ($V\%$), the reachable ranges were evaluated (H_{int} , H_{ext} , $V_{\{1, \dots, 8\}}$) and two scores were built on top of the reachable ranges (Q_5 , R_5).

Several versions of the test were evaluated on healthy subjects or through numerical simulations, to find a good compromise between the test's complexity (number of sensors and tracked segments), duration (amount of exercises), ease of use, accuracy and reliability. After this tuning process, the test was evaluated on 10 healthy subjects in a test-retest protocol. The later displayed a fair reliability ($ICC = 0.5$) of the test and a sound estimation of the R_{space} (0.174 m^3 on average, representing 67% of a sphere with the radius of a subject's UL, which is very similar to the findings of (Kurillo et al., 2012) on the evaluation of the envelope of the R_{space}).

In this laboratory version of the *Volfon* test, the total duration of the test, for one patient was of almost 30 minutes, it used a very affordable and robust setup, automatically displayed the results of the subject tested at the end of the test and remained moderately compact. The next phase of the project (Chapter 6) was to use the test in a standard medical consultation cabinet on real patients.

Early results indicated that the test was too long and strenuous for the patients. A shorter version of the test was developed, to last 10 to 15 minutes. This new version was evaluated on 16 patients with a broad range of shoulder affections (capsulitis, post-traumatic stiffness, rotator cuff reinsertion, ...) during a test-retest protocol.

This shorter version of the *Volfon* test was able to discriminate between the healthy and the pathologic side of patients, as long as the pathology caused a decrease of more than 20% of the R_{space} . The reliability of the test was excellent, with an ICC of 0.91 and a good reproducibility for the $V_{\% \text{ score}}$ ($ICC = 0.85$). It was also able to assess the reachable ranges of the patients ($ICC = 0.94$) and to compute a R_s with excellent reliability ($ICC = 0.87$). The average R_{space} on the healthy side of patients was of 0.188 m^3 ; slightly larger than the volume measured on healthy subjects with the previous test. The average R_{space} of the pathologic side was smaller at 0.115 m^3 .

Overall, a clinically usable instrument for the evaluation of the R_{space} was developed and its usability and validity were shown. Additional scores for the functional evaluation of the UL were also proposed and successfully evaluated using this new instrument.

7.2 Perspectives

The results of this thesis together with the evolution of the available technologies and the progresses of research, in particular in the fields of movement tracking, imaging and segmentation techniques, virtual reality and motor rehabilitation for the UL have opened new perspectives for the evaluation and simulation of the UL. Some recommendations to continue the current work and some more general recommendations for future works are proposed in the following sections.

7.2.1 Robot for the simulation of glenohumeral instability

A 5 DoFs of robot for the evaluation of the GH joint was developed (Chapter 3), allowing a high level of control on the full range of physiological forces found within this joint. This instrument could be used to model different elements affecting prosthetic GH joints stability. As an example, replacing the glenoid support material with softer or harder foams, before applying a motor sequence or a stability test to the joint could allow to better understand the phenomena leading to GH translation or, as observed with harder supports, to the accumulation of damages on the glenoid implants.

Reproducing the instability tests performed by combining the MS model with the robotic simulator, and adding forces to simulate the effects of some of the structures that were previously neglected might result in an improved model of GH instability. Reversely, using *in vivo* force patterns as provided on (Bergmann, 2009) and subtracting the simulated effect of a particular muscle or ligament, could provide insight in the importance of these structure for the overall joint's stability.

Further research on the elements and hypothesis that led the combined MS model and robotic simulator to diverge from the clinical outcomes may underline the importance of some generally neglected parameters such as the orientation of the humeral implant with respect to the humeral body or the importance of the subacromial and subcoracoid bursae. Such results would not only allow to correct the model, therefore enabling an instrument that would help shoulder surgeons to avoid installing unstable prosthetic configurations, but also help optimizing the treatment, by spending more time and attention on preserving the structures that matter the most to maintain the joint's stability. If successful, such a simulator would also be useful for the evaluation of modified prosthetic designs, such as glenoid implants, with asymmetric backing, to provide good support on eroded glenoid cavities, such as type B, C or D OA glenoid cavities, based on (Bercik et al., 2016).

Since the robotic simulator is essentially an open 5 DoFs joint manipulator, by changing the clamps, it could be adapted to study other joints of the body, such as the stability in knee, hip or ankle prosthesis. It could also be adapted to manipulate cadaveric joints

to evaluate their stability in different conditions, such as the cases of Bankart or labral lesions for the shoulder, comparing different treatments, or for the knee, cases of anterior cruciate ligament rupture and surgical replacement.

7.2.2 Volfon: A system for the instrumented functional evaluation of the upper limb

The results obtained in Chapter 6 give access to many further developments and improvements. First an evaluation with a larger number of patients suffering from specific motor affections would allow to evaluate the validity and reliability of the Volfon method to specific pathologies. Performing regular follow up recording of the patient's progresses would allow evaluating if the evaluation of the R_{space} could be used to monitor patients' progresses during their recovery.

The R_{space} could be divided in subparts (such as quadrants), which could be further evaluated and compared against the equivalent subpart on the contralateral side. The pattern of these relative volumes could either display patterns typical of a given traumatic injury (rotator cuff tear, impingement, etc) or of a specific pathology (tendonitis, frozen shoulder, etc.). This would require an adapted tool, with the option to divide the R_{space} in subparts and a clinical study to identify the pattern related to different pathologies. The author would suggest starting with pathologies that can be diagnosed by testing specific motions, such as tears in any of the rotator cuff muscles, or adhesive capsulitis.

Another interesting extension of this project would be to study how the use of VR, and of different ways to present the tasks in a virtual environment would be perceived by different age groups. This would allow to develop more efficient and motivational interfaces.

The actual setup could also be adapted to record other metrics about the UL function. Scores for the evaluation of the angular velocity, movement smoothness, time to target and of the total displacements could be created. Similarly, in pure reaching tasks, the profile velocity of healthy subject is a bell shape (Morasso, 1981). Moreover, in drawing tasks the movements will follow the two thirds law: $A = k \cdot C^{2/3}$ with A being the angular velocity, C the movement curvature and k a constant determined by the linear extent of each individual segment (Lacquaniti, Terzuolo, & Viviani, 1983). These movement invariants could also be added to the evaluation and their disfunction might be indicative of a particular set of neuromotor disorders.

Additionally, even if the lighthouse tracking technology is less accurate than the current gold standards for motion analysis, the tracking strategies used in this project could be extended to the tracking of the lower body to perform full body kinematic analysis with a simpler, cheaper and faster solution. Using four 2nd generation lighthouse base-stations instead of the actual two 1st generation base-stations, a tracking area of 10 by 10 m would be available, providing sufficient space for several locomotor tests, such as the *timed up and go* or *sit to stand* transitions. The ability to achieve a fully automated processing of the data would allow to study larger populations more easily, increasing the statistical power of most studies.

Even though current SteamVR Trackers provided a convenient solution for the tracking of the UL, developing a lighter and more ergonomic solution capitalizing on the SteamVR interface and on the TS4112 sensors (Triad semiconductors, NC, US) could make this technology more ergonomic for the use in the hospitals.

The use of other tracking solutions, such as a set of IMUs to evaluate the joints orientation, and through a rigid-body model, the displacements of the arm could present an alternative solution for the functional evaluation of the UL. Replacing the lighthouse trackers by IMUs would be convenient by removing the need to install two base-stations in the room and potentially allowing the patient to perform a self-test at home. However, at present the accuracy of the lighthouse trackers remains much higher for UL tracking applications.

The evolution of inside-out camera-based tracking solutions for virtual reality, such as presented on the Oculus Quest headset or on the HTC Cosmos could offer an interesting alternative to the lighthouse tracking solution, again by removing the need to equip a room with specialized hardware, such as the two lighthouse base-stations. However, this will pose new challenges for the tracking of the whole UL, since, at present, such systems track only the pose of the hands and of the head.

At present, the evolution of both the tracking technology and the VR technology are enabling the development of many new medical applications both for the instrumented evaluation of the patients and to ease and improve the rehabilitation process. Now there is a need to develop these applications, and to develop new scores and metrics adapted for these new possibilities. With this work, the author hopes to have clearly demonstrated the underreported potential that these technologies have to improve the future of the functional evaluation of the UL and of motor disorders in general.

References

- Aminian, K., & Najafi, B. (2004). Capturing human motion using body-fixed sensors: Outdoor measurement and clinical applications. *Computer Animation and Virtual Worlds*, 15(2), 79–94. <https://doi.org/10.1002/cav.2>
- Anderl, W., Kriegleder, B., Neumaier, M., Laky, B., & Heuberger, P. (2015). Arthroscopic partial shoulder resurfacing. *Knee Surg Sports Traumatol Arthrosc.*, 23, 1563–1570.
- Anglin, C, Wyss, U. P., & Pichora, D. R. (2000). Mechanical testing of shoulder prostheses and recommendations for glenoid design. *Journal of Shoulder and Elbow Surgery / American Shoulder and Elbow Surgeons ... [et Al.]*, 9(4), 323–331. <https://doi.org/10.1067/mse.2000.105451>
- Anglin, Carolyn, Tolhurst, P., Wyss, U. P., & Pichora, D. R. (1999). Glenoid cancellous bone strength and modulus. *Journal of Biomechanics*, 32.
- Angst, F., Schwyzer, H.-K., Aeschlimann, A., Simmen, B. R., & Goldhahn, J. (2011). Measures of Adult Shoulder Function. *Measures of Pathology and Symptoms*, 63(November), 174–188. <https://doi.org/10.1002/acr.20630>
- Balakrishnan, R., & MacKenzie, I. S. (1997). Performance Differences in the Fingers, Wrist, and Forearm in Computer Input Control. *Proceedings of the International Conference on Human Factors in Computing Systems (CHI'97)*, 303–310. <https://doi.org/10.1145/258549.258764>
- Bartelt, R., Sperling, J. W., Schleck, C. D., & Cofield, R. H. (2011). Shoulder arthroplasty in patients aged fifty-five years or younger with osteoarthritis. *Journal of Shoulder and Elbow Surgery*, 20(1), 123–130. <https://doi.org/10.1016/j.jse.2010.05.006>
- Baumgartner, D., Tomas, D., Gossweiler, L., Siegl, W., Osterhoff, G., & Heinlein, B. (2014). Towards the development of a novel experimental shoulder simulator with rotating scapula and individually controlled muscle forces simulating the rotator cuff. *Medical and Biological Engineering and Computing*, 52(3), 293–299. <https://doi.org/10.1007/s11517-013-1120-z>
- Beaton, D. E., Wright, J. G., Katz, J. N., Amadio, P., Bombardier, C., Cole, D., ... Punnett, L. (2005). Development of the QuickDASH: Comparison of three item-reduction approaches. *Journal of Bone and Joint Surgery - Series A*, 87(5), 1038–1046. <https://doi.org/10.2106/BJJS.D.02060>
- Bencardino, J. T., Beltran, J., Rosenberg, Z. S., Rokito, A., Schmahmann, S., Mota, J., ... Rose, D. (2000). Superior Labrum Anterior-Posterior Lesions: Diagnosis with MR Arthrography of the Shoulder. *Radiology*, 214(1), 267–271. <https://doi.org/10.1148/radiology.214.1.r00ja22267>
- Bercik, M. J., Kruse, K., Yalozis, M., Gauci, M. O., Chaoui, J., & Walch, G. (2016). A modification to the Walch classification of the glenoid in primary glenohumeral osteoarthritis using three-dimensional imaging. *Journal of Shoulder and Elbow Surgery*, 25(10), 1601–1606. <https://doi.org/10.1016/j.jse.2016.03.010>
- Bergmann, G. (2009). Orthoload Database. Retrieved 30 August 2018, from <https://orthoload.com/database/>
- Bernhardt, J., Bate, P. J., & Matyas, T. A. (1998). Accuracy of observational kinematic assessment of upper-limb movements. *Physical Therapy*, 78(3), 259–270. <https://doi.org/10.1093/ptj/78.3.259>
- Bigliani, L. U., Pollock, R. G., Soslowsky, L. J., Flatow, E. L., Pawluk, R. J., & Mow, V. C. (1992). Tensile properties of the inferior glenohumeral ligament. *Journal of Orthopaedic Research : Official Publication of the Orthopaedic Research Society*, 10(2), 187–197. <https://doi.org/10.1002/jor.1100100205>
- Bijlsma, J. W. J. (2002). Analgesia and the Patient With Osteoarthritis. *American Journal of Therapeutics*, 9(3), 189–197.
- Bohsali, K. I., Wirth, M. A., & Rockwood Jr., C. A. (2006). Complications of total shoulder arthroplasty. *The Journal of Bone & Joint Surgery A*, 88(10), 2279–2292.
- Bommas, Teubner, & Voss. (2008). Membre supérieur, Articulations. In DeBoeck (Ed.), *Cours d'anatomie* (2nd ed.). DeBoeck.
- Bonato, P. (2005). Advances in wearable technology and applications in physical medicine and rehabilitation. *Journal of NeuroEngineering and Rehabilitation*, 2, 2–5. <https://doi.org/10.1186/1743-0003-2-2>
- Bonnechère, B., Jansen, B., Salvia, P., Bouzahouene, H., Omelina, L., Moiseev, F., ... Van Sint Jan, S. (2014). Validity and reliability of the Kinect within functional assessment activities: Comparison with standard stereophotogrammetry. *Gait and Posture*, 39(1), 593–598. <https://doi.org/10.1016/j.gaitpost.2013.09.018>

- Bonnechère, B., Jansen, B., Salvia, P., Bouzahouene, H., Sholukha, V., Cornelis, J., ... Jan, S. V. S. (2014). Determination of the precision and accuracy of morphological measurements using the Kinect™ sensor: comparison with standard stereophotogrammetry. *Ergonomics*, 57(4), 622–631. <https://doi.org/10.1080/00140139.2014.884246>
- Bonneville, N., Melis, B., Neyton, L., Favard, L., Molé, D., Walch, G., & Boileau, P. (2013). Aseptic glenoid loosening or failure in total shoulder arthroplasty: Revision with glenoid reimplantation. *Journal of Shoulder and Elbow Surgery*, 22(6), 745–751. <https://doi.org/10.1016/j.jse.2012.08.009>
- Bot, S. D. M., Terwee, C. B., Van Der Windt, D. A. W. M., Bouter, L. M., Dekker, J., & De Vet, H. C. W. (2004). Clinimetric evaluation of shoulder disability questionnaires: A systematic review of the literature. *Annals of the Rheumatic Diseases*, 63(4), 335–341. <https://doi.org/10.1136/ard.2003.007724>
- Braun, B. S., Kokmeyer, D., & Millett, P. J. (2009). Shoulder Injuries in the Throwing Athlete Shoulder Injuries in the Throwing Athlete. *J Bone Joint Surg Am*, 91, 966–978. <https://doi.org/10.2106/JBJS.H.01341>
- Bruton, A., Conway, J. H., & Holgate, S. T. (2000). Reliability : What is it, and how is it measured ? *Physiotherapy*, 86(2), 94–99.
- Bryant, D., Litchfield, R., Sandow, M., Gartsman, G. M., Guyatt, G., & A., K. (2005). A comparison of pain, strength, range of motion, and functional outcomes after hemiarthroplasty and total shoulder arthroplasty in patients with osteoarthritis of the shoulder: a systematic review and meta-analysis. *The Journal of Bone & Joint Surgery A*, 87(9), 1947–1956.
- Büchler, P., Ramaniraka, N. A., Rakotomanana, L. R., Iannotti, J. P., & Farron, A. (2002). A finite element model of the shoulder: Application to the comparison of normal and osteoarthritic joints. *Clinical Biomechanics*, 17(9–10), 630–639. [https://doi.org/10.1016/S0268-0033\(02\)00106-7](https://doi.org/10.1016/S0268-0033(02)00106-7)
- Charbonnier, C., Chagué, S., Kolo, F. C., Chow, J. C. K., & Lädermann, A. (2014). A patient-specific measurement technique to model shoulder joint kinematics. *Orthopaedics and Traumatology: Surgery and Research*, 100(7), 715–719. <https://doi.org/10.1016/j.otsr.2014.06.015>
- Charlton, I W, & Johnson, G. R. (2006). A model for the prediction of the forces at the glenohumeral joint. *Proceedings of the Institution of Mechanical Engineers, Part H: Journal of Engineering in Medicine*, 220(8), 801–812. <https://doi.org/10.1243/09544119JEIM147>
- Charlton, Iain W., & Johnson, G. R. (2001). Application of spherical and cylindrical wrapping algorithms in a musculoskeletal model of the upper limb. *Journal of Biomechanics*, 34(9), 1209–1216. [https://doi.org/10.1016/S0021-9290\(01\)00074-4](https://doi.org/10.1016/S0021-9290(01)00074-4)
- Chillemi, C., & Franceschini, V. (2013). Shoulder Osteoarthritis. *Arthritis*, 2013, 1–7. <https://doi.org/10.1155/2013/370231>
- Clément, J., Raison, M., & Rouleau, D. M. (2017). Reproducibility analysis of upper limbs reachable workspace, and effects of acquisition protocol, sex and hand dominance. *Journal of Biomechanics*, 68, 58–64. <https://doi.org/10.1016/j.jbiomech.2017.12.010>
- Coley, B. (2007). *Shoulder function and outcome evaluation after surgery using 3D inertial sensors*.
- Collins, D. N., Harryman, D. T., & Wirth, M. A. (2004). Shoulder Arthroplasty for the Treatment of Inflammatory Arthritis. *Journal of Bone and Joint Surgery*, 86(11), 2489–2496.
- Conformis.com. (n.d.). Retrieved from <http://www.conformis.com/customized-knee-implants/products/ijig/>
- Connor, P. M., Banks, D. M., Tyson, A. B., Coumas, J. S., & Alessandro, D. F. D. (2003). American Journal of Sports Magnetic Resonance Imaging of the Asymptomatic Shoulder of Overhead Athletes, 31(5), 724–727.
- Constant, C. R., & Murley, A. H. (1987). A clinical method of functional assessment of the shoulder. *Clinical Orthopaedics and Related Research*, 214, 160–164.
- Cook, L. T., Cook, P. N., Lee, K. R., Batnitzky, S., Fritz, S. L., Ophir, J., ... Wong, B. Y. S. (1980). An Algorithm for Volume Estimation Based on Polyhedral Approximation. *IEEE Transactions on Biomedical Engineering*, BME-27(9), 493–500. <https://doi.org/10.1109/TBME.1980.326663>
- Crowson, C. S., O'Dell, J. R., & Romain, P. L. (2019). Epidemiology of, risk factors for, and possible causes of rheumatoid arthritis. Retrieved 14 October 2019, from <https://www.uptodate.com/contents/epidemiology-of-risk-factors-for-and-possible-causes-of-rheumatoid-arthritis>
- Cuff, D., Clark, R., Pupello, D., & Frankle, M. (2012). “Reverse shoulder arthroplasty for the treatment of rotator cuff deficiency: a concise follow-up, at a minimum of five years, of a previous report. *The Journal of Bone & Joint Surgery A*, 94(21), 1996–2000.

- Dare, S. S., & Godfrey, M. (2012). Determination of Angles of Torsion and Retroversion of the Humerus of Male and Female Skeleton Specimens in Uganda. *Asian Journal of Medical Sciences*, (October 2012).
- Day, J. S., Lau, E., Ong, K. L., Williams, G. R., Ramsey, M. L., & Kurtz, S. M. (2015). Prevalence and projections of total shoulder and elbow arthroplasty in the United States to 2015. *Journal of Shoulder and Elbow Surgery*, 19(8), 1115–1120. <https://doi.org/10.1016/j.jse.2010.02.009>
- de Beer, J., Bhatia, D., van Rooyen, K., & Du Toit, D. (2010). Arthroscopic debridement and biological resurfacing of the glenoid in glenohumeral arthritis. *Knee Surg Sports Traumatol Arthrosc.*, 18, 1767–1773.
- De Jesus, J. O., Parker, L., Frangos, A. J., & Nazarian, L. N. (2009). Accuracy of MRI, MR arthrography, and ultrasound in the diagnosis of rotator cuff tears: A meta-analysis. *American Journal of Roentgenology*, 192(6), 1701–1707. <https://doi.org/10.2214/AJR.08.1241>
- Debski, R. E., Sakane, M., Woo, S. L. Y., Wong, E. K., Fu, F. H., & Warner, J. J. P. (1999). Contribution of the passive properties of the rotator cuff to glenohumeral stability during anterior-posterior loading. *Journal of Shoulder and Elbow Surgery*, 8(4), 324–329. [https://doi.org/10.1016/S1058-2746\(99\)90154-4](https://doi.org/10.1016/S1058-2746(99)90154-4)
- Debski, R. E., Yamakawa, S., Musahl, V., & Fujie, H. (2017). Use of Robotic Manipulators to Study Diarthrodial Joint Function. *Journal of Biomechanical Engineering*, 139(February 2017), 1–7. <https://doi.org/10.1115/1.4035644>
- Denard, P. J., Wirth, M. A., & Orfaly, R. M. (2011). Management of Glenohumeral Arthritis in the Young Adult. *JBJS*, 93(9), 885–892.
- Dillon, M. T., Inacio, M. C. S., Burke, M. F., Navarro, R. A., & Yian, E. H. (2013). Shoulder arthroplasty in patients 59 years of age and younger. *Journal of Shoulder and Elbow Surgery*, 22(10), 1338–1344. <https://doi.org/10.1016/j.jse.2013.01.029>
- Duc, C. (2013). *Objective outcome evaluation of the shoulder and cervical function after surgery using body-fixed sensors*.
- Egons. (2011). How would one calculate a 3d Mesh volume in Unity? Retrieved 25 September 2018, from <https://answers.unity.com/questions/52664/how-would-one-calculate-a-3d-mesh-volume-in-unity.html>
- Engelhardt, C., Ingram, D., Müllhaupt, P., Farron, A., Becce, F., Pioletti, D., & Terrier, A. (2016). Effect of partial-thickness tear on loading capacities of the supraspinatus tendon: a finite element analysis. *Computer Methods in Biomechanics and Biomedical Engineering*, 19(8), 875–882. <https://doi.org/10.1080/10255842.2015.1075012>
- Favre, P., Moor, B., Snedeker, J. G., & Gerber, C. (2008). Influence of component positioning on impingement in conventional total shoulder arthroplasty. *Clinical Biomechanics (Bristol, Avon)*, 23(2), 175–183. <https://doi.org/10.1016/j.clinbiomech.2007.09.009>
- Favre, P., Senteler, M., Hipp, J., Scherrer, S., Gerber, C., & Snedeker, J. G. (2012). An integrated model of active glenohumeral stability. *Journal of Biomechanics*, 45(13), 2248–2255. <https://doi.org/10.1016/j.jbiomech.2012.06.010>
- Favre, P., Sussmann, P. S., & Gerber, C. (2010). The effect of component positioning on intrinsic stability of the reverse shoulder arthroplasty. *Journal of Shoulder and Elbow Surgery / American Shoulder and Elbow Surgeons ... [et Al.]*, 19(4), 550–556. <https://doi.org/10.1016/j.jse.2009.11.044>
- Franklin, J. L., Barrett, W. P., Jackins, S. E., & Matsen, F. A. (1988). Glenoid loosening in total shoulder arthroplasty. Association with rotator cuff deficiency. *J Arthroplasty*, 3(1), 39–46.
- Frich, L. H. (1994). *Glenoidal knoglestyrke og koglestruktur*. University Hospital Aarhus.
- Frich, L. H., & Odgaard, A. (1995). Bone architecture of the normal and rheumatoid arthritic glenoid. *Transactions of the Orthopaedic Research Society*.
- Fujie, H., Mabuchi, K., Woo, S. L. Y., Livesay, G. A., Shinji, A., & Tsukamoto, Y. (1993). The Use of Robotics Technology to Study Human Joint Kinematics: A New Methodology. *Journal of Biomechanical Engineering*, 115(1211)(August).
- Garner, B. A., & Pandy, M. G. (2000). The obstacle-set method for representing muscle paths in musculoskeletal models. *Computer Methods in Biomechanics and Biomedical Engineering*, 3(1), 1–30. <https://doi.org/10.1080/10255840008915251>
- Garner, B. A., & Pandy, M. G. (2001). Musculoskeletal model of the upper limb based on the visible human male dataset. *Computer Methods in Biomechanics and Biomedical Engineering*, 4(2), 93–126. <https://doi.org/10.1080/10255840008908000>
- Gartsman, G. M., Roddey, T. S., & Hammerman, M., S. (2000). Shoulder arthroplasty with or without resurfacing of the glenoid in

- patients who have osteoarthritis. *The Journal of Bone & Joint Surgery A*, 82(1), 26–34.
- Gatterman, D. M. I. (2005). Subluxation. The Articular Lesion. In Elsevier (Ed.), *Foundations of Chiropractic: Subluxation* (2nd ed., pp. 6–9).
- Gerber, C., & Nyffeler, R. W. (2002). Classification of glenohumeral joint instability. *Clin Orthop Relat Res*, 65–76.
- Gerber, Christian, & Ganz, R. (1982). Clinical assessment of instability of the shoulder with special reference to anterior and posterior drawer tests, 66(4).
- Gerber, Christian, Snedeker, J. G., Baumgartner, D., & Viehöfer, A. F. (2014). Supraspinatus tendon load during abduction is dependent on the size of the critical shoulder angle: A biomechanical analysis. *Journal of Orthopaedic Research : Official Publication of the Orthopaedic Research Society*, 32(7), 952–957. <https://doi.org/10.1002/jor.22621>
- Godfrey, J., Hamman, R., Lowenstein, S., Briggs, K., & Kocher, M. (2007). Reliability , validity , and responsiveness of the simple shoulder test : Psychometric properties by age and injury type. *Journal of Shoulder and Elbow Surgery Board*, 260–267. <https://doi.org/10.1016/j.jse.2006.07.003>
- Gregory, T., Hansen, U., Taillieu, F., Baring, T., Brassart, N., Mutchler, C., ... Emery, R. (2009). Glenoid loosening after total shoulder arthroplasty: an in vitro CT-scan study. *Journal of Orthopaedic Research : Official Publication of the Orthopaedic Research Society*, 27(12), 1589–1595. <https://doi.org/10.1002/jor.20912>
- Guery, J., Favard, L., Sirveaux, F., Oudet, D., Mole, D., & Walch, G. (2006). Reverse total shoulder arthroplasty: survivorship analysis of eighty replacements followed for five to ten years. *The Journal of Bone & Joint Surgery A*, 88(8), 1742–1747.
- Gummesson, C., Ward, M. M., & Atroshi, I. (2006). The shortened disabilities of the arm, shoulder and hand questionnaire (QuickDASH): Validity and reliability based on responses within the full-length DASH. *BMC Musculoskeletal Disorders*, 7, 1–7. <https://doi.org/10.1186/1471-2474-7-44>
- Hammond, L. C. D. R. J., Lin, E. C., Harwood, D. P., Juhan, T. W., Gochanour, E., Klosterman, E. L., ... Romeo, A. A. (2013). Clinical outcomes of hemiarthroplasty and biological resurfacing in patients aged younger than 50 years. *Journal of Shoulder and Elbow Surgery*, 22(10), 1345–1351. <https://doi.org/10.1016/j.jse.2013.04.015>
- Hayes, K., Walton, J. R., Szomor, Z. L., & Murrell, G. A. C. (2002). Reliability of 3 methods for assessing shoulder strength. *Journal of Shoulder and Elbow Surgery*, 11(1), 33–39. <https://doi.org/10.1067/mse.2002.119852>
- Hudak, P. L., & et al. (1996). Development of an upper extremity outcome measure: the DASH (Disabilities of the Arm, Shoulder, and Hand). *American Journal of Industrial Medicine*, 29(6), 602–608.
- Hughes, R. E., Niebur, G., Liu, J., & An, K. (1998). Comparison of two methods for computing abduction moment arms of the rotator cuff. *Journal of Biomechanics*, 31, 157–160.
- Hurschler, C., Wülker, N., Windhagen, H., Plumhoff, P., & Hellmers, N. (2001). Medially Based Anterior Capsular Shift of the Glenohumeral Joint. *American Journal of Sports Medicine*, 29(3), 346–353. <https://doi.org/10.1177/03635465010290031601>
- Inflammatory Arthritis. (2019). Retrieved 13 October 2019, from <https://www.arthritis.org/about-arthritis/types/inflammatory-arthritis/>
- Ingram, D. (2015). *Musculoskeletal Model of the Human Shoulder for Joint Force Estimation*.
- Ingram, D., Engelhardt, C., Farron, A., Terrier, A., & Müllhaupt, P. (2015). Muscle moment-arms: a key element in muscle-force estimation. *Computer Methods in Biomechanics and Biomedical Engineering*, 18(5), 506–513. <https://doi.org/10.1080/10255842.2013.818666>
- International, A. (2014). *Standard Test Methods for Dynamic Evaluation of Glenoid Loosening or Disassociation*. ASTM International.
- Jacxsens, M., Van Tongel, A., Henninger, H. B., Tashjian, R. Z., & De Wilde, L. (2017). The three-dimensional glenohumeral subluxation index in primary osteoarthritis of the shoulder. *Journal of Shoulder and Elbow Surgery*, 26(5), 878–887. <https://doi.org/10.1016/j.jse.2016.09.049>
- Jaggi, A., & Lambert, S. (2010). Rehabilitation for shoulder instability. *British Journal of Sports Medicine*, 44(5), 333–340. <https://doi.org/10.1136/bjsem.2009.059311>
- Jost, B., Zumstein, M., W. A. Pfirrmann, C., Zanetti, M., & Gerber, C. (2005). MRI Findings in Throwing Shoulders. *Clinical Orthopaedics and Related Research*, (434), 130–137. <https://doi.org/10.1097/01.blo.0000154009.43568.8d>

- Karduna, A. R., Williams, G. R., Williams, J. L., & Iannotti, J. P. (1997). Joint stability after total shoulder arthroplasty in a cadaver model. *Journal of Shoulder and Elbow Surgery*, 6(6), 506–511. [https://doi.org/10.1016/S1058-2746\(97\)90082-3](https://doi.org/10.1016/S1058-2746(97)90082-3)
- Kedgley, A. E., Mackenzie, G. a, Ferreira, L. M., Drosdowech, D. S., King, G. J. W., Faber, K. J., & Johnson, J. a. (2007). The effect of muscle loading on the kinematics of in vitro glenohumeral abduction. *Journal of Biomechanics*, 40(13), 2953–2960. <https://doi.org/10.1016/j.jbiomech.2007.02.008>
- Kidder, J. F., Rouleau, D., Pons-Villanueva, J., Dynamidis, S., Defranco, M., & Walch, G. (2010). Humeral head posterior subluxation on CT scan: Validation and comparison of 2 methods of measurement. *Techniques in Shoulder and Elbow Surgery*, 11(3), 72–76.
- Kido, T., Itoi, E., Lee, S., Neale, P. G., & An, K.-N. (2003). Dynamic Stabilizing Function of the Deltoid Muscle in Shoulders with Anterior Instability. *The American Journal of Sports Medicine*, 31(3), 399–403.
- Kirkley, A., Griffin, S., McLintock, H., & Ng, L. (1998). The development and evaluation of a disease-specific quality of life measurement tool for shoulder instability: The Western Ontario Shoulder Instability Index (WOSI). *American Journal of Sports Medicine*, 26(6), 764–771. <https://doi.org/10.1177/03635465980260060501>
- Klopcar, N., Tomsic, M., & Lenarcic, J. (2007). A kinematic model of the shoulder complex to evaluate the arm-reachable workspace. *Journal of Biomechanics*, 40, 86–91. <https://doi.org/10.1016/j.jbiomech.2005.11.010>
- Klopcar, Nives, & Lenarcic, J. (2005). Kinematic Model for Determination of Human Arm Reachable Workspace. *Meccanica*, 40, 203–219. <https://doi.org/10.1007/s11012-005-3067-0>
- Konrad, P. (2005). *The ABC of EMG*.
- Kreylos, O. (2016). Lighthouse tracking examined. Retrieved 24 November 2017, from <http://doc-ok.org/?p=1478>
- Kurillo, G., Chen, A., Bajcsy, R., & Han, J. J. (2013). Evaluation of upper extremity reachable workspace using Kinect camera. *Technology and Health Care*, 21(6), 641–656. <https://doi.org/10.3233/THC-130764>
- Kurillo, G., Han, J. J., Abresch, R. T., Nicorici, A., Yan, P., & Bajcsy, R. (2012). Development and Application of Stereo Camera-Based Upper Extremity Workspace Evaluation in Patients with Neuromuscular Diseases. *PLoS ONE*, 7(9). <https://doi.org/10.1371/journal.pone.0045341>
- Labriola, J. E., Lee, T. Q., Debski, R. E., & McMahon, P. J. (2005). Stability and instability of the glenohumeral joint: the role of shoulder muscles. *Journal of Shoulder and Elbow Surgery / American Shoulder and Elbow Surgeons ... [et Al.]*, 14(1 Suppl S), 32S-38S. <https://doi.org/10.1016/j.jse.2004.09.014>
- Lacquaniti, F., Terzuolo, C., & Viviani, P. (1983). The law relating the kinematic and figural aspects of drawing movements. *Acta Psychologica*, 54(1–3), 115–130. [https://doi.org/10.1016/0001-6918\(83\)90027-6](https://doi.org/10.1016/0001-6918(83)90027-6)
- Lee, S. H., Yoon, C., Chung, S. G., Kim, H. C., Kwak, Y., Park, H. W., & Kim, K. (2015). Measurement of shoulder range of motion in patients with adhesive capsulitis using a Kinect. *PLoS ONE*, 10(6). <https://doi.org/10.1371/journal.pone.0129398>
- Lemieux, P. O., Nuño, N., Hagemester, N., & Tétreault, P. (2012). Mechanical analysis of cuff tear arthropathy during multiplanar elevation with the AnyBody shoulder model. *Clinical Biomechanics*, 27(8), 801–806. <https://doi.org/10.1016/j.clinbiomech.2012.04.008>
- Lenarcic, J., & Umek, A. (1994). Simple Model of Human Arm Reachable Workspace. *IEE Transactions on Systems Man, and Cybernetics*, 24(8), 1239–1246.
- Lewis, A., Kitamura, T., & Bayley, J. I. L. (2004). (ii) The classification of shoulder instability: New light through old windows! *Current Orthopaedics*, 18(2), 97–108. <https://doi.org/10.1016/j.cuor.2004.04.002>
- Lighthouse. (n.d.). Retrieved 11 December 2018, from <https://xinreality.com/wiki/Lighthouse>
- Linsell, L., Dawson, J., Zondervan, K., Rose, P., Randall, T., Fitzpatrick, R., & Carr, A. (2006). Prevalence and incidence of adults consulting for shoulder conditions in UK primary care; patterns of diagnosis and referral. *Rheumatology*, 45(2), 215–221. <https://doi.org/10.1093/rheumatology/kei139>
- Lippitt, S. B. (1993). A practical tool for evaluating shoulder function. The Simple Shoulder Test. *The Shoulder; A Balance of Mobility and Stability*, 501–518.

- Lo, I. K. Y., Nonweiler, B., Woolfrey, M., Litchfield, R., & Kirkley, A. (2004). An Evaluation of the Apprehension, Relocation, and Surprise Tests for Anterior Shoulder Instability. *American Journal of Sports Medicine*, 32(2), 301–307. <https://doi.org/10.1177/0095399703258690>
- Lübbeke, A., Rees, J. L., Barea, C., Combescure, C., Carr, A. J., Silman, A. J., & Surgery, O. (2017). International variation in shoulder arthroplasty Incidence , indication , type of procedure , and outcomes evaluation in 9 countries. *Acta Orthopaedica*, 88(6), 592–599. <https://doi.org/10.1080/17453674.2017.1368884>
- Lyle, R. (1981). A performance test for assessment of upper limb function in physical rehabilitation treatment and research. *International Journal of Rehabilitation Research*, 4(4), 483–492.
- Magermans, D. J., Chadwick, E. K. J., Veeger, H. E. J., & Van Der Helm, F. C. T. (2005). Requirements for upper extremity motions during activities of daily living. *Clinical Biomechanics*, 20(6), 591–599. <https://doi.org/10.1016/j.clinbiomech.2005.02.006>
- Mancuso, M., Arami, A., Becce, F., Farron, A., Terrier, A., & Aminian, K. (2020). A Robotic Glenohumeral Simulator for Investigating Prosthetic Implant Subluxation. *Journal of Biomechanical Engineering*, 142(1). Retrieved from <https://asmedigitalcollection.asme.org/biomechanical/article/doi/10.1115/1.4044388/956200/A-Robotic-Glenohumeral-Simulator-for-Investigating>
- Martelli, S., Kersh, M. E., & Pandy, M. G. (2015). Sensitivity of femoral strain calculations to anatomical scaling errors in musculoskeletal models of movement. *Journal of Biomechanics*, 48(13), 3606–3615. <https://doi.org/10.1016/j.jbiomech.2015.08.001>
- May, S., Chance-larsen, K., Littlewood, C., Lomas, D., & Saad, M. (2010). Reliability of physical examination tests used in the assessment of patients with shoulder problems : a systematic review. *Physiotherapy*, 96(3), 179–190. <https://doi.org/10.1016/j.physio.2009.12.002>
- McMahon, P. J., Burkart, A., Musahl, V., & Debski, R. E. (2004). Glenohumeral translations are increased after a type II superior labrum anterior-posterior lesion: A cadaveric study of severity of passive stabilizer injury. *Journal of Shoulder and Elbow Surgery*, 13(1), 39–44. <https://doi.org/10.1016/j.jse.2003.09.004>
- Meislin, R., Sperling, J., & Stitik, T. (2005). Persistent shoulder pain: epidemiology, pathophysiology, and diagnosis. *American Journal of Orthopedics (Belle Mead, N.J.)*, 34(12), 5–9.
- Micera, S., Sabatini, A. M., Dario, P., & Rossi, B. (1999). A hybrid approach to EMG pattern analysis for classification of arm movements using statistical and fuzzy techniques. *Medical Engineering and Physics*, 21(5), 303–311. [https://doi.org/10.1016/S1350-4533\(99\)00055-7](https://doi.org/10.1016/S1350-4533(99)00055-7)
- Mizuuchi, I., Tajima, R., Yoshikai, T., Sato, D., Nagashima, K., Inaba, M., ... Inoue, H. (2002). The Design and Control of the Flexible Spine of a Fully Tendon-Driven Humanoid “Kenta”. In *International Conference on Intelligent Robots and Systems* (pp. 2527–2532). Lausanne, Switzerland.
- Morasso, P. (1981). Spatioal Control of Arm Movements. *Experimental Brain Research*, 42, 223–227.
- N.Bhatia, D., van Rooyen, K. S., du Toit, D. F., & de Beer, J. F. (2006). Arthroscopic technique of interposition arthroplasty of the glenohumeral joint. *Arthroscopy: The Journal of Arthroscopic & Related Surgery*, 22(5), 570.e1-570.e5.
- Nachar, N. (2008). The Mann-Whitney U: A Test for Assessing Whether Two Independent Samples Come from the Same Distribution. *Tutorials in Quantitative Methods for Psychology*, 4(1), 13–20. <https://doi.org/10.20982/tqmp.04.1.p013>
- Namdari, S., Skelley, N., Keener, J. D., Galatz, L. M., & Yamaguchi, K. (2013). What Is the Role of Arthroscopic Debridement for Glenohumeral Arthritis? A Critical Examination of the Literature. *Arthroscopy: The Journal of Arthroscopic & Related Surgery*, 29(8), 1392–1398.
- NDI Mesurement Sciences. (n.d.). Optotrak Certus Overview. Retrieved from <https://www.ndigital.com/msci/products/optotrak-certus/>
- OrthoToolKit. (n.d.). Retrieved 1 October 2019, from <https://www.orthotoolkit.com/>
- Parry, I., Carbullido, C., Kawada, J., Bagley, A., Sen, S., Greenhalgh, D., & Palmieri, T. (2014). Keeping up with video game technology: Objective analysis of Xbox Kinect™ and PlayStation 3 Move™ for use in burn rehabilitation. *Burns*, 40(5), 852–859. <https://doi.org/10.1016/j.burns.2013.11.005>
- Patil, S., Sethi, M., & Vasudeva, N. (2016). Determining Angle of Humeral Torsion Using Image Software Technique, 10(10), 6–9. <https://doi.org/10.7860/JCDR/2016/22121.8672>

- Patzer, T., Habermeyer, P., Hurschler, C., Bobrowitsch, E., Paletta, J. R., Fuchs-Winkelmann, S., & Schofer, M. D. (2011). Increased glenohumeral translation and biceps load after SLAP lesions with potential influence on glenohumeral chondral lesions: A biomechanical study on human cadavers. *Knee Surgery, Sports Traumatology, Arthroscopy*, 19(10), 1780–1787. <https://doi.org/10.1007/s00167-011-1423-2>
- Pennington, W. T., & Bartz, B. A. (2005). Arthroscopic glenoid resurfacing with meniscal allograft: A minimally invasive alternative for treating glenohumeral arthritis. *Arthroscopy: The Journal of Arthroscopic & Related Surgery*, 21(12), 1517–1520.
- Pichonnaz, C., Aminian, K., Ancey, C., Jaccard, H., Lécureux, E., Duc, C., ... Gleeson, N. (2017). Heightened clinical utility of smartphone versus body-worn inertial system for shoulder function B-B score. *PLoS ONE*, 1–17.
- Pichonnaz, C., Duc, C., Gleeson, N., Ancey, C., Jaccard, H., Lécureux, E., ... Aminian, K. (2015). Measurement Properties of the Smartphone-Based B-B Score in Current Shoulder Pathologies. *Sensors*, 15(Mdc), 26801–26817. <https://doi.org/10.3390/s151026801>
- Polhemus. (2010). G4 6DOF Wireless Electromagnetic Tracker. Retrieved from https://polhemus.com/_assets/img/G4_Brochure.pdf
- Prinold, J. A., Masjedi, M., Johnson, G. R., & Bull, A. M. (2013). Musculoskeletal shoulder models: a technical review and proposals for research foci. *Proc Inst Mech Eng H*, 227(10), 1041–1057.
- Quental, C., Folgado, J., Ambrósio, J., & Monteiro, J. (2016). A new shoulder model with a biologically inspired glenohumeral joint. *Medical Engineering and Physics*, 38(9), 969–977. <https://doi.org/10.1016/j.medengphy.2016.06.012>
- Quental, Carlos, Folgado, J., Ambrósio, J., & Monteiro, J. (2013). Critical analysis of musculoskeletal modelling complexity in multibody biomechanical models of the upper limb. *Computer Methods in Biomechanics and Biomedical Engineering*, (July 2014), 37–41. <https://doi.org/10.1080/10255842.2013.845879>
- Ragab, A. A. (2003). Validity of self-assessment outcome questionnaires: patient-physician discrepancy in outcome interpretation. *Biomedical Sciences Instrumentation*, 39, 579–584.
- Read, J. W., & Perko, M. (1998). Shoulder ultrasound: Diagnostic accuracy for impingement syndrome, rotator cuff tear, and biceps tendon pathology. *Journal of Shoulder and Elbow Surgery*, 7(3), 264–271. [https://doi.org/10.1016/S1058-2746\(98\)90055-6](https://doi.org/10.1016/S1058-2746(98)90055-6)
- Roach, K. E., Budiman-Mak, E., Songsiridej, N., & Lertratanakul, Y. (1991). Development of a Shoulder Pain and Disability Index. *Arthritis & Rheumatism*, 4(4), 143–149. <https://doi.org/10.1002/art.1790040403>
- Roach, N. T., Lieberman, D. E., Iv, T. J. G., Palmer, W. E., Thomas, J., & Ill, G. (2012). The effect of humeral torsion on rotational range of motion in the shoulder and throwing performance. *Journal of Anatomy*, (December 2011), 293–301. <https://doi.org/10.1111/j.1469-7580.2011.01464.x>
- Robinson, R., Herzog, W., & Nigg, B. (1987). Use of force platform variables to quantify the effects of chiropractic manipulation on gait symmetry. *Journal of Manipulative and Physiological Therapeutics*.
- Sabesan, V.J., Callanan, M., Youderian, A., & Iannotti, J. P. (2014). 3D CT assessment of the relationship between humeral head alignment and glenoid retroversion in glenohumeral osteoarthritis. *J Bone Joint Surg Am*, 96(8), 64.
- Sabesan, Vani J., Ackerman, J., Sharma, V., Baker, K. C., Kurdziel, M. D., & Wiater, J. M. (2015). Glenohumeral mismatch affects micromotion of cemented glenoid components in total shoulder arthroplasty. *Journal of Shoulder and Elbow Surgery*, 24(5), 814–822. <https://doi.org/10.1016/j.jse.2014.10.004>
- Sarshari, E., Mancuso, M., Terrier, A., Farron, A., Pioletti, D., & Mullhaupt, P. (2019). Motion reconstruction in upper extremity in the absence of scapula kinematics measurement-devices. *Submitted to CMBBE*.
- Sarshari, Ehsan. (2018). *A Closed-Loop EMG-Assisted Shoulder Model*.
- Sarshari, Ehsan, Boulanaache, Y., Becce, F., Farron, A., & Terrier, A. (2019). Effects of CT-scan based on patient-specific data in evaluation of joint reaction force after total shoulder arthroplasty. In *CMBBE*.
- Sarshari, Ehsan, Farron, A., Terrier, A., Pioletti, D., & Mullhaupt, P. (2017). A simulation framework for humeral head translations. *Medical Engineering & Physics*, 49, 140–147. <https://doi.org/10.1016/j.medengphy.2017.08.013>
- Savoie FH, 3rd, Brislin, K., & Argo, D. (2009). Arthroscopic glenoid resurfacing as a surgical treatment for glenohumeral arthritis in the young patient: Midterm results. *Arthroscopy: The Journal of Arthroscopic & Related Surgery*, 25(8), 864–871.

- Sherman, S. C. (2015). Shoulder dislocation and reduction. *UpToDate*.
- Shin, J. H., Kim, M. Y., Lee, J. Y., Jeon, Y. J., Kim, S., Lee, S., ... Choi, Y. (2016). Effects of virtual reality-based rehabilitation on distal upper extremity function and health-related quality of life: A single-blinded, randomized controlled trial. *Journal of NeuroEngineering and Rehabilitation*, 13(1), 1–10. <https://doi.org/10.1186/s12984-016-0125-x>
- Shoulder Subluxation - Glenohumeral subluxation explained. (n.d.). Retrieved 5 January 2015, from <http://www.sportsinjuryclinic.net/sport-injuries/shoulder-pain/glenohumeral-instability-subluxation>
- Singapore Sports and Orthopaedic Clinic. (2019). Glenoid Labrum Tear. Retrieved 23 September 2019, from <https://www.orthopaedics.com.sg/conditions/shoulder-pain/glenoid-labrum-tear/>
- Sins, L., Tétreault, P., Hagemester, N., & Nuño, N. (2015). Adaptation of the AnyBody™ Musculoskeletal Shoulder Model to the Nonconforming Total Shoulder Arthroplasty Context. *Journal of Biomechanical Engineering*, 137(10), 101006. <https://doi.org/10.1115/1.4031330>
- Slater, M., Spanlang, B., Sanchez-Vives, M. V., & Blanke, O. (2010). First person experience of body transfer in virtual reality. *PLoS ONE*, 5(5), 1–9. <https://doi.org/10.1371/journal.pone.0010564>
- Smith, S. L., Li, L., Johnson, G., & Joyce, T. (2012). Commissioning of a multi-station shoulder joint wear simulator. In *Annual conference, British orthopaedic research society* (Vol. 16).
- Sodeyama, Y., Nishino, T., Namiki, Y., Nakanishi, Y., Mizuuchi, I., & Inaba, M. (2008). The designs and motions of a shoulder structure with a spherical thorax, scapulas and collarbones for humanoid “Kojiro”. *2008 IEEE/RSJ International Conference on Intelligent Robots and Systems*, 1465–1470. <https://doi.org/10.1109/IROS.2008.4651221>
- Sodeyama, Yoshinao, Yoshikai, T., Nishino, T., Mizuuchi, I., & Inaba, M. (2007). The designs and motions of a shoulder structure with a wide range of movement using bladebone-collarbone structures. In *IEEE/RSJ International Conference on Intelligent Robots and Systems* (pp. 3629–3634). San Diego, CA, USA: IEEE. <https://doi.org/10.1109/IROS.2007.4399241>
- Sperling, J. W., Cofield, R. H., & Rowland, C. M. (2004). Minimum fifteen-year follow-up of Neer hemiarthroplasty and total shoulder arthroplasty in patients aged fifty years or younger. *Journal of Shoulder and Elbow Surgery*, 13(6), 604–613. <https://doi.org/10.1016/j.jse.2004.03.013>
- Staudenmann, D., Kingma, I., Daffertshofer, A., Stegeman, D. F., & Dieën, J. H. Van. (2006). Improving Emg Based Muscle Force Estimation Using Principal Component Analysis on a High-Density Emg Array. *IEEE Transactions on Biomedical Engineering*, 53(4), 317–317.
- Suárez, D. R., van der Linden, J. C., Valstar, E. R., Broomans, P., Poort, G., Rozing, P. M., & van Keulen, F. (2009). Influence of the positioning of a cementless glenoid prosthesis on its interface micromotions. *Proc Inst Mech Eng H*, 223(7), 795–804.
- Terrier, A., Ston, J., Dewarrat, A., Becce, F., & Farron, A. (2017). A semi-automated quantitative CT method for measuring rotator cuff muscle degeneration in shoulders with primary osteoarthritis. *Orthopaedics and Traumatology: Surgery and Research*, 103(2), 151–157. <https://doi.org/10.1016/j.otsr.2016.12.006>
- Terrier, Alexandre, Larrea, X., Malfroy Camine, V., Pioletti, D. P., & Farron, A. (2013). Importance of the subscapularis muscle after total shoulder arthroplasty. *Clinical Biomechanics (Bristol, Avon)*, 28(2), 146–150. <https://doi.org/10.1016/j.clinbiomech.2012.11.010>
- Terrier, Alexandre, Merlini, F., Pioletti, D. P., & Farron, A. (2009). Total shoulder arthroplasty: downward inclination of the glenoid component to balance supraspinatus deficiency. *J Shoulder Elbow Surg*, 18(3), 360–365.
- Terrier, Alexandre, Ramondetti, S., Merlini, F., Pioletti, D. D., & Farron, A. (2010). Biomechanical consequences of humeral component malpositioning after anatomical total shoulder arthroplasty. *Journal of Shoulder and Elbow Surgery / American Shoulder and Elbow Surgeons ... [et Al.]*, 19(8), 1184–1190. <https://doi.org/10.1016/j.jse.2010.06.006>
- Terrier, Alexandre, Reist, A., Vogel, A., & Farron, A. (2007). Effect of supraspinatus deficiency on humerus translation and glenohumeral contact force during abduction. *Clin Biomech*, 22(6), 645–651.
- Terrier, Alexandre, Ston, J., & Farron, A. (2015). Importance of a three-dimensional measure of humeral head subluxation in osteoarthritic shoulders. *J Shoulder Elbow Surg*, 24(2), 295–301.
- Thomas, M., Bidwai, A., Rangan, A., Rees, J. L., Brownson, P., Tennent, D., ... Kulkarni, R. (2016). BESS / BOA Patient Care Pathways Glenohumeral osteoarthritis. *Shoulder & Elbow*, 8(3), 203–214. <https://doi.org/10.1177/1758573216644183>

- Tornier's_Test_Laboratory. (2018). *Subluxation and Loosening on Keeled glenoid component (RF/11640) (Following ASTM-F2028-08)*.
- Triangle Mesh Voxelisation. (2009). Retrieved from <http://blog.wolfire.com/2009/11/Triangle-mesh-voxelization>
- Tzannes, A., Paxinos, A., Callanan, M., & Murrell, G. A. C. (2004). An assessment of the interexaminer reliability of tests for shoulder instability. *Journal of Shoulder and Elbow Surgery*, 13(1), 18–23. <https://doi.org/10.1016/j.jse.2003.09.002>
- Van der Helm, F. C. T. (1994a). A finite element musculoskeletal model of the shoulder mechanism. *Journal of Biomechanics*, 27(5), 551–553, 555–569.
- Van der Helm, F. C. T. (1994b). A finite element musculoskeletal model of the shoulder mechanism. *Journal of Biomechanics*, 27(5), 551–569.
- Virani, N. a, Harman, M., Li, K., Levy, J., Pupello, D. R., & Frankle, M. a. (2008). In vitro and finite element analysis of glenoid bone/baseplate interaction in the reverse shoulder design. *Journal of Shoulder and Elbow Surgery / American Shoulder and Elbow Surgeons ... [et Al.]*, 17(3), 509–521. <https://doi.org/10.1016/j.jse.2007.11.003>
- Walch, G., Badet, R., Boulahia, A., & Khoury, A. (1999). Morphologic study of the glenoid in primary glenohumeral osteoarthritis. *J Arthroplasty*, 14(6), 756–760.
- Warner, J., & Caborn, D. (1992). Overview of shoulder instability. *Crit Rev Phys Rehab Med*, 4, 145–198.
- Weerdt, W. J. G. De, & Harrison, M. A. (1985). Measuring recovery of arm-hand function in stroke patients: A comparison of the Brunnstrom-Fugl-Meyer test and the Action Research Arm test. *Physiotherapy Canada*, 37(2), 65–70.
- What is Rheumatoid Arthritis? (2019). Retrieved 13 October 2019, from <https://www.arthritis.org/about-arthritis/types/rheumatoid-arthritis/what-is-rheumatoid-arthritis.php>
- Windolf, M., Götzen, N., & Morlock, M. (2008). Systematic accuracy and precision analysis of video motion capturing systems-exemplified on the Vicon-460 system. *Journal of Biomechanics*, 41(12), 2776–2780. <https://doi.org/10.1016/j.jbiomech.2008.06.024>
- Wirth, M. A., & Rockwood, C. A. J. (1996). Complications of total shoulder-replacement arthroplasty. *J Bone Joint Surg Am*, 78(4), 603–616.
- Wong, A. S., Gallo, L., Kuhn, J. E., Carpenter, J. E., & Hughes, R. E. (2003). The effect of glenoid inclination on superior humeral head migration. *J Shoulder Elbow Surg*, 12(4), 360–364.
- Wu, G., Helm, F. C. T. Van Der, Veeger, H. E. J. D., Makhsous, M., Roy, P. Van, Anglin, C., ... Buchholz, B. (2005). ISB recommendation on definitions of joint coordinate systems of various joints for the reporting of human joint motion — Part II : shoulder , elbow , wrist and hand. *Journal of Biomechanics*, 38, 981–992. <https://doi.org/10.1016/j.jbiomech.2004.05.042>
- Wuelker, N., Korell, M., & Thren, K. (1998). Dynamic Glenohumeral joint stability. *Journal of Shoulder and Elbow Surgery*, 7(1), 43–52. [https://doi.org/10.1016/S1058-2746\(98\)90182-3](https://doi.org/10.1016/S1058-2746(98)90182-3)
- Zhang, C., Skalli, W., Lagacé, P. Y., Billuart, F., Ohl, X., Cresson, T., ... Hagemeister, N. (2016). Investigation of 3D glenohumeral displacements from 3D reconstruction using biplane X-ray images: Accuracy and reproducibility of the technique and preliminary analysis in rotator cuff tear patients. *Journal of Electromyography and Kinesiology*, 29, 12–20. <https://doi.org/10.1016/j.jelekin.2015.08.002>
- Zheng, M., Zou, Z., Bartolo, P. jorge D. silva, Peach, C., & Ren, L. (2017). Finite element models of the human shoulder complex: a review of their clinical implications and modelling techniques. *International Journal for Numerical Methods in Biomedical Engineering*, 33(2). <https://doi.org/10.1002/cnm.2777>
- Zhou, H., & Hu, H. (2008). Human motion tracking for rehabilitation-A survey. *Biomedical Signal Processing and Control*, 3(1), 1–18. <https://doi.org/10.1016/j.bspc.2007.09.001>
- Zulkarnain, R. F., Kim, G. Y., Adikrishna, A., Hong, H. P., Kim, Y. J., & Jeon, I. H. (2017). Digital data acquisition of shoulder range of motion and arm motion smoothness using Kinect v2. *Journal of Shoulder and Elbow Surgery*, 26(5), 895–901. <https://doi.org/10.1016/j.jse.2016.10.026>

Glossary

2D	In two dimensions
3D	In three dimensions
Ant.	Anterior
b_v	Bias
BW	Bodyweight
CAP	Custom Actuator Products
CHUV	Centre Hospitalier Universitaire Vaudois, the partner local university hospital
CM	Centroid of the point cloud
CT	Computed Tomography
DoF	Degree of Freedom
EALS	EMG assisted load sharing
EE	End Effector
EMG	Electromyography or electromyogram
FF	Feedforward (loop)
GH	Glenohumeral
H_{ext} , H_{int}	Horizontal range of rotation, external(ext) or internal(int)
HMD	Head Mounted Display
IA	Inflammatory Arthritis
ICC	Intraclass Correlation Coefficient
Inf.	Inferior
IR	Infrared
LoA	Limits of Agreement
Lux.	Dislocation
MRI	Magnetic Resonance Imaging
MS	Musculoskeletal
MVC	Maximum Voluntary Contractions
PID	Proportional-Integral Derivative (control loop)
PID-FF	Combined use of PID and FF
pose	Position and orientation
Post.	Posterior
Q_s	Elevation score
RC, LC	Right Controller, Left Controller
RE, LE	Right Elbow, Left Elbow
RMS	Root Mean Square
RMSE	Root Mean Square Error
RoM	Range of Motion
R_s	Range score
RS, LS	Right Shoulder, Left Shoulder
R_{space}	Reachable Space
RW, LW	Right Wrist, Left Wrist
σ^2	zero-mean Gaussian noise with variance equal to σ^2
Sup.	Superior
s_v	Standard deviation
$task_{abd}$	Maximum abduction in the scapular plane with 2 kg weight in the hand
$task_{hand}$	Placing the hand behind the head
$task_{should}$	Touching the opposite shoulder
Tracker	SteamVR trackers

TSA	Total Shoulder Arthroplasty
UL	Upper Limb
V	Volume of the reachable space
$V_{\%}$	Volumetric symmetry
$V_{1,...,8}$	Vertical reachable range for the arcs 1 to 8
VR	Virtual Reality
V_{Sph}	Volume using the spherical estimator
α	Internal-external rotation angle of the shoulder
β	Abduction-adduction rotation angle of the shoulder
Vol_{theo}	Theoretical volume

Curriculum Vitae

Matteo Mancuso

Chemin des Philosophes 6
CH-1273 Arzier, Switzerland
+41(0)76 524 53 45
matteo1000@hotmail.com



Profile

Biological engineer with interests in motion tracking technologies, virtual reality and motor rehabilitation. With a background in electrophysiology and neural interfaces, with a very wide range of practical skills going from software programming to hardware design and manufacturing.

Well organized and accountable with a dynamic attitude and sense of discipline, who puts a high degree of involvement into situations which require personal extra engagement and initiative.

Education

2014 – 2019 : PhD at EPFL in the *Electrical Engineering Doctoral program*, on the topic of the *Evaluation and robotic simulation of the glenohumeral joint* (shoulder).

2012 – 2014 : Master at EPFL at the *Life Sciences and Technologies* department, *Bioengineering track*, *Biophotonics and bioimaging* orientation, *Neuroprosthetics* minor.

July-Sept. 2013: Internship in the R&D unit of Mindmaze SA (Lausanne).

2008 – 2012 : Bachelor at EPFL at the *Life Sciences and Technologies* department.

2005 – 2008 : Federal Maturity high school licence (Biology, Chemistry and Applied Mathematics) at Nyon's High School.

2001 – 2005 : Secondary school Baccalaureate (VSB), École de Grand-Champs, Gland VSB diploma and academic award as "Best Student for perseverance and investment at work".

Research projects

2019 : Hands-on doctoral project to develop a clinically usable solution for the functional evaluation of the reachable space of the upper limb, involving a customized optical tracking solution and the development of an immersive virtual reality environment to guide the patients through their exercises.

2019 : Hands-on doctoral project to develop robotic simulator for the evaluation of prosthetic instability in the shoulder complex, involving high force hydraulic actuators, high power DC motors, and complex mechanical structures.

2014 : Hands-on master project to develop a coordinated reaching (exoskeleton supported) and grasping (Neuro-Muscular Electrical Stimulation supported) rehabilitation framework, extended with environmental sensing capabilities based on a purpose-built 3D computer vision system.

2013 : Team project to develop a robot assisted reaching rehabilitation setup.

2013 : Hands-on team project aiming to develop a setup to study muscle synergies in healthy patients combining hand cinematic, EEG and EMG recordings and analysis.

2012 : Hands-on bachelor project on Near-Infrared Spectrometry, aiming to design, program and test a classifier to recognize different mental states.

Working experiences

- 2014-2019** : Research assistant in the Laboratory of Movement Analysis and Measurement (LMAM), École Polytechnique fédérale de Lausanne (EPFL), CH.
- July-Sept. 2013** : Internship at MindMaze SA on a project aimed to benchmark new models of neurophysiologic electrodes.
- July-Aug. 2012** : Professional diving assistant (PADI Divemaster) in Operation Wallacea scientific research team in Isla de la Juventud, Cuba.
- Aug. – Sept. 2010** : PADI Divemaster Internship at Oonas Diving Club in Sharm el Sheik (Egypt)
- 2005 - 2011** : Private lessons in Mathematics and French to secondary schools students.
- 2004 - 2006** : Found raising activities to support the CNN Triathlon club of Nyon.

Additionnal skills

Programming

- C#/Unity:** three years developing a set of virtual reality tests to guide patients through functional evaluation exercises
- C/C++:** three semesters practice at EPFL (Institute of Technology) along with two projects for “modelling the behaviour of organised animal societies: Ants and Birds”
- Matlab:** three semesters practice at EPFL, plus two projects of biological problems modelling. “The Biochemistry of Sea-shells formation” and “A Brain-Computer Interface based on Near-Infrared Spectroscopy”
- Labview:** Extensive use during the master project (1 semester), especially to build a computer vision system and to interface it with an exoskeleton, a microcontroller and a Neuro-muscular Electrical Stimulator.

Languages

- Italian:** Mother Tongue (perfectly bilingual)
- French:** Mother Tongue (perfectly bilingual)
- English:** Diploma Cambridge Level 3/2 and 6 years of studies at school. Current use of the language for academic purposes

Soft skills

- Leadership training:** within the framework of a professional PADI divemaster to direct teams of scubadivers in potentially life-threatening conditions.
- First aid training:** Niveau 1, Société Internationale des Sauveteurs du Léman; PADI rescue diver; EFR Oxygen provider.

Journal Papers

Mancuso, M., Arami, A., Becce, F., Farron, A., Terrier, A., and Aminian, K. (October 1, 2019). "A Robotic Glenohumeral Simulator for Investigating Prosthetic Implant Subluxation." ASME. *J Biomech Eng.* January 2020; 142(1): 015001

Conference Proceedings

M. Mancuso, A. Arami, A. Terrier, F. Becce, A. Farron, and K. Aminian, "Testing of a robotic platform for the evaluation of prosthetic stability of the glenohumeral joint," in International Shoulder Group, 2018

F. V. P. Goetti, M. Mancuso, N. Gallusser, K. Aminian, "VR-based Instrumented Test For The Objective Assessment Of The Shoulder Function," 2018

E. Sarshari, M. Mancuso, A. Farron, A. Terrier, D. P. Pioletti, and P. Mullhaupt, "EMG-based vs optimization-based prediction of muscle forces in human upper extremity," in 8th World Congress of Biomechanics, 2018, pp. 5–6.

M. Mancuso, A. Terrier, F. Becce, A. Farron, K. Aminian, Development of a robotic platform for the evaluation of prosthetic stability of the glenohumeral joint, 23rd Congress of the European Society of Biomechanics (ESB), Sevilla, Spain, 2017

M. Mancuso, A. Terrier, F. Becce, A. Farron, K. Aminian, Development of a robot for the simulation and surgical planning of total shoulder replacement, 5th Switzerland-Japan Workshop on Biomechanics (SJB), Zermatt, Switzerland, 2017

A. Farron, F. Becce, Y. Boulanaache, M. Mancuso, Simulated overcorrected glenoid implant, in Musculoskeletal Research day, Lausanne, Switzerland, 2016

M. Mancuso, N. Wang, F. Vauclair, K. Aminian, A novel virtual reality based approach towards the instrumented functional test of the shoulder, in International Shoulder Group, 2016